Dissertation

submitted to the

Combined Faculties for the Natural Sciences and for Mathematics

of the Ruperto-Carola University of Heidelberg, Germany

for the degree of

Doctor of Natural Sciences

Presented by

M.Sc. Sedef Dalbeyler

born in Izmir, Turkey

Oral examination: November 11, 2021

Transcriptional Profiling of Astrocytes in Major Depressive Disorder

Referees: Prof. Dr. Thomas Kuner
Prof. Dr. Rainer Spanagel

Acknowledgement

Throughout my doctoral journey, I have collected experiences, which influenced to shape my perception of science and helped me to develop as a human. It has been a long path with peaks and valleys where it would not have been possible to accomplish it without the inspiration and encouragement of many people.

First of all, I would like to thank my supervisor Dr. Michal Slezak, who gave me the opportunity to conduct my Ph.D. research in his laboratory. We have worked together for more than six years, during which he enabled me to acquire various prominent scientific skills. Michal gave me the chance to expand my knowledge in neuropsychology by encouraging me to attend top international conferences and schools. Thank you for our brainstorming meetings that helped me develop my scientific arguments and vision. Lastly, many thanks for the help during the writing process.

Next, I would like to thank Prof. Dr. Thomas Kuner for mentoring my project, supporting me through the frequent meetings with our research group, and providing essential input during my thesis writing. Besides, I would like to express my sincere gratitude to Prof. Dr. Rainer Spanagel for being on my Thesis Advisory Committee, giving valuable comments, and participating in my defense as a chairperson. Also, I am very thankful to Prof. Dr. Gudrun Rappold and Dr. Annarita Patrizi for the time spent evaluating my work and attending my defense.

My Ph.D. project was supported by the collaboration between Boehringer Ingelheim and BioMed X Institute. I would like to express my sincere gratitude to Prof. Dr. Bastian Hengerer for all the support and crucial contribution during the inspiring Topic Committee Meetings. I would also like to acknowledge Dr. Christian Tidona for providing such a dynamic and creative research environment at BioMed X.

Throughout my doctoral work, I have collaborated with many admirable people whom I want to thank here. I am very grateful to Prof. Dr. Christopher Pryce for the comprehensive training on the mouse model of chronic stress. Many thanks to Dr. Claudia Pitzer and Barbara Kurpiers for their assistance in setting up the infrastructure for animal work in the facility. I would also like to thank Dr. Vladimir Benes and the EMBL GeneCore Facility members for the training in RNA sequencing methodologies, the assistance in critical moments, and the friendly environment. Besides, I would like to express my gratitude to Dr. Coralie Viollet and Dr. Nathan Lawless for their contribution to my thesis and their insightful input to accomplish my RNA-sequencing experiments.

Many thanks to every member of my research group who helped this Ph.D. happen. Special thanks to Dr. Dolores Del Prete, who supported me throughout my doctoral work by offering me scientific and human advice. I would like to thank Dr. Valentyna Dubovik for her constant wise suggestions in diverse aspects. Also, Carmen Menacho Pando, who conducted the animal work presented in this thesis, thank you for the joyful moments during late evenings in the lab. A sincere thank you to Shringarika Singh for creating a constructive and supportive environment. Many thanks to Laura Schmidt for making the last months of work going smoothly and enjoyable. I would also like to thank the BioMed X family for the fruitful scientific conversations and friendly environment. Particularly, a big thank you to Yvonne Stappenbeck for all the understanding and positive support. Next, a sincere thank you to Dr. Özdemirhan Serçin, who provided me creative ideas and advised me throughout my Ph.D. path. Also, big thanks to Nicole Giebel for contributing to my thesis by offering me help with the translation.

I am especially grateful for the endless love, support, and sacrifice of my family. Although science was a new field for them, without hesitation, they jumped into the adventure and followed the path with me. Most importantly, special thanks to my mother, Zehra, who inspired me to follow my dreams, taught me to be comprehensive, and offered me the freedom to make mistakes and grow up as a strong person. Thank you for the love and courage, mother. Also, I would like to express my genuine appreciation to my brother Oğuz who provided me exceptional backing and encouragement, which without him, I would not be able to start my scientific path. Along with him, big thanks to Sevi, who strengthened the support and understanding for my decisions. A warm thank you to my little Su for the love and happiness she gives me. Moreover, I am thankful to my grandfather, who facilitated me to pursue my studies and illuminated a humanistic path to follow. Besides, I would like to thank my big family Buz, for understanding me and offering me help (particularly Fethiye and Tanguy), irrespective of distance. Also, a sincere thank you to my family de Jaime-Soguero for being comprehensive and endorsing my doctoral path. Especially, thank you for the generous support you offered me during the last weeks of my thesis; it helped me tremendously to finish it smoothly. In addition, I would like to thank my friend Selen for sharing wonderful moments during our studies and for encouraging me in every aspect despite being far.

Finally, I would like to express my gratitude to my husband, companion, colleague Anchel who supported me throughout my Ph.D. by relaxing me through Skype with piano concerts, sending me letters, and motivating me with his passion for science. I appreciate your understanding during the long-distance years and challenging moments. Your warm heart and true humanity provided me exceptional back-to-back support during these years. Thank you for inspiring me and for being a role model for the next generations by illustrating how one can be an outstanding scientist and have morals for humanity.

Abstract

Major depressive disorder (MDD) is a complex mental disease with a high medical, social, and economic burden. Despite this harm, still little is known about the pathophysiology of MDD, while available pharmacotherapy is only partially effective. Therefore, understanding depression by investigating the neurobiology of the disease is an essential step to help patients.

Numerous studies have discovered alterations in functional, morphological, cellular, and transcriptional properties of brain circuits controlling mood. Common findings reveal abnormal activity, changes in cellular composition, and molecular profile in the prefrontal cortex, a brain center of stress response. Nevertheless, investigation of the underlying pathology at cellular resolution has been hampered by the lack of tools enabling studies at required cellular and molecular specificity. Previous studies demonstrated that astrocytes mediate transcriptional effects of main stress hormones, glucocorticoids, on the brain. We, therefore, hypothesized that astrocytes' dysfunctions mediate biological symptoms of depression and that it would be possible to identify disease relevant cell-type-specific transcriptional changes.

In this project, we conducted a systematic approach to investigate changes in astrocytes' transcriptome in human depression and a rodent model of chronic stress. We established methods for efficient and specific RNA isolation from astrocytes and subsequently applied them to test our research hypothesis. Out of several available methods, we selected a strategy based on fluorescent-based cell sorting of human nuclei labelled with cell type-specific antibodies. When our project started, such methods were available only for two brain cell types: neurons and oligodendrocytes. Thus, we provide the first positive selection approach for isolating astrocytic nuclei from frozen human postmortem brain samples. Furthermore, we adopted standard strategies for isolation of astrocytes from adult mouse brain, and we optimized those techniques to be now applied for small tissue volume, like prefrontal cortex or hypothalamus.

Next, we employed these novel methods for gene expression studies of astrocytes' nuclei from frozen tissue samples from healthy controls and depressed suicides and in astrocytes isolated from the adult mice brain samples collected from animals exposed to chronic stress. As a result, we report novel genes linking astrocyte-specific molecular processes with altered neurobiological functions in depression.

In summary, we developed protocols to facilitate gene expression profiling of astrocytes in humans and mice. Our findings suggest that changes in astrocytes' molecular profile may underlie the neurotransmitter imbalance in depression. This study points to astrocyte-specific pathways as potential therapeutic targets for reversing psychiatric phenotypes.

Zusammenfassung

Die Depression (Major depressive disorder, MDD) ist eine komplexe psychische Erkrankung, die eine schwere medizinische, soziale und wirtschaftliche Belastung für die Gesellschaft darstellt. Trotz dieses Schadens ist wenig über die Pathophysiologie der Depression bekannt, während die vorhandenen Pharmakotherapien nur bedingt wirksam sind. Deshalb ist es unerlässlich, ein besseres Verständnis über die Neurobiologie der Depressionserkrankung zu erlangen, um den Patienten Hilfe leisten zu können.

Zahlreiche Studien entdeckten Veränderungen der funktionalen, morphologischen, zellulären und transkriptionalen Eigenschaften der Gehirnschaltkreise, die die Stimmung kontrollieren. Häufige Erkenntnisse umfassen abweichende Aktivitäten, Veränderungen in der Zellkomposition und des molekularen Profils des präfrontalen Cortexes, welcher ein Hirnzentrum für Stressantwort ist. Dennoch sind Untersuchungen der zugrunde liegenden Pathologie in zellulärer Auflösung durch das Fehlen von Werkzeugen erschwert, um Studien mit der dafür notwendigen zellulären und molekularen Spezifität durchzuführen. Vorangegangene Studien zeigten, dass Astrozyten transkriptionale Effekte von Hauptstresshormonen, den Glucocorticoiden, auf das Gehirn herbeiführen. Demzufolge stellen wir die Hypothese auf, dass Fehlfunktionen von Astrozyten biologische Symptome der Depression hervorrufen und somit für die Erkrankung relevante Zelltyp-spezifische transkriptionale Veränderungen identifiziert werden können.

In diesem Projekt untersuchten wir mit einer systematischen Herangehensweise Veränderungen im Transkriptom von Astrozyten bei Depressionspatienten, sowie in einem Nagetiermodell von chronischem Stress. Wir etablierten Methoden für die effiziente und spezifische RNA-Isolation von Astrozyten und nutzten diese anschließend für die Überprüfung unserer Hypothese. Aus den verschiedenen vorhandenen Methoden wählten wir eine Strategie aus, die auf Fluoreszenz-aktivierte Zellsortierung von humanen Zellkernen basiert, indem sie mit Hilfe von Zelltyp-spezifischen Antikörpern angefärbt werden. Bei Beginn unseres Projekts waren solche Methoden nur für zwei Gehirnzelltypen verfügbar: für Neuronen und Oligodendrozyten. Demnach bieten wir die erste positive Selektionsmethode für die Isolation von astrozytischen Zellkernen aus eingefrorenen menschlichen Gehirnproben. Zudem wendeten wir standardgemäße Strategien für die Isolation von Astrozyten aus dem adulten Mäusegehirn an. Diese Techniken optimierten wir für die Anwendung an kleineren Gewebevolumen, wie dem präfrontalen Cortex oder dem Hypothalamus.

Danach verwendeten wir diese neuen Methoden für die Genexpressionsanalyse von Astrozyten-Zellkernen aus eingefrorenen Gewebeproben von gesundem Kontrollgewebe, Gewebe von

Suizidopfern in Folge einer Depression, sowie Astrozyten aus adulten Mäusen, die chronischem Stress ausgesetzt waren. Wir identifizierten neue Gene, die Astrozyten-spezifische molekulare Prozesse mit veränderten neurobiologischen Funktionen bei der Depression in Verbindung bringen.

Zusammenfassend entwickelten wir jeweils ein Verfahren, welches die Erstellung von Genexpressionsprofilen von Astrozyten im Menschen und in der Maus vereinfacht. Unsere Ergebnisse deuten darauf hin, dass Veränderungen im molekularen Profil von Astrozyten dem Ungleichgewicht der Neurotransmitter bei der Depression zugrunde liegen. Deshalb sind Folgestudien notwendig, um zu untersuchen, inwieweit sich Astrozyten-spezifische Signalwege als potenzielle Angriffspunkte für die therapeutische Behandlung eignen, um das psychiatrische Erscheinungsbild rückgängig zu machen.

Declaration

I, Sedef Dalbeyler, hereby declare that the work in this thesis represents my original research results. The thesis has been written by myself using the references and resources indicated. Any work of other has been appropriately marked. The work has been conducted under the supervision of Dr. Michal Slezak at the BioMed X Institute, Heidelberg, Germany.

This thesis is being submitted for the degree of Doctor of Natural Sciences at Heidelberg University, Germany, and has not been presented to any other university as part of an examination or degree.

Heidelberg, 02.09.2021 .....

Sedef Dalbeyler

List of Abbreviations

^{1}H-MRS	^{1}H-magnetic resonance spectroscopy
5-HIAA	5-hydroxyindole acetic acid
5-HT	Serotonin
a.u.	Arbitrary units
ACC	Anterior cingulate cortex
ACSA-2	Astrocyte cell surface antigen-2
APC	Allophycocyanin
ATP	Adenosine 5'-triphosphate
BA	Brodmann area
bp	Base pairs
CNS	Central nervous system
CPM	Counts per million reads mapped
CSDS	Chronic social defeat stress
CSF	Cerebrospinal fluid
DA	Dopamine
DBCBB	Douglas Bell-Canada Brain Bank
DBS	Deep brain stimulation
ddH_2O	Double-distilled water
DEGs	Differentially expressed genes
dlPFC	Dorsolateral prefrontal cortex
DPBS	Dulbecco's phosphate-buffered saline
DSM	Diagnostic and Statistical Manual Disorders
EAATs	Excitatory amino-acid transporters
ECT	Electroconvulsive therapy
ER	Endoplasmic reticulum
FACS	Fluorescence-activated cell sorting
FDA	Food and Drug Administration
FDR	False discovery rate
fMRI	Functional magnetic resonance imaging
FPKM	Fragments Per Kilobase of transcript per Million mapped reads
G x E	Gene-environment
GABA	Gamma-aminobutyric acid
GLUL	Glutamine synthetase
GluRs	Glutamate receptors
GRs	Glucocorticoid receptors

GWAS	Genome-wide association studies
HAM-D	Hamilton Rating Scale for Depression
HB	Homogenization buffer
HDACs	Histone deacetylases
HPA	Hypothalamic-pituitary-adrenal
ICD-10	International Classification of Diseases
IDM	Iodixanol medium
iGluRs	Ionotropic GluRs
IHC	Immunohistochemistry
kDA	Kilodalton
LCM	Laser capture microdissection
MACS	Magnetic cell sorting system
MAO-A	Monoamine oxidase A
MDD	Major depressive disorder
mGluRs	Metabotropic GluRs
miRNAs	MicroRNAs
mPFC	Medial PFC
MRs	Mineralocorticoid receptors
NaSSA	Noradrenergic and specific serotonergic antidepressant
NDRIs	Norepinephrine-dopamine reuptake inhibitors
NE	Norepinephrine
NG2	Neural/glial antigen 2
NIM1	Nuclei isolation medium 1
NIM2	Nuclei isolation medium 2
NIMH	National Institutes of Mental Health
NMDA	Non-competitive N-Methyl-D-aspartic acid
OCC	Occipital cortex
OFC	Orbital frontal cortex
OPCs	Oligodendrocyte progenitor cells
PAN	Immunopanning-based
PBS	Phosphate-buffered saline
PE	Phycoerythrin
PET	Positron emission tomography
PFA	Paraformaldehyde
PFC	Prefrontal cortex
PGC	Psychiatric Genomics Consortium
PMI	Postmortem interval
PRSs	Polygenic risk scores

PVDF	Polyvinylidene difluoride
PVN	Paraventricular nucleus
RDoC	Research Domain Criteria
RIN	RNA integrity number
RT	Room temperature
rTMS	Repetitive transcranial magnetic stimulation
SB	Staining buffer
SC	Somatosensory cortex
SI	Specificity index
SNPs	Single nucleotide polymorphisms
SNRIs	Selective norepinephrine reuptake inhibitors
SSRIs	Selective serotonin reuptake inhibitors
TCAs	Tricyclic antidepressants
TRAP	Translating ribosome affinity purification
TRD	Treatment-resistant depression
vmPFC	Ventromedial prefrontal cortex
VNS	Vagus nerve stimulation
ZT	Zeitgeber time

Table of Contents

1. INTRODUCTION

1.1. Major Depressive Disorder

MDD is among the most prevalent forms of psychiatric illnesses. Data collected by Global Burden of Disease Study Group showed depression as the third leading cause of illness-induced disability worldwide[1]. Diagnosis and classification of depression stand on clinically significant symptoms, largely composed of behavioral and physical impairments. MDD is characterized by the lack of interest and enjoyment in ordinary situations, decreased motivation, and a series of associated emotional, cognitive, physical, and behavioral symptoms[2]. Depression is a complex, heterogeneous, and most of the time (>75%), chronic mental disease[3]. When it is long-lasting, depression can lead to suicide and increase the attempt to do it, which makes it a life-threatening disease[4].

Therapeutic approaches to MDD such as tricyclic antidepressants (TCAs) and selective serotonin reuptake inhibitors (SSRIs) are based primarily on the monoaminergic system[5]. However, the efficiency of antidepressants is highly variable, and one-third of patients do not respond properly to standard treatment[6]. The use of antidepressants does not depend solely on efficacy but largely on a favorable profile of adverse effects and tolerability[7]. Hence, patients often experience a trial-and-error-based drug adjustment. To overcome this challenge, it is crucial to better understand depression by exploring its neurobiological mechanisms and finding biomarkers (i.e., combining neuroimaging and -omics tools). Increasing our knowledge would result in developing advanced strategies of diagnosis, patients' stratification, and optimal treatment.

In this chapter, I briefly summarize the biological knowledge of the disease at multiple levels. First, I describe the current diagnosis and classification approaches and major risk factors to develop depression. Next, I will discuss the main behavioral symptoms, respective altered biological systems, and available therapeutic strategies. Finally, I will present the translational approach to psychiatric diseases established by National Institutes of Mental Health (NIMH) and emphasize the three core neurobiological units altered in depression; circuits, genes, and cells (i.e., astrocytes), which constitute the basis of my doctoral project.

1.1.1. Current Diagnosis and Classification Approaches

Clinical diagnosis for MDD, defined by The Diagnostic and Statistical Manual Disorders (DSM-V), is a qualitative assessment based on a repetitive presence of several behavioral symptoms in a

time window of two weeks[8]. These symptoms include increased irritability, decreased interest or pleasure, significant weight change (5%), changes in appetite, sleep, and activity, fatigue or energy loss, feeling of guilt and worthlessness, and suicidal thoughts[8]. A widely used manual for the classification of MDD is the Hamilton Rating Scale for Depression (HAM-D), which is quantitative and primarily indicates the severity of the symptoms defined by DSM-V[9]. An alternative and well-accepted approach is the International Classification of Diseases (ICD-10) - Classification of Mental and Behavioral Disorders[10]. This protocol provides descriptions of MDD and specific behavioral diagnostic criteria to define depressive episodes and discriminate from other mental illnesses. Taken together, all these protocols are largely based on behavioral observations and self-reports.

Attempts were made to sub-divide depression into clusters as depressed mood, anhedonic depression, cognitive depression, and somatic depression for a better classification. However, classifying MDD solely based on behavioral characteristics was weakly associated with the etiology and the treatment response[11]. Despite the current use of these manuals in clinics, the focus on behavioral observations and self-reports does not always allow a scientific approach for building biological models. In light of these drawbacks, the focus on MDD research has shifted toward the neurobiology of disease. With that respect, a significant amount of work has been dedicated to resolving disease origin and its physiological symptoms. These studies led to the agreement that both environmental and genetic risk factors contribute to depressive phenotypes.

1.1.2. Environmental and Genetic Risk Factors

1.1.2.1.Environmental Risk Factors

Environmental risk factors include demographic aspects (e.g., age, sex, and ethnicity), social and physical environments (e.g., income inequality, inadequate housing, and migration), lifestyle (e.g., smoking, alcohol use, and diet), dysregulated circadian cycle (e.g., night shift work), early life trauma and chronic exposure to stress[7]. The latter is the most widely accepted risk factor in depression etiology[12]. Stress is a physiological response of the organism to unpredictable and uncontrollable environmental challenge[13]. Moreover, stress activates various neuronal circuits in the brain and causes multiple changes in cellular and transcriptional levels with serving primarily adaptive purposes[14]. However, outstanding and/or chronic stress can impair neural architecture (e.g., reduced dendritic tree morphology in the prefrontal cortex) and synaptic plasticity. These permanent changes are largely the consequence of enduring aberrations in glucocorticoids (GCs), main hormones mediating long-term effects of stress, which were suggested to affect and excitatory and inhibitory neurotransmition[12]. Such changes were proposed to be the basis of mood alterations observed in depression[12,14].

1.1.2.2.Gene x Environment Studies

The susceptibility to develop depression stems from genetic and environmental risk factors affecting different biological functions, e.g., endocrine and monoaminergic systems[15–17]. The genetic susceptibility to depression based on the heritability of the disease was estimated to be around 30-40%[18]. Following gene x environment (G x E) studies pointed out multiple single nucleotide polymorphisms (SNPs) linked to human phenotypes[19]. For example, polymorphisms in the gene encoding serotonin transporter (*SLC6A4*)[20] were suggested to contribute to G x E interactions. Individuals with short promoter variant showed higher susceptibility to develop depression after being exposed to early life stress events, i.e., to child abuse, compared to individuals without this allelei[19–21].

Epidemiologic studies revealed that gene network controlled by GCs has predictive potential for MDD development and treatment[23,24]. For example, polymorphisms in the gene encoding FK506-binding protein 5 (*FKBP5*), a co-chaperone of the glucocorticoid receptors (GRs), were correlated with altered stress response, suicide attempt, and depression[25,26]. GRs are the essential components of the hypothalamic-pituitary-adrenal (HPA) axis mediating the feedback mechanism known to be impaired in depression (detailed explanation in section 1.1.3.1)[27]. Under the inactive state, GR takes part of a multiprotein complex (consisting of heat-shock protein 90, FK506-binding protein 4 (FKBP4), and co-chaperone p23) and localizes in the cytoplasm. When the ligand (glucocorticoid) binds, the FKBP5 is replaced by FKBP4, leading to GR translocation into the nucleus and binding to glucocorticoid response elements in the promoter of glucocorticoid-responsive genes and activates their transcription[26]. It was suggested that FKBP5 activity could regulate the GR sensitivity[28]. Upon FKBP5 binding to the multiprotein complex, the affinity of ligand binding was demonstrated to be diminished. Aberrant FKBP5 expression was one of the suggested mechanisms of 'glucocorticoid resistance', a typical biological symptom in depression (see below).

1.1.2.3.Epigenetics

Except for genetic predisposition, a number of post-translational modifications were suggested to contribute to MDD[29]. Two well-known epigenetic mechanisms operating in the core histones and implicated in depression are acetylation and methylation[29].

DNA acetylation describes the addition of the acetyl group to lysine residues by histone acetyltransferase. This process increases the open state of chromatin, which affects gene expression. The removal of acetyl is regulated by histone deacetylases (HDACs) and reduces transcription[30]. Alterations in histone acetylation were observed in depressed patients' postmortem brain and blood samples, such as increased acetylation[31] (in – acH3K14) and dysregulated HDAC

expression (reduced HDAC2, increased HDAC4[32], and decreased Sirtuin 1 (*SIRT1*))[33,34]. The latter study suggested that changes in the *SIRT1* levels correlate with remission. Consequently, *SIRT1* could be a potential biomarker for MDD.

DNA methylation is the addition of methyl group to cytosine residues of CpG dinucleotides, catalyzed by DNA methyltransferases[35]. This process mainly triggers a decline in gene expression. Studies performed in blood and brain samples[29,30] revealed alterations in the methylation of genes belonging to distinct pathways (i.e., glucocorticoid and glutamatergic systems)[29,30]. One study reported hypermethylation in the GR gene (*NR3C1*, reduced expression) in suicide patients with a childhood abuse history[36]. This finding emphasized that environmental factors (e.g., early life trauma) may lead to perturbed epigenetics regulations[29]. Another work showed hypomethylated regions in glutamate receptor (*GRIK2*, increased expression) and brain-enriched guanylate kinase-association protein (BEGAIN, decreased expression)[37] in suicide patients, in a particular cellular compartment - glial cells. These changes were suggested to contribute to impaired synaptic communication and/or synaptic plasticity because GRIK2 and BEGAIN are involved in excitatory synapse regulation[37].

1.1.2.4.Genome-Wide Association Studies

The latest meta-analysis of genome-wide association studies (GWAS) based on 246,363 cases and 561,190 controls, published by the Psychiatric Genomics Consortium (PGC), 23andMe, and UK Biobank collaboration, identified 102 independent-significant loci, 87 of which were confirmed in an independent sample[38]. The authors found risk genes (e.g., *SORCS3*, *NEGR1*, and *TCF4*) linked to various systems such as excitatory synapse, modulation of synaptic transmission, and behavior. Contradicting to the previous findings, in this study, serotonin-related genes, e.g., *SLC6A4*, were not directly associated with depression. These data support the argument that a single model system (i.e., alteration of serotonin system or any individual gene) is not enough to explain the complex and polygenic phenotype of MDD[39].

Interestingly, overlapping the identified genetic variants across 13 brain regions (employing the GTEx database) demonstrated a significant correlation between the frontal brain regions (Brodmann area (BA) BA9 and BA24) and depression (Fig. 1.1)[38]. Furthermore, the risk genes (e.g., *MEF2C* – involved in synaptic function and *TCF4* – implicated in excitability of prefrontal cortex neurons) analysis displayed a significant enrichment in the prefrontal cortex (PFC), highlighting the functional importance and implying the PFC as the network hub in the altered circuitry of depression.

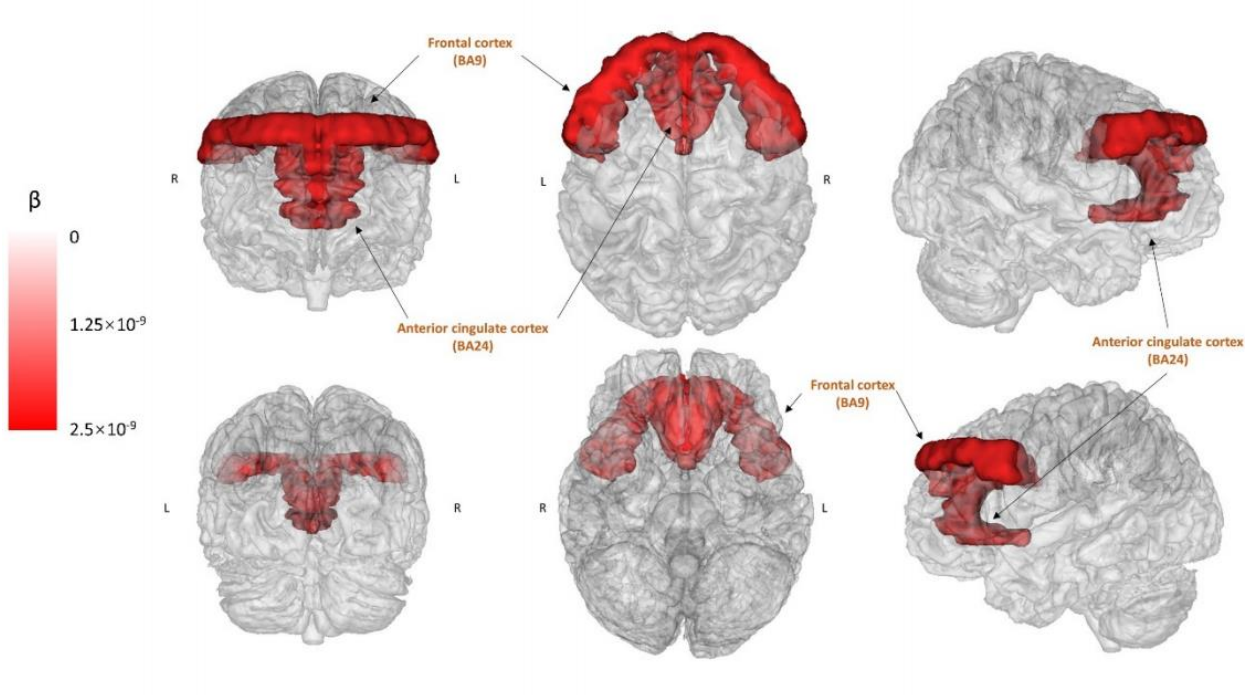

Figure 1.1. Association of Prefrontal Cortex and Depression. The brain regions (red) that were significantly enriched for depression variants. β: Enrichment estimation, BA: Brodmann area. From Howard et al. (2019)[38].

Additional efforts have been made to understand the complexity of the disease by assessing the polygenic risk scores (PRSs)[38,40], which give an individual-level estimation of the genetic liability to a trait[41]. Halldorsdottir et al. (2019) investigated whether a depression PRS, calculated from a GWAS conducted on adult subjects, can predict childhood depressive symptoms and the onset of the diseases[42]. Indeed, the authors reported that depression PRS might indicate depressive phenotypes at youth and early ages; however other parameters as environmental factors (e.g., childhood abuse) need to be considered in the prediction system[42].

Notably, genetic studies are beneficial for understanding depression and possibly for the identification and characterization of patients. Still, the clinical applicability of such investigations is premature. Further research involving well-controlled clinical studies is necessary to expand the sample size, study power, and heterogeneity of the cohorts for obtaining larger effect sizes.

Collectively, environmental risk factors are highly connected to genetic factors[7]. Together these factors can impair various systems, such as the endocrine system (i.e., HPA-axis), with a multitude of consequences on cellular signaling and behavioral phenotypes.

1.1.3. Biological Manifestations Associated with Depressive Symptoms

1.1.3.1. The Hypothalamic-Pituitary-Adrenal Axis

MDD symptoms, such as significant weight change, appetite change, and fatigue or energy loss, were attributed to the imbalance in the endocrine system. A common finding in MDD is the hyperactivity of the HPA-axis[5], a network of endocrine interactions regulated by innervations and hormones (Fig. 1.2)[43]. The end product of the HPA-axis activity is the release of glucocorticoids (cortisol in humans and corticosterone in rodents), which can bind to their receptors (mineralocorticoid receptors (MRs) and GRs) in several tissues and regulate physiological changes as metabolic, cardiovascular, immune, and behavioral processes[27,44].

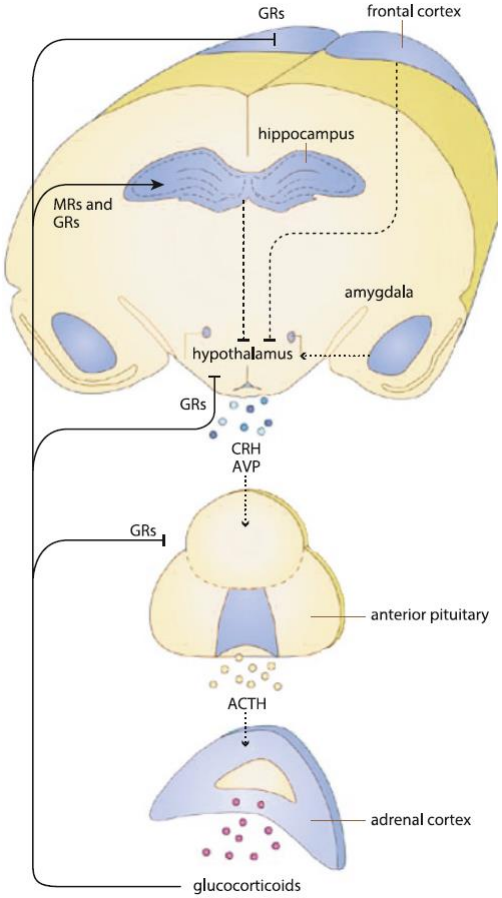

Figure 1.2. The Hypothalamic-Pituitary-Adrenal Axis. Triggered stress (i.e., initiated from the amygdala) response activates the HPA-axis and the release of hormones. The end product is the glucocorticoid, which can bind to the receptors (MRs and GRs) and affect peripheral and brain functions. The dashed lines illustrate the neural network involving the frontal cortex, hippocampus, and amygdala. The black lines show the negative feedback loop.
GRs: Glucocorticoid receptors, MRs: mineralocorticoid receptors, CRH: Corticotrophin-releasing hormone, AVP: Vasopressin, ACTH: Adrenocorticotrophic hormone. From Franklin et al. (2013)[43].

The regulation of this mechanism occurs via nongenomic and genomic effects. Nongenomic effects have more rapid actions and are regulated by a plasma membrane-bound MR[45]. Genomic effects are mainly operated through transcriptional actions of GCs on GRs (black lines, Fig. 1.2)[43,45]. GRs display low affinity to GCs, enabling a much higher dynamic range of response, being fully occupied at the circadian peak of plasma concentrations and upon stress exposure. In

addition, GRs mediate the negative feedback mechanism of the HPA-axis, primarily through transcriptional regulation of target genes[27].

Diverse findings linked the HPA-axis hyperactivity and biological phenotypes in depression. For instance, it was shown that hyperactivity could cause increased pituitary and adrenal volume and high glucocorticoid levels in the saliva, cerebrospinal fluid (CSF), blood, urine, and brain[5]. One possible explanation was that the diminished negative feedback mechanism of the HPA-axis (through aberrant GR signaling) could lead to the hyperactivity of the system in patients with depression[27].

Despite the arguments on the dysregulation of the HPA-axis and its potential use as a biomarker (e.g., assessments of blood GR levels and dexamethasone suppression test), no direct clinical applicability has been observed. One of the reasons might be that not all MDD patients present similar levels of alterations on the HPA-axis functioning. An extensive meta-analysis concluded that almost half of the MDD patients had similar cortisol levels before and after antidepressant treatments despite noticed clinical improvements[46]. This controversy might be due to; i. the variations among depressed patients, ii. responsiveness to treatment, and iii. the methodological discrepancy between the studies (e.g., samples collection time, since profound fluctuation of GCs blood concentration were reported in MDD).

To increase the translation towards clinics, Menke et al. (2019)[28] suggested combining neuroendocrine results with molecular profiling. The authors claimed that this approach could enhance the development of strategies for patients' stratification and matching them with appropriate treatments. Likewise, an independent study revealed the dexamethasone-stimulated gene expression assessment as a possible biomarker for depression-related GR resistance by testing glucocorticoid sensitivity and connecting to FKBP5 function[47].

1.1.3.2.Sleep

Sleep disturbances frequently associated with MDD include insomnia, hypersomnia, and restless legs syndrome[48,49]. Interestingly, sleep regulation in depressed patients was shown to vary from healthy individuals in terms of expanded periods of wakefulness and lowered sleep efficiency (i.e., elevated sleep onset latency and decreased total sleep time)[48]. Disruption of sleep and circadian rhythm was suggested either as a risk to develop depression or a core symptom of the disease itself[48]. Two known biological processes regulating sleep mechanisms are the circadian and homeostatic activities[48].

Circadian rhythms are 24-hour, physiological, and behavioral processes operated by the cellular and molecular oscillatory activities, which are mainly controlled by the suprachiasmatic nucleus[49].

The homeostatic process is involved in driving the person into sleep, and its activity is relative to the total of time elapsed since last sleep. Its function is to adapt the time passed until the next sleep by regulating the depth and duration of the sleep[48]. Hence, circadian clock and homeostatic activities are working concomitantly to keep proper sleep activity, while their alterations can result in sleep disruptions observed in depressed patients[48,49].

1.1.3.2.1. Sleep-Based Therapeutic Approaches

Wake-light therapy is supposed to counteract circadian rhythm and sleep disturbances in depression with long lasting effects. Patients usually stay awake for a night and/or the following day (max. 36 hours). A rapid effect is observed typically after the first wake therapy with a significant decrease in depressive symptoms (40-60% remission)[50]. Likewise, combining light therapies with conventional antidepressants was shown to enhance treatment efficiency[51]. Importantly, individual differences such as patient chronotype and lifestyle should be taken into consideration for the most efficient outcome[51]. Understanding the systemic mechanisms of wake-light therapy may help to expand and increase the efficiency of available pharmacotherapies (e.g., SSRIs).

1.1.4. Monoaminergic Theory of Depression

By far, the most explored concept in the neurobiology of MDD is a dysfunction of monoaminergic systems[5]. Serotonin (5-HT), dopamine (DA), and norepinephrine (NE) were postulated to mediate many of MDD symptoms, and a large body of evidence supporting their critical role in MDD stems from the fact that most current pharmacotherapies operate mainly through their receptors and transporters[5]. These systems share several anatomical and physiological features, like the release from small nuclei sending projections throughout the central nervous system (CNS) or their neuromodulatory function.

1.1.4.1.Serotonin

The primary source of serotonergic neurons is in the dorsal raphe nucleus, which projects towards almost all parts of the brain, maintaining multiple functions such as the regulation of energy metabolism (i.e., affecting the mitochondrial function), immune system (i.e., through cytokines), and emotional processes[52].

Clinical studies pointed out perturbations in the serotonergic system, such as lowered concentration of 5-hydroxyindole acetic acid (5-HIAA, the principle metabolite of serotonin) in CSF[21], reduced serotonergic neurons activity[53], and increased monoamine oxidase A (MAO-A) activity in the CNS of depressed patients[54]. In line with these findings, the efficacy of SSRIs was

postulated to operate through the increase of synaptic 5-HT concentration, thus reversing a reduction of serotonergic transmission[52]. However, contradictory clinical evidence demonstrated enhanced serotonergic activity in depression, such as increased levels of 5-HIAA in jugular vein[52] and elevated levels of serotonin metabolites in the plasma[7]. One of the main reasons for the controversy on serotonin level imbalance is the difficulty to measure serotonin transmission using available techniques (e.g., positron emission tomography (PET)), which assess the extracellular concentrations of serotonin by considering it as a 5-HIAA/5-HT ratio[52]. Furthermore, solely the changes in the concentration of serotonin may not be the leading cause of depressive states. Another factor, as adaptive changes, for instance, in the receptor sensitivity or density, may play a role[55].

For example, Johnson et al. (2011) reported reduced levels of R1 (cell division cycle associated 7 like, CDCA7L), an upstream transcriptional repressor of MAO-A, and increased levels and activity of MAO-A in postmortem brain samples (PFC, BA8/9) from MDD subjects[56]. Besides, the authors showed that SRRI treatment did not affect both R1 and MAO-A expression levels in the PFC samples. Hence, the proposed mechanism was that decreased levels of R1 could lead to increased MAO-A expression levels and activity. In turn, this finding brings up the possibility of R1 as a new target for pharmacological treatment[56].

Consequently, although highly implicated in MDD, the exact mechanism(s) underlying serotonergic system alterations observed in MDD patients is not fully understood.

1.1.4.2.Dopamine

Dopaminergic pathways arise from the substantia nigra and ventral tegmental area, from where they project towards the hypothalamus, pituitary, frontal cortex, striatum, and cingulate cortex, mediating the regulation of movement, reward pathway, and motivation[14,57].

As a result of being connected in the reward circuitry (i.e., positive affect network, Fig. 1.5), alterations in dopaminergic transmission in depression were associated with weakened motivation and anhedonia[5]. Particularly, reduced dopamine transmission (measured through PET imaging of DA transporter binding) was observed in a subgroup of MDD subjects with anhedonia[57]. Furthermore, upon amphetamine administration, MDD patients exhibited an enhanced rewarding phenotype, indicating the amphetamine induced dopamine transmission[57].

Evidence from studies conducted on the animal models suggested that alteration in dopaminergic receptors (D_2/D_3) expression and changes in DA binding sensitivity may contribute to the mechanism of SSRIs action[58]. Moreover, in an independent clinical study, administration of D_2/D_3 receptor antagonist to enhance dopaminergic transmission was suggested to improve striatal

response to reward in depressed patients (measured by functional magnetic resonance imaging (fMRI))[59]. Although the latest finding points out contributions of the DA receptors for drug response, further investigations need to be pursued to clarify the mechanism.

1.1.4.3.Norepinephrine

Noradrenergic neurons primarily project from the locus coeruleus towards multiple brain regions (limbic and cortical regions, cerebellum, and spinal cord)[14] regulating the central immunomodulatory processes, sleep, and emotional stress responses[60].

Literature data showed lowered levels of NE in CSF, increased MAO-A activity in CNS[21], and alterations in adrenergic receptors, particularly in the PFC of depressed patients[61,62]. However, the specific mechanism of action is unknown and clinical studies refer to efficient pharmacological treatments such as selective norepinephrine reuptake inhibitors (SNRIs), mainly based on observed amelioration of symptoms.

It is worth noting that 5-HT, DA, and NE display mutual regulation (Fig. 1.3)[63]. This interaction should be taken into account for better understanding of the disease and drug design.

1.1.4.4.Current Pharmacotherapies: Focus on Monoamines

First generation antidepressant drugs, monoamine oxidase inhibitors (phenelzine), and TCAs (imipramine) were discovered by serendipity while investigating antipsychotic drugs[64]. One of the suggested mechanisms is that TCAs inhibit the synaptic reuptake of monoamines, resulting in mood elevation[2]. Observed common side effects are dry mouth, sweating, changes in weight, tremor, and sexual problems[6]. The treatment mostly starts with a low dose (due to side effects), followed by progressive dosage elevation. Since the severity of the side effects (sedation and toxicity) is developing much faster than the therapeutic effect of the drugs, patients have difficulties tolerating the treatment and most often drop[2]. Consequently, TCAs are not the first choice to treat depression anymore.

Currently recommended first-line treatments are so-called second generation antidepressants such as SSRIs (fluoxetine), serotonin-norepinephrine reuptake inhibitors (venlafaxine), noradrenergic and specific serotonergic antidepressant (NaSSA) (mirtazapine), and norepinephrine-dopamine reuptake inhibitors (NDRIs) (bupropion)[65–67]. The significant side effects are nausea, headache, dizziness, insomnia, and effects similar to TCAs but less severe at the first approach[65].

The slow action of SSRIs is a bottleneck of successful therapy of depression. It can adopt up to eight weeks to see the effect of the treatments compared to their placebo controls[6]. The reasons for the delay are not completely understood. It is believed that monoamines contribute to

neurobiological adaptive changes occurring at pre-and post-synaptic levels. For example, animal studies showed that repeated SSRI treatment could reduce the functional sensitivity of the receptor. Thus, auto-receptor desensitization might explain the delayed outcome[66].

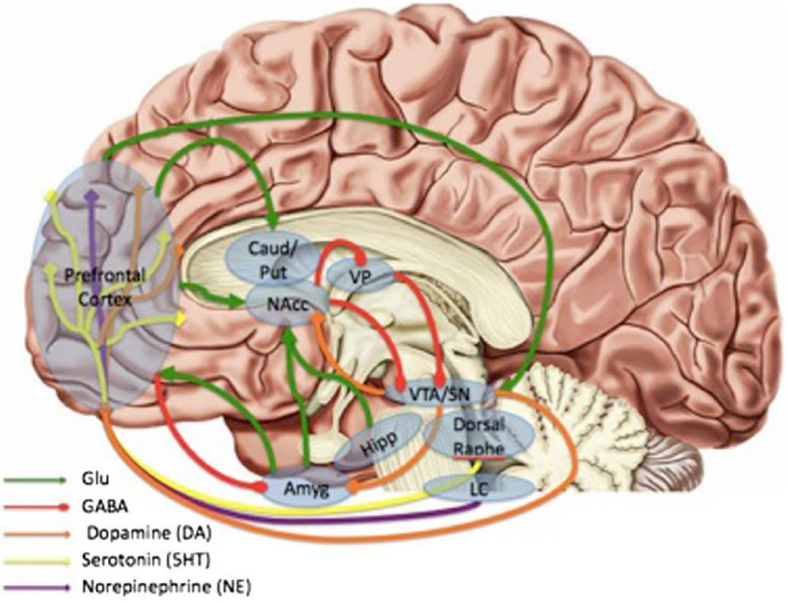

Figure 1.3. The Neurotransmitter Systems: The Brain-Wide Basis of Depression. The lines illustrate the projections of each neurotransmitter system.
Caud: Caudate, Put: Putamen, NAcc: Nucleus accumbens, VP: Ventral pallidum, VTA: Ventral tegmental area, SN: Substantia nigra, Hipp: Hippocampus, Amyg: Amygdala, LC: Locus coeruleus, Glu: Glutamate.
From Treadway et al. (2014)[63].

Considering the delayed action and side effects of classical treatments, the discovery of fast and sustained reversal of depressive symptoms by ketamine, a glutamatergic receptor antagonist, suggested that glutamatergic system dysfunction may directly mediate depressive symptoms[5].

1.1.5. Glutamatergic Theory of Depression

1.1.5.1.Glutamate

Glutamate acts through glutamate receptors (GluRs), composed of two prominent families, ionotropic GluRs (iGluRs) – ligand-gated ion channels and metabotropic GluRs (mGluRs) – G protein-coupled receptors[68]. Glial cells (i.e., astrocytes) regulate the uptake of glutamate from the extracellular space by presenting high-affinity excitatory amino-acid transporters (EAATs) and convert to glutamine with the enzyme glutamine synthetase (GLUL)[69]. Glutamine is further transported back into the neurons, where it is hydrolyzed. Under normal circumstances, the glutamatergic system mediates synaptic plasticity, learning, and memory[69,70].

Glutamatergic system dysfunction was frequently reported in patients with MDD through neuroimaging and transcriptomic findings (e.g., decreased expression levels of mGluR2/3 receptors in the anterior cingulate cortex (ACC))[70]. In addition, altered ratio of glutamate to glutamine ('Glx'), measured by ^{1}H-magnetic resonance spectroscopy (^{1}H-MRS), was reported in the frontal cortex (primarily in ACC) and the occipital cortex (OCC)[70]. Furthermore, diminished

Glx levels in the PFC were associated with disease severity and treatment response[70]. Interestingly, researchers reported different results when solely glutamate was examined in MDD patients, showing decreased levels or no changes in the ACC[71]. Thus, impairments in glutamine/glutamate cycling operated through glial cells are considered crucial in the pathophysiology of depression[71].

Transcriptome studies of brain samples from MDD patients repetitively reported altered expression of genes related to the glutamatergic transmission[37,72–74]. Moreover, decreased number of dendritic spines, a postsynaptic site hosting the majority of excitatory synapses, were observed in postmortem tissue of depressed patients, particularly in frontal cortical regions[75]. The causal relationship was suggested by reports in rodent models, where the exposure to chronic stress or prolonged exposure to corticosterone led to decreased number of spines throughout the cortex, and this loss correlated with depressive-like behavior[76–78].

In addition, epigenetics studies also pointed out the glutamate neurotransmitter system imbalance in depression. Nucleosome positioning is essential for transcription, which affects the accessibility of the genomic locus and its methylation sites. It can be regulated via microRNAs (miRNAs), small non-coding RNA that can suppress the translation of target genes[35]. Dysregulated miRNA levels were detected in depressed patients' blood and brain samples, such as reduced expression of brain-enriched miR-1202 in the prefrontal region (BA44)[79]. The metabotropic glutamate receptor-4 (*GRM4*) was suggested as a target of miR-1202[79]. Interestingly, GRM4 is known to regulate glutamatergic, dopaminergic, gamma-aminobutyric acid (GABA)-ergic, and serotonergic neurotransmission[79]. Besides, the authors demonstrated that low miR-1202 blood levels in MDD patients could be employed to measure antidepressant response at baseline. These results enlighten the possibility of finding targets that can be implemented in the clinics (i.e., blood measurements) for treatment prediction in depression.

1.1.5.2.GABA

GABA is carried via specific vesicular transporters, released into the synaptic cleft via exocytosis. Ionotropic $GABA_A$ and metabotropic $GABA_B$ receptors regulate the synaptic release or uptake of GABA[80]. Astrocytes contribute to the extracellular concentration of GABA by expressing transporters (e.g., GAT-3) and further metabolizing it to glutamate[81]. GABA is involved in essential roles in the CNS as neurogenesis, neuronal plasticity, and cognitive functions[82].

Low levels of GABA in the PFC and OCC were reported together with decreased GABA concentration in the blood and CSF of patients with depression[83]. Moreover, chronic treatment with SSRIs resulted in increased GABA levels in MDD patients, suggesting that antidepressants influence the GABAergic transmission in the brain[83].

1.1.5.3.Alternative Pharmacotherapies: Focus on Neurotransmitters

Overall, alterations in the excitatory/inhibitory system were linked to MDD pathology, including reduced metabolites' levels, altered expression of neurotransmitter receptors, and changes in signaling pathways involved in synaptic regulations[84].

These data launched broad explorations of pharmacological treatments focusing on the excitatory/inhibitory system, particularly in the glutamatergic system[69]. One of the therapeutic agents suggested to be effective in MDD patients is riluzole[69,85], a US Food and Drug Administration (FDA)-authorized drug used for amyotrophic lateral sclerosis. The potential mechanism of riluzoles' action is through inhibiting the glutamate release[69,85]. Preclinical studies and clinical trials demonstrated that depressed patients treated with riluzole experienced a significant improvement in the severity of their symptoms (measured by HAM-D)[69]. However, riluzole has additional activities such as increasing the glutamate reuptake and triggering the release of other neurotransmitters (i.e., dopamine, but not serotonin).

The non-competitive N-Methyl-D-aspartic acid (NMDA) receptor antagonist ketamine gained attention since it has fast antidepressant effects (which can last up to 1-2 weeks after infusion) in individuals with MDD[84,86]. The efficacy of ketamine was found to be significantly higher for the treatment-resistant depression (TRD), where at least two or more therapeutic approaches have been tried and showed no success (measured as decreased antidepressant responses and diminished likelihood of remission)[87]. Ketamine is used as an anesthetic agent, and its exact mechanism of action as an antidepressant is unknown. It was shown that ketamine triggers both glutamatergic and GABAergic pathways activity[84,86]. Furthermore, several signaling pathways affecting the synaptic transmission and cytoskeletal structure (e.g., in astrocytes) in the medial PFC (mPFC) were linked to the beneficial action of ketamine[88,89]. The nasal ketamine (S-ketamine) administration was recently approved by the FDA to be used in combination with an oral antidepressant for TRD[87]. One limitation is the short-term efficacy of ketamine, which varies on the administration way (i.e., intravenous infusion, oral, and nasal), subtypes of patients (disease severity), and pharmacokinetics. Accordingly, studies are ongoing to uncover the mechanisms of rapid acting treatment and the long-term efficacy and safety. Nevertheless, the case of ketamine provides an important proof of concept for the possibility of finding efficient MDD treatment beyond the monoaminergic systems.

Additional strategies are ongoing to develop fast acting drugs having fewer side effects. For that purpose, researchers focused on various biological pathways known to be altered in depression[65]. Example drugs are neurokinin-1 receptor antagonist (neuropeptide affecting neurotransmission and inflammatory process, i.e., orvepitant)[90], opioid modulation (opioid μ agonist, i.e.,

buprenorphine)[91], and anti-glucocorticoids (corticosteroid synthesis inhibitors, i.e., metyrapone)[92]. However, all these approaches have efficacy variances and side effects problems.

1.1.6. Research Domain Criteria

To maximize the probability of designing more efficient therapies, a detailed understanding of underlying neurobiology is mandatory. These studies would also help to guide personalized therapies, where drugs could be prescribed based on current premises, broaden with biological parameters, and better defined disease subtypes. To facilitate understanding psychiatric diseases in the context of dysfunctional biological systems, the NIMH developed an alternative strategy of categorizing mental disorders, namely Research Domain Criteria (RDoC)[93].

RDoC is based on different behavioral domains (negative valence, positive valence, social processes, cognitive system, and arousal/regulation), disrupted across psychiatric disorders[94]. These domains represent the principal human functioning as emotion, cognition, motivation, and social behavior. Every domain consists of relevant constructs, covering various aspects of that specific functioning by explaining the behavioral elements, processes, mechanisms, and responses. Furthermore, RDoCs' units of analysis are composed of paradigms, self-report, behavior, physiology, circuits, cells, molecules, and genes (Fig. 1.4)[95]. The relationship between individual units can be further investigated in biological models to understand mental disorders' mechanisms.

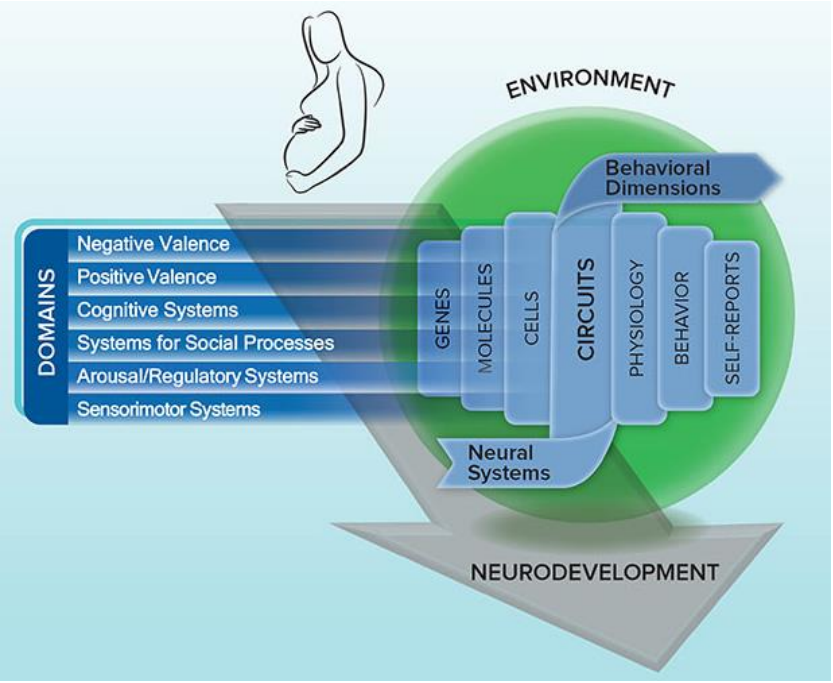

Figure 1.4. RDoC Framework. Schematic description of RDoC framework representing the domains and units of analysis (genes, molecules, cells, circuits, physiology, behavior, and self-reports)[95].

Principally, RDoC is not a diagnostic tool; instead, the initiative aims to re-orient the focus of research from behavior towards the biology of disease. Such an approach facilitates translational

research by revealing the contribution of brain circuits, genes, and cell types underlying the biological manifestation of depression[96]. Although characterizing psychiatric disorders as extremes of normal alteration in behavioral domains is arguable[97], RDoC could be a practical guideline to structure scientific research.

1.1.7. Three Core Neurobiological Units Altered in Depression: Circuits, Genes, and Cells

1.1.7.1.RDoC: Circuits

Abnormal activities in several cortical brain areas were reported in depression; the dorsolateral prefrontal cortex (dlPFC), ventromedial prefrontal cortex (vmPFC), dorsal and ventral ACC (dACC and vACC), orbital frontal cortex (OFC), and insula are well known examples[98]. Neuroimaging studies demonstrated hypoactivity (PET-based analysis) in the frontal cortical areas of individuals with depression[99]. Conversely, other researchers pointed out hyperactivity in those regions[99]. One possible explanation of these opposite findings is their association with distinct depressive behaviors. For example, it was suggested that hypoactivity in the frontal cortex causes psychomotor and executive function deficits. At the same time, hyperactivity in this region affects psychomotor agitation and rumination (repeated thinking and uncontrollable focus about the same thoughts or depressed mood)[5,100].

Subcortical brain areas were also implicated in depression, including the amygdala, hippocampus, and thalamus. Activity and volumetric changes in those brain regions affected different behavioral aspects; cognitive impairment, memory deficiency, response to negative stimuli, and social development[5,101]. Other important brain regions altered in depression are the basal ganglia and brain stem. Alterations in the basal ganglia were suggested to correlate with reward and motivation, while the brain stem can affect the arousal and reward systems by serotonergic, norepinephrine, and dopaminergic transmission[98].

A suggested explanation for the impact of stress is that upon stress exposure, aberrant overactivation of particular brain circuits could result in functional deficits due to the adaptation mechanisms in the local brain regions and ultimately cause hypoactivation[98]. Since complex behaviors engage multiple brain regions, researchers aimed to divide the neural circuit architecture into distinct networks encompassing specific psychiatric phenotypes: default mode, salience, negative affect, positive affect (reward), attention, and cognitive control circuits (Fig. 1.5)[102,103]. Certainly, these networks can overlap.

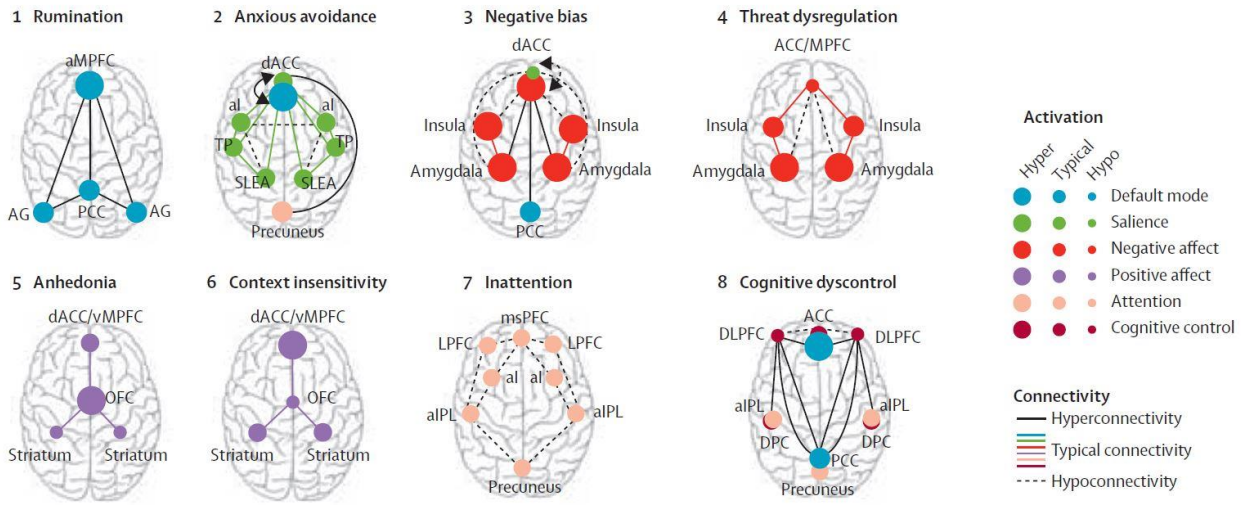

Figure 1.5. Circuits Dysfunction in Depression and Anxiety. aMPFC: Anterior medial prefrontal cortex, AG: Angular gyrus, PCC: Posterior cingulate cortex, dACC: Dorsal anterior cingulate cortex, al: Anterior insula, TP: Temporal pole, SLEA: Sublenticular extended amygdala, ACC/MPFC: Dorsal medial prefrontal cortex (includes dorsal ACC and vMPFC, including ventral-subgenual and pregenual-and rostal ACC), msPFC: Medial superior prefrontal cortex, LPFC: Lateral prefrontal cortex, alPL: Anterior inferior parietal lobule, MPFC: Medial prefrontal cortex, vMPFC: Ventromedial prefrontal cortex, OFC: Orbital prefrontal cortex, ACC: Anterior cingulate cortex, DLPF: Dorsolateral prefrontal cortex (includes anterior prefrontal cortex and inferior frontal cortex), PGG: Precentral gyrus, DPC: Dorsal parietal cortex. From Williams. (2016)[102].

i. Default mode network. It is considered as the network function when a person is in a task-free, resting state. The circuitry is defined by a functional connection of mPFC (engaged in the valuation of appetitive goals), posterior cingulate cortex (PCC) (involved in spatial navigation), and angular gyrus (participating in semantic and conceptual processes)[102,104]. As a result, reward stimuli and self-relational information in a spatial-temporal context were correlated to this network[100]. It was shown that in MDD patients, there is an overactivation and hyperconnectivity in the default mode network, which was associated with a rumination on depressive thoughts[100].

ii. Salience network. The salience circuit consists of connections between the ACC (decision making and socially driven processes), anterior insula (emotional and cognitive responses), and sublenticular extended amygdala (modulation of behavioral responses to emotionally salient stimuli), which are mainly involved in emotion, reward, and attention systems[102,105]. Imaging studies showed irregular activation in this circuitry, i.e., hypoconnectivity between the insula and amygdala and hyperconnectivity among the insula and ACC in depression. The suggested outcome was that MDD patients might have difficulties distinguishing the relevant salient cues and avoiding the negative situation stimulus[102]. Hence, patients may develop an environmental stimulus overload leading to anxiety[102,106].

iii. Negative affect network. The negative affect circuit connects the amygdala, brain stem regions, hippocampus, insula, frontal cortex, and ACC. This network comprises the perception and regulation of negative emotion cues, highly altered in depressed patients[102]. In MDD, there is a hyperresponsivity to negative stimuli, a negative bias to sadness. Likewise, a loss of responsiveness to positive stimuli was also observed[107]. In addition, helplessness and increased negative focus in depression were connected to hyperactivity in the lateral habenula, a brain region involved in negative valence signal[108].

iv. Positive affect network. The positive affect circuit (reward processing) comprises the striatal nucleus accumbens, ventral tegmental area, and frontal cortex[102]. fMRI studies showed a hypoactivation of this network in MDD, indicating a loss of sensitivity to positive stimuli, particularly to reward, which can cause anhedonic behavior and affect reward driven decision making[102].

v. Attention network. It connects the frontal cortices, anterior insula, anterior inferior parietal lobule, and precuneus that are linked to alertness and sustained attention [102]. Hypoconnectivity within this network was associated with a bias for sustained attention behavior in MDD patients. Likewise, dysregulated attention network was observed in individuals with anxiety disorders[102].

vi. Cognitive control network. The cognitive control circuit comprises the dlPFC, ACC, dorsal parietal cortex, and precentral gyrus. This circuitry is essential for cognitive functions as working memory and selective attention[102]. Besides, it takes a role in emotional functions, i.e., positive and negative emotion processing[109]. Depressed patients' brain imaging studies showed a hypoactivation in this circuit, resulting in a lack of cognitive control and emotional dysfunction[109].

Malfunctioning in the neural network can be assessed by neuroimaging techniques, which can provide valuable information for patients' stratification based on the altered circuitry. Still, several points need to be improved; development of a defined guideline for imaging and data analysis, sharing the imaging data across clinicians and performing more profound research to understand the mechanism underlying the circuit alterations[102].

1.1.7.1.1. Circuit-Based Therapeutical Strategies

Imaging findings encouraged the development of treatment approaches alternative to pharmacotherapies with the primary goal to target particular brain regions, which would result in the amelioration of depressive symptoms. Technically, such approaches are feasible through various strategies, such as repetitive transcranial magnetic stimulation (rTMS), electroconvulsive therapy (ECT), vagus nerve stimulation (VNS), and deep brain stimulation (DBS)[7].

The rTMS and ECT are non-invasive methods where the rTMS involves a magnetic focal exposure over the scalp that stimulates brain cells in a region relevant to depression[110]. The ECT sends an electric current via electrodes throughout the brain to stimulate an epileptic seizure while the patient is under anesthesia[111]. The VNS and DBS are more challenging and invasive techniques, considered particularly for individuals with TRD[110]. The VNS is based on implanting a stimulator (pulse generator) connected to an electrode wrapping the vagus nerve. In the DBS, in general, bilateral electrodes are implanted in a specific brain region (e.g., in vmPFC), and the electrodes are connected to a stimulus generator. Although all these approaches demonstrated considerable treatment efficacies (e.g., drop in depression severity, increase in remission rates, and rise in treatment responses)[110–112], severe side effects were also noticed in the short and long term (e.g., intense headaches, cognitive impairments, and surgery risk infections)[112–114]. A common difficulty for these therapies is the lack of apparent efficacy and scarcity of definitive guidelines for the clinicians.

In summary, the dysfunctions mentioned above show the brain-wide basis of depression and point out the PFC as a hub region. Considering the heterogeneity of the patients, it is necessary to answer the following critical questions: What are the molecular pathways responsible for the dysfunctions in the PFC? Which brain cell type(s) is mediating the neuronal network alterations in PFC? Answering those questions would help developing new diagnostic strategies and targeting the relevant neural pathway for an adequate treatment.

1.1.7.1.2. The Hub Brain Region in Depression: Prefrontal Cortex

The prefrontal cortex is a crucial brain region responsible for maladaptive responses to stress[84,115–117]. The PFC covers the brain areas active during emotional, social, motivational, and cognitive processes (e.g., decision making and goal directed activities)[118]. According to Brodmann areas, the anatomical delineations of the human PFC are BA8-14, BA24, BA25, BA32, and BA44-47 (Fig. 1.6A)[118]. The functional division (based on imaging data) can be broadly defined as dorsomedial PFC, dlPFC, ventrolateral PFC, OFC, and vmPFC (Fig. 1.6B)[118].

In humans, the vmPFC encompasses the lower mPFC and orbital PFC regions (i.e., BA11, 25, 24, and 32) (Fig. 1.6C)[118–120]. This circuit is involved in social and affective functions, emotion regulation, and value-based decision making[121]. The vmPFC can be further divided into subregions according to the functional differentiation such as the posterior vmPFC (BA25) – positively associated with negative affect network (Fig. 1.6C, red) and perigenual vmPFC (BA10, 32) – positively correlated with positive affect network (Fig. 1.6C, green)[119].

Imaging studies of vmPFC recorded increased posterior vmPFC (BA25) activity (Fig. 1.6C, red) and decreased perigenual vmPFC activity (Fig. 1.6C, green) in MDD patients, which were

associated with value based decision making, assigning abstract properties of reward value to stimuli, emotion regulation, rumination, and self-reflection[100,121]. These findings link known depressive symptoms with brain activity: i. heightened negative mood and bias to negative stimuli (negative affect circuit) to BA25 and ii. anhedonia (positive affect circuit) to perigenual vmPFC.

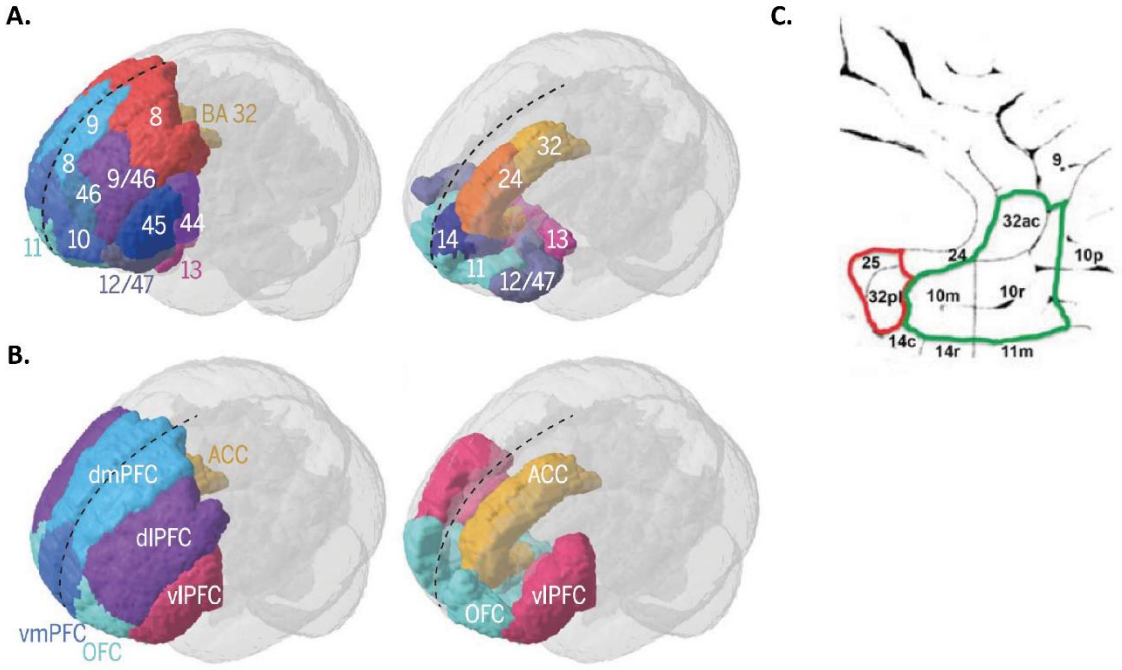

Figure 1.6. Anatomical and Functional Delineation of the Human Prefrontal Cortex. A., C. Schematic illustration of Brodmann areas (BAs) in the prefrontal cortex, including anterior cingulate cortex (ACC). **B.** Schematic illustration of common functional structures (based on neuroimaging data) in the prefrontal cortex, including ACC. **C.** Sub-regions of the medial prefrontal cortex is shown. dmPFC: dorsomedial prefrontal cortex, dlPFC: dorsolateral prefrontal cortex, vlPFC: ventrolateral prefrontal cortex, OFC: orbitofrontal cortex, vmPFC: ventromedial prefrontal cortex. Dashed black line shows sagittal midline. Not all the structures in the prefrontal cortex are shown in the scheme. From Marie Carlen (2017)[118] and Myers-Schulz et al. (2012)[119].

Furthermore, metabolic alterations in depressed patients' vmPFC emphasized the importance of this brain region. Functional imaging studies (using PET) revealed altered glucose metabolisms in the frontal cortex where the findings differed based on patient subtypes (i.e., reduced right dlPFC metabolism in severely depressed patients) and received treatment (i.e., lowered BA25 metabolism upon 6-weeks of fluoxetine treatment)[122,123]. In a recent study, patients with long term depression went under PET imaging analysis at two time points: baseline (pre-treatment) and post-treatment (with olanzapine and fluoxetine combination), where the glucose metabolism was measured in the amygdala and the subgenual/vmPFC (BA25, portions of BA32 and BA33)[124]. The authors demonstrated that only treatment responders showed a decreased activity in the right amygdala and the right subgenual/vmPFC while no changes were observed in the non-responders[124]. These

data show the heterogeneity of patients and highlight the need for biological parameters to be taken into account for patients' stratification.

Moreover, cortisol administration was suggested to reduce the activation of the BA25 to sad stimuli, thus the negative emotion (in the lack of any external stressors)[125]. Besides, vmPFC was implicated in the negative feedback loop of the HPA-axis as a suppressor of the axis upon stressor removal[27,43].

Literature findings implicated the frontal cortex, specifically the vmPFC, as a hub node in stress circuitry[99,119,121]. Imaging data collected from this region could be used to predict treatment response and efficacy, and classifying patients[99,121,124,126]. One important consideration is the complexity of brain-wide circuits, implicating that data from multiple brain regions' activity states should also be included in the analysis.

Notably, investigations (i.e., molecular studies) employing human samples, particularly postmortem tissues, from MDD and healthy patients, explore how these imaging findings in humans are related to functional alterations at molecular and cellular levels.

1.1.7.2.RDoC: Genes

Large genome-wide transcriptional profiling data sets reported significant gene expression changes in the brain, blood, or CSF samples of depressed patients. MDD pathology can be described as "multigene syndrome"; small changes may affect many other genes and ultimately the whole brain circuitry[127]. Co-expression network analysis revealed transcriptional alterations in multiple biological systems, for example, the HPA-axis, neurotransmitter signaling, cytoskeleton, and development/neurotrophic signaling[20,127].

Genes and HPA-axis. Expression of several genes from the GR-dependent network was shown to be altered in MDD, such as the *NR3C1* (nuclear receptor subfamily 3, group C, member 1), *FKBP5*, *SKA2* (spindle and kinetochore-associated protein 2), *DUSP1* (dual specificity phosphatase 1), *ZBTB16* (zinc finger and BTB domain containing 16), and *SGK1* (serum/glucocorticoid regulated kinase 1)[26,47,128,129]. Yin et al. (2016) demonstrated the possible association between the HPA-axis components and suicide depression: i. suicide attempt and SNPs on *FKBP5*, *SKA2* in blood, ii. suicide death and low expression of *NR3C1* in PFC, BA9, iii. MDD and decreased expression of *SKA2* in PFC, BA9[26].

One of the hypothesized mechanisms explaining the glucocorticoid resistance in the brain assumes that GR transport into the nucleus might be diminished by an excessive abundance of chaperone proteins, FKBP5 and SKA2. This deficit can lead to an insufficiency in the feedback inhibition and an over activation of the HPA-axis[26]. However, several variables need to be considered, such

as gender differences, technical variations (e.g., total gene or transcript levels measurements), and patient subtypes. For instance, reduced expression of *NR3C1* was associated with MDD, particularly in females[130] and decreased expression of GR variants was linked to suicide completers with a childhood abuse history[131].

Genes and PFC. A microarray study conducted on depressed suicide patients' PFC tissue samples (BA44, 45, 46, and 47) emphasized a brain region-specific differentially expressed genes (DEGs) pattern. Altered genes in BA44 were related to cell adhesion (*CNTNAP3*), GABAergic system (*GABRD*), and glutamatergic neurotransmission (*GLUL*)[132]. For BA45, dysregulated genes were involved in the regulation of adenosine 5'-triphosphate (ATP) production (*PTK2B*), neurotransmitter secretion (*SYN2*), and cell adhesion (*PCDH9*). In BA46, impaired pathways related to ATP processing (*AK3L1*), cell development (*S100β*), and GABA/glutamate neurotransmission (*GLUL*, *GRIA3*). Finally, in BA47, ATP processing (*AK3L1*) and glutamatergic system (*GRM3*) were shown to be changed[132].

In conclusion, excitatory/inhibitory imbalance and energy metabolism were reported as possible brain region-specific hallmarks of MDD. Most of the relevant genes (e.g., *CNTNAP3*, *GLUL*, *AK3L1*, *S100β*, and *GRM3*) were expressed mainly in glia, particularly astrocytes and oligodendrocytes. Interestingly, a recent study also correlated glial cell pathology with excitatory/inhibitory imbalance and cellular energy metabolism in a different sub-region of PFC, BA9[133].

Genes, Circuits, GWAS, and Cells. Anderson et al. (2020) explored the molecular signatures of depression using a multiscale approach by combining the neuroimaging findings with genetics, transcriptional, and cellular levels of analysis[134]. First, independent imaging data sets (UK Biobank, ENIGMA, and Brain Genomics Superstruct Project) were investigated for the following parameters: cortical thickness, resting-state functional amplitude, and global brain connectivity. Apart from the potential clinical value of findings (e.g., the link between the cortical thickness and history of recurrent depression), disrupted cortical anatomy and function were associated with depression and negative affect circuitry. Next, the correlation analysis between the neuroimaging and postmortem transcriptional data[135] revealed that *ex vivo* cortical gene expression profile in depression was linked to *in vivo* imaging phenotypes.

Furthermore, examining the cellular component suggested that: i. 4 out of 16 cell types (used database: cortical single nucleus transcriptome[136]) were enriched for genes associated with MDD-imaging data (i.e., astrocytes, oligodendrocyte progenitors, sub-class of excitatory neurons, and interneurons), ii. astrocyte-specific genes displayed the highest spatial correlation to depression-linked neuroimaging while predominantly expressed within mPFC, anterior temporal lobes, and insular cortex, iii. astrocytes and interneurons showed the strongest enrichment for downregulated

genes in *ex vivo* MDD samples, and iv. polygenic risk for depression (used database: GWAS data[40]) was only linked to interneuron-specific genes and not glial cells. Finally, biological terms such as glutamatergic signaling, GABAergic neurotransmission, monoaminergic systems, and noncanonical WNT signaling were associated with MDD-specific neuroimaging profiling[134]. Consequently, this influential study demonstrated how a combinatory *in vivo* and *ex vivo* data analysis, including a multi-omics approach, could be extremely valuable for understanding depression, as recommended by RDoC initiatives.

1.1.7.3.RDoC: Cells

The CNS comprises multiple cell types, mainly classified as neurons, glia, and vascular cells[137]. Glial cells, which are abundant as much as neurons[138], are divided into multiple groups: astrocytes, oligodendrocytes, oligodendrocyte progenitor cells (OPCs, alternatively named neural/glial antigen 2 (NG2) cells or also polidendrocytes), microglia, and ependymal cells[138].

Healthy astrocytes are imperative for maintaining brain homeostasis, as they perform various physiological functions: providing metabolic and trophic support to neurons[139], regulating synaptic plasticity, mediating neurotransmission, controlling brain metabolism, taking part in the BBB and fluid homeostasis, and influencing sleep homeostasis, just to name some examples[139–143]. Oligodendrocytes are taking part in the myelin formation around the axons, providing structural supports to neurons[144]. They are derived from OPCs, which can maintain their proliferative properties throughout adulthood and give rise to new mature oligodendrocytes[145]. Microglia are the immunocompetent and phagocytic cells of the CNS. They can recognize and hunt dead cells, pathogens, endogenous and exogenous complexes[146]. Lastly, ependymal cells form an epithelial layer on the walls of the ventricles in the brain and the central canal of the spinal cord[147]. They possess motile cilia and play roles in cerebral fluid balance, transport of the CSF, and toxin metabolism[147].

Cytoarchitecture alterations were observed across the entire brain in MDD, with the most prominent changes observed in the salience and negative affect circuitry (Fig. 1.5). Examples include lowered glial density and enlarged pyramidal neuron size in ACC and BA24, increased microglial cell density in ACC, BA24, 25 and 24/32, and diminished myelin content, axon numbers, mature oligodendrocyte numbers in BA9 and BA46[144,148,149]. It remains uncertain whether the observed changes are causative for circuit-specific phenotypes. One of the suggested mechanisms assumes that the reduced glial loss leads to excess extracellular glutamate, which causes cytotoxicity and further neuronal cell loss[84,150]. This hypothesis implicates that functional deficit exerted physiologically by glia, particularly astrocytes, may ignite a cascade resulting in deficits at glutamatergic and GABAergic synapses.

1.2. Astrocytes in Mammals

Based on their morphological features, human astrocytes are classified into four subtypes: interlaminar, protoplasmic, varicose projection, and fibrous astrocytes (Fig. 1.7A)[140,151]. This characterization highlighted the structural complexity in the human brain, which is distinguishable from their rodent counterparts. For instance, protoplasmic and fibrous astrocytes in the human brain are larger and have higher fine processes than rodents (Fig. 1.7B)[140,151]. Interestingly, the higher featured human astrocyte can contact and encompass up to two million synapses, while a single mouse cortical astrocyte can contact approximately 100,000 synapses[139].

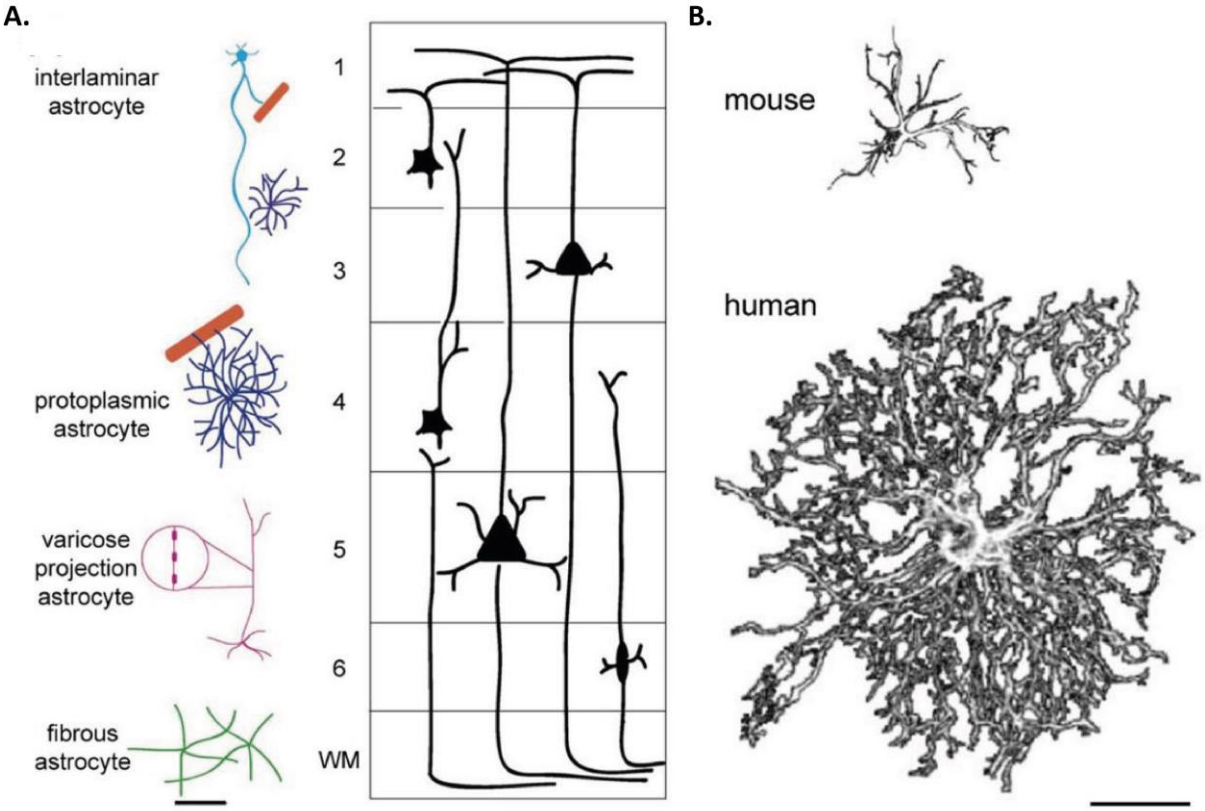

Figure 1.7. Distinct Morphology of Cortical Astrocytes. A. Schematic illustration of different sub-classes of human cortical astrocytes. Cortical layers are represented with numbers: 1-6. **B.** Graphical illustration of mouse and human astrocytes. VM: White matter. Scale bar: 25 µm. From Vasile et al. (2017)[140].

Cross-species morphological differences are also reflected by the molecular profile of different types of astrocytes[152]. For example, Zhang et al. (2016) reported that only a fraction (30%) of human astrocytic genes were also enriched in mice[152]. Notably, genes mediating crucial features and functions of astrocytes were shared, e.g., cytoskeletal protein: *GFAP* (glial fibrillary acidic protein), metabolically relevant: *ALDH1L1* (aldehyde dehydrogenase 1 family member 1) and

GLUL, membrane connexins: *GJB6* (gap junction protein beta 6) and *GJA1* (gap junction protein alpha 1), transporters of glutamate: *SLC1A2* (solute carrier family 1 member 2), and *SLC1A3* (solute carrier family 1 member 3) and water: *AQP4* (aquaporin 4)[152].

A subsequent meta-analysis corroborated these findings in five independent human and mice brain cell type-specific transcriptome datasets[153]. Besides, the authors performed functional evaluations and demonstrated that astrocyte-specific genes were primarily associated with the regulation of synaptic plasticity, glutamate secretion, and ATP metabolic processes[153]. Furthermore, similar to morphological characteristics, the unique set of genes enriched in human astrocytes displayed distinct distribution throughout the cortical layers, and this profile was similar in rodent cortical gray matter[154,155].

In summary, while human astrocytes display different morphology and molecular profile than those found in rodents, there is strong evidence that the fundamental function accomplished by astrocytes is similar across mammals.

1.2.1. The Role of Astrocytes in Depression

Deficits in glial cell number were among the first detected cellular hallmarks in MDD[156]. Multiple studies reported decreased areal fraction and packing density of GFAP-immunoreactive astrocytes in the dlPFC[157], hypertrophic fibrous astrocytes in the ACC[158], and lowered coverage of blood vessels by AQP4-immunoreactive astrocytes in the OCC of depressed patients[159]. Interestingly, numerous studies found that transcriptional deregulation of synaptic genes is accompanied by changes in a large fraction of genes enriched in astrocytes[37,72–74]. Furthermore, in animal models, astrocytes' depletion[160], blockade of glutamate transporters[161], or blockade of vesicular release from astrocytes[162] in PFC were sufficient to elicit depressive-like behaviors.

However, how proper astrocytes' functioning is changed in depression and how this deficit is translated to altered brain circuitry is not fully understood. A major reason for ignorance of astrocytic (dys)functions was the lack of tools to investigate their roles closely. For understanding the molecules and mechanisms involved by astrocytes, it is beneficial to employ techniques that can allow the acquisition of extensive gene (or protein) expression profiles.

1.2.2. Approaches to Study Astrocytes' Transcriptome in Human Depression

Progress in sequencing technology enabled the exploration of the molecular signature of multiple biological processes in parallel and unbiased ways. Notably, focusing on the changes at transcript or gene levels can influence the study's outcome. For example, a recent deep transcriptome sequencing study performed on postmortem brain samples (subgenual anterior cingulate cortex

(sgACC)) of multiple mental disorders revealed that subtle alterations in gene expression could be overlooked when the transcript-level expression analysis is not performed[163]. The authors demonstrated the importance of rare transcripts, representing functionally relevant genes related to cell junctions and synapse formation. Importantly, transcriptomics on bulk tissue homogenates have broadened the knowledge on average gene expression differences in a mixed cell population. However, gene expression changes in cell types with low transcript abundance might be undetected when total tissue RNA is studied[136]. Several solutions are available to resolve cell-type-specific molecular profiles, including astrocytes.

Astrocytes dramatically altered their gene expression profile and acquired the reactive phenotype when placed *in vitro*[164]. As a result, molecular profiling of astrocytes needs to be studied in the context of the complex cellular arrangement where it is fully functional, i.e., *in vivo* or rather *ex vivo*, through isolation methods. Together with the discovery of specific markers[165,166], efforts were made in acute cell isolation methods from postnatal rodents and fresh human brain samples obtained during surgeries[152]. Those approaches employed either transgenic mice expressing fluorophores under astrocyte-specific promoter or cell surface proteins (employing fresh rodent/human tissue)[152].

Several strategies are used to isolate different cell types from human brain tissues, such as immunopanning-based (PAN) technique[152], magnetic cell sorting system (MACS)[167], fluorescence-activated cell sorting (FACS)[168], and laser capture microdissection (LCM)[169]. All the methods can be adapted to investigate astrocytes according to the study goal and availability of resources, including equipment and starting material. When gene expression studies are conducted for investigating a disease state against a healthy condition, particular considerations should be taken. For example, the expression differences between the study groups can be rare and low. In this regard, the collected cell-type-specific population should be pure, and the genetic material has to be suitable for downstream analyses[170].

The PAN Technique. This technique is applicable to isolate major brain cells using fresh tissue samples[152]. The PAN protocol is an antibody-based selection method targeting cell type-specific surface proteins. Single-cell suspension generated upon tissue dissociation is transferred and incubated over a series of panning plates coated with antibodies, and after the washing step, either adherent cells (target population) are collected, or nonadherent cells (negative selection) are removed. Zhang et al. (2016) isolated astrocytes from fetal and adult human brain samples targeting the cell adhesion glycoprotein, HepaCAM (hepatic and glial cell adhesion molecule)[152]. This method was robust enough to compare astrocyte-specific gene expression profiles between healthy and epilepsy brains[152]. However, this protocol can be time and material consuming since

several rounds of plate incubation together with multiple antibodies are needed to enrich a specific cell type population.

MACS. The magnetic cell sorting system involves antibody labeling to target specific cellular membrane proteins using fresh tissue samples[171]. Dissociated single cell suspension is incubated with beads (coated with antibodies) and passed through the magnetic field where the labelled cells are collected. MACS protocol can be relatively fast and inexpensive since it does not require specialized expensive equipment. Furthermore, the method can enrich multiple cell types from single samples and is suitable for transcriptional analysis[172]. However, until now, only microglia was reported to be MACS-isolated from fresh human postmortem brain samples collected right after death[173].

FACS. The flow cytometry method can be applied to sort antibody-labelled cells from fixed and fresh human brain samples[168,174]. The single cell suspension is passed within a fluidic system where excitation lasers and fluorescence detectors are used to sort out cells based on the signal intensity. FACS enables to analyze and separate cells based on additional properties, such as size, granularity, and morphology, reflected in the light scatter parameters[170]. It can be used to isolate different cell types simultaneously and can be completed relatively quickly if the population of interest is abundant. A critical challenge in FACS is that the fluidic systems' stream force can cause shear stress on cells, impact their viability, and ultimately the quality of the extracted genetic material[170].

LCM. The protocol combines a fast staining procedure with laser microdissection of individual cells from fixed or frozen intact tissue samples[170,175]. Thin tissue sections should undergo either single fast penetrating staining, i.e., using HistoGene stain (for neurons)[169], or dual staining, i.e., using Nissl – GFAP (for astrocytes)[176] and peroxidase system – GFAP (for astrocytes)[175]. After that, cell isolation is performed under the microscope, essentially based on morphological assessment for the cell type of interest. The last step makes the technique laborious, subjective, and low throughput. LCM was previously used to profile gene expression of astrocytes isolated from postmortem brain samples of MDD subjects[176]. However, the low quality of isolated materials (cells and RNA) resulted in gene expression analysis of a limited gene number (via qPCR analysis). The authors could not replicate the results in an independent cell isolation experiment focusing on different brain regions[176]. Additional considerations for this technique are the exclusion of a particular cellular domain (due to microdissection), low pace, and costly equipment[170,175].

In the context of depression, there is an important limiting factor for the above-mentioned techniques, except LCM: the availability of fresh tissue, which is rarely collected from neuropsychiatric patients. The brain bank archives mostly consist of fixed or frozen postmortem

brain samples originating from healthy donors and those affected by mental illnesses. Long-term fixed tissue samples are not optimal since prolonged fixation may modify the RNA, providing low yields and quality of extractable genetic material. Consequently, gene expression studies can be performed and reproduced more accurately using fresh frozen brain samples[175,177].

This approach, however, inherits an important limitation: intact cells cannot be isolated from frozen samples. A viable alternative is to extract and purify nuclei, which contain DNA and most of RNA providing a valuable source to gain insights on epigenetic and transcriptional changes in a cell type-specific fashion[178]. Furthermore, isolated nuclei can offer insight into pre-translational RNA (e.g., long non-coding RNA and miRNA)[179]. The latter is vital for understanding the neurobiology of depression since the literature findings pointed out dysregulated long non-coding RNA (e.g., LINC00473)[180] and miRNAs (Section 1.1.5.1)[79] levels in postmortem brain samples.

Nuclei Isolation Approaches. Many efforts were made to isolate nuclei originating from different human brain cell types. Available methods are employing antibody-based FACS nuclei isolation approach targeting either nuclear membrane proteins (i.e., NEUN for neurons) or transcription factors (i.e., SOX10 for oligodendrocytes)[181] specific for the cell type of interest. This technique was shown to be robust, and reproducible transcriptome profiling was generated in both healthy and diseased samples when nuclei were purified primarily from neurons[182], oligodendrocytes[181], and to a less extend for microglia[183]. With respect to astrocytes, no protocol was published for a direct positive selection (i.e., antibody labeling of astrocyte-specific epitopes)[37].

A recently published study improved the specificity of available methods by sorting astrocytic nuclei population from non-neuronal fraction using a combination of antibodies[178]. In the strategy developed by Xu et al. (2018), the cerebellar astrocytic nuclei were isolated upon depletion of neurons and oligodendrocytes (i.e., NEUN-/OLIG2- population). However, this method was not replicable across a larger sample size[178].

Single nucleus gene expression profiling became an increasing area of interest as an alternative strategy to cell type-specific bulk nuclei isolation. Indeed, a recent work applied a single nucleus RNA sequencing approach to study transcriptional alterations in depression using fresh frozen postmortem brain samples[184]. However, two critical technical challenges were observed in this study; i. the number of transcripts obtained from glial nuclei were much lower compared to neuronal nuclei, and ii. known astrocytic transcriptional alterations in depression (previously published from the same research group and many others) could not be observed. The latter result could be due to the loss of astrocytes during the procedure, and sequencing depth may not be powerful enough to detect low abundant transcripts (personal communication).

Notably, a crucial limiting factor for single nuclei studies was the technical bias at distinguishing neuronal from glial cells[136]. This bias stands from the low fraction of glial cells captured during the nuclei isolation procedure and low RNA content in glial cells (resulting in a reduced number of detected transcripts)[136,184,185]. Likewise, a comprehensive investigation of cell types in the human cortex using single nuclei RNA-seq strategy revealed that a half of the non-neuronal nuclei population (i.e., glial cells) was not included in the data analysis, due to the poor quality and low content of RNA[186]. Consequently, astrocytes are underrepresented in single nucleus RNA-seq studies, most probably because of the relatively low RNA content in these cells.

Therefore, a method to purify selectively astrocytic nuclei is necessary to obtain a better insight into astrocytes' transcriptome. This approach requires using antibody targeting cell type-specific nuclear epitope, which is compatible with FACS and suitable to isolate astrocytes from depression-relevant brain regions (i.e., PFC).

1.2.2.1.Approaches to Study Astrocytes' Transcriptome in a Mouse Model of Chronic Stress

Even though recent investigations reported discrepancies between rodents and human astrocytes[152,154], the use of animal models can be beneficial in understanding many aspects of astrocytes' biology. Although there is no depression in rodents, valid animal models fulfilling the criteria of face, construct, and predictive validity are broadly employed[187].

The chronic social defeat stress (CSDS) paradigm applied to rodents was shown to recapitulate major molecular and behavioral alterations observed in depression, e.g., decreased social interaction, anhedonia, and neuroendocrine changes[187,188]. Importantly, astrocyte-specific dysfunctions, reminiscent of those observed in human depression, were reported in animals' brain samples after exposure to CSDS[189–191]. Nevertheless, these studies were performed using bulk homogenates of tissues, masking the exact cellular abnormalities of astrocytes in stress.

The technical approaches, which have been used to isolate cells from the human brain samples, are also valid for mice[152,165,172,192]. One additional technique available for mice is the translating ribosome affinity purification (TRAP)[193]. TRAP is based on the isolation of fluorescently labelled ribosomes, with the tag directed to a defined cell type thanks to the use of cell type-specific promoters. As a result, this method can only be applied in model animals, providing the availability of respective transgenic lines. Notably, Simard et al. (2018) employed the TRAP method to explore astrocyte contribution to depressive-like phenotypes in mice exposed to stress[194]. TRAP was performed using transgenic mice expressing GFP in ribosomes of Aldh1l1 positive cells isolated from the cortex. Following with RNA-seq, the authors reported altered gene expression associated with transcription regulation and extracellular matrix formation[194].

If research interest is to employ wild-type animals, then isolating astrocytes using endogenous surface antigens is more suitable. Considering the advantages and disadvantages of the techniques mentioned above, MACS is one of the best for isolating astrocytes and performing transcriptomics studies; it is cost-effective compared to other techniques, faster, less harmful for astrocytes due to less shear force than FACS[195]. The latter parameter is crucial to increase the viability of cells and RNA quality for further processing. Available MACS techniques are appropriate to isolate astrocytes from mice brains; however, they may require some optimizations for specific brain regions or a low amount of starting material, such as the PFC, which is highly implicated in depression.

1.3. Hypothesis and Objectives

Understanding depression by investigating the neurobiology of the observed phenotypes is an essential step for developing novel therapies. There exist rich evidence supporting the causal role of astrocytes for multiple phenotypes of MDD. Yet, glial cells remained largely ignored as a potential therapeutic focus. To facilitate target identification for developing agents, it is necessary to gain a systematic insight into the aberrant biology of astrocytes in MDD. One of the robust approaches is transcriptional profiling.

In the context of depression, this task can be accomplished through the isolation of astrocytic nuclei directly from fresh frozen human postmortem brain samples. Although efforts to realize this challenge were undertaken[178], the published approaches were not accurate. Hence, there is a need to establish a protocol for the positive selection of human astrocytic nuclei from the hub brain region in depression, the PFC (i.e., BA25).

Moreover, animal models could also be valuable to understand further the contribution of astrocytes developing depression[190,191]. However, the most convenient technique to sort rodent astrocytes, i.e., MACS, was employed mainly for big tissue size (e.g., whole cortex); thus, it may not be suitable for cell isolation from small brain regions (e.g., the PFC). Hence, the available protocols need to be adapted.

We hypothesize that astrocytes' dysfunctions underly biological manifestations of depression neuropathology and that it would be possible to identify disease relevant cell-type-specific transcriptional alterations.

The primary goal is to set up isolation methods suitable for next generation sequencing approaches to study astrocytes' biology in humans and mice. The ultimate goal is to expand the knowledge of MDD by revealing gene expression changes in astrocytes obtained from relevant circuits. Accordingly, the specific objectives are:

1. To establish a novel protocol for isolating astrocytic nuclei from fresh frozen human brain samples.
2. To optimize the protocol for isolating astrocytes from various brain regions of freshly dissected adult mouse brains.
3. To validate the protocols and evaluate the molecular profile of astrocytes from MDD brain samples and a rodent model of chronic stress.

2. MATERIALS AND METHODS

2.1. Establishing the Method for Astrocytic Nuclei Isolation from Fresh Frozen Samples of Human Brain

2.1.1. Materials

Reagents Name	Supplier	Article Numbers
RNaseZap	ThermoFisher	AM9780
UltraPure™ DNase/RNase-Free distilled water	ThermoFisher	10977035
16% Formaldehyde (w/v), Methanol-free	Fisher Scientific	28908
Ambion Buffer Kit	ThermoFisher	AM9010
Sucrose	Sigma	S0389-500G
DTT, 1M	ThermoFisher	P2325
Halt™ Protease Inhibitor Cocktail (100X)	Sigma	87786
RNasin® Ribonuclease Inhibitor, 40 U/µl	Promega	N261B
SUPERase In™ RNase Inhibitor, 20 U/µl	ThermoFisher	AM2696
Triton X-100	Sigma	T8787-100ML
Hoechst 33342, Trihydrochloride, Trihydrate, 10mg/ml	ThermoFisher	H3570
Trypan Blue, 0.4% Solution	Lonza	17-942E
Phosphate-Buffered Saline (10X) pH 7.4, RNase-free	ThermoFisher	AM9624
OptiPrep™ Density Gradient Medium	Sigma	D1556-250ML
Bovine serum albumin solution	Sigma	A7979-50ML
RNeasy FFPE Kit	Qiagen	73504
SuperScript™ III first-strand synthesis system	ThermoFisher	18080051
Taqman Fast Advanced Master Mix	ThermoFisher	4444556
Fast SYBR green master mix kit	Fisher Scientific	4385612
Agilent RNA 6000 pico kit	Agilent	5067-1513
SMARTer® Stranded Total RNA-Seq Kit v2-Pico Input	Takara	634413
Agencourt AMPure XP	Beckman Coulter	A63881
Qubit™ dsDNA HS assay kit	ThermoFisher	Q32854
Agilent High Sensitivity DNA kit	Agilent	5067-4626
Tween 20	Sigma	P9416-50ML

Aceton	Carl Roth	9372.1
Methanol	Carl Roth	P717.1
Phosphate-buffered saline (1X)	Carl Roth	9143.1
Normal goat serum	ThermoFisher	31873
ProLong™ Diamond Antifade Mountant	ThermoFisher	P36961

Equipment Name	**Supplier**	**Article Numbers**
Falcon® 50ml Centrifuge Tube, conical bottom, sterile	Neolab	352070
Falcon® 15ml Centrifuge Tube, conical bottom, sterile	Neolab	352096
Disposable Scalpels, sterile	Neolab	1-1565
Wheaton Dounce Homogenizer, 1ml	Neolab	9-0972
40 µm Cell Strainer, sterile	Neolab	352340
Heraeus™ Megafuge™ 16 Centrifuge, swing bucket	Thermofisher	75004270
Neubauer Counting Chamber	Carl Roth	T734.1
Axiovert 40 CFL, Inverted Microscope	Zeiss	-
Adjustable Rotator Plate	Neolab	2-1175
Microcentrifuge 5418 R	Eppendorf	5401000010
BD FACS Tubes with Strainer	Neolab	352235
BD FACSAria III, 4 Lasers Tube Sorter	BD	-
Nonstick, RNase-free Microfuge Tubes, 1.5 ml	ThermoFisher	AM12450
Eppendorf PCR Strip, 0.2 mL RNase and DNase free	Sigma	Z316156-1PAK
0.2 mL PCR Strip Magnetic Separator, 8 or 12 Strips	Permagen Labware	MSR812
Poly-L-lysine-coated slides	ThermoFisher	J2800AMNZ
Coverslips (1.5H, 24 x 50 mm)	Carl Roth	LH25.1
Staining Tray	Sigma	Z670146-1EA
PCR Thermocycler T100	Bio-rad	1861096
Qubit™ Assay Tubes	ThermoFisher	Q32856
Qubit Fluorometric Quantification	ThermoFisher	Q33327
2100 Bioanalyzer Instrument	Agilent	G2939BA
MicroAmp™ Optical 96-Well Reaction Plate	ThermoFisher	N8010560
Applied Biosystems QuantStudio 3	ThermoFisher	-
Fluorescence microscope Zeiss Axio Observer D1	Zeis	-

2.1.2. Reagents Set Up

Fixative Solution: Prepare in advance, and store at 4˚C.

Component	Volume (µl)	Final Concentration
16% Formaldehyde (w/v), Methanol-free	625	1%
RNase-free PBS, pH 7.4	9,325	-
RNasin, 40 U/µl	50	0.2 U μl^{-1}

Nuclei Isolation Medium 1 (NIM1): Prepare in advance, and store at 4˚C, for up to 6 months.

Component	Volume (µl)	Final Concentration (mM)
Sucrose, 1.5M	2,500	250
KCl, 2M	187.5	25
$MgCl_2$, 1M	75	5
Tris buffer, 1M, pH 8.0	150	10
Nuclease free water	12,087.5	-
Total volume	15,000	-

Nuclei Isolation Medium 2 (NIM2): Prepare freshly each time. Mix the components on ice.

Component	Volume (µl)	Final Concentration
NIM1	4,945	-
DTT, 1 mM	5	1 µM
100X Protease inhibitor	50	1X
Total volume	5,000	-

Homogenization Buffer (HB): Prepare freshly each time. Mix the components on ice.

Component	Volume (µl)	Final Concentration
NIM2	1,455	1X
RNasin, 40 U/µl	15	0.4 U μl^{-1}
SUPERase In, 20 U/µl	15	0.2 U μl^{-1}
Triton X-100, 10% (v/v)	15	0.1% (v/v)
Total volume	1,500	-

Staining Buffer (SB): Prepare freshly each time. Mix the components on ice.

Component	Volume (µl)	Final Concentration
RNase-free PBS, pH 7.4	9,810	-
RNase-free BSA, 35%	140	0.5% (wt/v)
RNasin, 40 U/µl	50	0.2 U μl^{-1}

Iodixanol Medium (IDM): Prepare in advance, store in 50 ml tube at 4˚C for up to 6 months.

Component	Volume (µl)	Final Concentration (mM)
1.5M sucrose	2,500	250
2M KCl	1,125	150
1M $MgCl_2$	450	30
1M Tris buffer, pH 8.0	900	60
Nuclease free water	10,025	-
Total volume	15,000	-

Optiprep Solutions: Prepare in advance, store in 50 ml tube at 4˚C for up to 6 months.

Component	Volume (µl)	Final Concentration
Optiprep, 60%	12,500	50%
IDM	2,500	-
Total volume	15,000	-
Optiprep, 60%	7,250	29%
IDM	7,750	-
Total volume	15,000	

2.1.2.1.Human Material and Ethical Permission

Frozen human postmortem brain samples were received from the Douglas Bell-Canada Brain Bank (DBCBB). The samples were originating from Caucasians of French-Canadian descent and sudden death individuals, where the cause of death was defined by the Quebec Coroner's office. Brains were dissected by trained neuroanatomists and stored at -80˚C in the DBCBB. This study was conducted under ethical permission issued by the Douglas Mental Health University Institute Research Ethics Board (REB, IUSMD-17-43), Canada.

2.1.3. Methods

All commercial kits were applied according to manufacturers' instructions. Any deviations from the original protocols are described below.

2.1.3.1.Nuclei Isolation from Frozen Human Brain Samples

The nuclei isolation method was adapted from the protocol of Krishnaswami et al. (2016)[186], and the final version is presented in section 3.1.6. The detailed version of the protocol can be found in Supplementary Information (Section 5.1).

2.1.3.2.Flow Cytometry

Nuclei were analyzed and sorted using a FACS system (BD FACS Aria III) and associated software (BD FACSDiva 8.0.1) in the FACS facility of the Zentrum für Molekulare Biologie der Universität Heidelberg (ZMBH). The facility prepared the FACS instrument for the droplet stream and the sorting delay, speed, and accuracy. The particles' overall event rate was set up to 200-4,000 events/second, the sample loading chamber was kept at 4˚C, and a 100 µm nozzle was selected for sorting.

2.1.3.3.RNA Extraction, Reverse Transcription, qPCR Analysis

RNA Extraction. Total RNA was extracted using RNeasy FFPE Kit (Qiagen, 73504) with an additional elution step at the end; RNA was eluted twice with the same eluate (20 µl) to increase the total amount. Eluted RNA was collected into 1.5 ml non-stick, RNase-free microfuge tubes (ThermoFisher, AM12450). For quality control, 2 µl of RNA was set aside in PCR strip tubes (Sigma, Z316156-1PAK) and, together with the rest of the eluted RNA, was stored at -80˚C.

Quantity and quality assessments of RNA were done using 2100 Bioanalyzer Instrument (Agilent G2939BA), with RNA 6000 Pico Kit (Agilent, 5067-1513).

Reverse Transcription and qPCR Analysis. cDNA was synthesized with the SuperScript III system (ThermoFisher, 18080051) using oligo(dT) priming following the manufacturers' guidelines in the PCR Thermocycler T100 (Bio-rad, 1861096). qPCR experiments were run using the Applied Biosystems QuantStudio 3 (ThermoFisher).

Two distinct approaches were used for qPCR analysis: TaqMan Probes or SYBR Green. Taqman probes specific for human species were synthesized and ordered following the suppliers' selection criteria (ThermoFisher) as listed in Table 2.1. All the probes were carrying a FAM reporter. For experiments employing SYBR Green, custom primers were designed based on the following criteria: i. primers were spanning exon-exon junction, ii. the envisaged size of the amplicon was

between 70-120 bp, and iii. primers had a low probability of self-dimerization, which were analyzed using the OligoAnalyzer Tool (IDT). A list of the primers used for SYBR Green analysis is presented in Table 2.2. The amplification efficiency of primers provided by the commercial supplier (Eurofins) was tested before the experiment, and the ones with 90-120% efficiency and a single peak on the melting curve were used for further experiments, employing the Fast SYBR Green Master Mix kit (Fisher Scientific, 4385612).

Table 2.1. qPCR Primers Used for the TaqMan Assay.

Gene ID	Primer ID
SLC1A2	Hs00188189_m1
ATP1B2	Hs01020302_g1
S100B	Hs00902901_m1
RAB3C	Hs00384846_m1
NEUN	Hs01370653_m1
PLP1	Hs00166914_m1
CX3CR1	Hs00365842_m1
CYC1	Hs00357717_m1

Table 2.2. qPCR Primers Used for the SYBR Green Assay. fw: forward primer sequences, rev: reverse primer sequences.

Gene ID	Pubmed Accession Number	Sequence, 5'→3'	Primer Efficiency, %
SOX9	NM_000346	fw: GTACCCGCACTTGCACAAC rev: TCTCGCTCTCGTTCAGAAGTC	93.8
SLC1A2	NM_004171	fw: TTCTTGAGCTTGGGATTGCCT rev: CCTTGTCCAAGCCTGCTTTCA	97.2
GJA1	NM_000165.4	fw: CAATCACTTGGCGTGACTTCA rev: ACCTTGTCAAGGAGTTTGCCTAA	102
WIF1	NM_007191.5	fw: CCAGGACTAGAGGGAGAGCA rev: TCGCAGACAGGCTTTGAACA	113.5
CX3CR1	NM_001171172.2	fw: GTGGTGCTGACAAAGCTTGGAA rev: TCACTGGGTGCCATCGTAAGAA	82.8

NEUN	NM_001385818.1	fw: TACGCAGCCTACAGATACGCTC rev: TGGTTCCAATGCTGTAGGTCGC	91.4
RAB3C	NM_138453	fw: ATCATCGGCAATAGCAGTGTG rev: AGGCTGTGGTGATAGTCCTGT	107.5
CNR1	NM_001160258	fw: ATGTGGACCATAGCCATTGTG rev: CCGATCCAGAACATCAGGTAGG	90.63
RELN	NM_005045.3	fw: CGTCCTAGTAAGCACTCGCA rev: TCGCCTAAGTGACCTTCGTC	96.3
PLP1	NM_001128834	fw: ACCTATGCCCTGACCGTTG rev: TGCTGGGGAAGGCAATAGACT	93
SDPR	NM_004657.5	fw: AAAGAGCGCATGGATAGGCA rev: TTTCCTCCTGGAAGATGAGCAC	114.8
SLC7A11	NM_014331	fw: GGTCCATTACCAGCTTTTGTACG rev: AATGTAGCGTCCAAATGCCAG	103
CYC1	NM_001916	fw: AGCCTACAAGAAAGTTTGCCTAT rev: TCTTCTTCCGGTAGTGGATCTTGGC	90.5

qPCR analysis of the abundance of cell-type-specific markers was performed to assess the purity of sorted populations. Markers were selected based on published expression data[152]: Astrocytes: *SLC1A2, ATP1B2* - ATPase Na+/K+ Transporting Subunit Beta 2, *S100B* - S100 Calcium Binding Protein B, *SOX9* - SRY-box transcription factor 9, *GJA1*, *WIF1* - Wnt inhibitory factor 1, and *SLC7A11* - Solute carrier family 7 member 11. Neurons: *RAB3C* - RAB3C member RAS oncogene family, *NEUN* - RNA binding fox-1 homolog 3, *CNR1* - Cannabinoid receptor 1, *RELN* - Reelin. Oligodendrocytes: *PLP1* - Proteolipid protein 1. Microglia: *CX3CR1* - Chemokine (C-X3-C motif) receptor 1. Endothelial cells: *SDPR* - Serum deprivation-response protein. Housekeeping gene: *CYC1* - Cytochrome c1.

qPCR analysis was determined using the relative abundance of a gene. Then, it was calculated by normalizing the targets' gene expression values to a housekeeping gene, according to formula $2^{(-\Delta Ct)}$, ($\Delta Ct = Ct_{Target\ gene} - Ct_{Housekeeping\ gene}$), represented in arbitrary units (a.u.).

2.1.3.4.Immunohistochemistry

Frozen human brain samples were sectioned using the cryostat (Leica), and 20 µM-thick sections were collected, mounted on poly-L-lysine-coated slides (ThermoFisher, J2800AMNZ), and stored at -80˚C. Prior to staining, frozen slices were fixed either with 4% paraformaldehyde (PFA) (Fisher Scientific, 28908) or a mixture of acetone:methanol (1:1) (Acetone – Carl Roth, 9372.1, Methanol – Carl Roth, P717.1). For PFA fixation, slices were incubated for 20 min. at room temperature (RT). For acetone:methanol fixation, sections were incubated for 15 min. at -20˚C.

Subsequently, PFA-fixed brain sections were permeabilized in washing solution containing 0.05% Tween 20 (Sigma, P9416-50ML) and 0.2% Triton X-100 (Sigma, T8787-100ML) in phosphate-buffered saline (PBS, 1X) (Carl Roth, 9143.1) for 15 min. at RT. The following steps were identical for PFA and acetone:methanol fixed section. Sections were blocked in blocking buffer containing 10% normal goat serum (ThermoFisher, 31873) and 0.2% Triton for 90 min. at RT. Next, samples were incubated in primary antibody dilution buffer (1% normal goat serum and 0.2% Triton in PBS) for 48 h at 4˚C. Antibody list is presented in Supplementary Table S1. After three washing steps (10 min. each in PBS, at RT), sections were incubated in antibody dilution buffer containing respective secondary antibodies for 3 h at RT. To ensure light protection, this step was accomplished in a staining tray (Sigma, Z670146-1EA). Then, sections were washed (three times, 10 min. each in PBS, at RT), and 1:1000 diluted Hoechst in PBS was added for 10 min. at RT. After the last washing step (three times, 10 min. each in PBS, at RT), the sections were air-dried, and mounting media (ThermoFisher, P36961) was added. Coverslips (Carl Roth, LH25.1) were sealed with nail polish, and the sections were dried overnight at RT. For long-term storage, slides were placed at 4˚C. Finally, imaging was performed under the inverted fluorescence microscope.

2.2. Optimizing the MACS Strategy for Isolation of Astrocytes from Multiple Regions of the Adult Mouse Brain

2.2.1. Materials

Reagents Name	Supplier	Article Numbers
RNaseZap	ThermoFisher	AM9780
UltraPure™ DNase/RNase-Free distilled water	ThermoFisher	10977035
Bovine serum albumin solution	Sigma	A7979-50ML
Dulbecco's phosphate-buffered saline without Ca^{2+}/Mg^{2+}	ThermoFisher	14190094
Adult brain dissociation kit	Miltenyi	130-107-677
DNase I	Worthington	LS002007
Myelin removal beads II, human, mouse, rat	Miltenyi	130-096-731
Anti-ACSA-2 microbead kit, mouse	Miltenyi	130-097-678
RLT buffer	Qiagen	79216
2-Mercaptoethanol	Fisher Scientific	21985023
RNeasy plus micro kit	Qiagen	74034

Agilent RNA 6000 pico kit	Agilent	5067-1513
SuperScript™ III first-strand synthesis system	ThermoFisher	18080051
Fast SYBR green master mix kit	Fisher Scientific	4385612
KAPA dNTP mix, 10 mM each	Sigma	KK1017
SuperScript™ II reverse transcriptase, 10,000 U	ThermoFisher	18064014
Recombinant RNase inhibitor, 5000 U	Takara	2313A
Betaine Solution, 5M	Sigma	B0300-1VL
KAPA HotStart ready mix	Kapa Biosystem	KK2601
Agencourt AMPure XP	Beckman Coulter	A63881
Qubit™ dsDNA HS assay kit	ThermoFisher	Q32854
Agilent High Sensitivity DNA kit	Agilent	5067-4626
Nextera XT index kit v2	Illumina	FC-131-200

Equipment Name	**Supplier**	**Article Numbers**
Falcon® 50ml Centrifuge Tube, conical bottom, sterile	Neolab	352070
Falcon® 15ml Centrifuge Tube, conical bottom, sterile	Neolab	352096
Low-profile disposable blades 819	Leica	14035838382
Adult mouse brain slicer matrix	Zivic Instruments	BSMAS001-1
Disposable Scalpels, sterile	Neolab	1-1565
Dumont #5/45 Forceps	F.S.T.	11251-35
Dumont #7 Forceps	F.S.T.	11271-30
Pasteur pipettes made of glass, 230 mm long	Neolab	44036
MACS Smart Strainers, 70 µm	Miltenyi	130-098-462
Heraeus™ Megafuge™ 16 Centrifuge, swing bucket	Thermofisher	75004270
MS Columns	Miltenyi	130-042-201
MACS MultiStand	Miltenyi	130-042-303
OctoMACS™ Separator	Miltenyi	130-042-109
Nonstick, RNase-free Microfuge Tubes, 1.5 ml	ThermoFisher	AM12450
Eppendorf PCR Strip, 0.2 mL RNase and DNase free	Sigma	Z316156-1PAK
PCR Thermocycler T100	Bio-rad	1861096
MicroAmp™ Optical 96-Well Reaction Plate	ThermoFisher	N8010560
Applied Biosystems QuantStudio 3	ThermoFisher	-

2.2.1.1.Mouse Material and Ethical Permission

Adult mice (8-18 weeks old) of C57BL6/J strain were used throughout the experiments. Mice were obtained either from in-house breeding at Interdisciplinary Behavioral Core (INBC, University of Heidelberg) or from a commercial supplier (Charles River). All experiments were performed under compliance with the permission of ethics (T-56/17 and G-233/16) issued by the Regierungspräsidium, Karlsruhe, Germany.

2.2.2. Methods

2.2.2.1.Tissue Dissection

During the entire isolation procedure, special care was taken to keep the working space and materials cold (working on ice), clean (sterilization with 70% ethanol), and RNase-free (ThermoFisher, AM9780).

Mice were sacrificed by cervical dislocation, and brains were kept in ice-cold Dulbecco's phosphate-buffered saline (DPBS) without Ca^{2+}/Mg^{2+} (ThermoFisher, 14190094). Dissection of brain regions was performed on ice. One mouse brain was used to dissect five brain regions, based on the stereotactic localization, guided by Allen Brain Atlas. Coronal slices (1-2 mm) were obtained using a mouse brain slicer matrix (Zivic Instruments, BSMAS001-1) and disposable blades (Leica, 14035838382). The hippocampus and hypothalamus were dissected from the remaining tissue without using the slicer since those regions are anatomically more accessible (Fig. 2.1). The prefrontal cortex (bregma 2.22 - 1.70), the motor cortex (bregma 1.32 - 1.10), and the somatosensory cortex (bregma 0.74 – (-2.92)) were dissected from the slices (Fig. 2.1).

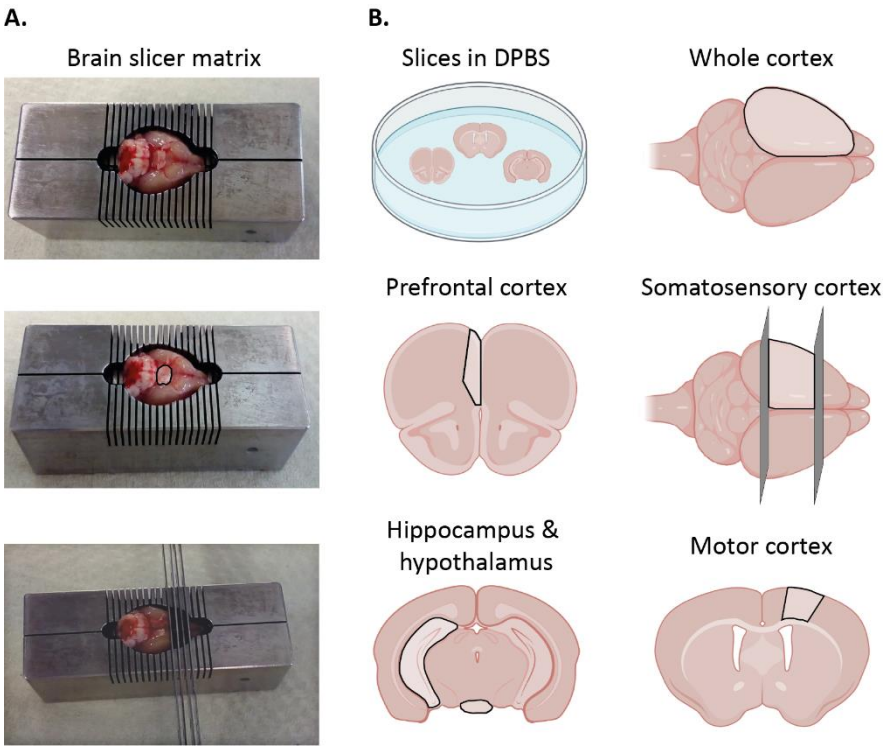

Figure 2.1. Dissection of Different Mouse Brain Regions. A. The adult mouse brain was placed in a ventral view position on a brain slicer matrix. Hypothalamus was dissected without slicing. Blades were positioned inside 1 mm intervals to slice the tissue. **B.** Slices were placed in a Petri dish containing ice-cold DPBS (w/o Ca^{2+}/Mg^{2+}), and the regions of interest – delineated with a black line in the scheme - were dissected out using forceps (F.S.T.). Dissected tissues were kept on ice in 1.5 ml Eppendorf filled with DPBS until the next step.

2.2.2.2.MACS-Cell Isolation Protocol

The optimization of cell isolation method was the subject of this thesis. The basic protocol was adapted from the manufacturers' (Miltenyi) instructions, including previously published strategies[172]. The final version is presented in section 3.2.4. The detailed version of the method can be found in Supplementary Information (Section 5.2).

2.2.2.3.RNA Extraction, Reverse Transcription, qPCR Analysis

RNA Extraction. RNA was extracted with RNeasy Plus Micro Kit (Qiagen, 74034). Eluted RNA (20 µl) was collected into 1.5 ml non-stick RNase-free microfuge tubes (ThermoFisher, AM12450), and was stored at -80˚C. Quantity and quality assessments of RNA were done as described previously (Section 2.1.3.3).

Reverse Transcription and qPCR Analysis. cDNA synthesis and qPCR analysis were conducted as described in section 2.1.3.3, with SYBR Green assay. The list of primers is presented in Table 2.3.

Table 2.3. qPCR Primers Used for the Mouse Samples. fw: forward primer sequences, rev: reverse primer sequences.

Gene	Pubmed Accession Number	Sequence, 5'→3'	Primer Efficiency, %
Aldh1l1	NM_027406.1	fw: GCAGGTACTTCTGGGTTGCT rev: GGAAGGCACCCAAGGTCAAA	92.4
Mbp	NM_001025251.2	fw: CATCCTTGACTCCATCGGGC rev: CAGGGTACCTTGCCAGAGC	95.5
Cx3cr1	NM_009987	fw: CGTGAGACTGGGTGAGTGAC rev: GGACATGGTGAGGTCCTGAG	99.9
Syt1	NM_001252342	fw: GGGAGGCACATCTGATCCATA rev: TTCCGGTGGACTTTTGTCTCA	106
Cspg4	NM_139001.2	fw: AGGCTGAGGTAAATGCTGGG rev: GCAGGTGGTGAGGACAGTAG	99
Ocln	NM_008756.2	fw: CCGCCAAGGTTCGCTTATCT rev: CGGACATGGCTGATGTCACT	116
Dcx	NM_001110222.1	fw: AGGTAACGACCAAGACGCAAA rev: GGGTGTAGAGATAGGAGACTGC	121
Cyc1	NM_025567.2	fw: TGCTCTTCCTGCCACAGC rev: GACCTCCACCTCCTCAGCC	120

To evaluate the purity of sorted population, markers were selected based on published data[152]: Astrocytes: *Aldh1l1* - Aldehyde dehydrogenase 1 family, member L1. Oligodendrocytes: *Mbp* - Myelin basic protein. Microglia: *Cx3cr1* - Chemokine, C-X3-C motif, receptor 1. Neurons: *Syt1* - Synaptotagmin I. NG2 cells: *Cspg4* - Chondroitin sulphate proteoglycan 4. Endothelial cells: *Ocln* - Occluding. Neuronal precursor cells: *Dcx* - Doublecortin. Housekeeping gene: *Cyc1*.

Data analysis was conducted by normalizing targets' gene expression values to a housekeeping gene ($\Delta Ct = Ct_{Target\ gene} - Ct_{Housekeeping\ gene}$). The enrichment in purified population was tested by comparison with an expression level in tissue homogenate and presented as the fold change expression over the latter ($2^{(-\Delta\Delta Ct)}$), represented in a.u.

2.3. Validation of the Protocols in Human Depression and Mouse Model of Chronic Stress

2.3.1. Materials

Reagents Name	Supplier	Article Numbers
Tween 20	Sigma	P9416-50ML
RIPA Buffer	Sigma	R0278-50ML
NuPAGE LDS Sample Buffer (4X)	ThermoFisher	NP0007
Halt™ Protease and Phosphatase Inhibitor Single-Use Cocktail (100X)	ThermoFisher	78442
BCA Protein Assay Kit	ThermoFisher	23225
4–12% Criterion™ XT Bis-Tris Protein Gel, 18 well, 30 µl	Bio-Rad	3450124
NuPAGE™ MOPS SDS Running Buffer (20X)	ThermoFisher	NP0001
Precision Plus Protein™ Dual Color Standards	Bio-Rad	1610374
NuPAGE™ Transfer Buffer (20X)	ThermoFisher	NP00061
TBS (10X)	Carl Roth	1060.1
Non-fat milk, Blotting grade blocker	Bio-Rad	1706404
ECL, Clarity Western ECL Substrate	Bio-Rad	1705061
Restore™ PLUS Western Blot Stripping Buffer	ThermoFisher	46430

Equipment Name	Supplier	Article Numbers
Wheaton Dounce Homogenizer, 1ml	Neolab	9-0972
Falcon® 15ml Centrifuge Tube, conical bottom, sterile	Neolab	352096
Microcentrifuge 5418 R	Eppendorf	5401000010
Immobilon-FL PVDF Membrane	Mercknillipore	IPFL00010
Blot Absorbent Filter Paper	Bio-Rad	1703965
Criterion™ Cell and PowerPac™ Basic Power Supply	Bio-Rad	1656019
Criterion Blotter	Bio-Rad	1704070
Vilber FUSION FX7	Vilber	-

2.3.1.1.Human Material and Ethical Permission

Brains were dissected from BA25 by trained neuroanatomists at the DBCBB and stored at -80˚C. Samples were originating from male subjects of Caucasians of French-Canadian descent and sudden death controls (N = 12), where the cause of death was determined by the Quebec Coroners' office. Cases (N = 15) met the criteria for MDD[37] and died by suicide (Project number: IUSMD-17-43). Healthy controls did not have evidence of any axis I disorders. Care was taken to match the samples for the age, postmortem interval (PMI), pH, and refrigeration delay, whenever possible. Details on the subjects' information are listed in Table 2.4.

Table 2.4. Subjects Characteristics.

Data are presented as the mean ± s.e.m. [a]An unpaired, two-tailed, Student's *t*-test. [b]Mann-Whitney test. *$P < 0.05$.
PMI: Postmortem interval. NA: Not available.
Substance at death: Morphine, benzodiazepines, antidepressants (TCA, SSRI, SNRI, NaSSA, SARI), cocaine and metabolites, lidocaine, cannabinoids, opioids, antipsychotics, alcohol, and substance name not available.
Psychiatric medication last 3 months: Benzodiazepines, classic antidepressants, and substance name not available.

Information	Controls (N = 12)	Cases (N = 15)	P-value
Age (years) [a]	43.75 ± 6.84	41.40 ± 2.95	0.7374
PMI (hours) [a]	41.94 ± 7.66	57.77 ± 7.66	0.1816
pH [b]	6.65 ± 0.06	6.823 ± 0.05	0.0480*
Refrigeration delay (hours) [b]	8.85 ± 2.85	27.57 ± 6.31	0.0143*
Cause of death	Accident (7), natural (5)	Suicide (15)	NA
Substance at death	7	11	NA
Psychiatric medication last 3 months	5	9	NA

2.3.1.2.Mouse Material and Ethical Permission

C57BL6/J adult mice (8-18 weeks old) and CD1 males (ex-breeders) were obtained from in-house breeding at INBC. All experiments were performed under compliance with the permission of ethics (G-233/16) issued by the Regierungspräsidium, Karlsruhe, Germany. Samples were originating from control (CONT, N = 7) and stressed (CSDS, N = 8) male mice.

2.3.2. Methods

2.3.2.1.FACS-Nuclei Isolation and Gene Expression Analysis

Nuclei Isolation. Nuclei from Hoechst+ and CX43+ populations were isolated following the optimized workflow described in section 3.1.6. Positively selected nuclei from both populations were collected into 100 µl of PKD buffer (Qiagen) and stored at -80˚C.

Gene Expression Analysis for Human Samples. RNA was extracted as explained in section 2.1.3.3, and library preparations were conducted as described in section 3.1.6.3 using SMARTer® Stranded Total RNA-Seq Kit v2 - Pico Input Mammalian kit (Takara, 634413) with modifications. For the Hoechst+ population, 1.5 ng of total RNA input was amplified with 12 PCR cycles. For the CX43+ population, max. amount of RNA (total volume: 8 µl) input was used, and 16 PCR cycles were performed to generate the libraries. RNA and library qualities were evaluated with Bioanalyzer using RNA Pico Kit (Agilent, 5067-1513) and High Sensitivity DNA Kit (Agilent, 5067-4626). Next, libraries were sent to the genomic facility in Boehringer Ingelheim (Germany), and RNA sequencing was conducted following their internal workflow on the Illumina HiSeq 4000 platform (using the dual indexing, paired-end 2 x 75 bp run system).

RNA-sequencing data analysis was performed by the bioinformaticians in Intelliseq (Poland). The quality of sequenced data was verified using FastQC (v.0.11.8), and these reports were aggregated with MultiQC (v1.10). The raw reads were aligned to GRCh38.p13 Ensembl (v.100 for CX43 samples and v. 102 for Hoechst samples) using Hisat2. Next, the gene abundances were calculated using htseq-count (v.0.11.2) and the GTF file from Ensembl (v.100 for CX43 and v.102 for Hoechst samples).

Statistics. Differential gene expression analysis between CON and MDD groups was done with *exactTest* function from *edgeR* (v.3.28.1) R package on filtered data (filterByExpr function, counts per million reads mapped (CPM) > 3 at least in 10 samples) for CX43 and Hoechst samples separately.

2.3.2.2.MACS-Astrocytes Isolation and Gene Expression Analysis

Chronic social defeat stress paradigm and evaluation of stress impact on mice behavior were conducted by our colleague Carmen Menacho Pando based on the published procedure[188]. Briefly, the protocol included exposing the submissive mice (C57BL6/J male, >8 weeks old) to a daily, short (5-10 min.) contact with the aggressive mice (CD1 males, ex-breeders). This episode was followed by the cohabitation of mice in a two-compartment cage hosted by an aggressive mouse, with perforated plexiglass placed in the middle to prevent physical contact while experiencing the presence of the aggressor. This protocol was applied for a minimum of 2 weeks with daily

alternation of the aggressor. Animals were housed in the reversed 12 h:12 h light:dark cycles to facilitate executing CSDS in the active phase of mice (i.e., during darkness). I contributed to MACS, RNA extraction, and library preparations.

Astrocytes Isolation. Cells were isolated following the optimized protocol as explained in section 3.2.4. ACSA-2+ cells were sorted into 350 µl RLT buffer (Qiagen) and stored at -80˚C.

Gene Expression Analysis for Mouse Samples. RNA was extracted as described in section 2.2.2.3, and libraries were prepared as explained in section 3.2.4.3 using Smart-seq2 protocol in collaboration with EMBL Genomics Facility, Heidelberg. Nextera XT DNA Library Preparation Kit was used at EMBL Genomics Facility following their internal protocol. The total RNA input, 3 ng, was amplified, and 0.2 ng of cDNA was used to generate libraries. Finally, pools of the sample (mix of 13-16 libraries in one tube) were sequenced using NextSeq 500 system (Illumina) at EMBL Genomics Facility.

RNA-sequencing data analysis was performed by the bioinformaticians in Intelliseq. The quality of sequenced data was verified using FastQC (v.0.11.7), and these reports were aggregated with MultiQC (v1.10). The raw reads were aligned to GRCm38.p6 and Ensembl (v.97) using Hisat2. Next, the transcripts and genes FPKM (Fragments Per Kilobase of transcript per Million fragments mapped) levels were quantified using Cuffquant, Cuffnorm (v.2.2.1), and GTF file from Ensembl (v.97). Finally, differential gene expression analysis between control and stressed groups was done on normalized FPKM values on filtered data (mean FPKM > 1 for analyzed samples).

Statistics. Statistical analyses were done using three-way ANOVA with factors: “brain region”, “sacrificed time”, “treatment”, and interaction between “sacrificed time” and “treatment”. Correction for multiple testing was done only on transcripts with mean FPKM values > 5 and < 100 using Bonferroni correction.

2.3.2.3.Western Blot

Frozen human tissue (100 mg) was homogenized with Dounce homogenizer in 300 µl of pre-cooled RIPA buffer (Sigma, R0278-50ML) containing 1X protease and phosphatase inhibitor (ThermoFisher, 78442). The lysate was incubated for 10 min. on ice, transferred into a new 1.5 ml Eppendorf tube, and sonicated for 1 min. Next, the lysate was centrifuged at full speed for 30 min. at 4˚C. Finally, the supernatant and the pellet were separated and stored at -80˚C.

Protein quantification was performed using BCA Protein Assay Kit (Thermofisher, 23225). Prior to protein running, the supernatants were mixed with the LDS sample buffer (ThermoFisher, NP0007) and incubated for 10 min. at 70˚C. For each sample, 20 µg of protein was run by electrophoresis with the Criterion™ Cell systems (Bio-Rad, 1656019) using precast gels with 4-

12% Bis-Tris (Bio-Rad, 3450124), in 1X MOPS-SDS buffer (ThermoFisher, NP0001). Next, proteins were transferred to polyvinylidene difluoride (PVDF) membranes (Merckmillipore, IPFL00010) with the Criterion Blotter systems (Bio-Rad, 1704070) in 1X transfer buffer (ThermoFisher, NP00061). Membranes were blocked in blocking buffer containing 5% of milk (Bio-Rad, 1706404), 1X of TBS (Carl Roth, 1060.1), 0.5% of Tween 20 (Sigma, P9416-50ML), for 1h at RT then incubated in primary antibody in dilution buffer (1.5% of milk, 1X of TBS, 0.5% of Tween 20) overnight at 4˚C (Antibody list is presented in Supp. Table S1). After three washing steps (10 min. each in 1X of TBS, 0.5% of Tween 20, at RT), membranes were incubated with the secondary antibodies conjugated to horseradish peroxidase in dilution buffer for 1 h at RT. After three final washing steps (10 min. each in 1X of TBS, 0.5% of Tween 20, at RT), protein bands were detected using the chemiluminescent reaction (Clarity Western ECL Substrate (Bio-Rad, 1705061)) under the Vilber FUSION FX7.

Data Analysis and Statistics. Protein levels were quantified using ImageJ software and calculated as a ratio of selected bands' relative density to the housekeeping protein β-ACTIN. Statistical analyses were conducted using the t-test or Mann-Whitney test when the data was not normally distributed based on the Shapiro-Wilk test.

3. RESULTS

3.1. Establishing a Novel Protocol for Isolating Astrocytic Nuclei from Fresh Frozen Human Brain Samples

3.1.1. Development of the Protocol

To isolate astrocytic nuclei, a protocol enabling positive selection strategy had to be developed. Several methods for isolating cell-type-specific nuclei from frozen human brain tissues have emerged during the past few years[178,181,186,196,197]. As a general principle, we decided to adapt the existing methods established for other cell types and optimized them for our specific research purpose. As a starting point, we chose the protocol of Krishnaswami et al. (2016), which was used to analyze transcriptional changes in individual neuronal nuclei sorted from frozen human postmortem samples[186]. We evaluated this method as the most suitable since it focused on preventing the damage of RNA throughout the isolation process for optimal transcriptomic analysis, which overlapped with our objective.

Principle steps (Fig. 3.1) of the protocol encompass: i. tissue homogenization, ii. immunolabelling of astrocytic nuclei with specific antibody, iii. fluorescence-based sorting, and iv. RNA extraction. Details of optimizing the original protocol were the subject of this thesis. The final version of the protocol is presented in section 3.1.6.

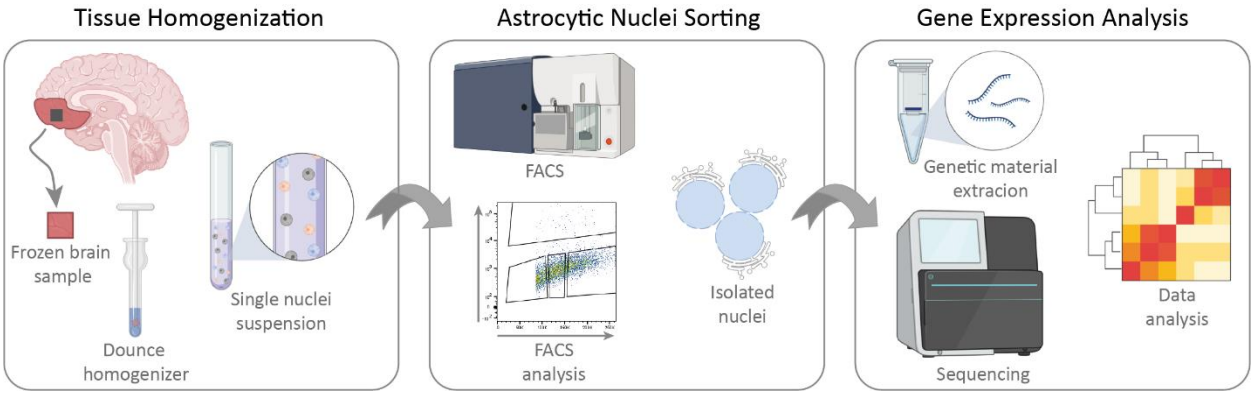

Figure 3.1. Workflow for Isolating Astrocytic Nuclei and Performing Transcriptomic Studies.

To establish the protocol, three critical objectives were defined: i. recapitulate the reference protocol by sorting neuronal nuclei, ii. find astrocyte-specific nuclear epitopes, and iii. validate the

quality of extracted genetic material for transcriptional studies. Hence, in the subsequent sections, the original approach[186], followed by the detailed description of introduced modifications, will be described.

3.1.2. Neuronal Nuclei Isolation from Fresh Frozen Brain Samples

In the reference protocol, the tissue dissociation was carried on using Dounce homogenizer[186]. Briefly, frozen tissue was chopped with a pre-chilled scalpel and placed into a Dounce homogenizer containing cold, freshly prepared homogenization buffer (the composition in section 2.1.2). The first step of homogenization was accomplished by applying five strokes using the loose pestle, while the second step was completed employing the tight pestle for another ten strokes. Once dissociation was completed, the homogenate was filtered through a cell strainer cap (35 µm pore size) of a FACS tube and concentrated by centrifugation.

To reproduce the reference protocol for neuronal nuclei isolation from the fresh frozen human cortex, we dissociated the tissue (less than 50 mg) according to the instructions, with the exception of employing a different cell strainer. A 40 µm strainer was used instead of the FACS tube with a strainer cap (35 µm) because filtering the dense homogenate through a small FACS tube cap was not efficient in our hands. The selected strainer had a larger surface area, which allowed easier and more effective filtering. A single nuclei suspension was obtained upon homogenization, rendering 6×10^5 nuclei, as counted using the Neubauer chamber.

For isolating all nuclei from tissue homogenate, a dye staining all nuclei, Hoechst, was employed. Labeling the neuronal nuclei was performed using a primary antibody targeting a nuclear membrane protein, anti-NEUN (5 µg/ml, Supp. Table S1). For fluorescent labeling, nuclei were incubated with secondary antibody conjugated to Alexa 594 (4 µg/ml, Supp. Table S1). Once immunolabelling was concluded, flow cytometry analysis was performed as suggested by Krishnaswami et al. (2016)[186]. In FACS, all intact nuclei were selected with 405 nm wavelength recognizing Hoechst+ nuclei population (Fig. 3.2A). From this population, NEUN-positive (NEUN+) nuclei fraction was extracted (Fig. 3.2C) based on the fluorescence intensity of the secondary antibody acquired with 561 nm laser. The latter was routinely normalized to the isotype control (5 µg/ml, Supp. Table S1), which served to set the FACS gating (Fig. 3.2B). A total of 37,000 NEUN+ nuclei were sorted into lysis buffer (0.2% Triton X and 2 U/µl RNase inhibitor).

Following the isolation, cDNA was amplified using a modified version of Smart-seq2 protocol[198], encompassing denaturation, reverse transcription, and pre-amplification. For denaturation, the KAPA dNTP mix and Oligo-dt_{30}VN primers were used at 2.3 mM and 1.1 µM final concentrations, respectively. Reverse transcription mixture contained TSO/LNA oligonucleotide at 1.5 µM final concentrations. Pre-amplification was accomplished using ISPCR primers at 0.04 µM final

concentration. PCR cycles were adjusted according to the sorted nuclei number (18-21 cycles). Consequently, cDNA was amplified from 37,000 NEUN+ nuclei, rendering 165 ng of total cDNA, as quantified using Qubit.

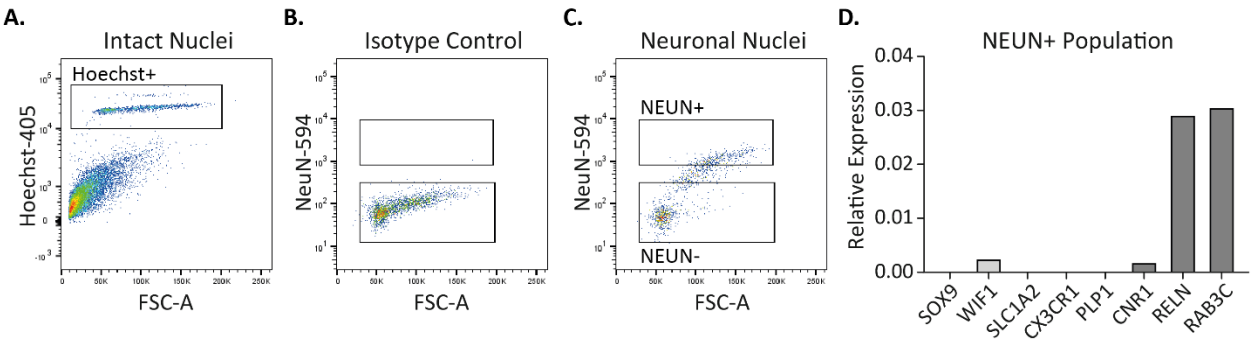

Figure 3.2. Replication of Neuronal Nuclei Isolation Protocol. A. Intact nuclei were selected by gating Hoechst+ events based on fluorescence intensity using a 405 nm laser and forward scatter (FSC-A) distribution. **B.**, **C.** NEUN+ population (**C**), sub-gated from the Hoechst+ fraction, was defined according to the fluorescence intensity (acquired with 561 nm laser) and size distribution in comparison to the isotype control (**B**). Flow cytometry revealed 24% NEUN+ nuclei (**C**), which were sorted into lysis buffer. **D.** qPCR analysis showed enrichment of neuronal markers. These results were obtained from a single cell isolation experiment (n = 1) using a tissue sample from one donor. The flow cytometry analysis was done emplying FlowJo software.
SOX9, WIF1, SLC1A2 - astrocytes, *CNR1, RELN, RAB3C* - neurons, *PLP1* - oligodendrocytes, *CX3CR1* – microglia, *CYC1* – housekeeping gene.

The purity of sorted populations was assessed with qPCR analysis of the abundance of cell type-specific markers. NEUN+ population primarily expressed neuronal markers as *CNR1* (0.002 a.u.), *RELN* (0.029 a.u.), and *RAB3C* (0.030 a.u.), and no other cell type-specific markers as *SOX9* (0.0 a.u.), *WIF1* (0.002 a.u.), *SLC1A2* (0.0 a.u.), *CX3CR1* (0.0 a.u.), and *PLP1* (0.0 a.u.) (n = 1, Fig. 3.2D). The data suggested that we could replicate the procedure of neuronal nuclei isolation from fresh frozen human brain samples.

Furthermore, we assessed the morphological quality of sorted nuclei under the bright-field microscope. After homogenization and immunolabeling steps, small tissue pieces and debris were observed as expected since we avoided excessive Dounce strokes and omitted debris removal (Fig. 3.3). Anyhow, the aggregates and the particles smaller than nuclei (i.e., Hoechst+ events) were eliminated in flow cytometry analysis (post sorting). Images in Figure 3.3 proposed the adequate conditions of our nuclei isolation method because intact nuclei could be observed after every essential step of the procedure: homogenization, immunolabeling, and sorting. Effective recapitulation of the reference protocol encouraged us to optimize the method for astrocytic nuclei isolation.

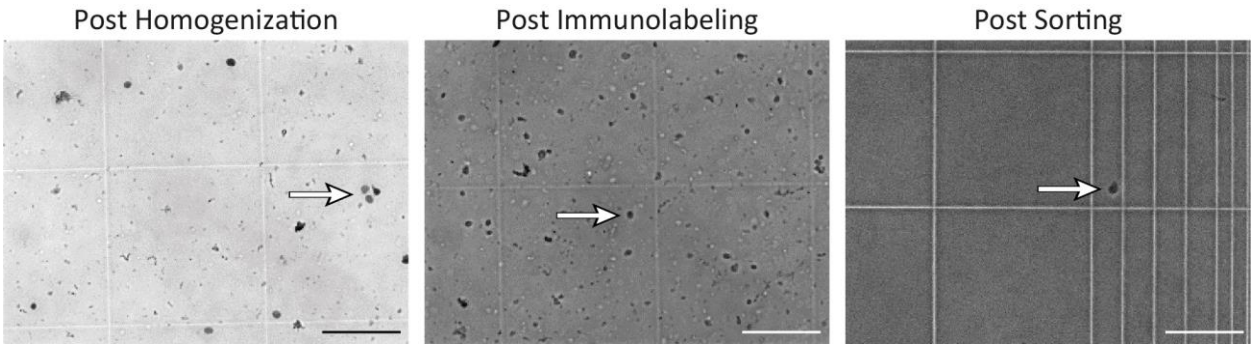

Figure 3.3. Structural Integrity of Isolated Nuclei. Nuclei were released upon tissue homogenization of frozen brain samples. An aliquot of nuclei suspension was stained with 0.2% (vol/vol) trypan blue, placed on a Neubauer chamber, and the morphological appearance was observed under a bright-field microscope. Images were acquired after tissue homogenization using Dounce homogenizer (Post Homogenization), incubations with antibodies (Post Immunolabeling), and FACS isolation (Post Sorting). Representative intact nuclei were indicated with white arrows. Images were acquired on 20X magnitude. Scale bar: 125 µm.

3.1.3. Astrocytic Nuclei Isolation from Fresh Frozen Brain Tissues

3.1.3.1. Selection of Astrocyte Specific Nuclear Epitope

A critical point to establish the protocol for the positive selection of human astrocytic nuclei was finding the antibody targeting astrocyte-specific nuclear protein. In the reference study (i.e., for neurons), this step was accomplished using an anti-NEUN antibody, recognizing the neuron-specific nuclear membrane epitope[186]. However, the analogical protocol was not reported for astrocytes. To find an appropriate epitope, we performed a systematic literature search. We reasoned that transcription factors are promising candidates due to their subcellular localization, the nucleus. We hence investigated literature metadata generously provided by Boehringer Ingelheim, which was assembled from several sources: mRNA sequencing data of human primary astrocytes, induced pluripotent stem cells-derived astrocytes, and a curated data set of transcription factors in human and mouse[199]. The metadata analysis revealed SOX9 as the strongest candidate (based on expression values), followed by other transcription factors expressed in astrocytes, such as GLI family zinc finger 1 (GLI1) and GLI family zinc finger 3 (GLI3).

Our selection was supported by literature evidence. A study conducted by Sun et al. (2017) demonstrated specific expression of SOX9 in astrocytes in human and mouse brain cortical samples[200]. In addition, the authors employed SOX9 as a nuclear epitope to isolate astrocytic nuclei from fresh mouse brain samples. Further validation confirmed the specific expression of SOX9 in astrocytes in the CNS (Jax info, Gtexportal, and Protein atlas). We next searched for the

availability of antibodies using Labome, and the antibody from Abcam (ab185966, Supp. Table S1) was selected for pilot experiments.

To test the specificity of the selected antibody, immunofluorescence was conducted on human tissue samples (Fig. 3.4). Cryosections of the frozen human brain cortex were post-fixed either with PFA or acetone:methanol (1:1) solution. The latter condition was included to test whether the antibody would recognize the native antigen, ensured by acetone:methanol fixation. Imaging data suggested positive signals and nuclear localization of SOX9 in both conditions (n = 2 independent experiments, Fig. 3.4). Taken together, the tested anti-SOX9 antibody was chosen as the epitope to sort astrocytic nuclei in the FACS experiments.

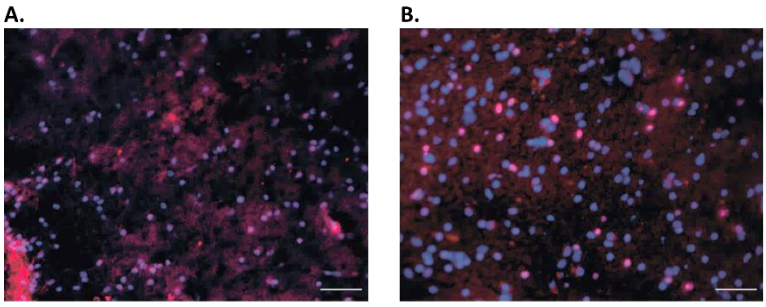

Figure 3.4. Nuclear Localization of SOX9. Cryosections from frozen brain tissues were either post-fixed in 4% PFA (**A**) or acetone:methanol (1:1) (**B**) solutions. Slices were stained with anti-SOX9 antibody, and Hoechst 33342 (blue) was used for broad nuclear staining. Images were taken under a fluorescence microscope and indicated nuclear localization of SOX9 protein in human cortical tissue (red). Two independent experiments were conducted (n = 2). Images were acquired on 40X magnitude. PFA: paraformaldehyde. Scale bar: 50 µm.

3.1.3.2.Astrocytic Nuclei Isolation Targeting SOX9 Epitope

For FACS isolation of astrocytic nuclei from frozen human postmortem brain samples, we replicated the homogenization described in section 3.1.2. Approximately 50 mg of frozen tissue was homogenized, and single nuclei suspension was obtained (number of nuclei: 3.6×10^5). Before flow cytometry, nuclei labeling was performed with a primary anti-SOX9 antibody (12 µg/ml, ab185966, Supp. Table S1) and a secondary antibody conjugated to phycoerythrin (PE) (4 µg/ml, Supp. Table S1). In FACS, Hoechst+ events, representing the intact nuclei, were initially selected (Fig. 3.5A). Then, SOX9-positive (SOX9+) nuclei population was chosen according to the fluorescence intensity of the PE and by sub-gating set based on the isotype control (12 µg/ml, Supp. Table S1). The percentage of SOX9+ events was 0.01% (Fig. 3.5C), resulting in only 190 nuclei sorted into lysis buffer. Due to the low yield (4 ng of cDNA), successful amplification in qPCR and cell-type-specific marker expression analysis were not accomplished. Our interpretation of this data was that the selected primary antibody used to target SOX9 was not efficient for FACS

sorting of astrocytic nuclei. Thus, we sought to improve the methodological parameters of the approach.

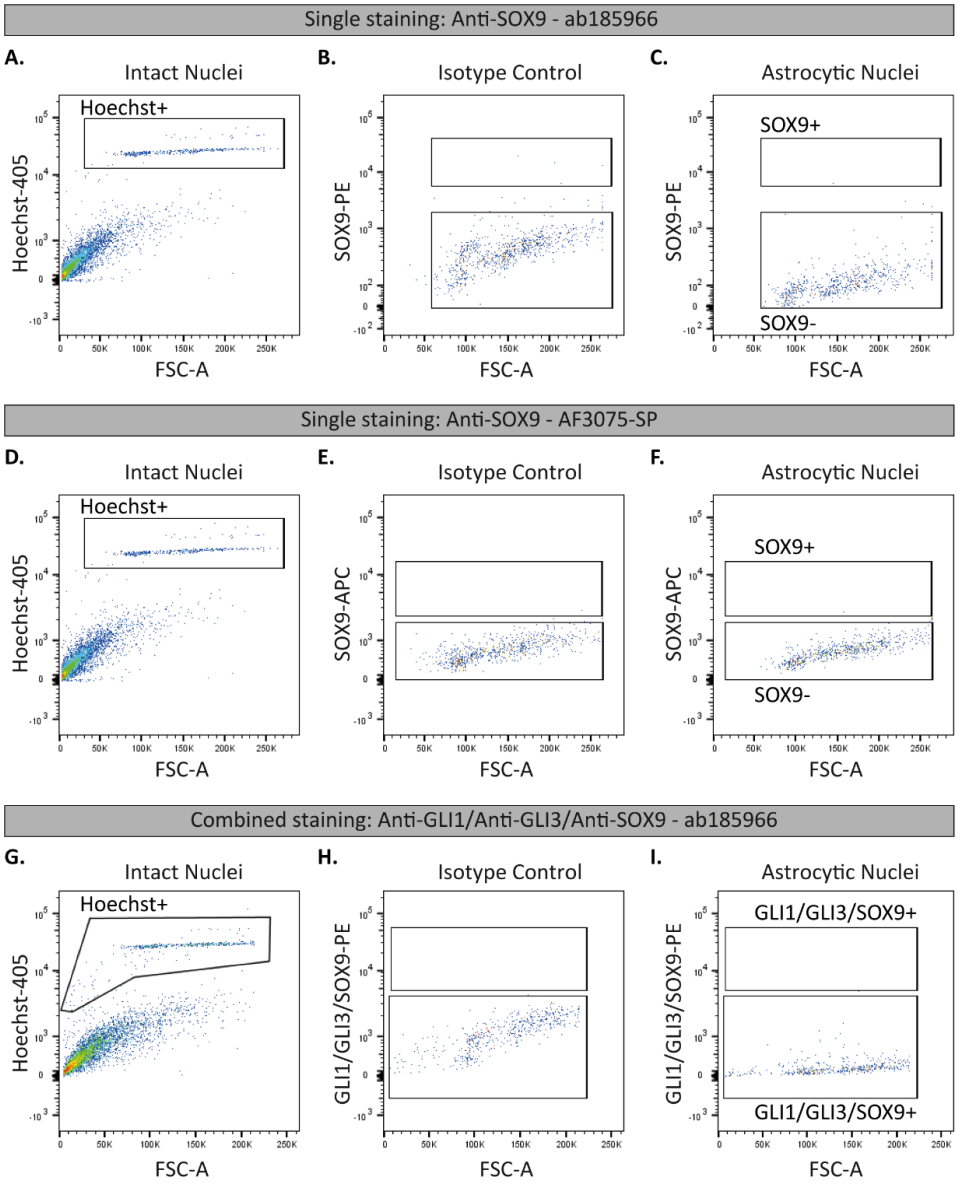

Figure 3.5. Specificity of Antibodies for Astrocytic Nuclei Isolation. Three independent FACS experiments were performed to sort astrocytic nuclei from frozen human samples. Upon tissue homogenization, single nuclei suspension was either immunolabelled with anti-SOX9-ab185966 (**A-C**), anti-SOX9-AF3075-SP (**D-F**), or a combination of three antibodies (anti-GLI1, anti-GLI2, and anti-SOX9) (**G-I**). **A.**, **D.**, **G.** In flow cytometry, intact nuclei (Hoechst+) were selected by gating with respect to fluorescence intensity (405 nm laser) and FSC-A distribution. From the Hoechst+ population, astrocytic nuclei population was defined based on fluorescence intensity (561 nm (**C**, **I**) and 630 nm (**F**) lasers) compared to isotype controls. The percentages of positive events in astrocytic nuclei populations were 0.01% (**C**) and 0% (**F**, **I**). None of the antibodies used to isolate astrocytic nuclei were specific enough to sort astrocytes reliably; however, anti-SOX9 (ab185966) resulted in a positive signal (**C**). The flow cytometry analysis was done using FlowJo software. FSC-A: forward scatter area.

We tested an antibody combination (primary and secondary) used in the study of Sun et al. (2017) for mouse tissue samples[200]. Accordingly, immunolabelling was performed using the anti-SOX9 primary (2 µg/ml, AF3075-SP, Supp. Table S1) and a secondary antibody conjugated to allophycocyanin (APC) (1 µg/ml, Supp. Table S1). However, in flow cytometry analysis, no positive signal was observed in the SOX9+ population (0%, n = 1, Fig. 3.5F) compared to the isotype control (12 µg/ml, Supp. Table S1).

Next, we tested a strategy of combining three primary antibodies from the same species (i.e., rabbit), reasoning that if any of them worked, subsequent tests with individual antibodies would let us identify the working one. We labelled nuclei simultaneously with antibodies targeting GLI1, GLI3, and SOX9 (n = 1, Fig. 3.5G-I). Immunolabeling was done with staining buffer containing primary antibodies combination anti-GLI1 (10 µg/ml, ab151796, Supp. Table S1), anti-GLI3 (10 µg/ml, PA5-28029, Supp. Table S1), and anti-SOX9 (12 µg/ml, ab185966, Supp. Table S1). A unique secondary antibody conjugated to PE (4 µg/ml, Supp. Table S1) was employed. However, FACS analysis did not reveal any positive signal for astrocytic labeling compared to the isotype control, as seen in Figure 3.5H-I. This finding was surprising since employing only anti-SOX9 (ab185966) antibody gave a weak but positive signal in flow cytometry. Hence, we decided to continue using anti-SOX9 (ab185966) for the subsequent experiments and examine whether modifying other parameters in the protocol can enhance the immunostaining efficiency.

To increase the number of isolated nuclei, a prerequisite for the purity analysis, we doubled the amount of tissue used for the experiment. As expected, upon tissue homogenization, this modification increased the total number of nuclei to 2.1 x 10^6. Prior to FACS, single nuclei suspension was incubated with anti-SOX9 antibody (12 µg/ml, ab185966) and a secondary antibody conjugated to PE (4 µg/ml, Supp. Table S1). In the flow cytometry analysis, the fraction of the SOX9+ population was 9.9%, without impacting the number of positive events in the isotype control population (n = 1, Fig. 3.6B, C). We were able to sort 5,400 SOX9+ nuclei into lysis buffer, from which 185 ng cDNA was amplified.

Improvement of the yield allowed us to perform qPCR analysis of the purity of isolated population. We calculated the abundance of the markers for astrocytes (*SLC1A2*: 0.002 a.u., *GJA1*: 0.001 a.u.), microglia (*CX3CR1*: 0 a.u.), oligodendrocytes (*PLP1*: 0.007 a.u.), and neurons (*NEUN*: 0.06 a.u., *RAB3C*: 0.03 a.u.) (n = 1, Fig. 3.6D). The data suggested that the expression levels of astrocytic markers were low compared to the other cell-type-specific markers, implicating that further optimization of the protocol was necessary. Considering the increase in the percentage of the positive events, we decided to keep using 100 mg of tissue for the following experiments.

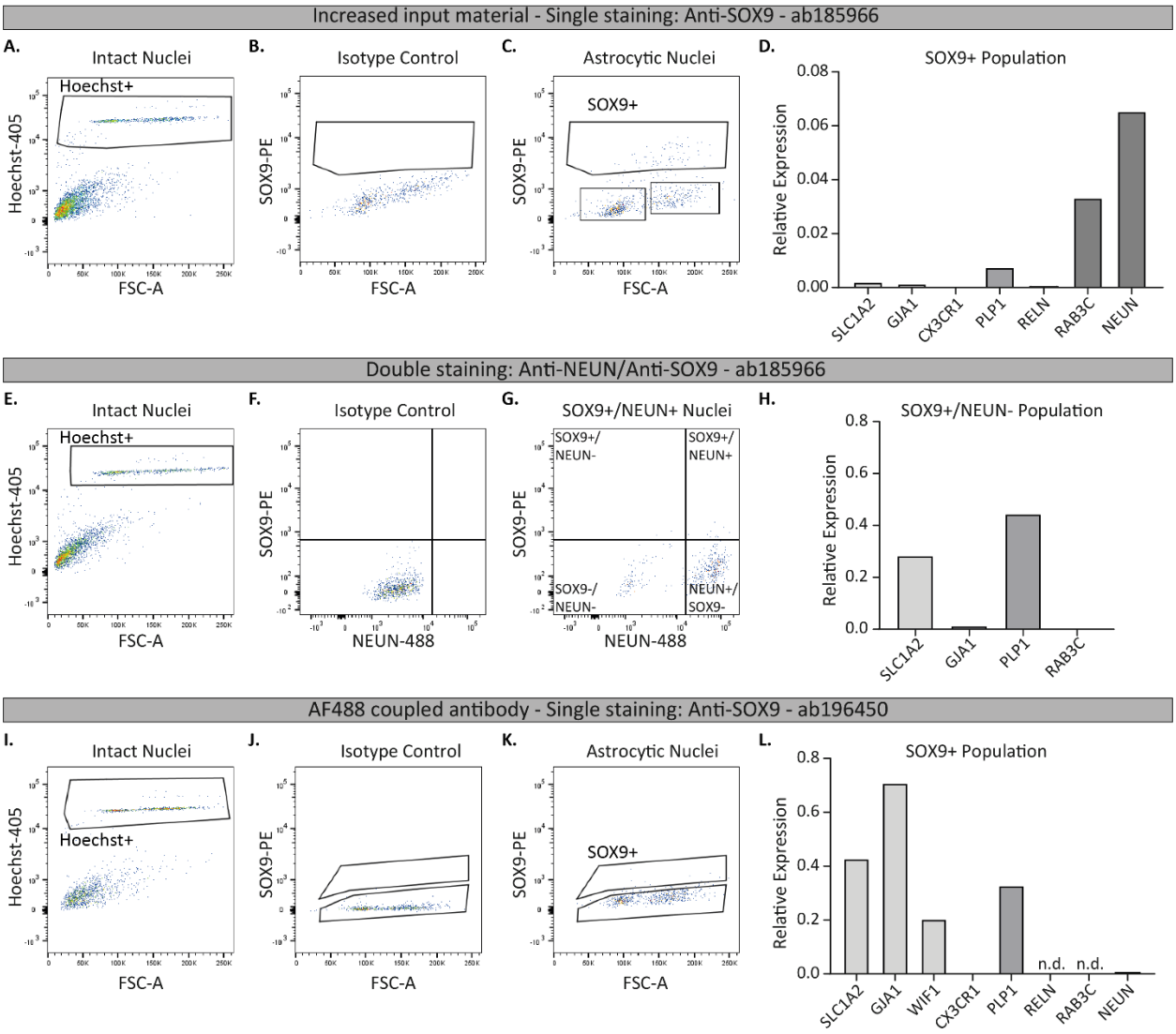

Figure 3.6. Evaluation of Different Strategies to Improve the Yield and Purity of Astrocytic Nuclei. Three independent FACS experiments were performed to sort astrocytic nuclei from frozen human samples. For each experiments single qPCR analysis was conducted. **A-D.** Higher input material improved the signal intensity in FACS (**C**), but qPCR data demonstrated that the antibody was unspecific and labelled neurons (**D**). **E-H.** The double labeling strategy decreased the contamination of neurons but also the yield of sorted material. The isolated population did not consist of pure astrocytes (**H**). **I-L**. Already conjugated anti-SOX9 antibody revealed higher efficiency in FACS (**K**). However, the sorted population consisted of astrocytes and oligodendrocyte mixture (**L**). The flow cytometry analysis was done using FlowJo software.
FSC-A: forward scatter area. n.d.: Not determined. *SLC1A2*, *GJA1*, *WIF1* - astrocytes, *PLP1* - oligodendrocytes, *CX3CR1* – microglia, *RELN*, *RAB3C*, *NEUN* - neurons *CYC1* – housekeeping gene. SYBR Green assay was employed for qPCR analysis.

We next tested a dual strategy, encompassing simultaneous negative selection of neuronal nuclei with positive selection of astrocytic nuclei. For this double staining approach, nuclei were labelled

with anti-NEUN (5 µg/ml, MAB377, Supp. Table S1) and anti-SOX9 (12 µg/ml, ab185966, Supp. Table S1) antibodies. Secondary antibodies were either conjugated to Alexa 488 (4 µg/ml, Supp. Table S1) or PE (4 µg/ml, Supp. Table S1), respectively. Therefore, four distinct groups were defined (Fig. 3.6G): SOX9+/NEUN-, SOX9+/NEUN+, SOX9-/NEUN+, and SOX9-/NEUN- (n = 1, Fig. 3.6F). The population of interest was the SOX9+/NEUN-, constituting 0.5% of Hoechst+ nuclei, which translated to sorting 400 nuclei into lysis buffer, from which 13 ng of cDNA was amplified.

Due to low input material, we could perform qPCR analysis using only four markers for cell-type-specific gene expression assessment (n = 1, Fig. 3.6H). As desired, the *RAB3C* expression was eliminated (0.0 a.u.), and the expression of astrocytic markers increased since *SLC1A2* and *GJA1* reached 0.3 a.u. and 0.01 a.u., respectively. However, the expression level of *PLP1* was detected as 0.4 a.u. (Fig. 3.6H). In summary, although double immunolabeling decreased the contamination of neurons and increased the expression level of astrocytic markers, oligodendrocyte contamination remained an issue, as was the low number of sorted nuclei.

We reasoned that the loss of nuclei may be related to the number of centrifugation steps and that reducing the latter may be beneficial. Likewise, using an antibody conjugated with a fluorophore would eliminate the need for incubation with secondary antibody, washing steps, and one centrifugation. Hence, we tested another anti-SOX9 primary antibody, which was already conjugated to Alexa 488 (ab196450, Supp. Table S1). Frozen human tissue was homogenized, and immunostaining was conducted with anti-SOX9-AF488 antibody (5 µg/ml, ab196450, Supp. Table S1). Flow cytometry analysis shown in Figure 3.6K revealed 2.2% of SOX9+ events in Hoechst+ nuclei. As a result, 4,900 nuclei were sorted into lysis buffer, and 54 ng of total cDNA was amplified.

qPCR assessment for purity analysis was performed, and the expression levels of *SLC1A2*, *GJA1*, and *WIF1*, were measured as 0.5 a.u., 1.9 a.u., 0.2 a.u., respectively (n = 1, Fig. 3.6L). The levels of neuronal markers were either below detection (*RAB3C*: not determined (n.d.) and *RELN*: n.d) or very low (*NEUN*: 0.008 a.u.). However, as previously, we noted high expression levels of *PLP1* (0.6 a.u.). Consequently, flow cytometry and qPCR analyses suggested that the anti-SOX9-AF488 antibody (ab196450) was more efficient in labeling astrocyte-specific nuclei, without neuronal contamination. Nevertheless, the sorted SOX9+ nuclei population was not pure enough and consisted of astrocytes and oligodendrocyte mixture, raising the need for further improvement.

To eliminate oligodendrocytes, we followed a size-based exclusion approach. We noted that a mixed population of nuclei (Hoechst+, Fig. 3.7D) was distributed along the forward scatter axis, FSC-A, reflecting the size. It has been shown that glial cells have smaller nuclei than neuronal cells[186], and the two were distinguishable based on physical features (e.g., nuclei size, shape, and

granularity)[201]. Interestingly, it was reported that the size of astrocytic nuclei is comparable to small neuron size, and oligodendrocytes and microglia have much smaller size of nuclei than astrocytes.

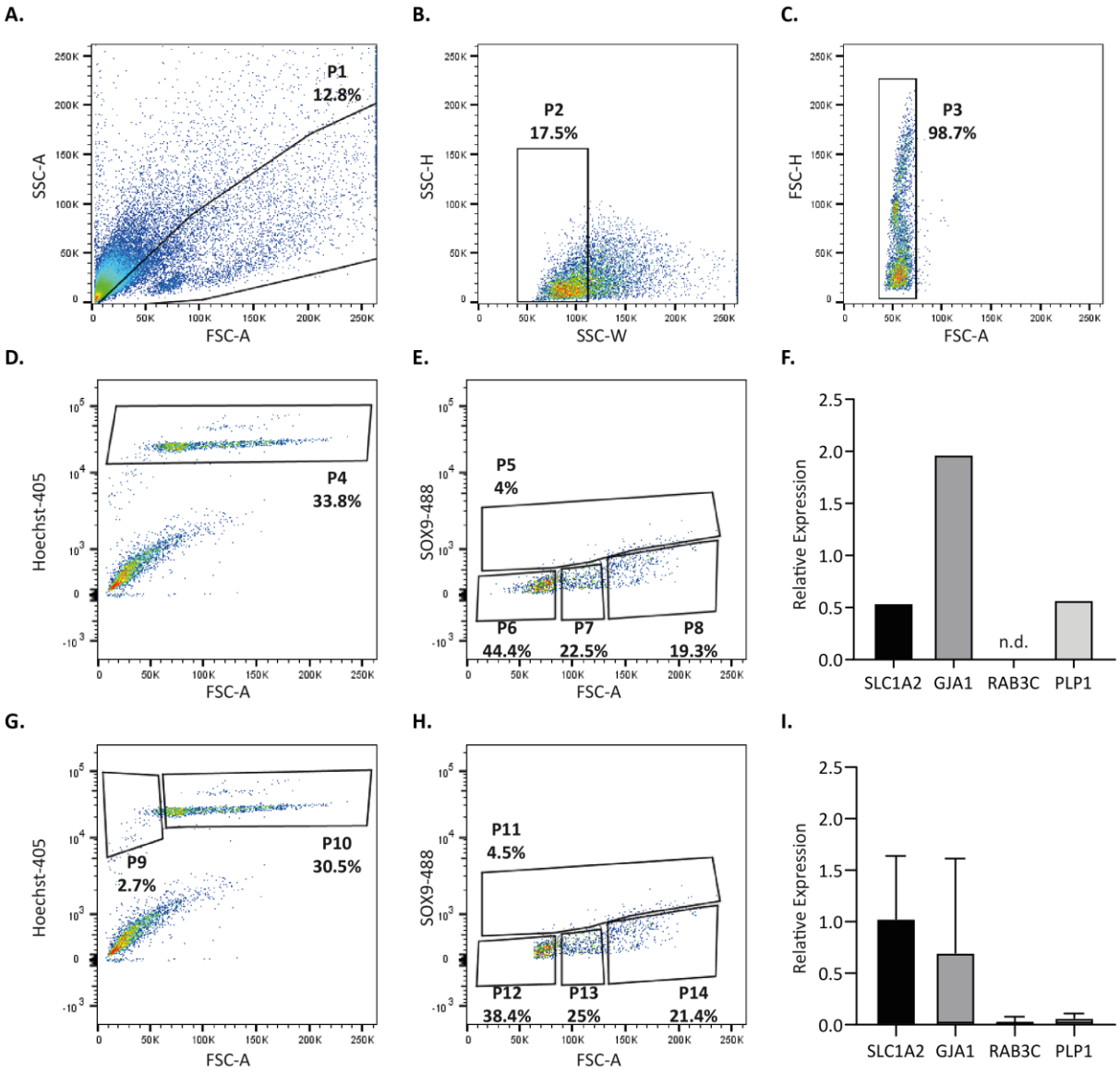

Figure 3.7. Astrocytic Nuclei Isolation Targeting SOX9 Epitope. FACS experiments were performed to sort astrocytic nuclei labelled with AF488-coupled anti-SOX9 (ab196450). Hierarchical gating strategy in flow cytometry started by unselecting debris (**A**) and doublets (**B**, **C**) using side and forward scatter channels. Next, intact nuclei were selected by sub-gating on Hoechst (**D**, **G**), and SOX9+ population was selected based on fluorescence intensity (**E**, **H**). Percentages of positive populations are shown in the dot plots. **F.** qPCR data generated from P5 showed expression levels of astrocytic markers together with oligodendrocyte marker. **G – I.** Small-sized nuclei were unselected in FACS (P9), and SOX9+ events were sub-gated from Hoechst+ population (P10) (**G**, **H**). Relative expression levels of astrocytic markers were higher compared to other cell type-specific markers (**I**), indicating enhanced purity. Four independent experiments were conducted using samples from two separate donors (**G-I**). The flow cytometry analysis was done using FlowJo software.
SSC-A: side scatter area, SSC-H: side scatter height, SSC-W: side scatter width, FSC-A: forward scatter area, FSC-H: forward scatter height. N.d.: not determined. *SLC1A2* and *GJA1* – astrocytes, *RAB3C* - neurons, *PLP1* - oligodendrocytes, and *CYC1* – housekeeping gene. SYBR Green assay was employed for qPCR analysis.

To explore to which extent those features can be implemented in our sorting strategy, in the next experiment, we unselected the small-sized nuclei in the FACS analysis (Fig. 3.7G, P9), assuming those are composed mainly of oligodendrocytes. Single nuclei suspension was immunolabelled after tissue homogenization using an anti-SOX9-AF488 antibody (5 µg/ml, ab196450). Before FACS analysis, the labelled sample was divided into two equal sub-samples. For one sample, flow cytometry assessment was conducted as before, and SOX9+ events (Fig. 3.7E, P5) were extracted by normalizing to the isotype control (5 µg/ml, Supp. Table S1). For the other sample, once SOX9+ events were defined (Fig. 3.7H, P11), the gating strategy was modified, and approximately 10-15% of the smallest nuclei were excluded from Hoechst+ events (Fig. 3.7G, P9). This strategy increased a fraction of SOX9+ events to 4.5%, as seen in Figure 3.7H, P11. Moreover, in this fraction, we observed a higher abundance of astrocyte-specific markers (average of 4 independent experiments ± standard deviation (SD), *SLC1A2*: 1.02 ± 0.61 a.u., *GJA1*: 0.70 ± 0.91 a.u.) and concomitant reduction of oligodendrocytes marker (*PLP1*: 0.06 ± 0.05 a.u.) as shown in Figure 3.7I. Thus, we decided to implement the size-based selection strategy in our astrocytic nuclei isolation protocol.

Taken together, we systematically optimized the method for astrocytic nuclei isolation from frozen postmortem human brain samples. The summary of modified parameters is presented in Table 3.1. Following improvements were made: i. using at least 100 mg of tissue, ii. labeling astrocytes with an AF-488-conjugated antibody against SOX9 (ab196450), and iii. performing size selection in FACS analysis prior to sorting. Consequently, we were able to sort astrocytes and perform gene expression analysis using qPCR.

Table 3.1. List of Modified Parameters for Improving Immunostaining Efficiency in FACS.

Modified Parameters	Epitope	Antibody Supplier, article #	Results
Antibody selected from reference study, Sun et al.[200]	SOX9	R&D system (AF3075-SP)	No positive signal (FACS analysis)
Combined staining approach using astrocytic epitopes	GLI1, GLI2, SOX9	ThermoFisher (PA5-28029), Abcam (ab151796), Abcam (ab185966)	No positive signal (FACS analysis)
Increase of input material, using 100 mg of tissue	SOX9	Abcam (ab185966)	No astrocyte enrichment (qPCR analysis)
Double staining approach using neuronal and astrocytic epitopes	NEUN SOX9	Merckmillipore (MAB377) Abcam (ab185966)	No astrocyte enrichment (qPCR analysis)
New antibody selected to improve labelling efficiency	SOX9	Abcam (ab196450)	Astrocyte enrichment but not pure (qPCR analysis)

3.1.3.3.Gene Expression Analysis

Given the improved purity of sorted astrocytic nuclei, we assessed the compatibility of the protocol with RNA sequencing. Isolated samples (amplified cDNA) from the last four experiments (Fig. 3.7G) were sent to the genomic facility of Boehringer Ingelheim for preliminary sequencing. Upon cDNA amplification, its quality was evaluated using Bioanalyzer (Fig. 3.8A). The expected distribution of the amplified products was observed in the electropherograms, with the median size around 2000 base pairs (bp) and a single peak (Fig. 3.8A). Samples were subjected to pair-end sequencing run in NextSeq sequencing platform, followed by quality control, performed by the Computational Biology unit in Boehringer Ingelheim. Obtained data revealed variations in the number of reads for the mapping and alignment features between samples (Fig. 3.8B). The analysis of reads alignment indicated that intronic and non-coding regions were present more than coding regions (Fig. 3.8B). This finding was not unexpected since, due to the nature of the RNA in the nucleus, the intronic reads likely captured an abundance of nascent RNA transcripts that were present.

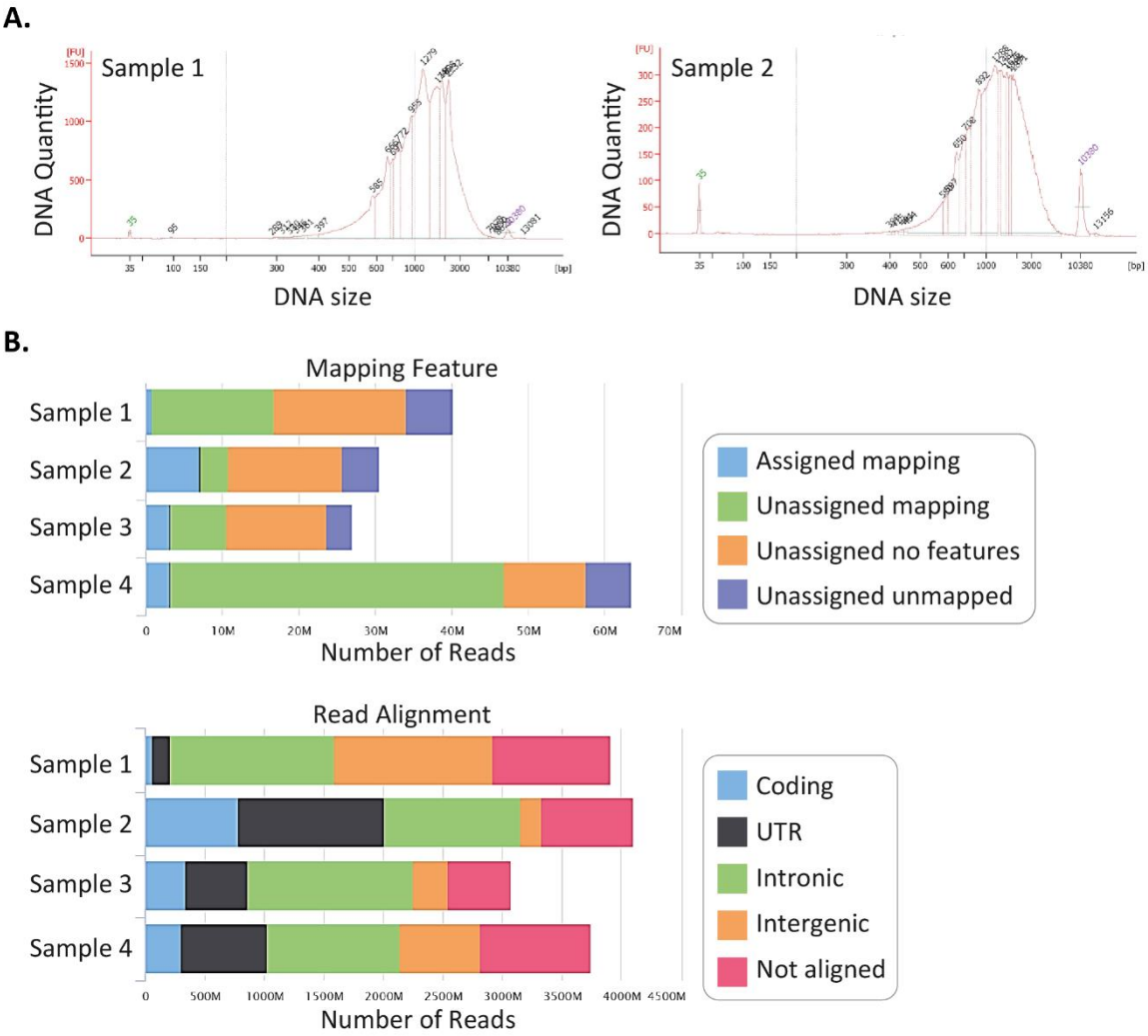

Figure 3.8. Quality Check of Amplified cDNA and Sequencing Data. cDNA was generated from SOX9+ nuclei samples (Fig. 3.7H, P11) obtained in 4 independent experiments. The quality of amplified cDNA was evaluated with Bioanalyzer using High Sensitivity DNA Kit. **A.** Representative electropherograms illustrated single peak and appropriate cDNA size (2000 bp). **B.** Quality check of RNA sequencing focused on the mapping feature; the number of reads that are mapped to a known sequence (assigned mapping) and the read alignments data that specifies the features of the sequenced data as coding, untranslated region (UTR), intronic, intergenic, and not aligned regions. Both results showed high variability of features between samples and a low number of coding sequences and reads (**B**). Quality control of the sequencing data was conducted by the Computational Biology unit in Boehringer Ingelheim. FU: fluorescence intensity.

However, because of the low number of assigned mappings (Fig. 3.8B) and heterogeneity between samples (also observed in qPCR data in Figure 3.7I), we concluded that our methodology was not sufficient for comparative gene expression analysis. High variability across control samples can create a source of variability precluding detection of significant differences between experimental groups. Consequently, we decided to reevaluate the details of our protocol, focusing on improving initial steps of sample preparation for genetic material extraction.

3.1.4. Tissue Homogenization and Nuclei Isolation from Post-Fixed Samples

Considering that the RNA in postmortem human brain samples is fragile and prone to degrade, we assumed that the low quality of sequencing data and the heterogeneity between samples could be due to the loss of genetic material during the long nuclei isolation procedure. Although we put special attention to conduct the experiment on ice, degradation of the frozen tissue could start as soon as it was taken out of -80˚C. Hence, to keep the integrity of the tissue, nuclei, and the genetic materials, we explored the option of gentle fixation of the frozen tissues.

Recently published studies on cell-type-specific nuclei isolation methods using human postmortem samples implemented fixation step, which improved antibody penetration[178,197]. The strategy used by Xu et al. (2018)[178] was to homogenate frozen tissues in a detergent-free solution and to fix the single nuclei suspension before immunolabelling in 1% formalin for 8 min. at RT. In turn, the approach adopted by Amamoto et al. (2020)[197] was to fix the frozen tissue in 1% PFA - 0.2 U/µl RNase inhibitor for 5 min. on ice, homogenate tissues using the same buffer as applied in our protocol (with a detergent, Triton X-100), and re-fix the single nuclei suspension before immunolabelling through incubation in 4% PFA for 15 min. on ice. We decided to adopt a mild fixation step before tissue homogenization, aiming to keep the integrity of the nuclei structure starting from the initial step of the procedure. In addition, we reasoned that adding RNase inhibitor to a fixation solution and performing brief fixation on ice would avoid further degradation of RNA due to crosslinking in the fixative solution.

Since the human tissues are precious and difficult to access, to test whether fixation would improve the quality of the RNA, a series of preliminary experiments were performed using cell lines (HEK 293 and U-251) (Fig. 3.9). We employed the protocol as above (Section 3.1.3.2), with the inclusion of a fixation step prior to dissociation. Frozen HEK cells were incubated in a solution of 1% PFA containing 0.2 U/µl RNase inhibitor for 8 min. on ice. Upon Dounce homogenization, Hoechst was added into the single nuclei suspension, and FACS analysis was performed. We omitted the immunolabelling of nuclei since, at this moment, the priority was to evaluate the impact of fixation on the nuclei integrity (measured by sorted nuclei number) and genetic material quality (measured by gene expression levels). For comparison, in parallel, we employed an identical sorting protocol, omitting the fixation. According to the treatment of the cells (fixation or not), various RNA extraction methods were also tested. For unfixed cells, nuclei were sorted into two distinct lysis buffers: RLT buffer for RNA extraction (Fig. 3.9A) or lysis buffer for direct cDNA amplification (Fig. 3.9B). In contrast, nuclei isolated from fixed cells were sorted into PKD buffer, and RNA was obtained with the RNeasy FFPE kit (Fig. 3.9C), designed to purify RNA from fixed cells[202].

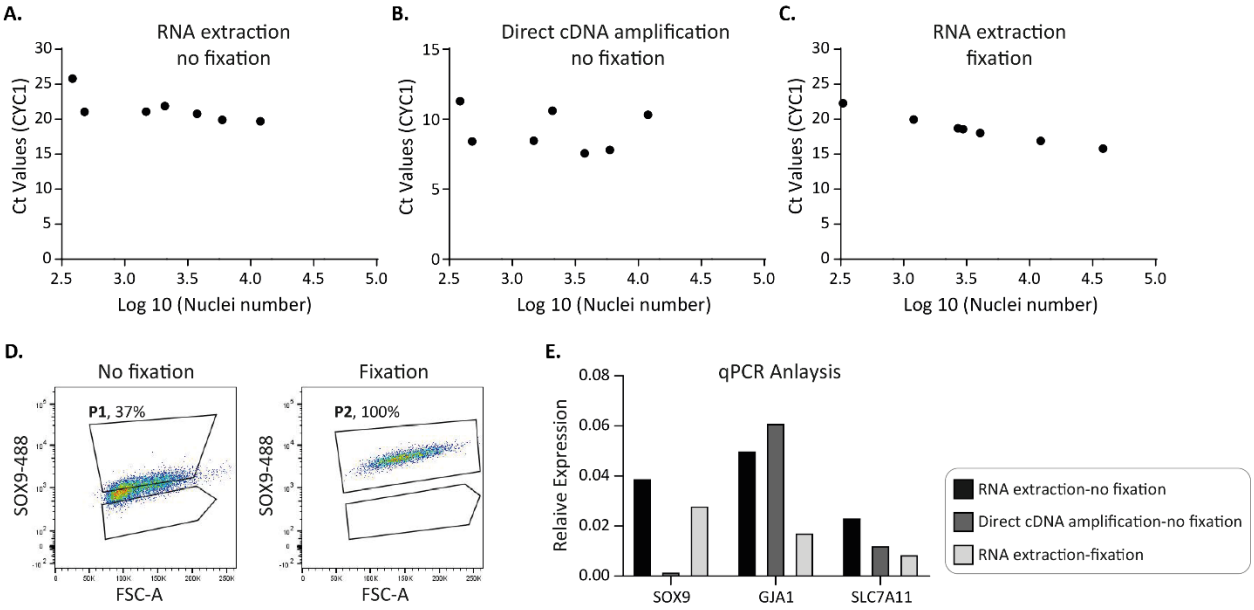

<u>Figure 3.9.</u> Mild Fixation Effects on Extracted Genetic Materials, Immunostaining, and Gene Expression. Nuclei were isolated from frozen fixed or not fixed HEK (**A**-**C**) and U-251 (**D**-**E**) cells. Genetic material was purified in the form of RNA (**A**, **C**) and cDNA (direct amplification) (**B**). The correlation between the sorted nuclei number (FACS-counted) and the abundance of *CYC1* (using qPCR) was evaluated. **A-C.** Cell fixation before nuclei sorting and RNA extraction resulted in best correlation (R^2 = 0.97) (**C**). **D**-**E.** Nuclei suspensions were stained with AF488-couple anti-SOX9 (ab196450) antibody. **D.** Flow cytometry revealed that mild fixation of cells increased the binding efficiency of the antibody. **E.** qPCR analysis assessing the gene expression levels of astrocyte-specific markers. Findings pointed out that RNA extraction and fixation approaches did not impair the relative expression level of the markers. These results were obtained from a single cell isolation experiment using 3 different types of starting materials. FSC-A: forward scatter area. SYBR Green assay was employed for qPCR analysis (n = 1).

We found that isolating nuclei from mildly fixed cells resulted in a better correlation between nuclei number and the abundance of a housekeeping gene (a measure of the total RNA amount), as shown in Figure 3.9C (n = 1, R^2 = 0.97). In contrast, we observed a poor correlation between calculated nuclei number and a total RNA in both protocols where fixation was omitted (n = 1, no RNA extraction and no fixation: R^2 = 0.56, direct cDNA amplification: R^2 = 0.05, Fig 3.9A-B) As a result, the combination of mild fixation and RNA extraction improved the nuclei integrity and gene expression quality, respectively.

Next, we took advantage of the fact that U-251 cells (human glioblastoma astrocytoma cell line) express SOX9, and we examined the impact of the mild fixation on the performance of the anti-SOX9-AF488 antibody in the FACS procedure. Single nuclei suspension, obtained from unfixed or fixed U-251 cells, was incubated with an anti-SOX9+ (5 µg/ml, ab196450) antibody. As seen in Figure 3.9D, mild fixation resulted in adequate sorting of 100% of the nuclei, indicating the

nuclei and epitope integrity. This result was expected because the FACS isolation was performed using a cell line, which is homogenous, opposite to multicellular brain tissue.

Furthermore, we tested whether employing a fixative solution would impact the expression levels of known astrocyte markers in the U-251 cell line. We found that applying the modification and performing RNA extraction did not impair the detection of astrocyte markers as *SOX9*, *GJA1*, and *SLC7A11* in qPCR analysis (n = 1, Fig. 3.9E). Considering these data, we decided to implement the mild fixation of frozen tissue for further experiments.

3.1.5. Astrocytic Nuclei Isolation from Post-Fixed Brain Samples

At this moment of the project, we experienced an unexpected and critical turn: the anti-SOX9-AF488 (ab196450), polyclonal antibody, was discontinued. This situation could have been avoided if a monoclonal antibody was selected from the start. We examined a new lot of the same antibody, which resulted in a lower fraction of FACS sorted cells (3% of SOX9+ events, compared to 4.5%, as seen in Figure 3.7H), and no pure astrocytes population were found in qPCR assessments (data not shown). Nevertheless, as we made significant improvements in the general procedure of nuclei isolation, we continued our exploration for a monoclonal antibody that could be employed for our purpose. Ideally, the antibody should already be coupled to a fluorophore, as was the case for the previously validated antibody (ab196450). We tested a fluorophore-coupled, anti-SOX9-AF647 (5 µg/ml, ab196184, Supp. Table S1) antibody provided by the same supplier, but this antibody did not give any positive signal in flow cytometry analysis (data not shown).

After this failure, we searched for an alternative approach and oriented our focus to the work of Xu et al. (2018)[178]. These authors reported that isolated nuclei were not entirely pure but contained the endoplasmic reticulum (ER)[178]. Accordingly, the employed positive selection approach for sorting different types of human neuronal nuclei from cerebellum samples by double labeling with antibodies directed against NEUN and ITPR (inositol 1,4,5-Trisphosphate Receptor Type 1). The latter localizes to the ER/nuclear membrane in neurons[178]. Considering this finding, we repeated the literature survey to identify astrocyte-specific markers expressed either in the nucleus or endoplasmic reticulum.

3.1.5.1. Selection of a Novel Astrocyte Specific Nuclear Epitope

We started by exploring the top 100 genes enriched in astrocytes, as reported by Mc Kenzie et al. (2018)[153]. This study is a comprehensive analysis of brain cell type-specific gene expression patterns by comparing several human and mice cell type-specific RNA expression data sets. We next investigated the subcellular expression patterns of those genes using an online tool, GeneCards[203]. This search resulted in a list of 17 genes, which were highly expressed in the nucleus

and/or ER of astrocytes. Next, we used databases, such as Uniprot[204], Gtex portal[205], and Pubmed, to broaden the information about the 17 candidates. Based on this search, the top five potential markers were listed (Table 3.2) to be further explored and selected for FACS isolation experiments.

Table 3.2. List of Top Five Candidates for Labeling Astrocytic Nuclei. Astrocyte-specific proteins and their subcellular localization.

Gene Symbol	Gene Name	Subcellular localization	
		GeneCards	Uniprot
GJA1	Gap Junction Protein Alpha 1	Nucleus, endoplasmic reticulum, plasma membrane, mitochondrion	Endoplasmic reticulum, plasma membrane
IL33	Interleukin 33	Nucleus, extracellular	Nucleus, extracellular
ID4	Inhibitor of DNA Binding 4, HLH Protein	Nucleus	Nucleus
CLU	Clusterin	Nucleus, extracellular, mitochondrion	Nucleus, cytoplasm, extracellular
RGS20	Regulator of G Protein Signaling 20	Nucleus	Nucleus

As seen in Table 3.2, among five astrocytic proteins, only connexin 43 (CX43), a gap junction protein, was expressed in the nucleus and ER. The other four (IL33, ID4, CLU, and RGS20) were mainly reported to be expressed in the nucleus. Additionally, *CX43* was the gene with highest expression in astrocytes compared to other candidates listed in Table 3.2. Importantly, we found an available monoclonal antibody targeting the CX43 epitope in humans. Consequently, we chose CX43 as a marker and continued with FACS experiments to check its specificity to sort astrocytic nuclei.

3.1.5.2.Astrocytic Nuclei Isolation Targeting CX43 Epitope

To examine if CX43 was a suitable marker, FACS experiments were performed using 100 mg of frozen human brain tissue, and mild fixation was applied before Dounce homogenization (Fig. 3.10A-C). Upon tissue dissociation, a further modification was included by implementing the debris removal step in our protocol. Debris could be an additional factor in lowering the quality of the sorted material, and recently published nuclei isolation protocols strongly suggested implementing this step[178,183,197]. Moreover, removing debris can improve staining, cell/nuclei sorting, and sequencing quality by decreasing the aggregates and clumps formation[186,206]. Hence, immunolabeling was conducted using the anti-CX43 primary antibody (5 µg/ml, 13-8300, Supp.

Table S1) and Alexa 488 conjugated secondary antibody (4 µg/ml, Supp. Table S1). FACS data shown in Figure 3.10C revealed the fraction of CX43 positive events as 1.2%. A total of 317 CX43+ nuclei were sorted into PKD buffer, and the amount of extracted RNA was 8 ng.

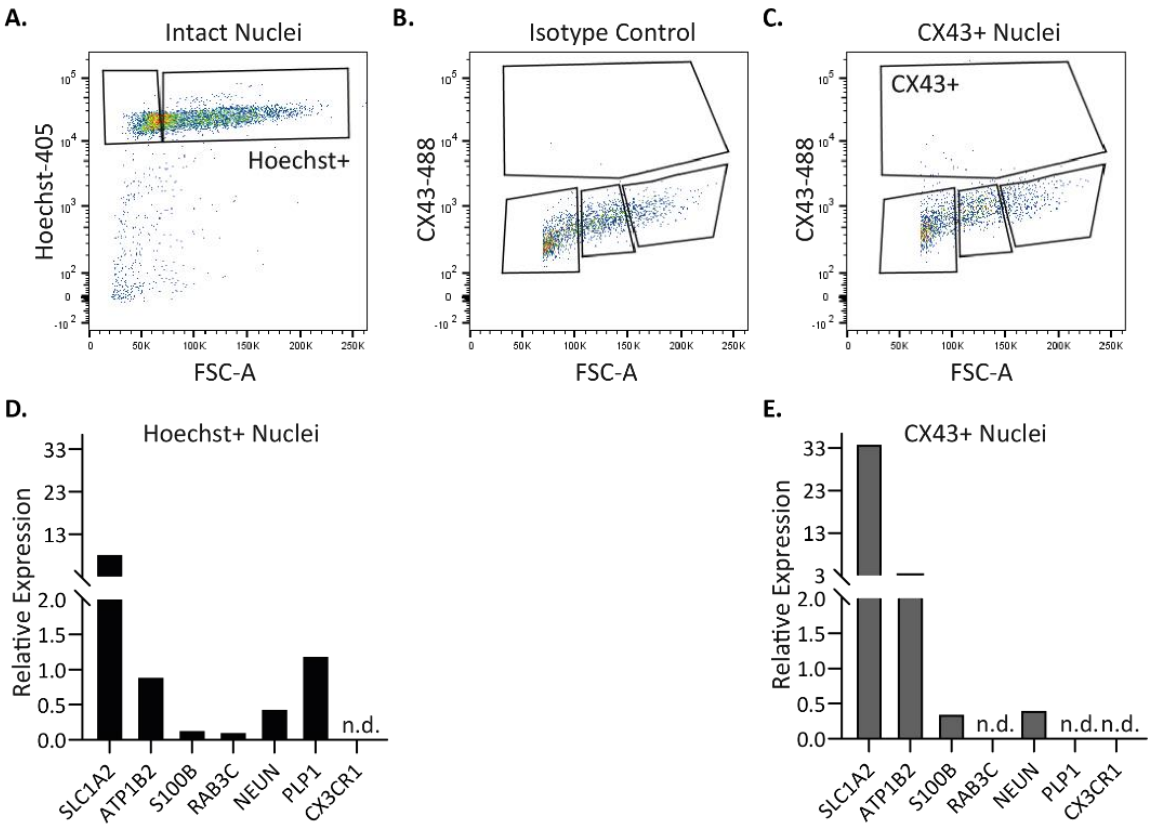

Figure 3.10. Astrocytic Nuclei Isolation with Antibody Targeting CX43 Epitope. Mildly fixed samples were homogenized, and single nuclei suspension was labelled with an anti-CX43 antibody. **A.**, **C.** CX43+ population (**C**) subgated from Hoechst+ fraction (**A**), was defined according to the fluorescence intensity (acquired with 488 nm laser) and size distribution compared to the isotype control (**B**). **D**-**E.** The abundance of known brain cell-type-specific marker expression was observed in Hoechst+ population (**D**) and enrichment of astrocyte markers were measured in CX43+ population (**E**). The flow cytometry analysis was done using FlowJo software.
FSC-A: forward scatter area. n.d: not determined. *SCL1A2, ATP1B2, S100B* – astrocytes, *RAB3C, NEUN* - neurons, *PLP1* - oligodendrocytes, *CX3CR1* – microglia, and *CYC1* – housekeeping gene. Taqman assay was used for qPCR analysis (n = 1).

Furthermore, as shown in Figure 3.10E, qPCR assessment of purity pointed out the enrichment of astrocytic markers, *SLC1A2*: 34.1 a.u., *ATP1B2*: 3.6 a.u., and *S100b*: 0.4 a.u. Notably, the expression levels of other cell type-specific markers were below the detection limits (n.d.), except for the neuronal marker, *NEUN* (0.4 a.u.). As a result, astrocyte-specific markers in the CX43+ population (n = 1, Fig. 3.10E) were enriched compared to the mixed cell-type population (Fig.

3.10D). Consequently, flow cytometry and qPCR analyses suggested that the anti-CX43 antibody was specific and suitable to sort astrocytic nuclei.

In summary, our protocol was thoroughly revised and optimized by modifying the following key parameters: implementing post-fixation of frozen tissue, performing debris removal, and sorting positive nuclei using an antibody against CX43. We successfully applied the adapted protocol to isolate nuclei from distinct astrocytes and assessed the purity by qPCR analysis. Because of the high purity of the sorted population, the low number of nuclei became an acceptable shortcoming of the protocol.

3.1.5.3.Gene Expression Analysis

Considering the improvement of the astrocytic nuclei yield and the purity, we aimed to confirm the compatibility of the modified protocol with RNA sequencing. For this purpose, Hoechst+ and CX43+ nuclei from 100 mg of fresh frozen human brain samples were sorted into PKD buffer and processed for RNA extraction, library preparation, and sequencing (Fig. 3.11).

We extracted RNA from sorted nuclei with RNeasy FFPE Kit and measured the quantity and quality using Bioanalyzer. Poor RNA quality was observed for both populations, Hoechst+ (n = 7, Fig. 3.11A) and CX43+ (n = 2, Fig. 3.11B). This outcome was expected because previous studies already indicated that mild fixation of postmortem brain samples resulted in low RNA quality[178].

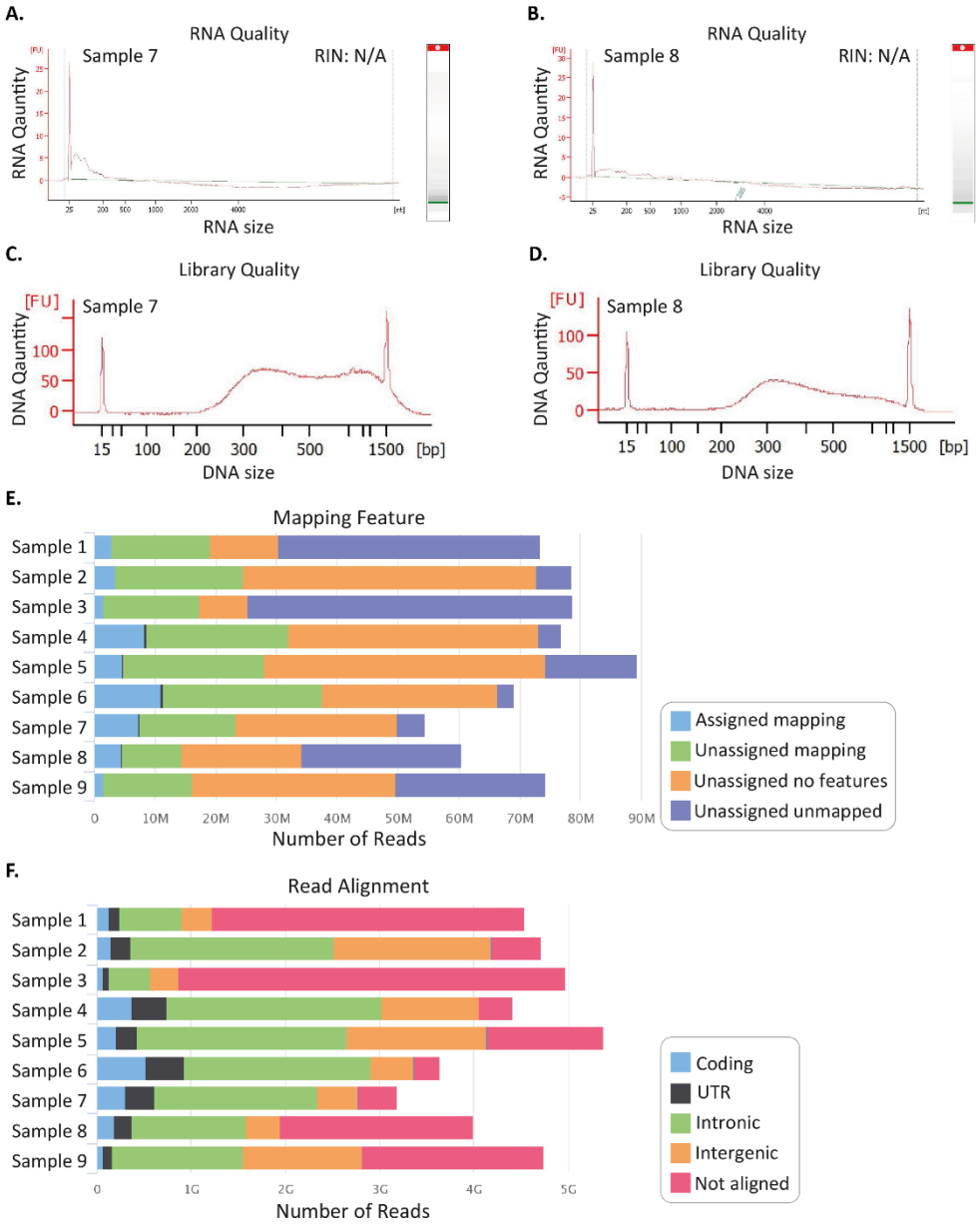

Figure 3.11. Quality Check of Extracted RNA, Generated Libraries, and Sequencing Data. RNA was extracted from Hoechst+ (**A**) and CX43+ (**B**) populations. **A.**, **B.** Representative electropherograms indicated degraded RNA where no peak was observed. Due to poor RNA quality, RIN values were not calculated (RIN: N/A). **C.**, **D.** Libraries were generated from extracted RNA, and the quality was assessed with Bioanalyzer using High Sensitivity DNA Kit. Representative electropherograms for Sample 7 (Hoechst+) (**C**) and Sample 8 (CX43+) (**D**) demonstrated libraries at expected fragment sizes. **E.**, **F.** Sample 2-7 and Sample 9: Hoechst+ nuclei population and Sample 1 and Sample 8: CX43+ nuclei population. Quality check of RNA sequencing focused on the mapping features, representing the number of the reads that are mapped to a known sequence (assigned mapping) and the read alignments data indicating the features of the sequenced data as coding, untranslated region (UTR), intronic, intergenic, and not aligned regions. Both results showed good mapping features, illustrated with the high number of reads. Quality check of sequencing data was conducted by the Computational Biology unit in Boehringer Ingelheim. RIN: RNA integrity number, FU: fluorescence intensity, N/A: not available.

Libraries were prepared with SMARTer Stranded Total RNA-Seq v2 Kit, designed for generating cDNA from highly degraded and low input RNA obtained from fixed material. To amplify cDNA, 16 PCR cycles were run, the highest number of PCR cycles recommended for highly degraded and low input RNA. Representative electropherograms showed that the amplified products were at expected distribution (> 200 bp) for both, Hoechst+ and CX43+ nuclei populations (Figure 3.11C-D). However, we found an overamplification of cDNA samples (second peak occurring around 1000 bp), particularly in the Hoechst+ nuclei population (Fig. 3.11C). This outcome could be due to the variation of the input material, obtained from two separate populations, since libraries were generated using 8.7 ng RNA extracted from 77,000 Hoechst+ nuclei (Fig. 3.11C) and 0.2 ng RNA extracted from 163 CX43+ nuclei (Fig. 3.11D). Considering the data, we decided to adopt the number of PCR cycles according to the input materials and sorted nuclei numbers for our future experiments. Although RNA was highly degraded, another improvement could be made by implementing a fragmentation step before DNA amplification, which would decrease the overamplification and enhance the quality of DNA[207].

To explore further the extent to which our samples were suitable for RNA sequencing, generated libraries were sent to the genomic facility in Boehringer Ingelheim. RNA sequencing was performed on the Illumina HiSeq 4000 platform. Assessing the quality control of the sequencing revealed good mapping features (Fig. 3.11E) and read alignment properties (Fig. 3.11F). Notably, variation between samples within the same population was diminished, suggesting good reproducibility of the procedure. Furthermore, coding regions alignments were improved compared to previous data (Fig. 3.8B) even though the samples were obtained from two different groups, Hoechst+ (Sample 2 to 7 and sample 9) and CX43+ (Sample 1 and 8) nuclei (Fig. 3.11E-F). This data validated the compatibility of our approach with RNAseq-based transcriptomics studies.

In conclusion, we successfully established a novel nuclei isolation protocol suitable for astrocytes isolation from fresh frozen postmortem brain samples.

3.1.6. Final Version of The Protocol: Isolation of Astrocytic Nuclei from Fresh Frozen Human Brain Samples

3.1.6.1. Tissue Homogenization

Fixation. 100 mg of frozen tissue was thawed on ice for 2 min. and was fixed with pre-cooled fixative solution (1% formaldehyde, 0.2 U μl^{-1} RNasin in PBS) for 8 min. on ice. Then, the fixative solution was discarded, and the tissue was washed with 1 ml of staining buffer (0.5% BSA, 0.2 U μl^{-1} RNasin in PBS) by centrifugation at 400 × g for 5 min. at 4˚C.

Homogenization. The tissue was divided into two parts with a pre-chilled scalpel, and each half was transferred into a Dounce homogenizer containing a cold, freshly prepared homogenization buffer (the composition in section 2.1.2). Homogenization was initiated by applying 5 strokes using the loose pestle and completed with the tight pestle for another 10 strokes. The homogenates from two halves were combined and filtered using the cell strainer (40 µm pore size). Finally, the nuclei were pelleted by centrifugation at 1000 × g for 10 min. at 4˚C, and the supernatant was removed.

Debris removal. The pellet was resuspended with 250 µl of staining buffer and another 250 µl of 50% (vol/vol) Optiprep solution (the composition in section 2.1.2) was added on top and mixed gently to make 25% Optiprep-nuclei mixture. In a new tube, 500 µl of 29% Optiprep solution (the composition in section 2.1.2.) was placed, and the 25% Optiprep-nuclei mixture was layered on top. Next, two layers were obtained by centrifugation at 10,000 rpm for 30 min at 4˚C. Then, the supernatant was discarded without disturbing the pellet. Lastly, the pellet was resuspended with 1 ml of staining buffer and continued directly with immunostaining.

3.1.6.2.Nuclei Sorting

Immunostaining. Nuclei were blocked with staining buffer for 15 min. on ice, then incubated with 1000 µl of staining buffer containing primary antibodies for 1 h at 4˚C on a tube rotator. Nuclei were labelled with monoclonal anti-CX43 (2.5 µg/ml, 13-8300, Supp. Table S1), while the isotype control sample was labeled with mouse IgG1, kappa monoclonal antibody (2.5 µg/ml, ab91353, Supp. Table S1). Nuclei were washed with staining buffer by centrifugation at 400 × g for 8 min. at 4˚C. Next, nuclei suspension was incubated with the secondary antibody coupled to Alexa 488 (4 µg/ml, A-11029, Supp. Table S1) for 45 min. at 4˚C on a tube rotator. Finally, after a washing step, the pellet was resuspended with 500 µl of staining buffer containing Hoechst (10 ng/ml), and samples were kept on ice until flow cytometry analysis.

FACS. First gating was performed using side and forward scatter channels for excluding debris and doublets. Intact nuclei were selected by sub-gating on Hoechst (using 405 laser), and CX43+ nuclei populations were defined based on fluorescence intensity (using 488 laser) compared to negative controls (isotype and secondary antibody controls). After that, the size-based selection was performed, and 10-15% of smallest nuclei were excluded (Supp. Fig. S1). Selected populations were sorted into collection tubes containing 100 µl of PKD buffer and stored at -80˚C until RNA extraction.

3.1.6.3.Gene Expression Analysis

RNA extraction and library preparation. RNA was extracted using the RNeasy FFPE kit (Section 2.1.3.3), and libraries were prepared using SMARTer® Stranded Total RNA-Seq Kit v2 - Pico Input Mammalian according to the manufacturers' instruction. For all samples, first-strand cDNA synthesis and fragmentation (94˚C for 2 min.) were performed. The input material (RNA amount) and PCR cycles should be optimized for each new set of samples using the guidelines presented by the manufacturer. RNA and library quality controls were assessed using Bioanalyzer system, RNA 6000 Pico Kit and Agilent High Sensitivity DNA kit.

RNA sequencing. Generated libraries were sent to the genomic facility in Boehringer Ingelheim, and RNA sequencing was performed on the Illumina HiSeq 4000 platform (dual index, paired-end 2 x 75bp run).

3.2. Optimization of the Protocol for Isolating Astrocytes from Various Brain Regions of Freshly Dissected Adult Mouse Brains

3.2.1. Development of the Protocol

We chose the industry standard, MACS technology, to isolate astrocytes from different brain regions of wild-type mice. Two immunolabeling approaches, ACSA-1[208] and ACSA-2[172,209–211], were commercialized by Miltenyi and used widely to sort astrocytes from mouse brain samples. The ACSA-1 strategy was developed to target the glutamate transporter (i.e., GLAST), broadly expressed in astrocytes, and it was primarily applied for early postnatal tissue samples[208]. On the other hand, the ACSA-2 system was shown to be suitable for early and adult postnatal mouse tissue[195]. Moreover, Batiuk et al. (2017) revealed the molecular identity of ACSA-2 epitope as ATP1B2 (ATPase Na+/K+ transporting subunit beta 2) protein and *bona fide* membrane astrocyte-specific marker[172]. ATP1B2 belongs to the family of Na+/K+ ATPases and forms the non-catalytic part of the enzyme that catalyzes the ATP hydrolysis[203]. The exact function of the protein is not known, but it was implicated in regulating neuronal and astrocytic cell adhesion processes[204]. Importantly, the rodent *Atp1b2* levels were shown to be expressed throughout the postnatal ages[212].

In the course of the project, we discovered that the original protocols were performing poorly (e.g., low astrocytes yield) when applied to brain regions implicated in stress-related mental disorders, i.e., PFC. The PFC is a smaller brain region than the cortex or hippocampus, for which the protocols were initially established. Consequently, we decided to modify the standard method to

accommodate the isolation of a sufficient number of viable astrocytes from much lower tissue volume.

The general workflow (Fig. 3.12) of the protocol encompasses i. tissue homogenization, including dissection of brain regions, trituration, and debris removal, ii. astrocyte isolation based on the positive selection of cells labelled with defined antibody, and iii. gene expression analysis, where obtaining a high yield of good quality RNA is the necessary prerequisite.

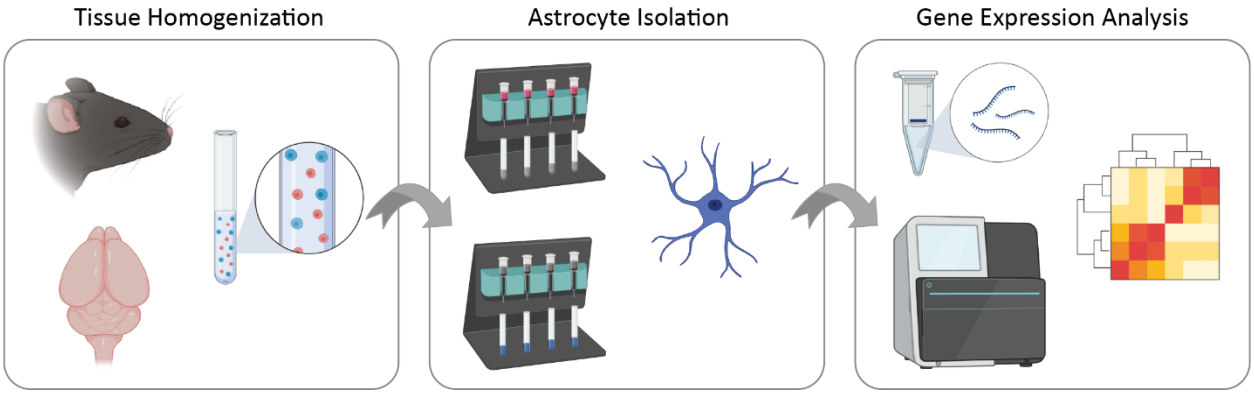

Figure 3.12. Workflow for Isolating Astrocytes from Adult Mouse Brain.

To start, we followed the manufacturers' instructions (Miltenyi) and published methods[172,209,210]. We faced two critical challenges: first, to sort a sufficient number of viable astrocytes from small brain regions, i.e., PFC and hypothalamus (3.3.2. First Optimization) and second, to extract high-quality RNA from sorted cells, suitable for RNA-sequencing (3.2.3. Second Optimization). The original method, followed by a detailed explanation of introduced modifications to adapt it for our specific goal, is described in the subsequent sections.

3.2.2. First Optimization

3.2.2.1. Tissue Homogenization and Astrocyte Isolation

The Adult Mouse Brain Dissociation kit (Miltenyi) was used following the manufacturers' instructions to generate a single-cell suspension. The enzymatic digestion was performed with papain and followed by mechanical trituration using a semi-automated dissociator device (gentleMACS dissociator, Miltenyi). Upon tissue dissociation, cells were filtered through a 70 µm strainer to remove the remaining tissue clumps. Next, the cell suspension was subjected to debris removal using a gradient centrifugation approach. As the last step, red blood cells were eliminated, and the rest of the cells were collected as a pellet.

The standard tissue trituration method suggested by Miltenyi was to use the semi-automated dissociation device. This recommendation was, however, adjusted for big tissue volume (> 60

mm^3) and could not be used for smaller tissues (< 20 mm^3), which would instead stick to the wall of the dissociating tube, preventing proper dissociation. Hence, we decided to apply a manual trituration method using a serological pipette adapted from Batiuk et al. (2017)[172] (a well-established protocol of astrocyte isolation from the whole mouse cortex). We dissected out PFC from a single mouse brain (Fig 2.1), and we performed enzymatic digestion with papain, as recommended by the protocol (Miltenyi), followed by trituration of the tissue with a 1 ml serological pipette. However, we failed to obtain any viable astrocytes (cell numbers were assessed using Neubauer chamber).

We, therefore, switched to an alternative method previously applied to obtain single-cell suspension from several brain regions[213], and we validated its reliability for the isolation of astrocytes from the whole cortex. This protocol implements manual trituration using fire-polished glass pipettes of three diminishing pore sizes intertwined with enzymatic digestions at 37˚C. The first round of manual trituration was performed using unpolished glass pipettes (1 mm, ten strokes). After 5 min. of enzymatic digestion, the second trituration was done with a medium-sized polished pipette (0.6-0.8 mm, ten strokes), followed by 10 min. incubation in papain. Final trituration was performed using small-sized polished pipettes (0.3-0.4 mm, ten strokes).

Upon tissue homogenization, we followed precisely the manufacturers' protocol by performing debris and red blood cell removal, and isolating astrocytes with astrocyte cell surface antigen-2 (ACSA-2) beads. The immunolabeling method was based on the use of magnetic beads covered with an antibody recognizing a cell type-specific membrane epitope, Atp1b2. Subsequently, astrocytes were retained within the magnetic field of the column, washed, and finally eluted. Viable astrocytes were successfully isolated from the whole cortex in average number of $3.8 \times 10^5 \pm 2.1$ (n = 2 independent experiments).

The purity of sorted astrocytes was assessed with qPCR analysis (n = 1, Fig. 3.13, black bars). We observed an enrichment of astrocyte marker (*Aldh1l1*) together with oligodendrocyte marker (*Mbp*). This finding was not unexpected, since Batiuk et al. (2017)[172] also reported oligodendrocyte contamination when they sorted astrocytes using the same labeling system (ACSA-2). Accordingly, the authors applied an additional step: depletion of myelin using Myelin Removal Beads II kit (Miltenyi) with a negative selection strategy through the magnetic field. Following the same approach, myelinated cells were removed before sorting astrocytes. Indeed, an increase in fold change expression (normalized to tissue homogenate) of astrocytic marker (*Aldh1l1*) from 2.49 a.u. to 3.0 a.u., and a decrease of oligodendrocyte marker (*Mbp*) from 1.32 a.u. to 0.01 a.u. were observed (n = 1, Fig. 3.13, grey bars).

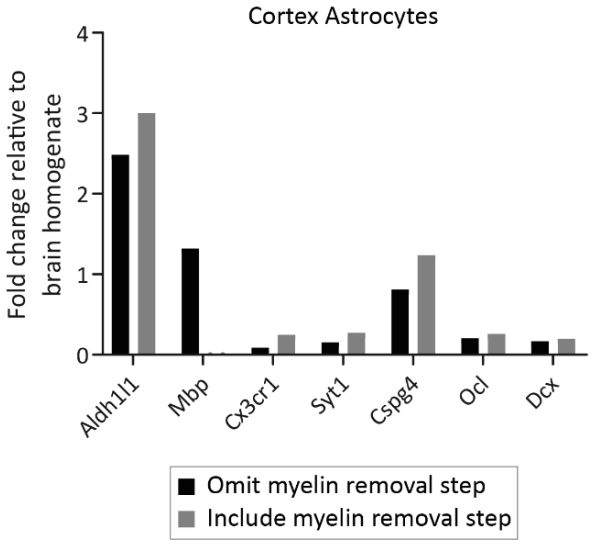

Figure 3.13. Impact of Myelin Removal Step on Cell Purity. qPCR analysis (n = 1) was conducted for evaluating the expression of cell type-specific markers in isolated cortical astrocytes. RNA was extracted using RNeasy Micro kit, and cDNA was reverse transcribed. Performing the myelin removal step increased the enrichment of astrocyte marker – *Aldh1l1* and decreased oligodendrocyte marker – *Mbp* (**grey bar**).
Aldh1l1 - astrocytes, *Mbp* - oligodendrocytes, *Cx3cr1* - microglia, *Syt1* - neurons, *Cspg4* - NG2 cells, *Ocln* - endothelial cells, *Dcx* – neuronal precursors, and *Cyc1* - housekeeping gene. Fold change relative to brain homogenate: $2^{(-\Delta\Delta Ct)}$, $\Delta Ct = Ct_{Target\ gene} - Ct_{Housekeeping\ gene}$.

After effectively isolating astrocytes from the whole mouse cortex, the protocol was adapted to sort cells from the brain regions of our interest (i.e., hippocampus, motor cortex, hypothalamus, and PFC). During manual trituration, the stroke numbers were adjusted for each brain region by visually inspecting the fraction of dissociated tissue (i.e., 5 strokes/trituration step for PFC, hypothalamus, motor cortex, and 10 strokes/trituration step for the hippocampus).

Furthermore, the effect of debris removal was assessed in a separate experiment, where astrocytes were isolated from the hypothalamus. The yield of astrocytes decreased when we applied this procedure (cell number: 2.7×10^4) compared to the parallel experiment omitting this step (cell number: 4×10^4). Therefore, to prevent loss of cells, in the subsequent experiments debris and red blood cell removal steps were omitted (the latter procedure was also excluded in Batiuk et al. (2017)[172]). Finally, we depleted myelin and collected ACSA-2 positive cells. With these modifications, we obtained the following numbers of isolated astrocytes from a single brain sample using both hepmispheres, PFC: 2×10^4, hypothalamus: 3.2×10^4, motor cortex: 2.5×10^4, and hippocampus: 5×10^4 (n = 1).

Finally, we assessed the purity of the sorted astrocytes population, evaluating the expression levels of cell type-specific markers (n = 1, cells were pooled from 3 independent ACSA-2 isolation, Fig. 3.14). qPCR data suggested enrichment of astrocyte-specific marker (*Aldh1l1*) in isolated cells from every brain region, with concomitant decrease of other cell types. Taken together, we assumed that we successfully optimized the MACS system for sorting astrocytes from various, freshly dissociated, brain regions.

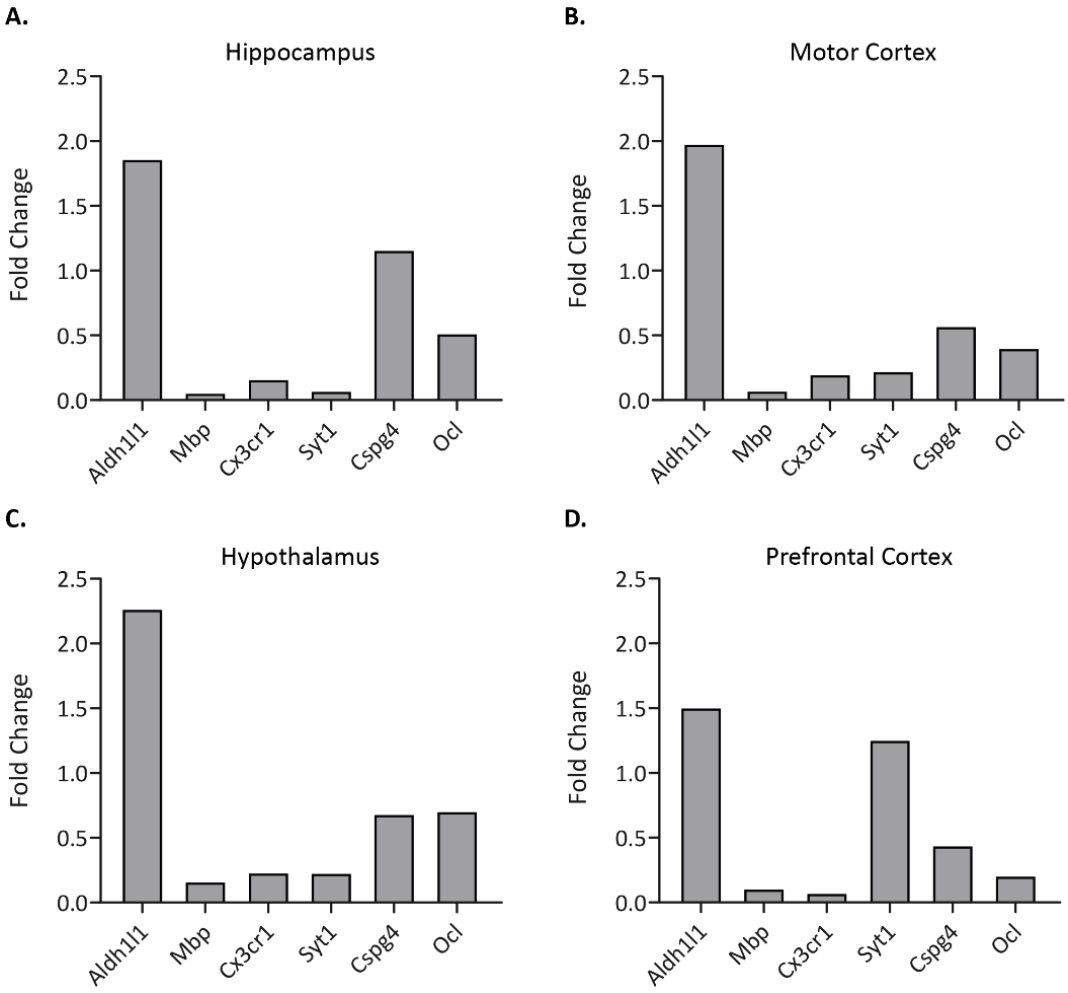

Figure 3.14. Purity Analysis of Astrocytes Isolated from Different Brain Regions. Graphs represent the expression levels of cell-type-specific markers in the sorted astrocytes population from 4 brain regions. These results were obtained from a single experiment, where astrocytes were pooled from 3 independent ACSA-2 isolations.

Aldh1l1 - astrocytes, *Mbp* - oligodendrocytes, *Cx3cr1* - microglia, *Syt1* - neurons, *Cspg4* - NG2 cells, *Ocln* - endothelial cells, and *Cyc1* – housekeeping gene. Fold change (relative to brain homogenate): $2^{(-\Delta\Delta Ct)}$, $\Delta Ct = Ct_{Target\ gene} - Ct_{Housekeeping\ gene}$.

3.2.2.2.Gene Expression Analysis

To test the quality of RNA extracted from astrocytes we used a cohort of mice (Cohort-1, N = 24) to isolate astrocytes from two brain regions, hippocampus, and PFC, as described above. These two brain regions were selected since they represent the two opposite poles with respect to the yield of astrocytes. As a result, we obtained on average $3 \times 10^4 \pm 8.5 \times 10^3$ cells per one hippocampus and $9.3 \times 10^3 \pm 4.3 \times 10^3$ cells per PFCs (from both hemispheres). Astrocytes were sorted directly into lysis buffer (RLT buffer) and were stored at -80˚C. Downstream processes,

including RNA extraction, library preparations, and RNA-seq data analysis were performed in the genomic facility of Boehringer Ingelheim.

The quality control of our samples was assessed by analyzing RNA quantity and integrity with Bioanalyzer (Fig. 3.15). The measurements indicated that the quantity of RNA extracted from hippocampal astrocytes was on average 172 ± 151.1 ng, higher than PFC, yielding on average 16.5 ± 13.3 ng (*P < 0.0001*, N = 24, Fig. 3.15A). This variation could be explained by the difference in isolated astrocyte numbers from those regions. However, the quality of RNA was poor, particularly in the PFC, with a mean RIN value of 3.9 ± 3.5 (N = 24, Fig. 3.15B). In addition, high inconsistency on RNA integrity between samples was observed for both brain regions. As a result, the RNA sequencing data was of low quality; the read alignment indicating high intronic (47%) and intergenic reads (13%) in contrast to low exonic reads (39%) (data not shown). Hence, downstream gene expression analysis was not pursued.

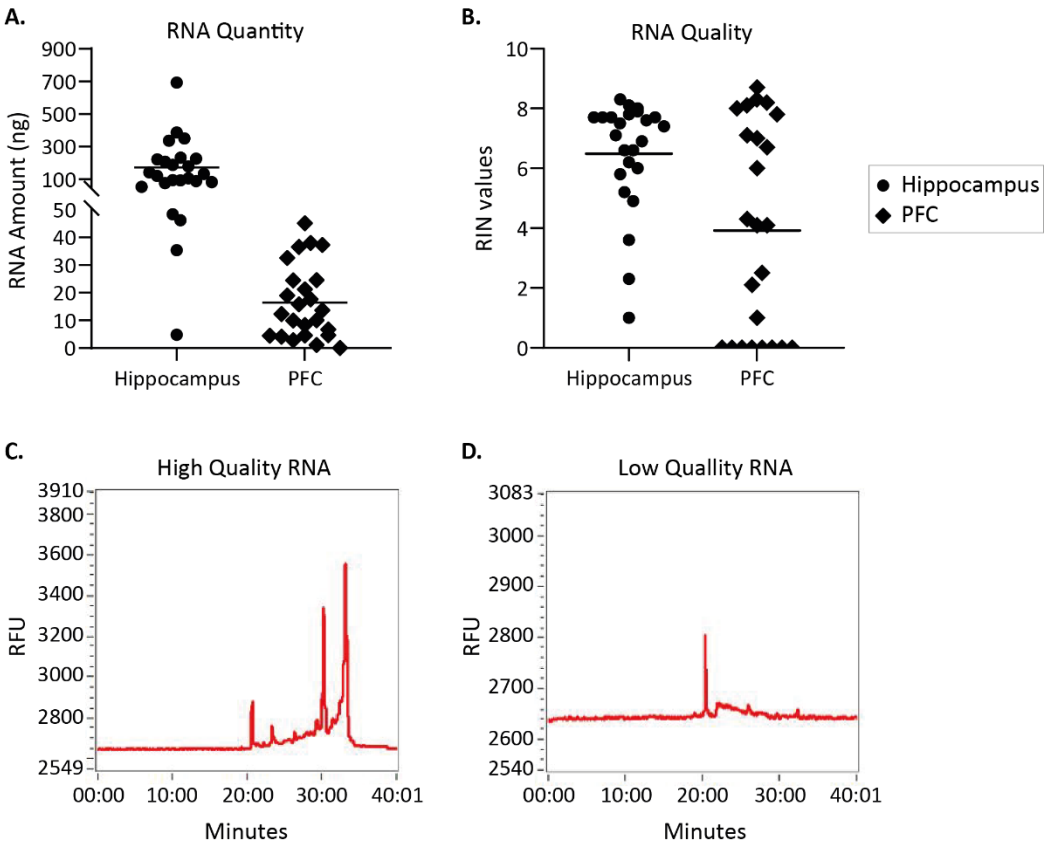

Figure 3.15. Parameters of Extracted RNA from Cohort-1. Astrocytes were isolated from the hippocampus (dots) and PFC (rhombus) obtained from 24 mice (Cohort-1). **A.** The graph represents the quantity of RNA extracted from sorted cells, which was sufficient (threshold, 10 ng) for performing downstream sequencing. Quantity of RNA, Hippocampus vs PFC: $P < 0.0001$. **B.** The integrity of RNA was evaluated according to the RIN values. Samples from PFC showed low and inconsistent RIN values, Hippocampus vs PFC: $P = 0.034$. **C.**, **D.** Representative electropherograms indicate high quality (**C**) and low quality (**D**) of RNA. The data was generated by the Computational Biology unit in Boehringer Ingelheim. RNA quantity and quality were measured with Bioanalyzer using RNA 6000 Nano Kit.
RIN: RNA integrity number, 1 being entirely degraded RNA and 10 fully intact. RFU: Relative fluorescence units, indicating the amount of RNA at a particular size/time. The X-axis shows time in minutes as the RNA fragments are separated during electrophoresis. Mann-Whitney test was performed since the data was not normally distributes based on the Shapiro-Wilk test.

In summary, in the first optimization, we achieved our first goal: high yield of viable astrocytes from low tissue volume, i.e., the prefrontal cortex, hypothalamus, and motor cortex. However, the second challenge remained open, as we failed to obtain high-quality genetic material suitable for RNA-seq (Fig. 3.15). Since the latter criterion is a crucial parameter to get biologically significant transcriptomic data, we performed a second round of optimization experiments to overcome this problem.

3.2.3. Second Optimization

3.2.3.1. Tissue Homogenization and Astrocyte Isolation

To improve the quality of sorted material, we addressed several parameters by putting emphasis on the tissue homogenization step (Table 3.3): i. DNAse I addition. ii. debris removal. iii. size of cell strainer. iv. performing the entire experiment at 4˚C. v. dead cell removal. These steps were tested using the hippocampus, since it offered a decent dynamic range of viable astrocytes fractions, enabling evaluating the beneficial effect of each modification.

i. Previously, we combined enzymatic digestion with manual trituration performing three sequential homogenization steps. We used three types of fire-polished glass pipettes and adapted stroke numbers to respective brain regions. To test alternative approach, after the second round of trituration, we separated half of the suspension (already dissociated cells) to prevent cell loss due to excessive trituration. Besides, DNase I was added, as suggested in the literature[172], to reduce DNA leakage, which could cause an increase in viscosity and formation of cell clumps. Indeed, the addition of DNase I increased the quantity and quality of RNA (Table 3.3).

ii. Another critical factor was the inclusion of debris removal in our protocol. Manufacturer (Miltenyi) instructions and several published studies[172,210] suggested including this step since debris and dead cells can inhibit antibody staining, decrease the sorting efficiency, and interfere

with RNA quality. Indeed, including this step lowered astrocyte yield but increased the quantity and quality of RNA (Table 3.3).

Furthermore, we tested iii. a smaller-sized cell strainer (40 µm instead of 70 µm) to filter out remaining tissue clumps, iv. we performed the entire cell isolation experiment at 4˚C to retain cell/RNA integrity, and v. we eliminated dead cells through a commercial kit (Miltenyi), which could be combined with the MACS system. However, as shown in Table 3.3, these modifications did not improve the quality of sorted materials.

In summary, the effects of the resulting parameters on extracted RNA (i.e., quantity and quality) are provided in Table 3.3. We concluded that the necessary modifications that ameliorated quality of RNA were DNase I addition and the debris removal step. Therefore, these two steps were included in the protocol.

Table 3.3. List of Modified Parameters for Improving RNA Quality. The table represents all the parameters tested to improve the quality of RNA extracted from sorted hippocampal astrocytes. RT: Room temperature.

Modified Step	Cell Number x 10^3	RNA Concentration, ng/µl Nanodrop | Bioanalyzer		RIN Values
DNase I addition	11.5	9.2	74	8.7
Debris removal	10.5	3.5	19.7	8.2
40 µm filter at 4˚C	7	3.4	15.1	7.9
40 µm filter at RT	5.5	4.4	6.7	7.6
Dead cells removal-MACS	1.8	3.7	2.1	1
Dead cells removal-FACS	0.5	3.9	1.5	1

Following the optimization of the tissue homogenization using the hippocampus, astrocytes were isolated from PFC and extracted RNA quantity and quality were assessed. As expected, we noticed that homogenization of PFC with debris removal step decreased the yield of astrocytes and RNA quantity (Fig. 3.16, grey dots). However, omitting the debris removal while maintaining the addition of DNase I to the cell suspension enhanced the yield of isolated RNA (Fig. 3.16, purple dots).

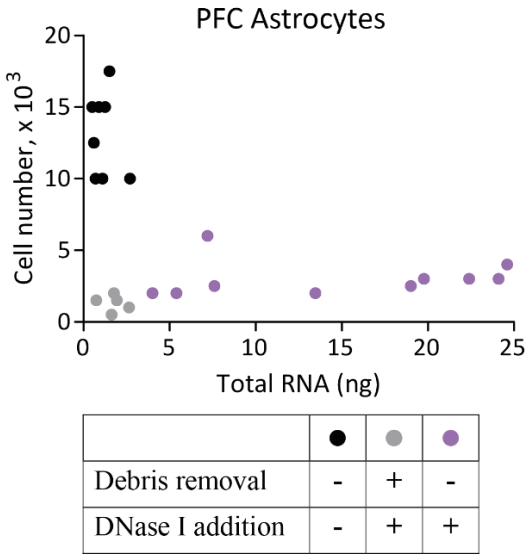

Figure 3.16. Optimization of Tissue Homogenization Step for PFC. The graph indicates the impact of different types of tissue manipulations on sorted astrocytes. PFC was homogenized using 3 procedures: without debris removal or DNase I addition (**black dots**, N = 8), the inclusion of both steps (**grey dots**, N = 5), and only DNase I addition (**purple dots**, N = 10).
Cells were counted with Neubauer chamber. RNA quantity was measured with Bioanalyzer using RNA 6000 Pico Kit.
"N" indicates the number of mice used in each group during independent experiments.

Based on this data, we decided to include the debris removal step only when astrocytes were isolated from big tissue volumes (e.g., whole cortex, hippocampus, and somatosensory cortex) and to omit this step for lower tissue volumes (e.g., PFC, hypothalamus).

Consequently, our final adapted protocol for the generation of single-cell suspension consisted of performing sequential homogenization steps, preventing over trituration of cells by separating half of the suspension after the second round of homogenization step, the addition of DNase I, and debris removal step for big tissue volumes.

3.2.3.2.Gene Expression Analysis

After the second optimization, we tested our protocol for compatibility with RNA sequencing. Astrocytes were isolated from a new cohort of mice (Cohort-2, N = 15). For this occasion, RNA extraction and library preparation were performed in collaboration with EMBL Genomics Facility (as explained in section 3.2.4.3).

To evaluate the impact of steps incorporated in the second optimization, we compared several parameters between the genetic material extracted from the hippocampus and PFC in Cohort-1 (first optimization, N = 24) and Cohort-2 (second optimization, N = 12). For both brain regions, the number of cells obtained in Cohort-1 (mean $(\overline{x})_{(hippocampus)}$: 30 x 10^3 ± 8.5 x 10^3 and $\overline{x}_{(PFC)}$: 9.3 x 10^3 ± 4.3 x 10^3) were higher than Cohort-2 ($\overline{x}_{(hippocampus)}$: 15.9 x 10^3 ± 6.4 x 10^3 and $\overline{x}_{(PFC)}$: 3.7 x 10^3 ± 1.4 x 10^3) (Fig. 3.17A), pointing out that the latter protocol caused loss of cells.

Likewise, RNA quantity in Cohort-2 ($\overline{x}_{(hippocampus)}$: 34.1 ± 15.5 ng) was lower when cells were isolated from the hippocampus compared to Cohort-1 ($\overline{x}_{(hippocampus)}$: 172 ± 151.1 ng) (Fig. 3.17B),

probably due to the additional debris removal step. However, as seen in Figure 3.17C, the second optimization increased the RNA quality (i.e., RIN values) in Cohort-2 ($\overline{x}_{(hippocampus)}$: 7.7 ± 0.5 and $\overline{x}_{(PFC)}$: 7.2 ± 0.5) and made it more consistent across the samples in comparison to Cohort-1 ($\overline{x}_{(hippocampus)}$: 6.5 ± 1.9 and $\overline{x}_{(PFC)}$: 3.9 ± 3.5). Since the RIN value is a crucial parameter for performing high-quality transcriptomic analysis, we implemented the respective changes into our main workflow.

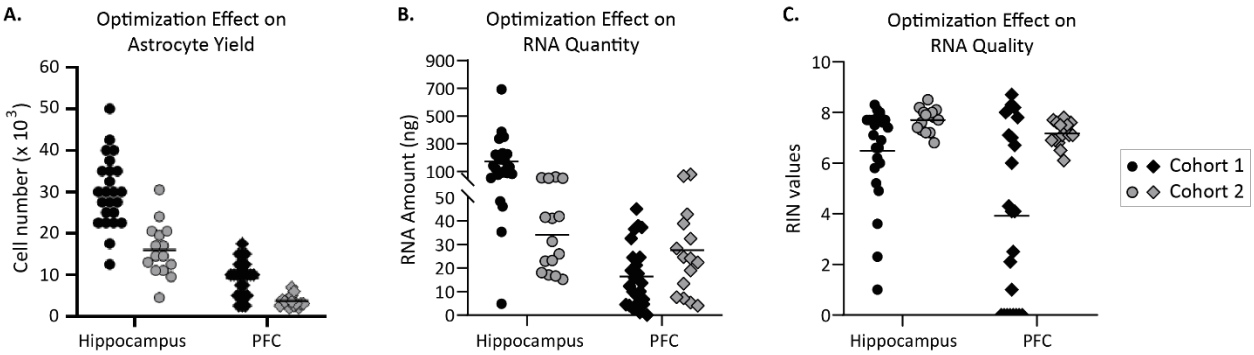

Figure 3.17. Comparison Between Cohort-1 and Cohort-2: Cell Number, RNA Quantity, and Quality. Two independent data sets are generated with Cohort-1 (N = 24) and Cohort-2 (N = 15). Astrocytes were isolated from the hippocampus (dots) and PFC (rhombus). The graphs show number of sorted cells (**A**), the yield of extracted RNA (**B**), and the RNA quality (**C**). **A.** Optimization steps decreased astrocyte yield sorted from both brain regions in Cohort-2. Cohort-1 vs. Cohort-2, hippocampus: $P < 0.0001$ and PFC: $P < 0.0001$. **B.** Second optimization caused a reduction in RNA quantity for hippocampal tissue. Cohort-1 vs. Cohort-2, hippocampus: $P < 0.0001$ and PFC: $P = 0.091$. **C.** Quality of RNA increased and became more consistent within samples for both brain region in Cohort-2. Cohort-1 vs. Cohort-2, hippocampus: $P = 0.005$ and PFC: $P < 0.001$.
Cells were counted with Neubauer chamber. RNA was extracted using RNeasy Plus Micro Kit. RNA quantity and quality were measured with Bioanalyzer using RNA 6000 Pico Kit. Multiple Mann-Whitney test was performed. "N" indicates the number of mice used in each group.

To assess whether sorted materials are suitable for RNA sequencing, libraries were generated from extracted RNA using a modified version of Smart-seq2 protocol[198] (in collaboration with EMBL Genomics Facility) and preliminary quality control of sequenced data was performed by a trained bioinformatician (collaboration with Intelliseq). This analysis revealed that the improved RNA quality of our samples enabled us to obtain better sequencing performance; the read alignment indicated low intronic (Cohort-2: 7% vs. Cohort-1: 47%) and intergenic reads (Cohort-2: 16% vs. Cohort-1: 13%) compared to high exonic reads (Cohort2: 76% vs. Cohort-1: 39%) (data not shown).

In conclusion, we successfully optimized the published protocol for isolating mouse astrocytes from freshly dissected brain regions, i.e., hippocampus and PFC. Importantly, this amelioration allows reliable RNA-seq with single mouse resolution.

3.2.4. Final Version of The Protocol: Isolation of Astrocytes from Various Brain Regions of Freshly Dissected Adult Mouse Brains

3.2.4.1. Tissue Homogenization

Homogenization. Freshly dissected mouse tissues were homogenized using the Adult Mouse Brain Dissociation kit (Miltenyi) with implemented modifications. Brain tissues were minced with a pre-cooled scalpel on ice (omitted for PFC and hypothalamus), transferred into the tube containing pre-heated Enzyme mix 1 (50 µl Enzyme P + 1900 µl Buffer Z), and incubated for 10 min. at 37˚C. Next, Enzyme mix 2 (10 µl Enzyme A + 20 µl Buffer Y) was added, and the first round of trituration was performed (5 strokes, for whole-brain and cortex: 10 strokes) with an unpolished Pasteur pipette. After incubating for 5 min. at 37˚C, the second trituration was conducted (5 strokes, for whole-brain and cortex: 10 strokes) with a medium-sized fire-polished Pasteur pipette. Then, 1 ml of cell suspension was placed into a new tube and kept on ice. The remaining homogenate was incubated for 10 min. at 37˚C. Next, 125 U/ml of DNase I was added, and final trituration was done (5 strokes, for whole-brain and cortex: 10 strokes) using a small-sized fire-polished Pasteur pipette. Finally, the homogenate was filtered (the remaining 1 ml cell suspension kept on ice was applied as well), and the cells were pelleted by centrifugation at 300 × g for 10 min. at 4˚C (Supp. Fig. S2).

Debris removal. This step was performed only when astrocytes were isolated from the whole-brain, cortex, somatosensory cortex, and hippocampus. If simultaneously astrocytes needed to be isolated from smaller-sized brain tissues (i.e., PFC, hypothalamus, and motor cortex), pellets from the previous step were resuspended in 100 µl of PB buffer (DPBS, pH 7.2, and 0.5% BSA) and were kept on ice until debris removal was completed. Exclusion of debris was conducted according to the manufacturers' instructions with slight modification; buffer volumes were adjusted according to the tissue size (indicated in Supplementary Information 5.2). The pellet from the homogenization step was resuspended in cold DPBS and mixed with a cold debris removal solution. Next, cold DBPS was gently overlayed to obtain clear two phases and centrifuged at 3000 × g for 10 min. at 4˚C with full acceleration and full brake. The top two phases were discarded (Supp. Fig. S2), cold DPBS was added to a final volume of 15 ml and was gently mixed by inverting the tubes 3 times. Next, cells were pelleted by centrifugation at 1000 × g for 10 min. at 4˚C with full acceleration and full brake.

3.2.4.2.Astrocyte Isolation

Myelin Removal. Myelin removal step was performed using Myelin Removal Beads II kit (Miltenyi) following the manufacturers' instructions. The pellets were resuspended in PB buffer (volumes are indicated in Supplementary Information 5.2), myelin removal beads were added, mixed by pipetting up and down, and incubated for 15 min. at 4˚C. Cells were washed with PB buffer and centrifuged at 300 × g for 10 min. at 4˚C. Next, myelinated cells were removed through a magnetic separator using MS columns. Myelin-positive cells were retained in the column, and the flowthrough (myelin-negative cells) were collected and centrifuged at 300 × g for 10 min. at 4˚C.

ACSA-2+ cell isolation. Anti-ACSA-2 MicroBeads kit (Miltenyi) was used to purify astrocytes precisely following the manufacturers' protocol. Positive selection was performed where astrocytes were magnetically labelled with the beads, retained within the column during the magnetic field, and eluted. Next, cells were pelleted by centrifugation at 300 × g for 10 min. at 4˚C, washed with 500 µl of cold DPBS, and centrifuged again at 300 × g for 5 min. at 4˚C. Finally, the pellets were resuspended in 350 µl of RLT buffer containing β-mercaptoethanol (10 µl of β-ME per 1 ml of RLT buffer) and stored at -80˚C.

3.2.4.3.Gene Expression Analysis

RNA extraction and library preparation. RNA was extracted using the RNeasy Plus Micro kit (as described in section 2.2.2.3), and cDNAs were prepared using a modified version of Smart-seq2 protocol[198] in collaboration with EMBL Genomics Facility. Nextera XT DNA Library Preparation Kit (Illumina) was used following the internal protocol of EMBL Genomics Facility. Maximal amount of RNA (2.4 µl) was employed to generate cDNA, and 0.2 ng of amplified cDNA was used with 20-40 ng/µl custom-made Tn5 enzyme (EMBL Genomics Facility) for the tagmentation of cDNA. Next, PCR amplification was performed for adapter-ligand fragments adding a unique pair of i5 and i7 adapters (Illumina) in the reaction. Lastly, RNA and library quality controls were done using Bioanalyzer system, RNA 6000 Pico Kit and Agilent High Sensitivity DNA kit.

RNA sequencing. The sample pools (mix of 13-16 libraries in one tube) were sequenced using NextSeq 500 system (Illumina) at EMBL Genomics Facility (dual index, paired-end 2 x 75bp run).

3.3. Applicability of the Protocols for Studying Astrocytes' Transcriptome in Human MDD and Mouse Model of Chronic Stress

3.3.1. Nuclear RNA Sequencing in the Prefrontal Cortex of Depressed Suicides

To investigate transcriptional changes specific to the vmPFC (i.e., BA25), the nuclei isolation protocol (as described in section 3.1.6) was applied to fresh frozen human postmortem brain samples. Two nuclei fractions, i.e., Hoechst+ and CX43+, were isolated from the postmortem tissue blocks of healthy controls (CON, N = 12) and suicide completers (MDD, N = 15). Due to the focus of the study, samples were chosen from a previously characterized cohort[37], where low expression of astrocyte-specific genes was reported in two PFC areas: BA8/9 and BA10[37]. The selected suicide subjects displayed a significant decrease in the expression of at least 5/7 genes (*GFAP*, *ALDH1L1*, *SOX9*, *GLUL*, *SLC1A3*, *GJA1*, and *GJB6*)[37], and the controls were individuals who died suddenly. We reasoned that a detailed investigation of astrocyte transcriptional profiles would deepen insight into the deregulation of astrocyte-specific molecular pathways, leading to a better understanding of the underlying pathology. There were no statistically significant differences in pre-and postmortem variables, such as age and PMI, within the selected groups of controls and suicide cases (Table 2.4). However, significant differences were found between the CON and MDD patients for the confounding factors, pH ($P < 0.048$) and refrigeration delay ($P < 0.014$, Table 2.4).

3.3.1.1. Validity of the Technical Parameters in Isolation of Hoechst+ and CX43+ Nuclei Populations

Two nuclei fractions were isolated from CON and MDD subjects (Fig. 3.18A). The number of Hoechst+ nuclei and fraction of Hoechst+ population were similar between CON and MDD (Fig. 3.18B-C). Likewise, there was no statistically significant difference among CON and MDD in the CX43+ nuclei yield and the fraction of the CX43+ population (Fig. 3.18B-C). These data suggested that Hoechst+ and CX43+ nuclei are equally numerous in controls and suicide completers. A total yield of Hoechst+ population (average nuclei count: 77,795 ± 43,072) was higher compared to CX43+ populations (average nuclei count: 776 ± 640, $P < 0.0001$). This result was expected, since the Hoechst+ population represented all nuclei within the tissue homogenate, while CX43+ population was only a fraction of nuclei expressing the targeted epitope.

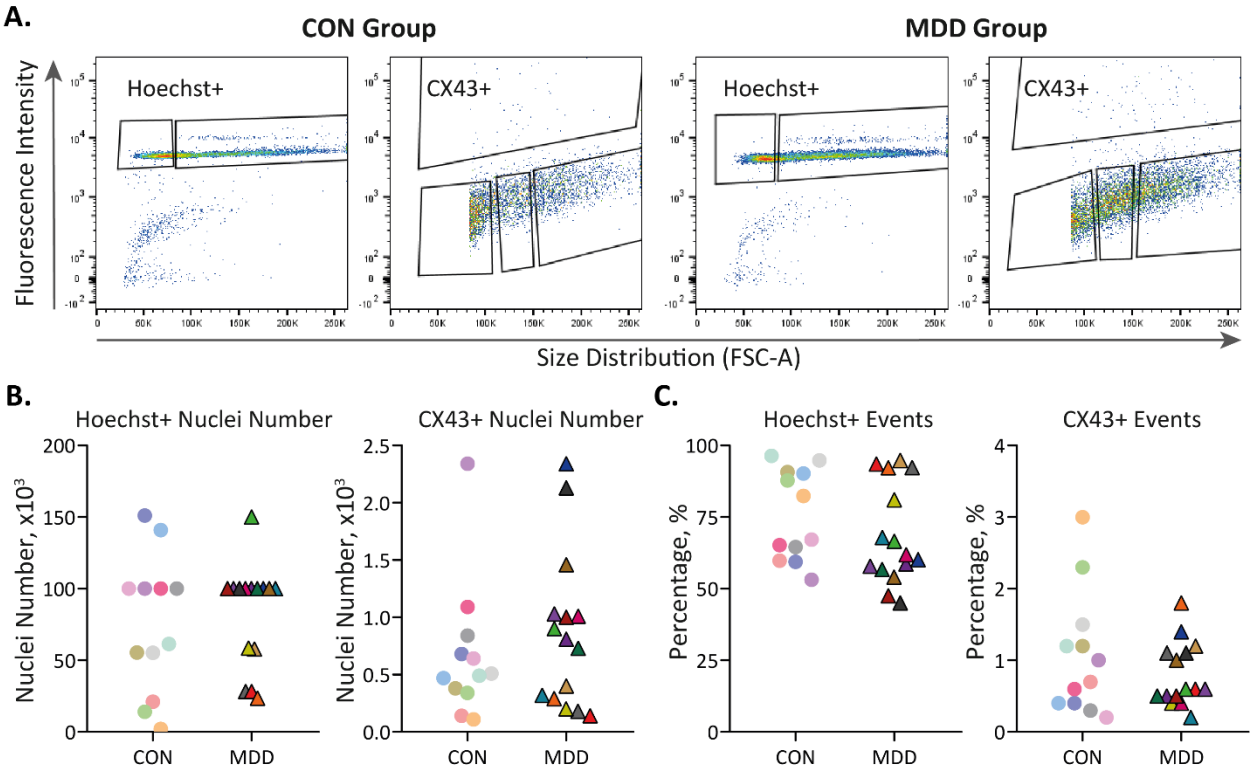

Figure 3.18. FACS Nuclei Isolation from CON and MDD Brain Samples. A. Representative flow cytometry plots illustrating the gating for Hoechst+ and CX43+ populations in CON and MDD groups. **B.** Nuclei numbers isolated from both populations were similar between the study groups (CON (dots) vs MDD (triangles), Hoechst+, *P = 0.56* and CX43+, *P = 0.48*. **C.** No statistically significant difference was found among the study groups for the positive events, CON vs. MDD, Hoechst+: *P = 0.29* and CX43+: *P = 0.62*. On **B** and **C** each symbol represents a value from a single donor. The flow cytometry analysis was done using FlowJo software.
FSC-A: forward scatter area. Mann-Whitney test was performed since the data was not normally distributes based on the Shapiro-Wilk test.

Importantly, no statistically significant differences between the CON and MDD groups were detected within populations for the RNA quantity (Fig. 3.19A) and quality (Fig. 3.19B). The total yield of extracted RNA was much higher from the Hoechst+ population (average RNA amount: 114.1 ± 87.5 ng) than from the CX43+ population (average RNA amount: 1.2 ± 0.4 ng) (*P < 0.0001*, Fig. 3.19A). As expected, poor quality of RNA was observed for both populations, Hoechst+ (average RIN value: 2.9 ± 0.9) and CX43+ (average RIN value: 1.5 ± 0.3) (Fig. 3.19B). Low RIN values were reported as a typical feature of mild fixation of postmortem brain samples prior to nuclei isolation[178]. Therefore, RNA was processed for the construction of SMARTer Stranded Total RNA-Seq libraries.

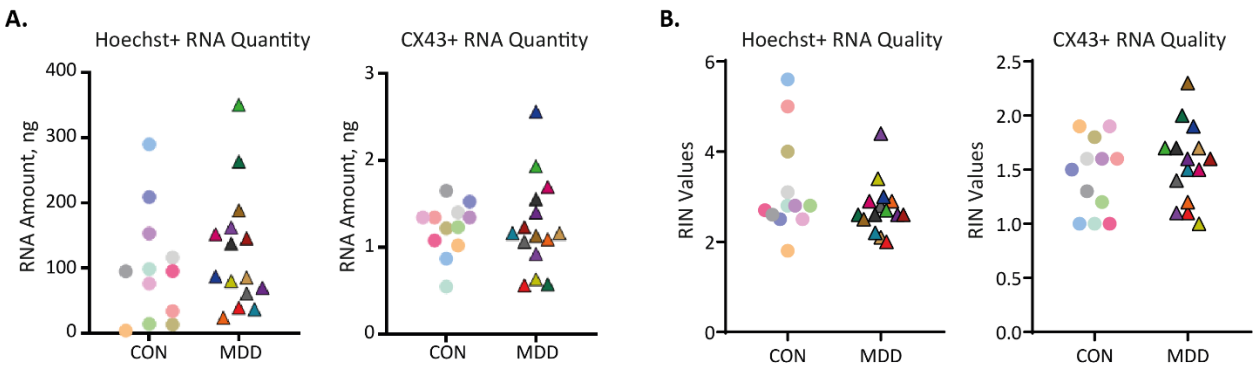

Figure 3.19. RNA Quantity and Quality Comparison Between CON and MDD Samples. RNA was extracted from Hoechst+ (N = 27) and CX43+ (N = 27) nuclei. **A.** RNA quantities from both populations were similar between the study groups, CON (dots) and MDD (triangles), Hoechst: CON vs. MDD, *P = 0.52* and CX43: CON vs. MDD, *P = 0.94*. **B.** No statistically significant difference was found among the study groups for the RIN values, Hoechst: CON vs. MDD, *P = 0.42* and CX43: CON vs. MDD, *P = 0.46*. Data from each donor is represented individually.

RNA was extracted using RNeasy FFPE Kit. Quantity and quality of RNA were measured with Bioanalyzer using RNA 6000 Pico Kit. Either t-test or Mann-Whitney test was performed when the data was not normally distributes based on Shapiro-Wilk test. RIN: RNA integrity number.

The quality check of generated libraries revealed fragment sizes at an expected range (> 200 bp) for both nuclei populations (Fig. 3.20). However, libraries generated from Hoechst+ samples displayed a second peak around 1000 bp (Fig. 3.20A). In contrast, libraries originating from CX43+ samples showed a single peak only at the expected size (~350 bp, Fig. 3.20C), thus demonstrating a better quality. We attempted to improve the quality of libraries in the Hoechst+ population by modifying several parameters (i.e., the amount of input material (RNA and DNA), number of PCR cycles for DNA amplification, and DNA purification steps). Nevertheless, these experiments did not result in noticeable improvement.

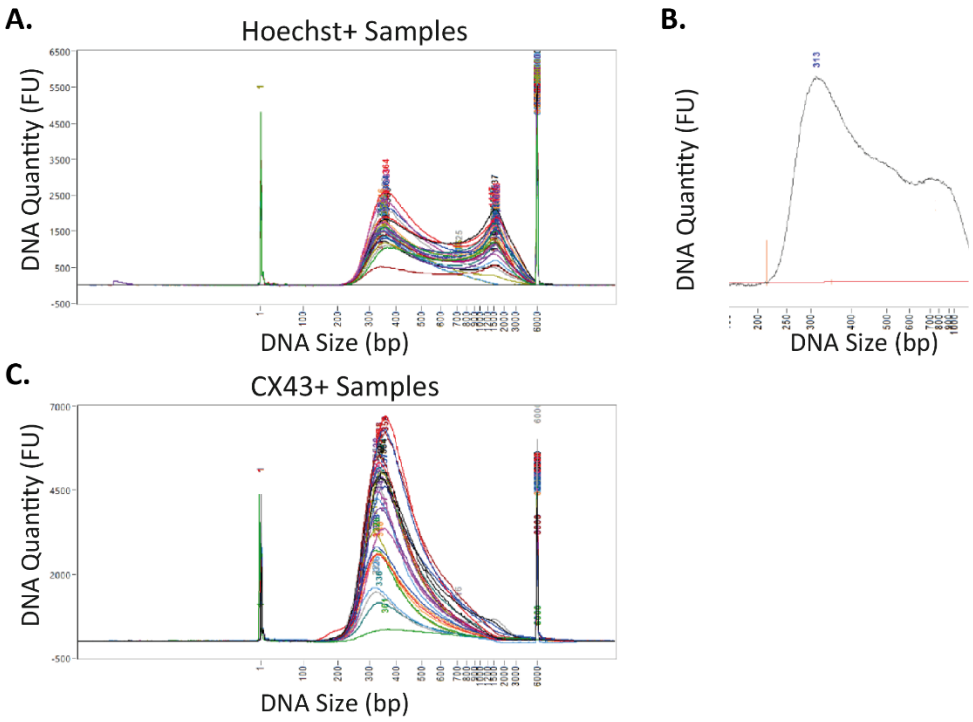

Figure 3.20. Quality Check of Generated Libraries. Libraries were generated from extracted RNA, and the quality was assessed with Bioanalyzer using High Sensitivity DNA Kit**. A.**, **C.** Electropherograms of amplified DNA from Hoechst+ (**A**) and CX43+ (**C**) samples illustrated fragment sizes at an expected range, > 200 bp, where libraries were generated using SMARTer Stranded Total RNA-Seq Kit. **A.** Libraries constructed from Hoechst+ samples had a second peak around 1000 bp. **B.** Re-generated libraries using the NEB Next Ultra II Directional RNA approach (conducted by the Computational Biology unit in Boehringer Ingelheim) displayed better quality (one prominent peak). **C.** Libraries generated from CX43+ samples showed a single peak at the expected size, 350 bp. Data from each donor is represented individually. The electropherograms were produced by the Computational Biology unit in Boehringer Ingelheim. FU: Fluorescence unit. bp: base pair.

Interestingly, we observed a similar peak distribution previously in libraries generated from Hoechst+ nuclei populations (section 3.1.5.3, Fig. 3.11C). We reasoned that the selected method to generate libraries might not be suitable for the Hoechst+ population due to the high input material, i.e., nuclei number (average nuclei count: 77,795). Consequently, libraries from the Hoechst+ population were re-generated by employing the NEB Next Ultra II Directional RNA approach (conducted by the Computational Biology unit in Boehringer Ingelheim), suitable for high input material. These libraries displayed one prominent peak at the expected size range (> 200 bp) with a short shoulder in the electropherogram. Thus, we concluded that the quality was ameliorated (Fig. 3.20B).

Prior to gene expression analyses, post-RNA-seq quality control was evaluated. The percentage of uniquely mapped reads (Hoechst: 60-80% and CX43: 20-40%) together with mapping features and read alignment properties (Supp. Fig. S3) were comparable to the literature (i.e., nuclear RNA-

seq data)[178,214]. The percentage of uniquely mapped reads in the CX43+ population was lower than the Hoechst+ population, possibly due to the low number of nuclei. Not surprisingly, most of the reads were mapped to introns because of the nature of the nuclear RNA representing the nascent and pre-mature RNA transcripts (Supp. Fig. S3C, D). Importantly, we did not observe any differences in sequencing performance between the study groups, CON and MDD. Moreover, unbiased clustering through principal component analysis did not reveal major effects of MDD on gene expression profiles (Supp. Fig. S4). Although few outliers were noticed (e.g., S244 in Hoechst and S42 in CX43, Supp. Fig. S4), all the samples were included in the downstream analysis due to the restricted sample size.

Notably, because of differences in the cell type compositions, library preparation method, and post-sequencing quality, CX43+ and Hoechst+ populations were analyzed separately. Taken together, our data displayed that the generated libraries from sorted nuclei populations were suitable to complete further gene expression studies.

3.3.1.2.Purity Analysis in the CX43+ Population

To test the composition of the sorted nuclei fraction, we evaluated the expression profiles of cell-type specific markers (Fig. 3.21). We found the expression levels of astrocytic markers as (mean Log2(CPM) values ± SD in arbitrary units): *SLC1A2*: 9 ± 1.3 a.u., *ATP1B2*: 6.6 ± 0.8 a.u., and *S100B*: 3.5 ± 1.7 a.u. (Fig. 3.21). However, neuronal markers were also expressed (*RAB3C*: 7 ± 0.7 a.u., *RBFOX3*: 9.3 ± 0.8 a.u.). Furthermore, we assessed the expression levels of the top 10 genes known to be primarily enriched in human cortical astrocytes, neurons, oligodendrocytes, and microglia (using the data set from McKenzie et al. (2018)[153] as reference). The data revealed that most astrocyte-specific genes were expressed in the CX43+ population together with the neuronal markers. In addition, oligodendrocytes and microglia markers were also detected but to a lesser extent than astrocyte markers (Supp. Fig. S5). These findings showed that the CX43+ nuclei fraction contained a mixed population composed of astrocytes and neurons.

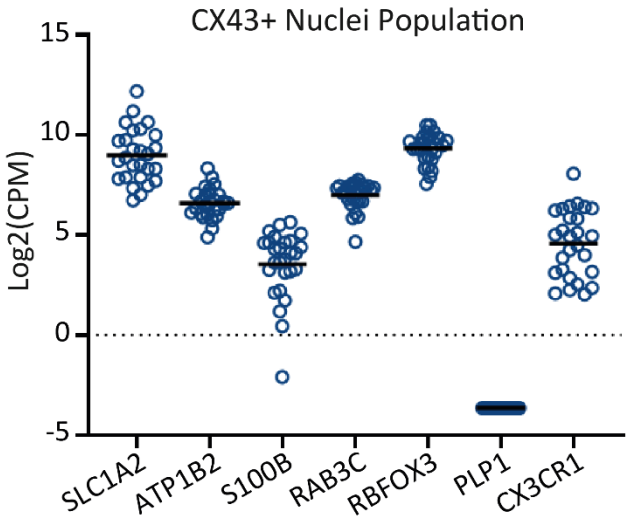

Figure 3.21. Cell-Type-Specific Gene Expression Profiles in CX43+ Population. The abundance of cell-type-specific marker expression was evaluated in the CX43+ nuclei population using transcriptomic data. The graph represents the expression levels (mean Log2(CPM) values) of 7 markers from each donor individually. CX43+ nuclei population was largely composed of astrocytes and neurons. The Log2(CPM) values were calculated by Intelliseq.
SCL1A2, *ATP1B2*, *S100B* – astrocytes, *RAB3C*, *RBFOX3* - neurons, *PLP1* - oligodendrocytes, *CX3CR1* – microglia.

3.3.1.3.Gene Expression Changes in the vmPFC of Depressed Suicides

DEGs analysis was conducted for both nuclei fractions to generate BA25-associated transcriptional profiles of healthy controls and depressed suicides. In the Hoechst+ population, a total of 105 genes were differentially expressed ($P < 0.005$, Fig. 3.22). The gene list consisted of 91 protein-coding genes and 13 long non-coding RNAs, where most of the genes were downregulated in the MDD group (a total of 96 genes). However, none of the genes passed the strict selection criteria (false discovery rate (FDR) < 0.1).

We evaluated whether the list of DEGs in the Hoechst+ population contained previously identified genes altered in depression. To this end, an extensive literature search was conducted, and among the studies, seven were found using PFC tissue samples originating from either MDD or depressed suicide patients (Supp. Table S2). While these studies used various significant criteria, for the purpose of comparison, we admitted all reported DEGs, which were 1213 genes in total. We found 19 shared genes between those studies and our findings in the Hoechst+ population, of which 11 were known to be enriched in astrocytes such as *SLC7A11*, *EDNRB*, *SLC1A2*. Taken together, although the RNA-seq data analysis in the Hoechst+ nuclei population resulted in low statistical power, we were able to detect expression changes in the genes previously associated with depression and propose new ones altered in the vmPFC.

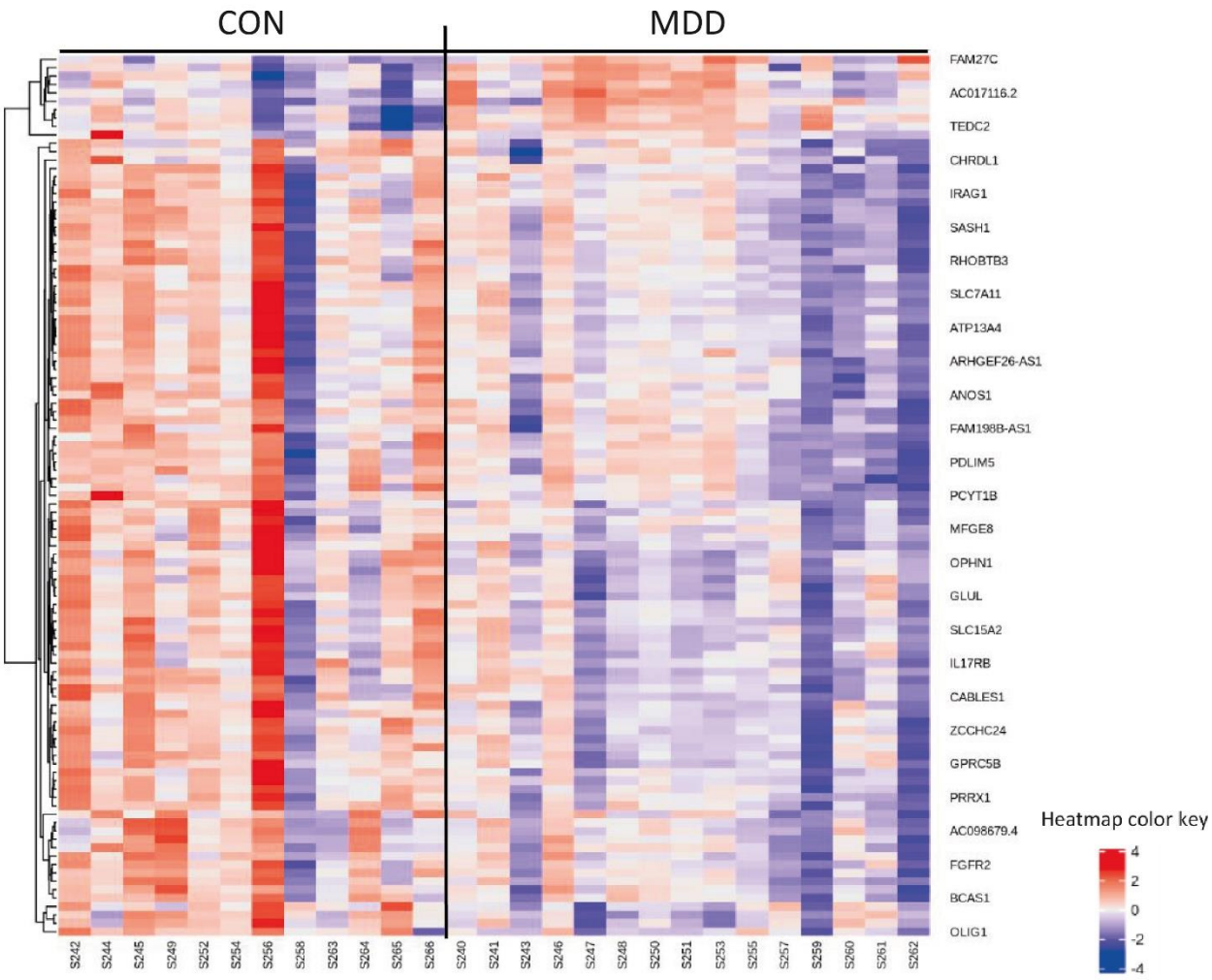

Figure 3.22. Heatmap for Differentially Expressed Genes in the Hoechst+ Population. Hierarchical clustering for DEGs per subject in each study group, CON and MDD. Representative gene names are illustrated on the right, individual sample IDs on the bottom. A total of 105 genes were differentially expressed (*P < 0.005*) but did not pass the strict FDR < 0.1 criteria. Most of the genes (91.4%) were downregulated. Heatmap color represents the Log(FC) values (red shows high expression level and blue shows low expression levels). The heatmap was

In the CX43+ nuclei population we found a total of 260 genes differentially expressed between CON and MDD, which passed the FDR < 0.1 criteria (Fig. 3.23, Full list in Supp. Table S3). While most genes were protein-coding (83.1%), a smaller fraction (14.6%) comprised long non-coding RNA. Importantly, we analyzed the expression of cell type-specific markers (reference database: McKenzie et al. (2018)[153]) and found that almost half of the genes were enriched in astrocytes (72 genes), and a smaller fraction was enriched in neurons (11 genes).

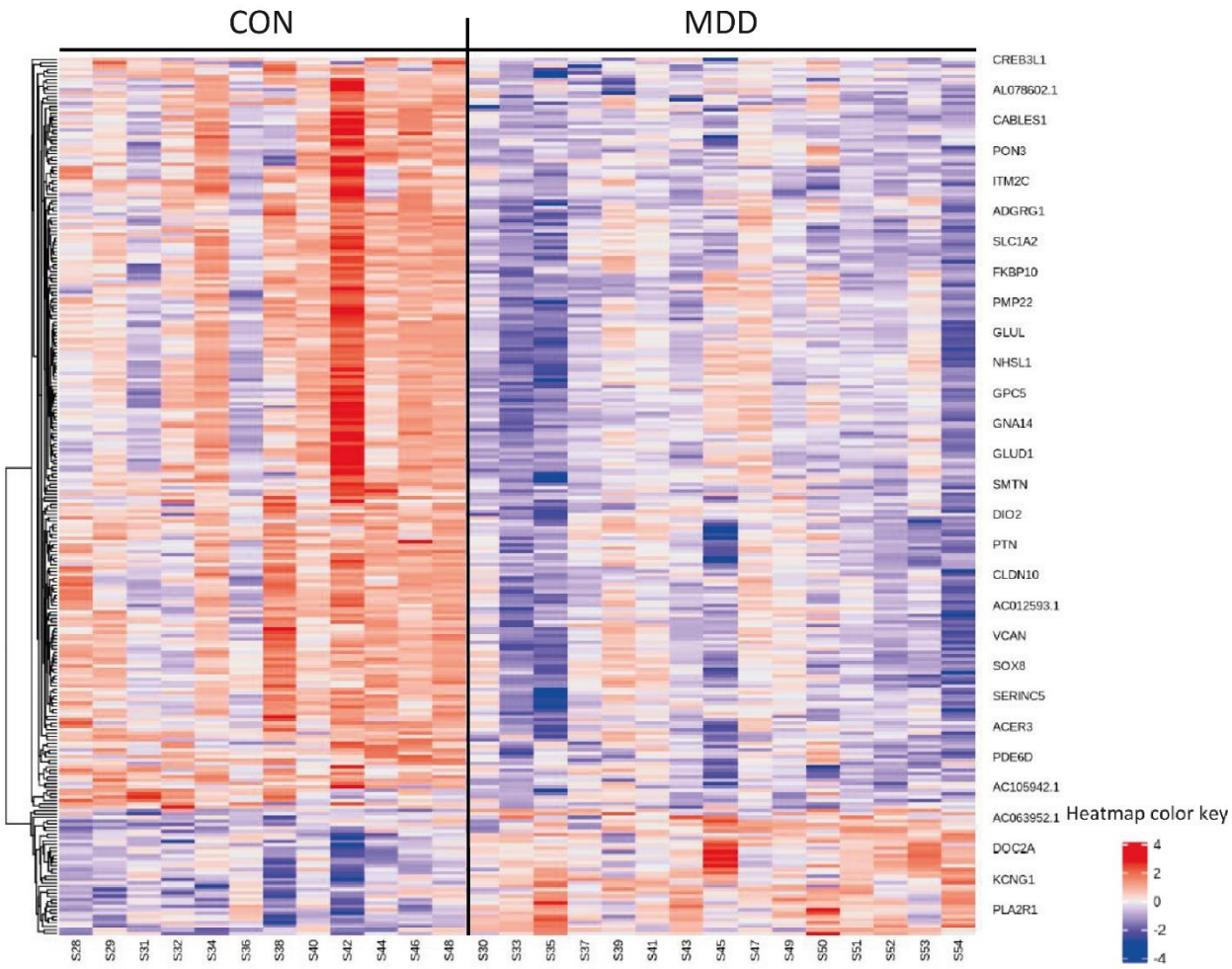

Figure 3.23. Heatmap for Differentially Expressed Genes in the CX43+ Population. Hierarchical clustering for DEGs per subject in each study group, CON and MDD, in the CX43+ population. Representative gene names are illustrated on the right, individual sample IDs on the bottom. A total of 260 genes were significantly differentially expressed (FDR < 0.1) in the CX43+ nuclei population (full list is in Supp. Table S3). Most of the genes (85.8%) were downregulated. Heatmap color represents the Log(FC) values (red shows high expression level and blue shows low expression levels). The heatmap was generated by Intelliseq.

Majority of genes (a total of 223 genes) were downregulated, which is consistent with previously published transcriptome studies of MDD[133,184]. The list of downregulated DEGs contained 188 protein-coding and 34 long-non-coding RNA. Remaining genes were upregulated, and in this group 28 encoded for proteins and 4 non-coding long RNA. These data provide the list of DEGs in the CX43+ population, revealing the molecular deficits in the BA25 of suicide completers.

We also investigated whether the list of DEGs in the CX43+ population included previously discovered astrocyte-specific genes altered in the PFC of MDD subjects (reference studies are presented in Supp. Table S2). Side-by-side comparison of our data to the literature findings (a total

of 80 genes) identified 23 shared genes, which contained crucial astrocytic genes such as *SLC1A2*, *GLUL*, *GJB6*, *SLC4A4*, and *GRIN2C* (Fig. 3.24, circled in black). All these common genes were downregulated in MDD.

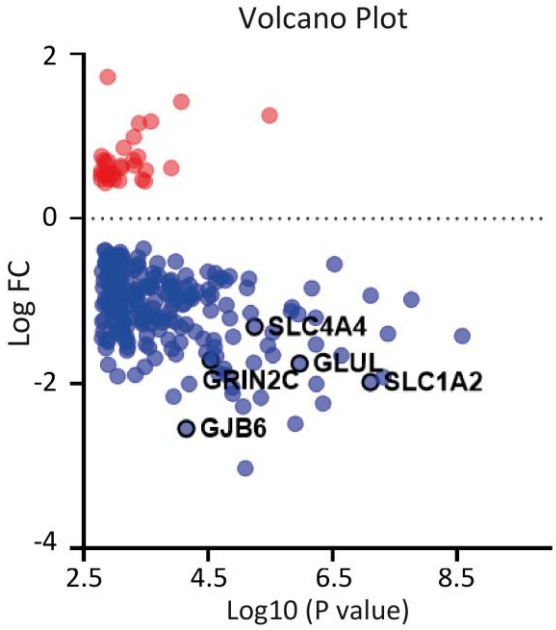

Figure 3.24. DEGs in the CX43+ Population Associated with Previous Findings in Depression. A volcano plot was created with the list of DEGs in the CX43+ population. The majority of the genes were downregulated (blue dots) in which 23 of them overlapped with previous findings (reference studies are presented in Supp. Table S2). Notably, these genes are known to be enriched in human astrocytes, e.g., *SLC1A2*, *GLUL*, *GJB6*, *SLC4A4*, and *GRIN2C* (circled in black). None of the upregulated genes in the CX43+ population (red dots) overlapped with literature data; hence they were novel findings. The Log(FC) was calculated by Intelliseq.

A further comparative analysis using PsyGeNET[215], a tool for investigating psychiatric illnesses and their linked genes, revealed that 28 of 260 DEGs in the CX43+ population were previously associated with mental disorders such as depression (a total of 10 genes), bipolar disorder, and schizophrenia (Supp. Fig. S6). The top 5 genes linked to those diseases, i.e., *MAOA*, *GLUL*, *VEGFA*, *SLC1A2*, and *FYN*, were downregulated in the CX43+ population. Interestingly, these genes are known to be enriched in human astrocytes[153]. Taken together, our results pointed out that we could recapitulate published MDD findings and identified new genes (e.g., all upregulated genes in the CX43+ population) associated with the disease.

3.3.1.4.Biological Functions Altered in the CX43+ Population of Depressed Suicides

To investigate the functional relevance of our findings, we used DAVID Bioinformatics Resources[216] and performed analyses for gene ontology (GO), pathway enrichment, and gene functional classification. Since the upregulated gene list for the CX43+ population was noticeably shorter than the one of downregulated genes, the statistical power of the upregulated genes analysis was insufficient (calculated with Fisher Exact *P*-value by DAVID). Nonetheless, detected major GO terms were the "lipid transport" (*P = 0.08*, *GULP1*), "intracellular membrane-bounded organelles" (*P = 0.02*, *KCNG1*), and "ATP binding" (*P = 0.08*, *ATAD3B*).

We identified significantly (*P < 0.05*) enriched terms for biological processes such as "dermatan sulfate biosynthesis", "glycosaminoglycan metabolism", and "glutamate catabolic process" for the downregulated gene list. The major GO terms categorized for cellular compartments involved "synaptic membrane", "plasma membrane", and "extracellular component". Likewise, "GTP binding", "heparin binding", and "extracellular matrix structural constituent" terms were the molecular functions enriched for the list of downregulated genes in the CX43+ population. Moreover, pathway enrichment analysis revealed "focal adhesion", "fatty acid metabolism", and "nitrogen metabolism" related biological systems. Next, we explored the functional groups in the downregulated gene list and detected 3 clusters, consisted of terms as "glycoprotein" (e.g., *GPM6A*, *ADORA2B*, *GRM3*), "transmembrane region" (e.g., *NKAIN3*, *SLC4A4*, *TMEM19*), and "signal" (e.g., *IL17RB*, *KREMEN1*, *PTPRZ1*). These results suggest that essential biological functions in the CX43+ nuclei population might be altered in the MDD group. Complete results from DAVID are shown in Supplementary Table S4-S8.

To further extend our findings between the downregulated genes in the CX43+ population and the associated biological systems, we conducted STRING network analysis[217]. The overall interaction among the proteins encoded by DEGs was significantly higher than for a random set of proteins of similar size ($P < 1x10^{-16}$, calculated by STRING) (Fig. 3.25). Examples for the overrepresented biological processes (a total of 103 terms) include "nervous system development" (protein count: 46/2206), "dermatan sulfate biosynthesis" (protein count: 5/12), and "regulation of signaling" (protein count: 55/3360). In addition, strongly enriched cellular compartments (a total of 21 terms) consisted of the "membrane" (protein count: 117/8420) and "extracellular region" (protein count: 39/2505) (Fig. 3.25). Interestingly, the "transport of small molecules" was the unique enriched pathway in STRING analysis, which encompassed proteins such as SLC25A18, ATP13A4, and SLCO1C1.

Notably, STRING analysis did not reveal any network for the upregulated genes since the list was relatively short, and the statistical power was insufficient to have significantly more interactions than expected by chance (*P = 0.07*, calculated by STRING).

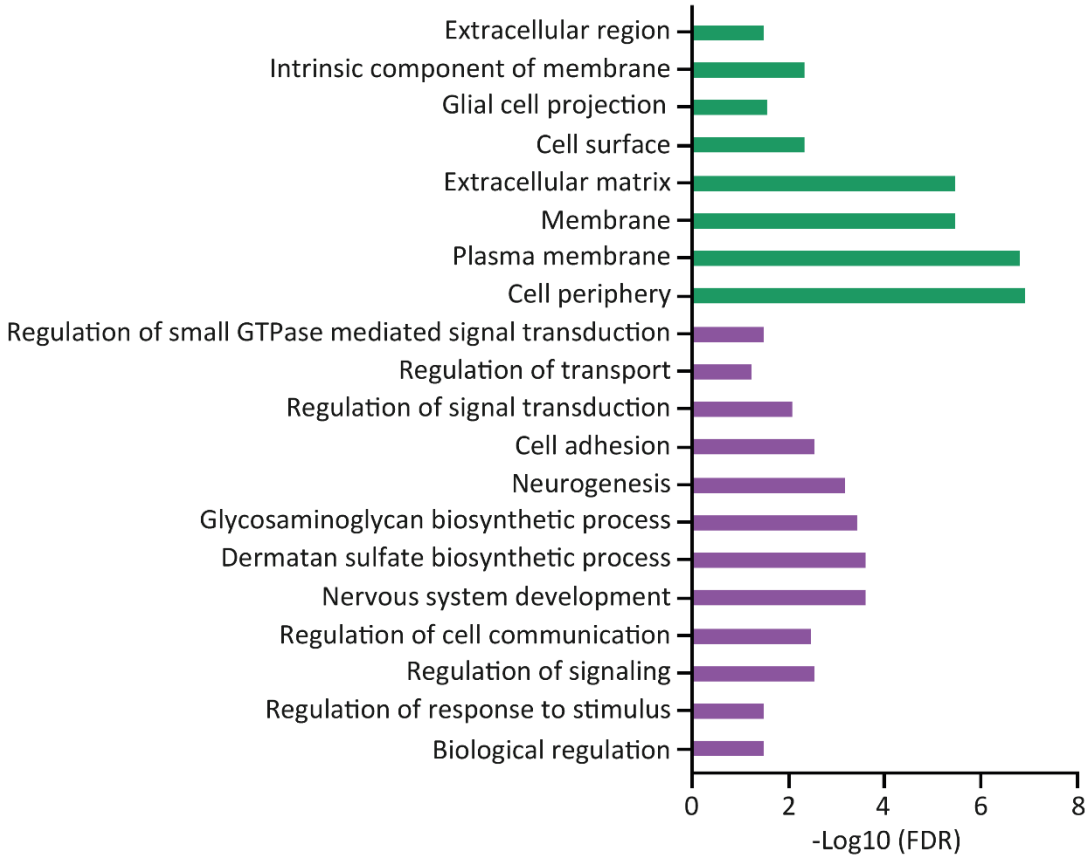

Figure 3.25. GO Ontology Terms Analysis for Downregulated Genes in the CX43+ Population. STRING network analysis was performed, and representative GO terms associated with genes altered in the CX43+ nuclei fraction are shown in the graph. The cellular compartments (green bar) and biological processes (purple bar) were plotted based on the -Log10 (FDR) values.

A clustering analysis (MCL clustering in STRING) was run based on protein interaction scores, which associated several clusters of functionally related proteins (Fig 3.26). Proteins in cluster A were linked to the "synapse and glutamate receptor signaling pathway". The functional enrichment for cluster B consisted of "metabolic process", "nervous system development", and "dermatan sulfate biosynthesis". Cluster C encompassed known astrocytic proteins where the biological systems as "positive regulation of transport", "glutamate biosynthetic process", and "neurotransmitter uptake" were over-represented. The "fatty acid metabolic process" was strongly associated with the proteins represented in cluster D (Fig 3.26). Taken together, the identified set of genes downregulated in the CX43+ nuclei fraction originating from vmPFC were encoding proteins functionally linked to essential biological systems in the brain. While most of these biological functions were previously associated with MDD[218,219], our findings provided complementary data by identifying new components in these clusters.

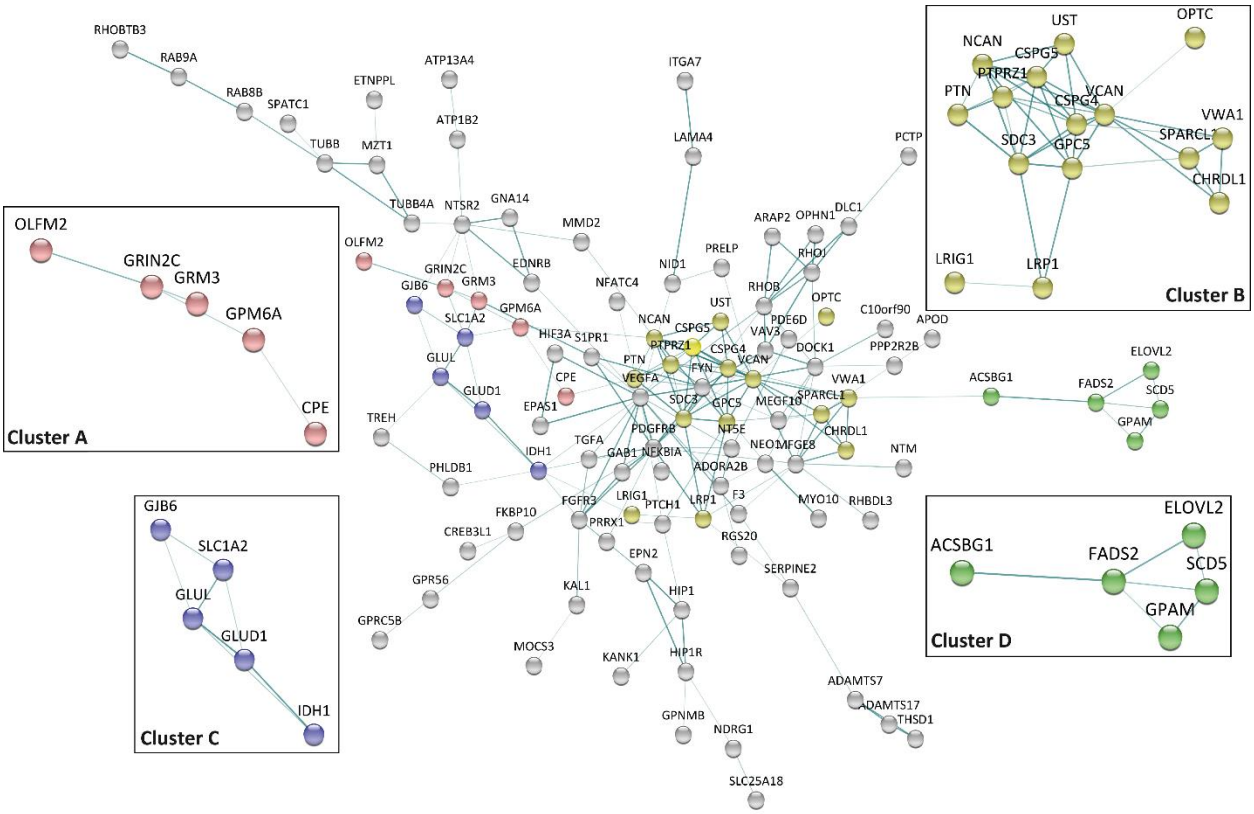

Figure 3.26. Protein Clustering Analysis for Downregulated Genes in the CX43+ Population. Four major clusters of functionally related proteins were found using STRING (MCL clustering). Cluster A was associated with "synapse and glutamate receptor signaling pathway", cluster B was linked to "metabolic process", "nervous system development", and "dermatan sulfate biosynthesis", cluster C consisted of "positive regulation of transport", "glutamate biosynthetic process", and "neurotransmitter uptake", and cluster D encompassed the "fatty acid metabolic process". The nodes indicate both functional and physical protein associations.

3.3.1.4.1. Validation of Identified Gene Expression Changes

To validate the gene expression changes identified in the CX43+ population, we performed western blot analyses for several proteins: SLC1A2, SLCO1C1, SLC4A4, SLC25A18, and GLUL. We selected those proteins since they regulate the critical biological function of astrocytes, namely glutamate homeostasis. Importantly, genes encoding those proteins were previously implicated in MDD and were known to be enriched in human astrocytes[37,153,218,220]. Note that due to the low yield of FACS-isolated CX43+ nuclei, we decided to employ homogenates of BA25 originating from CON (N = 8) and MDD (N = 8) subjects, which were used for the gene expression study. As seen in Figure 3.27A, only SLC1A2 at 140 kDa size was significantly ($\overline{x}_{(CON)}$: 1.1 ± 1.0 a.u. vs. $\overline{x}_{(MDD)}$: 0.4 ± 0.2 a.u., *P = 0.03*, n = 1 repeat in blotting experiments) downregulated in the MDD group.

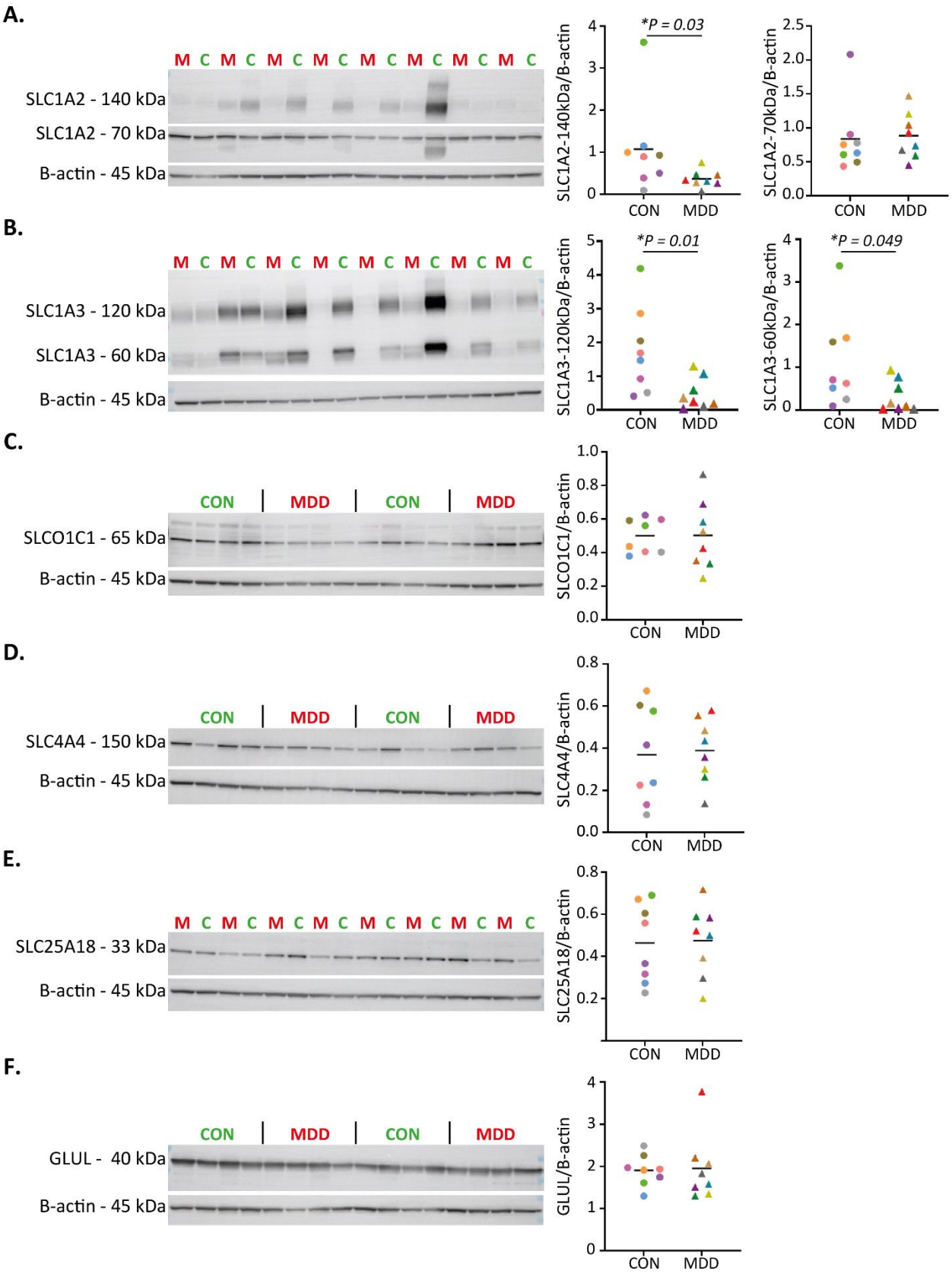
A.
M C M C M C M C M C M C M C M C
SLC1A2 - 140 kDa
SLC1A2 - 70 kDa
B-actin - 45 kDa
*P = 0.03
SLC1A2-140kDa/B-actin
SLC1A2-70kDa/B-actin
CON
MDD
B.
M C M C M C M C M C M C M C M C
SLC1A3 - 120 kDa
SLC1A3 - 60 kDa
B-actin - 45 kDa
*P = 0.01
*P = 0.049
SLC1A3-120kDa/B-actin
SLC1A3-60kDa/B-actin
C.
CON MDD CON MDD
SLCO1C1 - 65 kDa
B-actin - 45 kDa
SLCO1C1/B-actin
D.
CON MDD CON MDD
SLC4A4 - 150 kDa
B-actin - 45 kDa
SLC4A4/B-actin
E.
M C M C M C M C M C M C M C M C
SLC25A18 - 33 kDa
B-actin - 45 kDa
SLC25A18/B-actin
F.
CON MDD CON MDD
GLUL - 40 kDa
B-actin - 45 kDa
GLUL/B-actin

Figure 3.27. Validation of DEGs by Western Blot. Western blot experiments were conducted using tissue homogenates from CON (N = 8, C, dots) and MDD (N = 8, M, triangles) groups. Samples were selected from the same cohort used for the transcriptional study. Western blots and graphs illustrate the quantification of the relative protein levels. **A.** SLC1A2 protein levels at 140 kDa were significantly (*P = 0.03*) decreased in MDD subjects. B. SLC1A3 protein levels at 120 kDa (*P = 0.01*) and at 60 kDa (*P = 0.049*) were significantly reduced in MDD subjects. No statistical differences were observed for the isoform of SLC1A2 at 70 kDa size. We did not detect statistically significant changes for the SLCO1C1 (**C**), SLC4A4 (**D**), SLC25A18 (**E**), and GLUL (**F**).
20 µg of protein was loaded for each sample. Bands were imaged with Vilber FUSION FX. Protein quantification was done using ImageJ software and calculated as a ratio of the relative density of selected bands to the housekeeping protein, β-ACTIN. The t-test or Mann-Whitney test was performed when the data was not normally distributed based on the Shapiro-Wilk test.

Moreover, we measured the protein levels of SLC1A3, another astrocyte-specific protein involved in the glutamate homeostasis. Although *SLC1A3* expression was not changed in the CX43+ population, the gene encoding this protein was downregulated in the Hoechst+ nuclei population isolated from MDD samples. The protein analysis showed that SLC1A3 at 120 kDa ($\overline{x}_{(CON)}$: 2.8 ± 1.6 a.u. vs. $\overline{x}_{(MDD)}$: 1.0 ± 0.6 a.u., *P = 0.01*) and 60 kDa ($\overline{x}_{(CON)}$: 1.1 ± 1.0 a.u. vs. $\overline{x}_{(MDD)}$: 0.3 ± 0.3 a.u., *P = 0.049*) were significantly reduced in suicide completers (n = 1 repeat in blotting experiments, Fig. 3.27B).

On the contrary, the other proteins were not significantly changed (Fig. 3.27C-F) in the CX43+ population. The discrepancy between the gene and protein levels could be because gene expression analysis was conducted in the CX43 labelled nuclei population, whereas the protein expression was evaluated using brain homogenate. Hence, the changes in a specific cellular compartment could be masked when the mixed cell population was analyzed. Furthermore, we observed high variability in protein expression within the study groups, which might diminish the statistical power.

In summary, the nuclei isolation protocol was applied to investigate astrocyte-specific gene expression changes in depression. First, we validated the compatibility of our established protocol for RNA-sequencing analysis. Isolated CX43+ nuclei fraction largely consisted of astrocytes and neurons. Next, we detected sets of DEGs in both nuclei populations, i.e., Hoechst and CX43, which were mostly downregulated in depressed suicides. Importantly, the list of downregulated genes in the CX43+ population contained previously discovered astrocytic genes associated with MDD. Together with the upregulated gene list in the CX43+ population, we also identified new genes altered in MDD. Finally, functional implications of DEGs were evaluated, and we found connectivity between essential biological systems and proteins expressed primarily in astrocytes, e.g., extracellular matrix, neurotransmitter uptake, and glutamate homeostasis. Consequently, we

explored transcriptional changes specific to the vmPFC and identified altered molecular pathways in a subgroup of depressed suicides.

3.3.2. Astrocyte-Specific Molecular Changes Elicited by Chronic Stress in Mice

The protocol for astrocyte isolation from the adult mouse brain samples (as described in section 3.2.4) was used to uncover astrocyte-specific molecular changes and pathways elicited by CSDS. Hence, the CSDS paradigm was applied to mice, and assays were conducted to evaluate the impact of CSDS on depressive-like behavior (by Carmen Menacho Pando). As a proof of concept, here I solely present the applicability of the optimized strategy of magnetic cell sorting, which was employed to isolate astrocytes from control (CONT, N = 7) and stressed (CSDS, N = 8) animals. The first goal of the experiment was to explore the regional heterogeneity of the CSDS-induced transcriptional profile of astrocytes. Therefore, cells were isolated from 4 brain regions: hippocampus, hypothalamus, PFC, and somatosensory cortex (SC). The second goal was to highlight those transcriptional deviations regulated by glucocorticoid signaling. Since glucocorticoids physiologically regulate circadian metabolism, brain samples were obtained from identically treated mice at different times of the circadian cycle: Zeitgeber time (ZT) 1 (08:00) and ZT11 (18:00), where ZT0 depicts the beginning of the active phase (lights off).

3.3.2.1.Validity of the Technical Parameters of MACS-Isolated Astrocytes

We evaluated the technical properties of the MACS-isolated astrocytes from CONT and CSDS animals. As shown in Figure 3.28, no statistically significant differences were observed in isolated cell number, RNA quantity, and quality between CONT to CSDS group (statistics are presented in Supp. Table S9). As expected, the number of astrocytes sorted from the hippocampus ($\overline{x}_{(hippocampus)}$: 15.9 x 10^3 ± 6.4) and SC ($\overline{x}_{(SC)}$: 13.9 x 10^3 ± 9.6) were higher than the hypothalamus ($\overline{x}_{(hypothalamus)}$: 3.8 x 10^3 ± 1.3) and PFC ($\overline{x}_{(PFC)}$: 3.7 x 10^3 ± 1.4) (for all the comparisons: $P < 0.0001$).

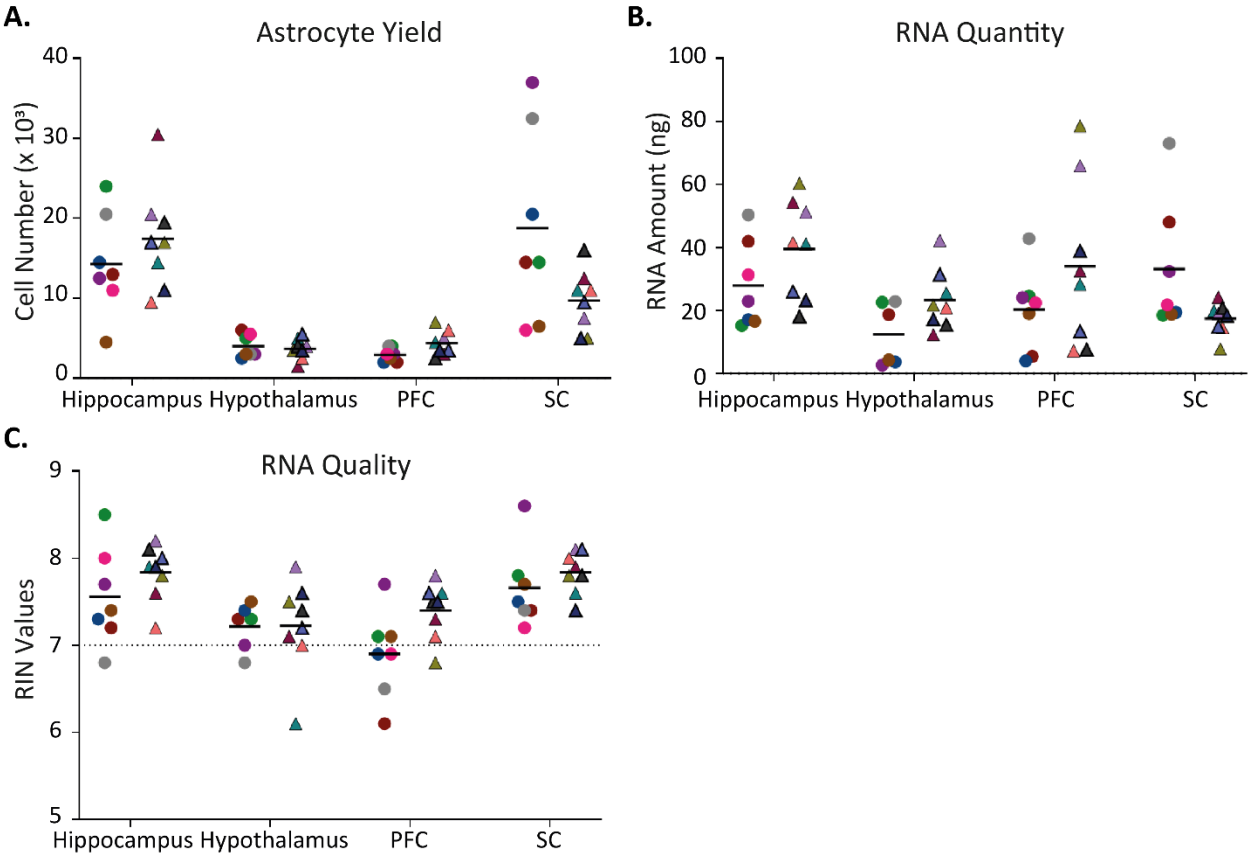

Figure 3.28. Astrocyte Yield, RNA Quantity, and Quality Assessment. RNA was extracted from astrocytes isolated from the hippocampus, hypothalamus, PFC, and somatosensory cortex (SC). Comparison of astrocyte yield (**A**), RNA quantity (**B**), and quality (RIN values) (**C**) between CONT (dots) and CSDS (triangles) group. Dashed line indicated RIN = 7, generally acceptable threshold for the RNA quality. No statistically significant differences were found between the study groups (Supp. Table S9). Data from each sample is represented individually. PFC: Prefrontal cortex, SC: Somatosensory cortex.

RNA was extracted using RNeasy Plus Micro Kit. Quantity and quality of RNA were measured with Bioanalyzer using RNA 6000 Pico Kit. Cell isolation experiments were conducted with Carmen Menacho Pando. Either t-test or Mann-Whitney test was performed when the data was not normally distributes based on the Shapiro-Wilk test. RIN: RNA integrity number.

Next, we evaluated the quality of the libraries. Fragment sizes were detected at an expected range (> 200 bp) for all the samples (Fig. 3.29). The quality check of RNA-seq revealed adequate sequencing performance; as such, the read alignment indicated low intronic (7%) and intergenic reads (16%), and high exonic reads (76%) (data not shown). Taken together, these findings showed that genetic material extracted from isolated astrocytes was suitable to pursue RNA sequencing and further gene expression analysis between the two study groups, CONT and CSDS.

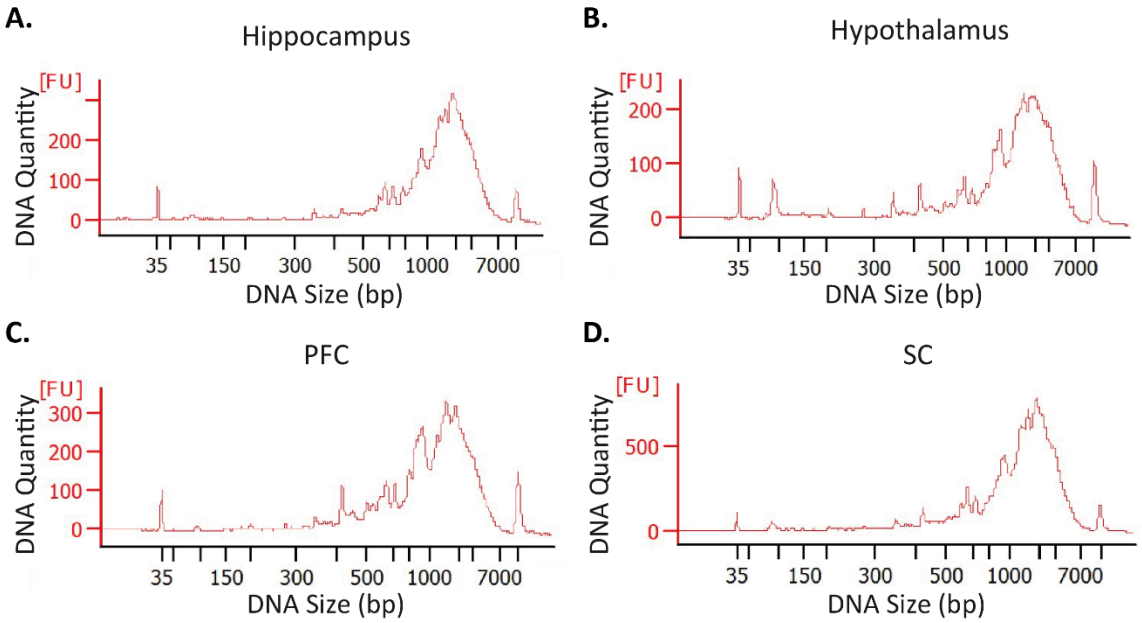

Figure 3.29. Quality Check of Generated Libraries. Libraries were generated from RNA extracted from 4 brain regions of adult mouse brain, and the quality was assessed with Bioanalyzer using High Sensitivity DNA Kit**. A - D.** Representative electropherograms of amplified DNA in astrocytes sorted from the hippocampus (**A**), hypothalamus (**B**), PFC (**C**), and SC (**D**). The fragment sizes were observed at an expected range, > 200 bp. Smart-seq2 protocol was used to generate the libraries in collaboration with EMBL Genomics Facility and Carmen Menacho Pando. FU: Fluorescence unit. bp: base pair. PFC: Prefrontal cortex, SC: Somatosensory cortex.

3.3.2.2.Purity Analysis in Isolated Astrocytes

To determine the gene expression profile of ACSA-2 labelled astrocytes in different mouse brain regions, our datasets were first compared with the previously published work of Zeisel et al. (2015)[221]. In this study, the authors conducted single-cell RNA-seq to identify subclasses of known major cell types in the mouse somatosensory cortex and hippocampal regions[221]. Hence, the gene abundances (FPKM values) for each sample were correlated with gene expression of each cell type (based on Zeisel et al. (2015)[221]) as shown in the heatmap (Fig. 3.30). As a result, we found that isolated ACSA-2+ cells were strongly correlated ($r > 0.7$) with mouse astrocytes and, to a less extend ($r < 0.5$) with ependymal cells (Fig. 3.30). Besides, the evaluation of the percentage of variance explained by any cell type revealed that the transcriptome variance in ACSA-2+ cells was strongly associated (>80%) with the gene expression profiles of mouse astrocytes (Supp. Fig. S7).

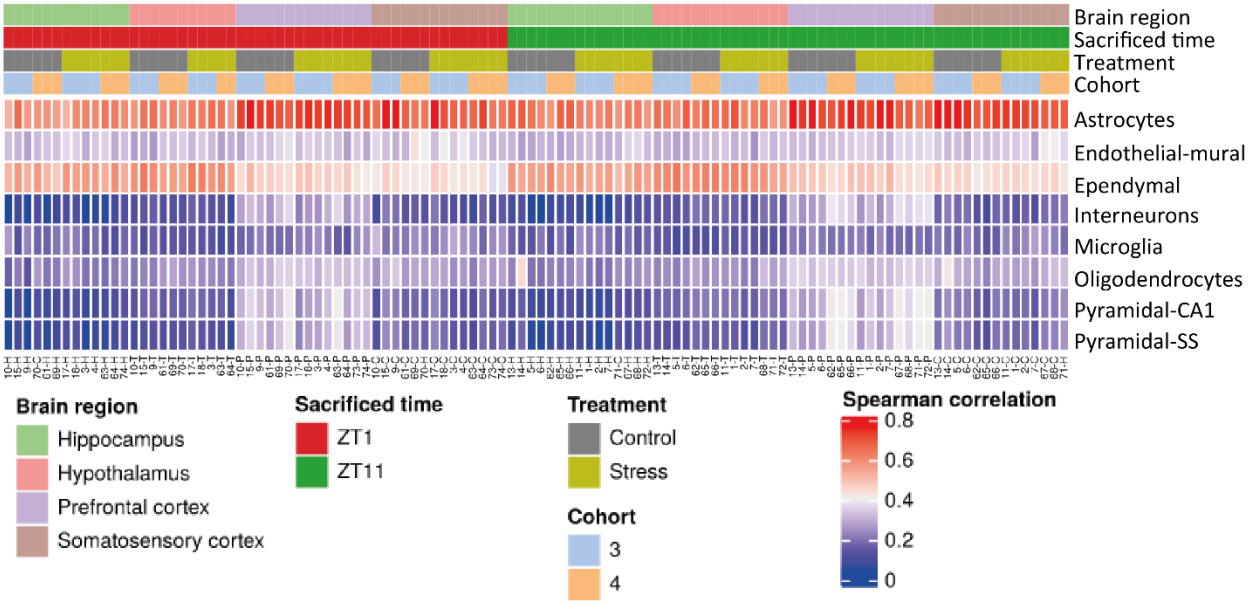

Figure 3.30. Purity Analysis for MACS Isolated Astrocytes. The heatmap shows the Spearman correlation of the FPKM values for each sample (columns) with gene expression for each cell type (rows). The top 100 genes from each cell type were used based on reference database[221]. MACS isolated ACSA-2+ cells showed a strong correlation (> 0.7) with mouse astrocytes. The data in the heatmap consisted of cell isolation experiments conducted for two independent cohorts of mice (N = 29). The heatmap was generated by Intelliseq. FPKM: Fragments Per Kilobase of transcript per Million mapped reads, ZT: Zeitgeber time.

Additionally, we assessed the expression profiles of cell-type-specific markers used in the qPCR analysis (Fig. 3.14). We found enrichment of astrocyte marker (*Aldh1l1*) in isolated cells (Fig. 3.31A). Notably, *Atp1b2* (encoding the epitope targeted by ACSA-2) was highly enriched compared to other cell-type markers (Fig. 3.31A). As expected, the expression levels of the markers were distinct in each brain region.

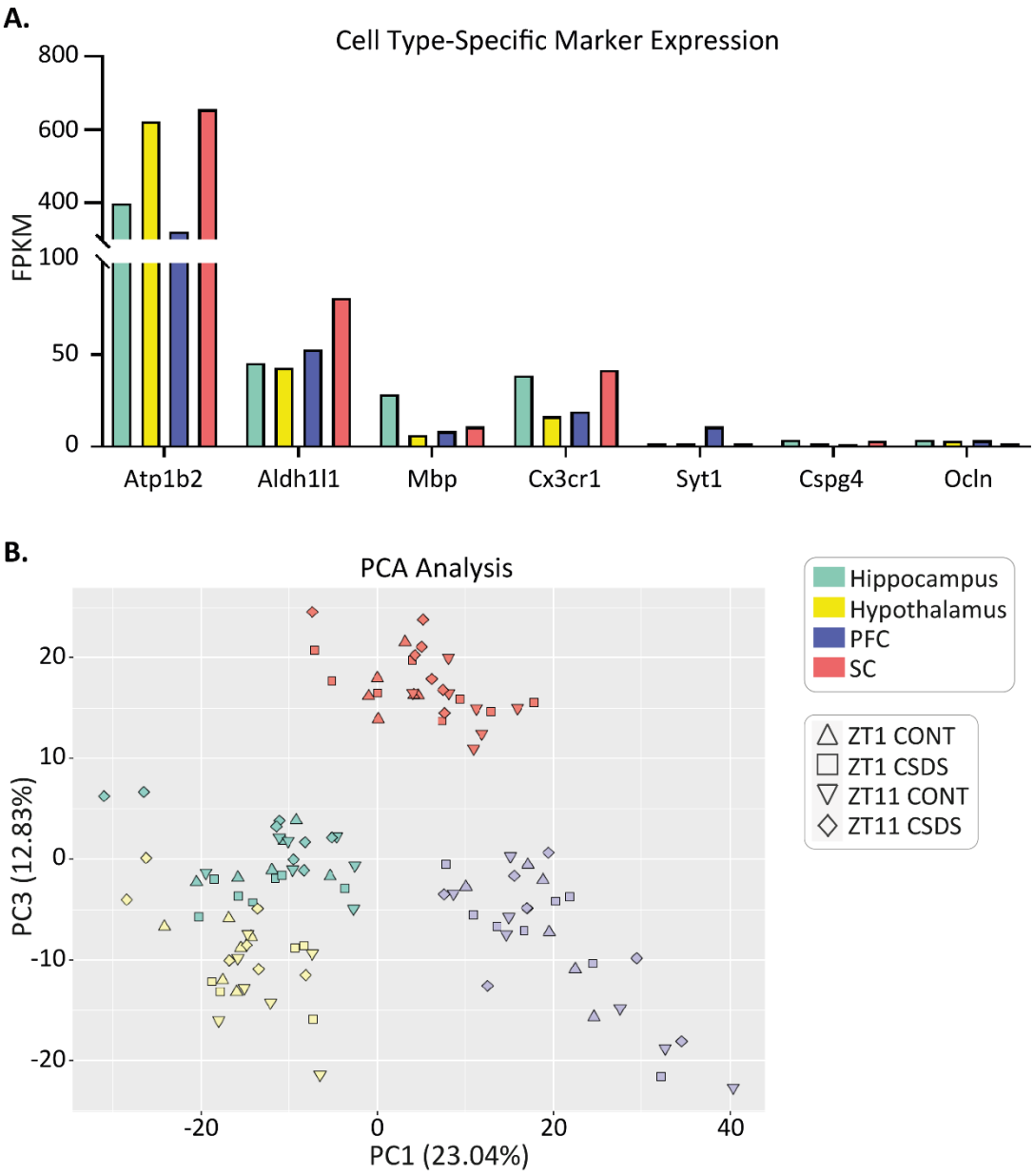

Figure 3.31. Brain Region-Specific Gene Expression Profiles of Astrocytes. A. The graph represents the mean FPKM values of 7 markers in ACSA-2+ cells sorted from the hippocampus (green), hypothalamus (yellow), PFC (purple), and SC (red). Astrocyte-specific markers (*Atp1b2* and *Aldh1l1*) were enriched in all the brain regions. **B.** PCA revealed the associations of samples respective to each brain region. The proportion of variance explained is indicated in parentheses. Each dot indicates one sample. The data in the PCA consisted of cell isolation experiments conducted for two independent cohorts of mice (N = 29). FPKM values and the PCA were generated by Intelliseq.

Atp1b2, *Aldh1l1* - astrocytes, *Mbp* - oligodendrocytes, *Cx3cr1* - microglia, *Syt1* - neurons, *Cspg4* - NG2 cells, *Ocln* - endothelial cells.

The PCA analysis of all samples revealed that astrocytes isolated from each brain region clustered, and the transcriptome of subcortical (i.e., hippocampus and hypothalamus) astrocytes grouped together (Fig. 3.31B). Hence, these data were in line with previous studies demonstrating brain region-specific subtypes of astrocytes in mice[155,222]. Importantly, we did not observe any variation in astrocytes sorted from CONT and CSDS animals (Fig. 3.31B). Consequently, the RNA-seq data showed that isolated ACSA-2+ cells represent an enriched astrocyte population and displayed diversity across brain regions.

3.3.2.3.Gene Expression Changes in Astrocytes of CSDS Mice

The optimized protocol was routinely employed to explore astrocyte-specific molecular deficits upon chronic stress exposure. To confirm the protocols' applicability, we presented astrocyte-specific differential transcript expression analysis between control and stress animals (Supp. Fig. S8).

In this project, we primarily focused on the PFC circuits; therefore, here, we illustrated alterations in astrocytes-specific transcripts when cells were isolated from the PFC (Fig. 3.32). The ANOVA test with Sacrifice Time x Treatment interaction was used to detect statistically significant difference in gene expression between 4 groups of mice: CONT sacrificed at 8am, CONT sacrificed at 6pm, CSDS sacrificed at 8am and CSDS sacrificed at 6pm. A total of 66 transcripts were found to pass the criteria of differential expression ($P < 0.001$, Fig. 3.32).

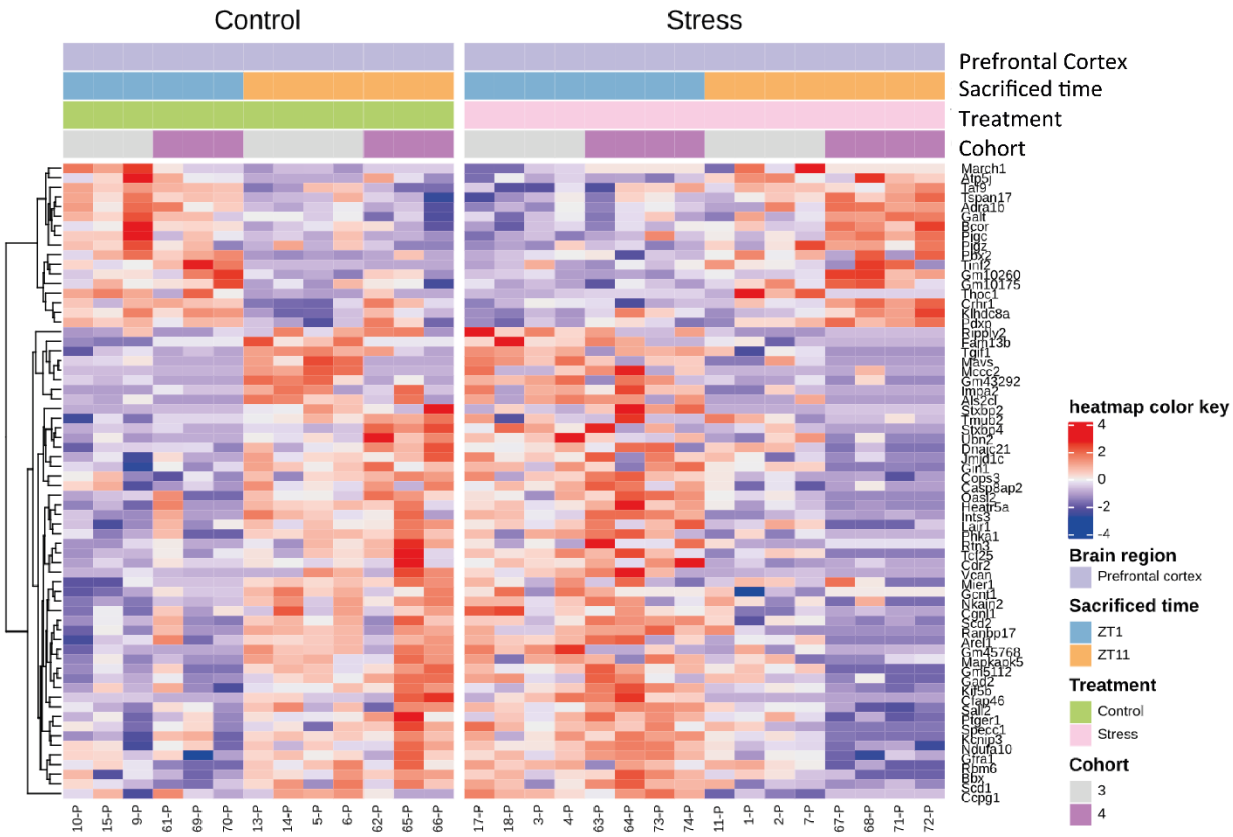

Figure 3.32. Heatmap for Differentially Expressed Transcripts in Astrocytes Isolated from the PFC. Hierarchical clustering for differentially expressed transcripts per sample in each study group, CONT (green) and CSDS (pink). A total of 66 transcripts were significantly differentially expressed (*P < 0.001*, ANOVA with interaction) in the PFC upon stress exposure and the names are illustrated on the right, individual sample IDs on the bottom. The data consisted of cell isolation experiments conducted for two independent cohorts of mice (N = 29). Heatmap color represents the normalized FPKM values (red shows high expression level and blue shows low expression levels). The heatmap was generated by Intelliseq.

In summary, the MACS isolation protocol was successfully applied to study astrocyte-specific molecular alterations elicited by chronic stress in mice. First, the purity of ACSA-2+ cells was confirmed by RNA-seq data, representing an enriched astrocytes population. Next, in line with the literature, a brain region-specific gene expression profile was observed. Finally, differentially expressed transcripts were detected in astrocytes isolated from control and stressed mice (detailed analysis was skipped since it was not the purpose of this project). Consequently, we offered an optimized method for astrocytes isolation allowing cell-type-specific transcriptomic studies in low volume tissue samples, i.e., PFC and hypothalamus, dissected from adult mouse brain.

4. DISCUSSION

In this project, we conducted a systematic approach by establishing methods for investigating gene expression of astrocytes in humans and rodents. This effort was driven by a hypothesis stating that astrocytes' dysfunctions underlie neurobiological features of depression and that it would be possible to identify disease relevant cell-type-specific transcriptional alterations. There were no available methods for positive selection of human astrocytic nuclei at the beginning of this project, and the published strategies for isolating astrocytes from adult mouse brains had to be modified for small tissue volume. Eventually, we successfully used these optimized techniques for gene expression studies of astrocytes in human depression and rodent model of chronic stress to identify differentially regulated astrocytic genes.

4.1. Establishing Astrocytic Nuclei Isolation Method for Human Brain Samples

We developed a nuclei isolation method suitable for investigating the transcriptomic profile of astrocytes from human samples. When our project started, positive nuclei selection strategies were available only for two brain cell types: neurons and oligodendrocytes[181]. Thus, this project provided the first positive selection approach for isolating astrocytic nuclei from frozen postmortem human brain samples.

The major strengths of our protocol are as follows: i. the isolation of nuclei could be employed to investigate archived fresh frozen brain samples, ideally from resources where the medical history of patients is well documented, ii. the combination of CX43-positive nuclei selection with sized-based nuclei collection step provided a unique approach for obtaining a population enriched in astrocytic nuclei, iii. conducting the entire procedure on ice or at 4˚C and including RNAse inhibitors in every buffer allowed maintaining the tissue and RNA as intact as possible, and iv. the collection of bulk astrocytic nuclei offered a gene expression study in a cell type with low RNA abundance.

In previous efforts, the negative selection was a strategy to study astrocytes, defined as non-neuronal nuclei (i.e., NEUN-) population in FACS using frozen human postmortem brain samples[37]. Astrocytes were considered the primary glial cells presented in the NEUN- nuclei population[37]. However, depleting neurons from glial cells did not lead to isolating pure astrocyte populations. In fact, we isolated neuronal nuclei using an antibody targeting NEUN to recapitulate

the reference protocol of Krishnaswami et al. (2016)[186]. Upon successful isolation of neurons, we assessed the purity of both sorted populations, NEUN+ and NEUN-. qPCR analysis suggested the enrichment of neuronal markers in the NEUN+ nuclei fractions compared to other cell type-specific markers. Interestingly, we observed a mixed composition of the NEUN- fraction, with the enrichment of oligodendrocytes marker, *PLP1* (data not shown). This analysis showed that depletion of neurons led to a population with the majority of cells being oligodendrocytes, while astrocytes constituted a minor fraction. Hence, to investigate specifically astrocytic transcriptome at an appropriate resolution, it was essential to enrich the nuclei population with astrocytes.

At the time we started our work, the protocol of Krishnaswami et al. (2016)[186] was the leading approach for isolating single neuronal nuclei through positive selection from frozen human brain samples and extracting genetic materials suitable for RNA-seq analysis. The core steps of our method, i.e., fresh frozen tissue homogenization and technical features of FACS, were established according to the reference protocol[186]. Special care was taken throughout the isolation method to keep the nuclei intact and compatible with RNA-seq as possible through: i. adjusting the number of Dounce homogenizer strokes – to avoid the damage of free nuclei in the suspension, ii. using Triton X-100 as a nonionic-mild detergent – to keep nuclear envelop and proteins intact, iii. establishing FACS parameters – to select intact nuclei without clog formation, and iv. implementing density gradient centrifugation – to remove the debris aggregates[186]. The cumulative outcome of employing these technical details was the protocol, which largely replicated published astrocyte-specific gene expression changes in human MDD obtained with tissue homogenates, but additionally uncovered a number of pathways altered in BA25, which may represent the novel hallmark of depression.

4.1.1. Challenge I. Identification of Astrocyte-Specific Nuclear Epitopes

One of the most challenging parts of the project was to identify nuclear proteins specific to astrocytes. We initially focused on the transcription factors since they are localized in the nucleus. Similarly, Lutz et al. (2017) isolated nuclei of oligodendrocytes from frozen human brain samples, using an antibody to label the transcription factor SOX10[181]. Our literature research identified SOX9 as the strongest candidate. SOX9 has essential roles in CNS development (e.g., glial fate specification, including astrocytes) and in the adult brain (e.g., a regulator of synaptic plasticity and astrocytes' gap junction protein expression, i.e., CX30)[74,200]. Furthermore, genomic data representing brain cell type-specific expression patterns in adult mice and humans showed that SOX9 was enriched in astrocytes compared to other brain cell types[153].

Indeed, Sun et al. (2017), employed Sox9 as a nuclear epitope to isolate astrocytic nuclei from fresh mouse cortical samples[200]. However, our attempt to isolate mouse cortical astrocyte nuclei

employing the same antibody against the Sox9 epitope failed (data not shown), which may suggest batch-to-batch variance.

We found a working anti-SOX9 polyclonal antibody coupled to AF488, which resulted in high nuclei yield and it was crucial in many improvements applied in the final protocol. At the same time, the use of a polyclonal anti-Sox9 antibody turned out a critical drawback of our protocol. Although polyclonal antibodies can recognize multiple epitopes and have a high affinity against the antigen, batch-to-batch variability is a disadvantage. In contrast, monoclonal antibodies maintain the affinity and specificity across distinct lots[223]. The breakdown of a supply of the anti-SOX9-AF488 antibody led us to turning to a new epitope for labeling astrocytes; the gap junction protein, CX43.

CX43 is highly enriched in human astrocytes[153] and is implemented in various molecular functions as regulating excitatory synaptic transmission[224], potassium buffering[225], and ATP signaling[224]. Furthermore, CX43 can be localized in multiple compartments, such as the plasma membrane, nucleus, ER, and mitochondria[203,226]. We attempted to confirm these diverse locations through immunohistochemical (IHC) staining of frozen human postmortem brain sections, but we failed to acquire comprehensive imaging data (data not shown). High-quality of IHC against a protein with punctate profile in human samples would require tedious optimization, which was not possible due to time restrictions of the project.

Nevertheless, in a test experiment astrocytic nuclei could be isolated by a direct labeling approach employing an anti-CX43 antibody. Due to significant delay in the time-fixed project and the limited amount of the material, we relied on this experiment and processed experimental samples with the anti-Cx43 antibody. Evidently, multiple replications would be beneficial to further improve the purity and yield of the sorted fraction of nuclei.

Notably, during the FACS experiments, we did not observe any background signal in the negative control samples, e.g., isotype control. In addition, the anti-CX43 antibody was selected based on the reference publications provided by the supplier (ThermoFisher), which illustrated its use in the human brain (western blot), rat brain (co-localization with CX30, IHC), and confirming its specificity with knockout experiments in the human cell line (western blot). It was specified that the selected antibody could recognize the unphosphorylated and some phosphorylated forms of CX43 (ThermoFisher). Nevertheless, different anti-CX43 antibodies could also be tested. Likewise, the antibody dilution could be optimized to find the best specificity for immunolabeling with low background. Such pilot experiments were initially performed for the SOX9 antibodies; however, they were omitted for the anti-CX43 antibody due to time and material limitations.

Alternative astrocyte-specific epitopes could be evaluated for the isolation of astrocytes from humans. For example, Xu et al. (2018) used a combination of NEUN and the glutamate transporter, EAAT1, to sort mouse astrocytic nuclei (NEUN-/EAAT1+ nuclei) from the cerebellum[178]. Although EAAT1 was known to be expressed in the plasma membrane of astrocytes[140], the authors showed that EAAT1 was also localized in the ER/nuclear membrane[178]. Likewise, we assessed the EAAT1 as an option, and FACS isolated EAAT1+ nuclei fraction from frozen human postmortem brain samples (data not shown). However, the positive events did not clearly separate in the flow cytometry compared to the isotype control, contrary to CX43 labeling. Furthermore, we conducted a double labelling approach using antibodies against the CX43 and EAAT1. Even though we observed a better separation in FACS analysis, the qPCR data indicated poor purity (enrichment of neuronal and oligodendrocyte markers) for the CX43+/EAAT1+ nuclei population (data not shown). Still, alternative anti-EAAT1 antibody and staining conditions could be assessed as a possible epitope for isolating human astrocytic nuclei.

4.1.2. Challenge II. Developing a Method Compatible for RNA Sequencing Studies

Another crucial aspect of this project was the compatibility of the method with RNA sequencing. We initially replicated the reference protocol[186], where the selected nuclei population was sorted into lysis buffer, followed by direct cDNA amplification (omitting RNA extraction step). However, the sequencing quality check revealed a low genome mapping and read alignment, and high variability across the test samples. The low number of reads mapped to the genome was also reported in the reference protocol for the non-neuronal nuclei[186]. Notably, the goal of Krishnaswami et al. (2016)[186] was to conduct a single neuronal nucleus RNA-seq, where their choice was justified, as the method was suitable for detecting an acceptable number of sequenced reads from a single nucleus. Even though we sorted a low number of nuclei (between 380 to 1700 nuclei), the selected method for genetic material extraction was unsuitable for our purpose (i.e., to study bulk nuclei). One possible explanation for the lower quality of our RNA-seq data could be the inadequate lysis of bulk nuclei and inefficient cDNA synthesis, leading to the observed variability. The latter result was a critical limitation since the primary reason for developing our protocol was to employ it for a comparative transcriptional study, in which high variability would largely preclude the identification of small transcriptional changes resulting from the disease. Another reason for the low quality could be RNA degradation, manifesting through low coverage for coding genes[186].

These circumstances led us to adopt a mild fixation step before tissue homogenization. This procedure led to diminished quality of the RNA. Therefore, alternative conditions for fixation could be further tested to extract RNA of better quality, such as other fixatives (e.g., ethanol),

diverse PFA concentrations (e.g., lower than 1%), different incubation periods, and other RNA isolation methods. However, recent studies employing fixation steps for cell-type-specific nuclei isolation protocols consistently reported low RNA quality, which did not hamper the RNA-seq data analysis[178,197]. Furthermore, it is known that fixation might impair the protein conformation and the antigenicity[227]. Therefore, alternative conditions for fixation could also be evaluated for this aspect. One of the latest studies employed ethanol as a fixative solution and isolated astrocytic nuclei by targeting a cytoskeleton protein, GFAP[228]. Note that organic solvents (e.g., methanol, ethanol) might also lead to the extraction of nuclear proteins[229].

Collectively, applying post-fixation of frozen tissue, along with performing debris removal and extracting RNA, increased the percentage of mapped reads, the coverage for coding genes, and lowered the variability between samples. These parameters are essential for comprehensive downstream bioinformatics studies[230].

In line with previous nuclear RNA-seq studies[178,214], we noticed higher intronic reads than exonic reads, possibly representing the nascent and pre-mature RNA transcripts. A recent study characterized the nuclear and cytoplasmic RNA transcripts in the dlPFC of human brain samples and pointed out that nuclear-enriched transcripts were longer (presumably due to the time required for transcription) and displayed a high number of intronic reads and noncoding genes[231]. Furthermore, the authors revealed similar levels of nuclear- and cytoplasmic-enriched transcripts in each brain cell type, including astrocytes (using post RNA-seq bioinformatics analysis)[231]. There are no direct comparison studies for the nuclear and cytoplasmic transcriptome of sorted astrocytes. Nevertheless, several studies revealed the high similarity between nuclear and whole-cell transcriptome in other brain cell types (e.g., neurons[154,232], microglia[233]). It was also reported that transcripts expressed in the nuclear compartment were valid to study gene expression changes in psychiatric illnesses such as schizophrenia, bipolar disorder, and autism spectrum disorder[231]. These data suggest that nuclear RNA-seq is suitable for investigating mental disorders in a cell type-specific manner.

4.1.3. Current Developments for Astrocytic Nuclei Isolation from Human Samples

Our protocol is timely since the interest in transcriptomic studies with the cell-type resolution has been expanding, particularly to investigate disease states and defining the primary cell type(s) involved in the pathology. In this context, alternative nuclei isolation protocols have been developed in the course of our project for specific cell types in the brain, including astrocytes[228,234,235]. One approach described by Srinivasan et al. (2020) was used to profile the gene expression pattern in four different brain cell types from Alzheimer's disease vs. healthy individuals' postmortem samples (originating from the frontal cortex)[228]. First, frozen samples

(100-200 mg) were dissociated (in Accutase, by pipetting), nuclei were fixed (in ethanol, on ice), and immune-labelled before FACS (anti-GFAP, for 20 min.). Next, GFAP-positive nuclei (average yield of nuclei: 40,000) were collected in lysis buffer, and RNA was extracted (with a kit suitable for unfixed materials). Similar to our result, the authors reported low RNA quality and related it to the dissociation conditions and the fixation step. Importantly, the GFAP-positive nuclei population was shown to express known astrocyte-specific markers. The fact of labeling astrocytes using GFAP was somewhat surprising since GFAP is a known cytoskeleton protein[203].

Considering successful isolation of nuclei with antibodies against the cytoskeletal protein (Srinivasan et al. (2020)[228]), ER protein (this study) or membrane protein (Xu et al. (2018)[178]) provokes the hypothesis of minimal damage of astrocytes in frozen material. A detailed study of the integrity of cellular organelles in frozen and homogenized material could be beneficial for resolving this issue and may suggest even more epitopes suitable for astrocytes' isolation.

Tome-Garcia et al. (2020) reported a strategy based on a simultaneous selection of OPC (targeting OLIG2) and astrocytic nuclei from non-neuronal fractions[234]. The authors applied the method to profile the gene expression pattern of isolated nuclei population in human epilepsy (from the temporal lope). The workflow consisted of tissue homogenization (200-500 mg frozen samples, in the same hypotonic buffer as ours, by Dounce homogenizer strokes), antibody labeling (for 1h), and flow cytometry. Next, RNA was extracted from sorted nuclei populations using the standard phenol/chloroform method, and RNA-seq was performed. The protocol did not involve a tissue fixation step, resulting in better RNA quality. However, no information was provided with respect to the quality of the extracted genetic material and RNA-seq data. Initially, two approaches were evaluated to sort astrocytic nuclei fraction by selecting either NEUN-/OLIG2-/SOX9+ (referred to as SOX9+) population or NEUN-/OLIG2-/PAX6+ (referred to as PAX6+). Since the purity analysis (by qPCR) demonstrated higher enrichment of astrocytic markers for the PAX6+ fraction, the authors decided to continue with that epitope. PAX 6 (Paired Box 6) is a transcription factor enriched in astrocytes, particularly in fetal astrocytes[152]. It has essential roles during the development of multiple tissues such as the brain and eye[236].

The most recent published protocol for nuclei isolation of multiple brain cell types was developed to be employed for chromatin immunoprecipitation-sequencing studies[235]. Hence its applicability for RNA-seq analyses was not evaluated. Here, tissue samples (150 mg) were fixed (in 1% formaldehyde) and homogenized (by pellet pestle grinder) at the same time. Next, Dounce homogenization was performed (in the same hypotonic buffer as ours), and single nuclei suspension was incubated with antibodies (overnight). Finally, FACS-sorted astrocytic nuclei (average yield of nuclei: 100,000) were collected for downstream analysis. Astrocytic nuclei were labelled using two antibodies, where the NEUN-/LHX2+ nuclei fraction was selected. LHX2

(LIM/Homeobox 2) is a transcription factor involved in the development of the brain and is primarily expressed in fetal astrocytes and, to a lesser extent, in mature astrocytes[152]. Importantly, the authors presented a detailed description of the protocol, which might be adapted for transcriptomic studies. However, no information was provided concerning the purity of the isolated astrocytic nuclei population.

Consequently, recently published protocols used a combination of antibodies to facilitate the separation of other brain cell types from astrocytic nuclei, such as NEUN-/OLIG2-[178], NEUN-/OLIG2-/PAX6+[234], and NEUN-/LHX2+[235]. Therefore, an essential advance to improve the purity in our study could be to implement the depletion of neuronal nuclei population and use a double staining approach, i.e., NEUN-/CX43+.

4.2. Transcriptional Alterations of Astrocytes in Human Depression

The novel nuclei isolation method was applied to investigate transcriptional changes of astrocytes in human BA25 frozen tissue samples from healthy controls and depressed suicides.

4.2.1. The Nuclei Protocol was Suitable for Comparative Transcriptional Study in Humans

The use of postmortem human brain samples is inevitable in the context of depression. Fortunately, well archived brain samples can be acquired through brain banks specialized in the disease. However, several critical components, e.g., sample quality and patient history, need to be considered when RNA sequencing is performed to study disease states using frozen postmortem samples[230]. For instance, postmortem factors such as PMI, agonal state (e.g., refrigeration delay), and freezing procedures were shown to affect the RNA quality by reducing the brain pH and increasing RNA degradation rate[230,237,238]. Although care was taken to match the samples chosen for this study for those factors, we observed significant differences between the CON and MDD patients for the confounding factors, pH and refrigeration delay. Notably, the differences in pH among the CON and MDD groups was very low (Table 2.4). Additionally, increased refrigeration delay in MDD samples could be due to the cause of death (i.e., suicide) and the difficulty to monitor for the agonal state. Importantly, we did not detect a reduced pH in the MDD samples as a result of enhanced refrigeration delay. Note that we also checked the initial RNA quality of a fraction of postmortem brain samples and measured moderate RIN values (N = 6, average RIN values: 5.3 ± 0.8). We also did not find diagnose-dependent differences between two populations; Hoechst+ and CX43+ in the number of sorted nuclei, the quantity and quality of extracted genetic material, and on sequencing performance (i.e., mapping features and read alignments).

4.2.2. Challenge III. Validation of the Purity of CX43+ Nuclei Population

Ideally, our approach should result in pure fraction of astrocytic nuclei. However, we repetitively observed contamination of other cell-type specific markers in the qPCR analysis of FACS-sorted nuclei. Oligodendrocytes and OPCs were repetitively reported in protocols employing astrocyte-specific epitopes[200]. Therefore, we followed an alternative approach by implementing size-based exclusion of oligodendrocytes during our flow cytometry analysis. This method resulted in almost complete elimination of oligodendrocytes nuclei from the desired fraction.

In our final RNA-seq analysis, we observed the enrichment of neuronal and microglial markers together with astrocytic markers, which we did not detect in the test experiment with anti-CX43 antibody. The differences between the two results might be due to the relatively lower sensitivity of the qPCR measurement and low specificity of the primer pair employed. Besides, RNA-seq data provided higher detection power and allowed us to assess multiple cell-type-specific markers. Notably, cell type-specific markers were selected from the meta-analysis published by McKenzie et al. (2018)[153]. We selected this database because we also employed it to choose astrocyte-specific nuclear epitope (i.e., CX43). However, a technical disparity was that McKenzie et al. (2018) presented data generated from whole-cell RNA (isolated from fresh brain samples) and not nuclear RNA. Besides, the authors evaluated the marker expression in the human cortex, while CX43+ nuclei were isolated from vmPFC (BA25), which may display regional characterization of astrocytes.

One possible solution to avoid this issue would be conducting a preliminary RNA-seq experiment with a smaller sample size to expand the gene expression profile of the markers. Additionally, enrichment analysis by qPCR should be repeated in independent experiments. However, time restrictions and the limited number of samples prevented us from further optimization. Furthermore, the chosen markers for enrichment analysis might not be compatible with our study because of methodological differences. Cell type-specific gene expression analysis must consider differences in cellular abundance and heterogeneity in every brain region. Since an analogical study (i.e., transcriptomic data on human astrocytic nuclei sorted from the vmPFC brains samples) was missing, an alternative approach could be to use the recently published nuclear RNA-seq data generated from frozen archived PFC brain samples[185]. Alternatively, the specificity index (SI) algorithm implemented by Xu et al. (2018)[178] might be employed to evaluate the purity of the CX43+ nuclei population. This bioinformatics approach could enhance the sensitivity and the power of the analysis.

Nevertheless, while existing contaminations outcome precludes assigning detected changes to a single cell type, the enrichment of astrocytes was evident and majority of previously reported

alterations of astrocyte-specific gene expression was recapitulated. Importantly, we found a number of novel genes being either down- or upregulated at very strict statistical criteria (FDR < 0.1) in BA25 of a subpopulation of suicide completers. We consider this discovery a major finding of this project.

4.2.3. Differential Expression Analysis for the Hoechst+ Population Resulted in Low Statistical Power

Defining the transcriptional changes in the Hoechst+ population would be beneficial to understand the broad alterations in the vmPFC and would complement previously published MDD studies conducted in brain homogenates. Unfortunately, in the Hoechst+ nuclei population, none of the genes (a total of 105 genes) passed the strict selection criteria, FDR < 0.1, hence we could not find a strong correlation for DEGs between the CON and MDD groups. Therefore, we did not perform further downstream pathway analyses. One possible explanation for this result could be that the subtle alterations in gene expression might be masked due to the mixed cell composition. As discussed previously, astrocytes transcriptome can be underrepresented in RNA-seq analysis conducted on a mixed cell population; thus, we might not reach the statistical power to detect them. Another reason for this outcome could be that the transcriptional deficits could be specific to astrocytes in the selected subjects. We observed that 19 DEGs were in common with literature findings investigating gene expression changes in the PFC of depressed patients. Interestingly, the majority of these genes were astrocyte-specific, which confirmed that our efforts of broadening the insight into this cell type were fully justified.

4.2.4. Astrocyte Deficits in the vmPFC of Depressed Suicides

A total of 260 DEGs were identified in the CX43+ nuclei isolated from the vmPFC of depressed suicides, and the majority of the DEGs were downregulated in MDD. Our results were in line with the literature findings in several aspects: i. our gene list was associated with mental illnesses, including depression, ii. DEGs encompassed known astrocytic genes, which were previously linked to MDD, and iii., DEGs were largely enriched in astrocytes compared to neurons. Moreover, we identified new genes either downregulated, e.g., *MGST1*, *KREMEN1*, and *SERPINE2*, or upregulated, e.g., *ASL*, *GULP1*, and *LIG1*, in MDD, which were known to be expressed in human astrocytes. This result pointed out that labeling nuclei with CX43 enabled us to detect subtle gene expression changes associated with astrocytes.

Importantly, our findings suggested a disruption largely in the modulation of signaling and transport system in MDD patients where the plasma membrane proteins might take primary roles. The proteins encoded by the downregulated genes clustered under various biological processes

known to be regulated by human astrocytes. For example, the proteins in cluster A (OLFM2, GRIN2C, GRM3, GPM6A, and CPE) were associated with the synapse and glutamate receptor signaling. In addition, most of the proteins in cluster A (except OLFM2) were previously linked to the altered glutamatergic system in MDD[184,220,239]. Likewise, the proteins in this cluster were primarily localized in the plasma membrane[216], suggesting a potential effect on glutamatergic transmission. Consequently, our data provided complementary information to the literature by highlighting possible new components of this system, which might be involved in the pathology of the disease. However, further studies are necessary to confirm the functional interactions of these proteins and understand the altered mechanism mediated by astrocytes.

We next explored whether genes downregulated in the CX43+ nuclei compartment were associated with previously observed astrocytic deficits in this group of patients. Nagy et al. (2015) studied DNA methylation patterns and reported increased DNA methylation for BEGAIN accompanied by decreased gene expression[37]. Moreover, the authors linked BEGAIN with postsynaptic density 95 (PSD95), which regulates excitatory/inhibitory balance through its localization in excitatory synapses. As a result, a possible impairment in synaptic communication and/or synaptic plasticity mediated by astrocytes was suggested[37].

To compare our findings, we conducted a STRING analysis and found significant interactions between PSD95, BEGAIN, and the proteins in cluster A (Supp. Fig. S9). The hub protein in this interaction network was GRIN2C (glutamate ionotropic receptor NMDA type subunit 2c), a glutamate binding subunit of NMDA receptor[203]. Although their functionality is still controversial, NMDAR subunits' expression, including *GRIN2C*, were reported in cultured human and mouse cortical astrocytes[240]. Interestingly, Chandley et al. (2014) revealed increased expression levels of *GRIN2C* and *GRIN2B* in the LC neurons (collected by LCM) but not in the PFC pyramidal neurons (BA10) in MDD patients[241]. Additionally, the authors suggested an alteration in the NMDAR subunit composition and disruption in glutamatergic input to the noradrenergic LC[241]. Contrary, Dean et al. (2016) reported no change in the expression levels of *GRIN2C* and *PSD95* in the BA10, BA46, and BA24 from MDD subjects; instead, the authors showed higher levels of *GRIN2D* in the BA10[242]. Moreover, reduced *GRIN2C* expression was observed in the BA46 of bipolar disorder[242].

Taken together, in consonance with the literature, our data proposed changes in the glutamatergic function in subjects with MDD highlighting the possible roles of astrocytes in this pathology. Further studies are needed to explain the specific regional and cellular variations in the excitatory/inhibitory system in depression.

4.2.5. Limitations and Advantages of the Study Design

The suicide completers were selected from a previously characterized subgroup of patients based on the low expression of astrocytic genes (at least 5/7 genes) in BA8/9 and BA10[37]. We chose to study this subpopulation of subjects to broaden the insight into the transcriptional alterations of astrocytes. Our data showed the downregulation of 3/7 genes in the Hoechst+ population and 4/7 in the CX43+ population. This result was comparable to the reference study[37] and confirmed the possible astrocyte deficits in the BA25 of selected patients. Importantly, it is known that MDD patients are highly heterogeneous (e.g., display diverse biological symptoms and treatment responses)[28,124], and it is difficult to explain such polygenic disease under a common biological mechanism[39]. Therefore, studying a subgroup of subjects with a defined molecular deficit could facilitate the development of new strategies for classifying patients and matching them with appropriate treatments.

All the subjects in our study were males. Notably, transcriptional changes associated with MDD were reported to be distinct in females[220]. Furthermore, although we did not observe technical differences between the CON and MDD groups, and our samples were largely matched for the postmortem factors, the treatment history of the subjects should be further evaluated as a potential confounder.

In conclusion, we presented the applicability of our nuclei isolation protocol to study transcriptional changes in MDD. We reported new DEGs specific to BA25, demonstrating evidence of astrocytic dysfunction. Furthermore, our data suggested deviations in essential biological functions of astrocytes, highlighting the impairment of astrocytes as one of the crucial hallmarks of depression. Future studies are necessary to reveal the potential interactions between other brain cell types in this particular brain region. Likewise, further investigations, e.g., using animal models, could explain the mechanisms of identified biological functions.

4.3. Optimization of Astrocyte Isolation Methods for Various Adult Mouse Brain Region

The second goal of this project was to modify available protocols for astrocyte isolation for small brain regions using a magnetic cell sorting system. To start, we followed the manufacturers' instructions (Miltenyi) and well-established relevant protocols[172,209–211]. Due to initial suboptimal results, we progressively improved several parameters of the original protocols overcoming two main challenges: sorting viable astrocytes from small brain regions (i.e., PFC and hypothalamus)

and extracting high quality RNA from isolated cells suitable for RNA-sequencing. We demonstrated that our approach was suitable for employing low volume tissue samples dissected from a single mouse brain and compatible with RNA sequencing. This progress enables now comparing the transcriptome from small brain regions in mouse-to-mouse fashion, which is crucial to correlate individuals' behavior to transcriptome and limits the number of animals required for such studies.

4.3.1. Advantages of MACS System for Isolation of Astrocytes

Among available techniques, we opted to use the MACS approach because it was suitable to enrich viable astrocytes from wild-type adult mouse brain tissues and generate genetic material compatible with RNA sequencing analysis[210]. Furthermore, the MACS system did not require expensive specialized equipment and was relatively fast to sort astrocytes from multiple samples (max. 8 samples simultaneously).

Interestingly, a recent study compared the two widely used techniques, MACS, and FACS, for astrocytes' isolation from the whole mouse brain[195]. MACS-enriched astrocytes showed higher yield (MACS: 23 x 10^4 cells vs. FACS: 14 x 10^4 cells), slightly greater viability (for both systems, above 85%), and MACS protocol took less time than FACS (MACS: 25-30 min. vs. FACS: 1.5-2h, after antibody staining step)[195]. Moreover, the authors conducted a comprehensive gene expression analysis to assess the purity of FACS- and MACS-sorted astrocyte populations. The qPCR data suggested that both systems provided similar levels of enriched astrocytes, however with slight contamination of endothelial cells (i.e., *Pecam1*, *Ocln*) and oligodendrocytes (i.e., *Cspg4*)[195]. This finding was consistent with our qPCR data, in which we also detected minor enrichment of *Cspg4* marker in sorted astrocyte population from different brain regions.

4.3.2. Challenge IV. Adapting Methodological Parameters to Sort Astrocytes from Low Tissue Volumes

We pursued a step-by-step approach to revise the available protocols, and the first critical parameter we modified was the step of generating single-cell suspension. To this end, the enzymatic digestion (incubation with papain) was combined with a manual trituration process using fire-polished pipettes instead of a semi-automated device (Miltenyi)[209,211] or oxygen perfusion system[210]. The mechanical dissociator was not suitable for low tissue volume (< 20 mm^3). Likewise, the oxygen perfusion system was not established in our laboratory infrastructure, including that it would require an additional manual trituration step to acquire effective dissociation of cells from the tissue. Eventually, our approach was suitable to obtain intact single-cell suspension from various mouse brain regions in a cost-effective way.

4.3.3. Challenge V. Isolation of Pure Astrocyte Population

Our initial findings pointed out the necessity to include the myelin removal step due to the contamination of oligodendrocyte, as also recommended by Batiuk et al. (2017)[172]. Myelin levels are known to be higher in adult mice brains compared to the early postnatal animals[195]. Likewise, recent studies implemented this additional step, indicating that ACSA-2 labels also mature oligodendrocyte population[171,243]. An intriguing question was the presence of an NG2 cell marker (i.e., *Cspg4*) that was detectable in isolated astrocytes. This membrane protein was known to be expressed in several cell types in the brain, such as in pericytes or OPC[152]. Interestingly, *Cspg4* and *Atp1b2* were reported to be co-expressed in a small fraction of astrocytes, suggesting that the ACSA-2+ cell population may express it as well[166]. Nevertheless, our result was consistent with the study that we followed as a reference method paper (i.e., Batiuk et al. (2017)), which showed the expression of *Cspg4* in the astrocyte population sorted from the cortex[172].

An unexpected result of our method was the presence of neuronal marker (*Syt1*) in the astrocyte fraction isolated from the PFC. This finding could be due to the increased number of neurons or increased expression of the marker itself. To resolve this point, we conducted a qPCR analysis on brain homogenates obtained either from PFC or the whole brain. We found that the relative expression level of *Syt1* was much higher in the PFC (relative expression: 3.5 a.u.) than whole brain tissue (relative expression: 0.1 a.u.) (data not shown). Similarly, the RNA-seq data showed high expression level of the neuronal marker, *Syt1*, in the population of ACSA-2+ cells from PFC astrocytes, pointing out the differences in cellular abundance and regional heterogeneity. Another explanation for this result could be that there might be a dependent vesicular release from astrocytes expressing exocytotic proteins, including *Syt1*[244].

Eventually, RNA-seq data analysis revealed that ACSA-2+ cells represented a population highly enriched with astrocytes. Notably, the transcriptome of ACSA-2+ cells weakly correlated with the gene expression profile of ependymal cells, particularly in two brain regions, the hippocampus and hypothalamus. One possible explanation for this result could be that astrocytes and ependymal cells are developmentally related[245]. Ependymal cells are types of glial cells, which form an epithelial layer on the walls of the ventricles in the CNS and the central canal of the spinal cord[147]. They possess motile cilia and play roles in cerebral fluid balance, transport of the CSF, and toxin metabolism[147]. Ependymal cells can be derived from radial glial cells (during the development) and astrocytes (in the adult brain)[147]. Similarly, it was shown that astrocytes and ependymal cells are transcriptionally related[245]. Indeed, in the selected reference database[221], 53 out of the top 100 genes enriched in either type were shared between astrocytes and ependymal cells. Additionally, Kantzer et al. (2017) reported that in flow cytometry, a small fraction of cells (6-9%) in the adult mouse brain were positive for both ACSA-2 and CD24, a marker for ependymal cells[211]. Hence,

we might have sorted a small population of ependymal cells together with astrocytes. Nonetheless, our analysis showed that > 80% of the variance in the gene expression data was explained by astrocytes.

4.3.4. Challenge VI. Extraction of High Quality RNA from Sorted Astrocytes

To extract high quality RNA, two necessary modifications were implemented: DNAse I addition and debris removal. DNAse I is known to cleave the free DNA released during tissue dissociation, which also helps to avoid clumps formation[227]. Furthermore, a fraction of the cells die and form debris during mechanical tissue trituration, which can aggregate and affect the immunolabeling efficiency[208]. Excluding debris can ameliorate isolated cells' viability and the quality of extracted genetic material. Initially, we omitted the debris removal step to minimize cell loss when using a low amount of the input material. Nevertheless, we decided to implement both parameters in our protocol and fine-tune it according to the brain region of interest (i.e., omitting debris removal when cells were isolated from PFC and hypothalamus). As a result, the RNA of better quality (judged by RIN values) was extracted from astrocytes isolated from all the brain regions and shown to be suitable for RNA-seq experiments.

4.3.5. Current Developments for Astrocytes' Isolation Using MACS

The MACS system was recently reported to enable the isolation of astrocytes from low volume tissue samples, i.e., hippocampus[247] and hypothalamus[243] of the adult mouse brain. Tertil et al. (2018) sorted hippocampal astrocytes using the ACSA-1 kit and studied the cells in the context of stress-induced alterations and aversive memory[247]. Notably, the authors pooled hippocampi from two animals, possibly to increase yield of sorted astrocytes. Another study investigating hypothalamic glial cells utilized the ACSA-2 approach for astrocytes and microglia isolation from hypothalamus[243]. Nonetheless, due to the low input material, they had to pool samples from five mice to sort an adequate number of cells for downstream analysis. These studies highlight the necessity of our efforts to adjust the protocol for low volume tissue samples.

4.4. Gene Expression Studies of Astrocytes in a Mouse Model of Chronic Stress

We applied the optimized protocol to explore astrocyte-specific molecular deficits elicited by chronic stress. Note that extended investigation of the chronic stressed-induced, brain region- and

time point-specific analysis of gene expression changes was beyond the scope of this thesis. Hence, only the applicability of the protocol and the quality of resulting RNA-seq data are discussed.

4.4.1. The Protocol for Astrocytes Isolation was Suitable for Comparative Transcriptional Study in Mice

We were able to isolate astrocytes from a cohort of mice without observing statistical differences in isolated cell numbers, RNA quantity, and quality between the study groups, CONT and CSDS. Furthermore, the extracted genetic materials (both RNA and libraries) were suitable to conduct comprehensive RNA-sequencing. In comparison to the available protocols[243,247], our approach enabled us to study astrocytes' transcriptome in low tissue volume samples dissected from a single mouse brain.

4.4.2. Astrocytes' Transcriptome Displayed Brain Region Specific Gene Expression Profile

In line with previous studies[155,222], we detected distinct gene expression profiles of astrocytes in every brain region. In addition, we explored the expression of the *Atp1b2* gene, encoding for the protein recognized by ACSA-2, and observed its enrichment in astrocytes isolated from all brain regions. This finding confirmed that ACSA-2 selectively labels astrocyte populations in adult mouse brains. In line with our data, the expression level of the astrocytic marker, ATP1B2 was also shown to be variable throughout the brain (judged by immunostaining), and lower protein levels were detected in the PFC (judged by immunoblotting)[172].

Batiuk et al. (2020) recently employed the ACSA-2 strategy and explored cortical and hippocampal astrocyte subtypes at a single cell resolution[222]. The authors revealed common (in > 60% of cells) and specific genes across astrocyte subtypes. For example, *Agt* was enriched in hippocampal astrocytes subpopulation, and *Chrdl1* was prominent in cortical astrocytes[222]. We examined the expression of both genes in the hippocampus, PFC and SC, and we found similar results; *Agt* was enriched in astrocytes isolated from the hippocampus, and *Chrdl1* was increased in the PFC and SC (data not shown). These genes are essential for astrocytes functions such as synapse function/plasticity (*Agt*) and synaptogenesis (*Chrdl1*)[222]. Hence, comparable to published studies, our RNA-seq data suggested region-specific gene expression profiles of astrocytes relevant to their local functions.

4.4.3. Limitations and Advantages of the Study Design

Several factors could still be improved in our experimental approach. One major limitation for the MACS was that the system is not compatible with simultaneous isolation of multiple cell types as it offered, for example, by FACS[246]. Instead, MACS requires sequential isolation steps, making it

more time consuming. However, since we focused solely on studying astrocytes' transcriptome, this factor was not critical for our project.

Next, assessing the expression levels of multiple cell type-specific markers in a sorted astrocyte population would increase the confidence about the purity of isolated cells in our qPCR analysis. With that respect, genes as *Aqp4* and *Gja1* (astrocytes), *Pdgfra* and *Plp1* (OPC and oligodendrocyte), and *Reln* and *Rbfox3* (neurons) could be used as additional specific markers. However, the number of isolated astrocytes from a single brain region was limited, precluding a more extensive analysis. As a possible solution, after sorting, we pooled cells from multiple mice tissues to increase the yield and genetic material used for qPCR. Still, we could only quantify five cell type-specific markers. Another adjustment to improve the quality and quantity of RNA would be adding RNase inhibitors into the cell suspension to prevent RNA degradation. Further experiments would be necessary to optimize the concentration of RNase inhibitors. Interestingly, none of the published protocols implemented this step.

A common consideration for cell type-specific studies is that antibody labelled, and sorted cells might represent only a sub-population of the analyzed cell type. While we cannot exclude this possibility, in a recent study, Batiuk et al. (2020) employed the ACSA-2 system and identified cortical and hippocampal astrocyte sub-types at a single cell resolution[222].

Furthermore, we applied ACSA-2+ cell isolation to investigate the transcriptome of astrocytes, and we did not provide any information on its applicability to study the proteome. Therefore, further improvement might be necessary to adopt the protocol for proteomics. Next, one might need to consider additional adjustments (e.g., in the tissue homogenization step) if astrocytes are to be isolated from different small brain regions like the amygdala or habenula, which were previously implicated in depression[248], and where gene expression changes were reported in mice exposed to CSDS[188]. Likewise, the variation in *Atp1b2* expression levels across brain regions cannot be excluded.

In summary, we illustrated that the established method enabled to study of astrocytes-specific alterations in multiple cohorts of mice exposed to CSDS. The key strength of this protocol was that astrocytes were isolated from low tissue volumes at a single animal resolution. It is important to keep the individual differences when animal models are employed to correlate behavioural alterations (e.g., stress-related phenotypes such as decreased social interactions) to the gene expression changes.

4.5. General Remarks and Future Perspectives

The presented work offers methods for astrocytes' isolation to explore their transcriptome in human depression and mouse model of chronic stress. Employing these approaches enabled us to identify novel genes linking astrocyte-specific molecular processes with altered neurobiological functions in depression.

4.5.1. Are the Selected Astrocyte-Specific Epitopes Suitable to Study Stress and Depression?

A general consideration for cell isolation methods is whether the expression of the selected marker to isolate the cells is affected by pathological conditions. Expression changes of CX43 genes in several brain areas were linked to depression[72,74,249]. Notably, suicide completers in this study were chosen from a previously characterized cohort for which the CX43 levels were reported to be downregulated in the BA8/9 and BA10[37]. To a less extend, decreased levels of *Atp1b2* were reported in the amygdala of rat animal model of depression[250]. Interestingly, increased *ATP1B2* expression in humans was observed in the hippocampus and BA10 of suicide completers without depression[251,252]. Importantly, our studies did not detect significant changes in the number of isolated human astrocytic nuclei (CX43+ nuclei fraction) and mouse astrocytes (ACSA-2+ cells) among the study groups. Furthermore, we evaluated the protein levels of the CX43 in the brain homogenates (BA25) from CON (N = 8) and MDD (N = 8) subjects and we did not observe a significant change ($\overline{x}_{(CON)}$: 0.065 ± 0.02 a.u. and $\overline{x}_{(MDD)}$: 0.069 ± 0.04, $P = 0.83$, n = 1 single blotting experiment).

Astrocytes have essential cellular functions in the brain, such as regulating synaptic plasticity[139], neurotransmitter uptake[143], and mediating the brain metabolism[143]. Mounting evidence demonstrated the gene expression changes for the core components of astrocytes in chronic stress and depression, e.g., *GFAP*, *EAAT1*, *PAX6*, *CX43*, and *ATP1B2*[85,135,249,253]. Hence, it is not easy to find an astrocyte-specific epitope, which is highly abundant, broadly expressed, and not implicated in MDD and/or CSDS. Nevertheless, the most recent published protocol sorted human astrocytic nuclei, i.e., NEUN-/LHX2+ nuclei fraction for chromatin immunoprecipitation-sequencing analysis[235]. Up to date, LHX2 has not been associated with depression. Therefore, adapting this protocol for transcriptomic studies could be an alternative strategy to study astrocytes in stress-related mental disorders. Likewise, astrocytic Stonin 2 (STON2), an adaptor molecule known to be expressed in the nucleus, plasma membrane, and lysosome[203], could be another optional marker, which has not been involved in MDD.

4.5.2. Role of Astrocytes in Stress and Depression

Considering the heterogeneity of the patients, we still do not know how physiological changes observed in MDD translate to brain dysfunction. It is essential to gain insight into the aberrant biology of the most relevant brain regions and to find out the brain cell type(s) underlying the neuronal network alterations in this brain region. We hypothesized that astrocytes' dysfunctions in BA25 mediate biological symptoms of depression and that it is possible to identify disease relevant cell-type-specific transcriptional alterations. Thanks to the novel protocols, we identified such alterations and revealed substantial changes in genes engaged in the essential functions of astrocytes.

4.5.2.1.Astrocytes and Synaptic Plasticity

The tripartite synapse formation is a complex structure where astrocytes cover the pre-and postsynaptic parts of the synapses. Astrocytes were shown to mediate synapse formation, maturation, elimination, and maintenance by secreting factors and signaling molecules: cholesterol (increase synapse development), syndecans (SDCs, induce neurite outgrowth), thrombospondin (enhance synapse formation and decrease neuronal excitability), wingless/WNT (promote synaptic glutamate receptor), and TNF-α (homeostatic scaling of synapse)[139,254–256].

Crucial components of astrocytes involved in the regulation of synapse formation and functioning were also implicated in depression. For instance, astrocytes were suggested to take part in synaptogenesis disruption based on their ability to synthesize and secrete neurotrophins and expressing several neurotrophic factors (i.e., BDNF and glial cell-derived neurotrophic factor (GDNF), fibroblast growth factor receptor (FGFR), SPARC-like 1 (SPARCL1, also known as HEVIN))[85,257,258]. Decreased gene expression levels of BDNF in patients' blood were reported to be associated with antidepressant treatment response[259,260]. Likewise, we also observed downregulation of genes encoding extracellular proteins, such as *SDC3*, *FGFR3*, *GPC5*, *SPARCL1*, and *CHRDL1*, in the CX43+ nuclei fraction of depressed subjects. While our data is in line with previous findings, e.g., expression levels of *FGFR3* were shown to be diminished in the LC[72], dlPFC[258], ACC[258] of depressed patients, we also provide new astrocyte-specific components involved in synaptic plasticity, e.g., chordin like 1 (CHRDL1). However, how disruption in neurotrophins or growth factors levels leads to develop depression and what is the direct role of astrocytes in this framework are not fully known yet. Astrocytes can control neurons' activity and survival by regulating extracellular ion and neurotransmitter levels in dynamic and bidirectional ways[152,261]. Hence, emerging therapeutic approaches to increase the expression of astrocyte-derived neurotrophic factors might be an option for alternative therapies in depression.

Nevertheless, further studies are necessary to differentiate between astrocytic and neuronal participation of these factors in the development of depression.

Interestingly, WNT signaling was involved in the pathology of mood disorders, including depression[134,262]. Postmortem brain samples (obtained from PFC) showed changes in expression levels of *FZD10* (frizzled-10, up-regulated), *FZD2* (frizzled-2, up-regulated), and *WIF1* (WNT inhibitory factor 1, down-regulated)[74,220]. These genes are expressed in astrocytes, and they are involved in regulating the excitatory synaptic receptor clustering[139]. *In vitro* studies proposed that antidepressants (i.e., fluoxetine) can affect WNT-related components (i.e., GSK3B, glycogen synthase kinase 3 beta), which in turn may lead to activation of WNT signaling and enhance neuroplasticity[262]. A component of this pathway, *KREMEN1*, was downregulated in our data. This gene is expressed in human astrocytes and encodes a receptor for Dickkopf (DKK1) proteins involved in the inhibition of WNT signaling[203]. Note that since WNT signaling and related proteins participate in various other processes, such as inflammation, cytoskeletal functioning, and cellular metabolism, it is challenging to depict their exact role in depression pathology.

4.5.2.2.Astrocytes and Glutamate Homeostasis

Astrocytes can control spatial and temporal synaptic transmission by the removal of neurotransmitters from the extracellular space by expressing specific transporters for glutamate, EAAT1 (SLC1A3), EAAT2 (SLC1A2), or GABA, SLC6A11 (solute carrier family 6 member 11, known as GAT-3)[140]. The glutamate in astrocytes can be converted to glutamine via the cytosolic enzyme GLUL; then, glutamine can be shuttled back to the presynaptic neurons by sodium-dependent transporter[263]. In neurons, glutamine can be used to synthesize glutamate (by glutaminase) for cellular storage or as a precursor of GABA. Once extracellular GABA is taken up into astrocytes, it is further degraded by GABA-transaminase (GABA-T) and ultimately leads to glutamate formation[264]. Astrocytes also express glutamate (MGLUR3 – GRM3) and GABA ($GABA_AR$) receptors responding to glutamate and GABA, respectively[68,81]. As a result, astrocytes have key homeostatic roles in these complex excitatory and inhibitory neurotransmission systems in the brain.

Postmortem cellular data showed decreased density in the GLUL-immunoreactive astrocytes in the dlPFC, sgACC, and anterior insular cortex, but no changes in the nucleus accumbens samples collected from MDD patients[218]. Interestingly, the authors explored the cellular specificity of the observed phenotype by taking into consideration GLUL-immunoreactive oligodendrocytes, which did not reveal any alterations. An independent postmortem study comparing the protein levels of the GLUL in the PFC (BA47) reported no significant changes in the MDD group[265]. Discrepancies between findings could be due to methodological differences, brain region of interest, including

expression differences across cortical layers, and patients' distribution (disease and treatment history).

The evidence for the alteration in glutamine/glutamate cycling involving astrocyte components was expanded with transcriptional studies[249]. Investigations on bulk tissue homogenates consistently reported reduced gene expression levels in *EAAT1*, *EAAT2*, *GLUL*, and *GRM3*[72–74,132,266]. Notably, similar findings were made in multiple brain regions, i.e., locus coeruleus, hippocampus, and frontal cortex (dlPFC, ACC, and vmPFC). In line with these data, we also observed decreased expression of astrocyte-specific excitatory/inhibitory neurotransmission and glutamate metabolism components in BA25, such as *EAAT2*, *GLUL*, *GRM3*, *GRIN2C*, *GLUD1*. Interestingly, we identified a new component of this pathway, i.e., *SLC25A18*, which was downregulated in the CX43+ nuclei fraction isolated from the vmPFC of depressed patients.

The functional imaging studies also suggested altered glutamate concentrations in MDD patients[85,267]. However, there are still open questions: Is the reduced expression of astrocytic components an adaptive glial response to decreased synaptic glutamate levels? Are the deficits in astrocytes lead to increased extracellular glutamate concentrations? Furthermore, taking into account the transcriptional changes (i.e., related to glutamate pathway) occurring in the neuronal compartment[72], a systematic approach studying the transcriptome of multiple brain cells may help answer those questions and understand the mechanism underlying neurotransmitter imbalance in depression.

In summary, these observations show major deficits in transcriptional programs underlying glutamate homeostasis in astrocytes. Consequently, we propose that astrocytes may constitute a primary cellular locus responsible for deficient glutamate signaling in MDD.

5. SUPPLEMENTARY INFORMATION

5.1. Detailed Procedures: Isolation of Astrocytic Nuclei from Fresh Frozen Human Brain Samples

Clean the working place and equipment with ethanol (70%) and RNaseZap. Pre-cool the reagents and tools on ice.

Fixation

1. Take out the tissue (~100 mg) from -80˚C and placed it on ice for 2 minutes. Transfer the tissue into pre-cooled 1 ml of 1% fixative solution and incubate for 8 minutes on ice.
2. Discard the fixative solution and add 1 ml of SB to wash. Centrifuge at 400 × g for 5 min. at 4˚C.

Homogenization

1. Prepare beforehand two Dounce homogenizers and pestles. Fill each homogenizer with 1 ml of cold HB and keep them on ice.
2. After centrifugation, discard the SB and immediately divide the fixed tissue into two by transferring each half into pre-cooled Dounce homogenizers.
3. Homogenize the tissue on ice, using a chilled loose pestle with 5 strokes. Then, continue with the tight pestle performing 10 strokes. The number of strokes should be optimized based on the tissue type and amount. The homogenization should be done gently to prevent the loss of nuclei. Avoid bubble formation.
4. Place a 40 µm cell strainer on top of a 50 ml Falcon tube and wet it with 10 ml of SB. Pour out the buffer from the tube to discard it. Filter and combine both homogenates into one 50 ml Falcon tube.
5. Pellet the nuclei by centrifugation at 1000 × g for 10 min. at 4˚C. Aspirate the supernatant without disturbing the pellet.
6. Re-suspend the nuclei with 250 µl of SB. Add 250 µl of 50% (vol/vol) Optiprep solution on top of the nuclei and mix gently. (This will make 25% Optiprep solution-nuclei).
7. In a new 1.5 ml Eppendorf tube, place 500 µl of 29% Optiprep solution. Then, slowly, layer the 25% Optiprep solution-nuclei.

8. Centrifuge at 10,000 rpm for 30 min. at 4˚C. Aspirate both layers without disturbing the pellet.
9. Re-suspend the pellet with 1 ml of SB and assess the number of the nuclei with Neubauercell counting chamber. On average, from ~100 mg of frozen human brain tissue, 1.5 x 10^6 nuclei are obtained.

Immunostaining

1. Incubate the nuclei in SB buffer for 15 min. on ice for blocking.
2. Divide the nuclei into different 15 ml Falcon tubes for immunostaining at a final volume of 1000 µl. Use the same number of nuclei and identical antibody concentration for the Control samples and Sample-anti-CX43, as following:

Sample Content	Primary Antibody	Antibody Concentration	Secondary Antibody	Dilution	Hoechst
Control – nuclei	-	-	-	-	-
Control – Hoechst	-	-	-	-	10 ng/ml
Control – secondary	-	-	Alexa 488	4 µg/ml	10 ng/ml
Control – isotype	Mouse IgG1	5 µg/ml	Alexa 488	4 µg/ml	10 ng/ml
Sample – anti-CX43	Anti-CX43	5 µg/ml	Alexa 488	4 µg/ml	10 ng/ml

3. Incubate the samples with primary antibodies (total volume 1000 µl) on a tube rotator for 1 hour at 4˚C.
4. Add 500 µl of SB into each tube and centrifuge at 400 × g for 8 min. at 4˚C to perform washing.
5. Incubate the samples with the secondary antibody on a tube rotator for 45 min. at 4˚C.
6. Add 500 µl of SB into each sample and centrifuge at 400 × g for 8 min. at 4˚C to perform washing.
7. Aspirate the supernatant, resuspend the samples in 500 µl of SB containing Hoechst (except the control-nuclei sample) and transfer them into FACS tubes through the filtering cap. Keep the samples on ice and protect them from light until FACS analysis.

FACS – Nuclei Isolation

1. Prepare the collection tubes (1.5 ml Eppendorf) containing 100 µl of PKD buffer (from Qiagen FFPE RNA kit) and keep them on ice.
2. The FACS instrument is prepared by the facility. The droplet stream is optimized, and the sorting delay, speed, and accuracy are calibrated using beads. Keep the instrument loading chamber at 4˚C. The 100 µm nozzle was selected for sorting.

3. First, load the control-nuclei sample. Using BD FACSDiva 8.0.1 software, adjust the gating and voltage parameters to prevent sorting doublets or groupings of attached nuclei (use side and forward scatter channels). Keep the overall event rate for particles to 200-4,000 events/second on the FACS instrument.
4. Second, load the control-Hoechst sample and select the Hoechst positive populations (P1 and P2, Fig. S1A). Select the P2 (Fig. S1A) population as a parental gate for further hierarchical gating to sort CX43 positive nuclei.
5. Next, load the control-secondary and control-isotype samples. Define the negative populations based on the signal intensity at 488 nm (Fig. S1B).
6. Finally, load the sample anti-CX43 for astrocyte isolation. First, define the positive population based on negative controls (P3, Fig. S1C). Next, perform size-based selection and unselected approximately 10-15% of small-sized nuclei from the P4 (Fig. S1C) population by excluding the P1 from Hoechst+ events (Fig. S1A).
7. Sort the nuclei into the collection tubes containing 100 µl of PKD buffer, place them on ice and store them at -80˚C until RNA extraction.

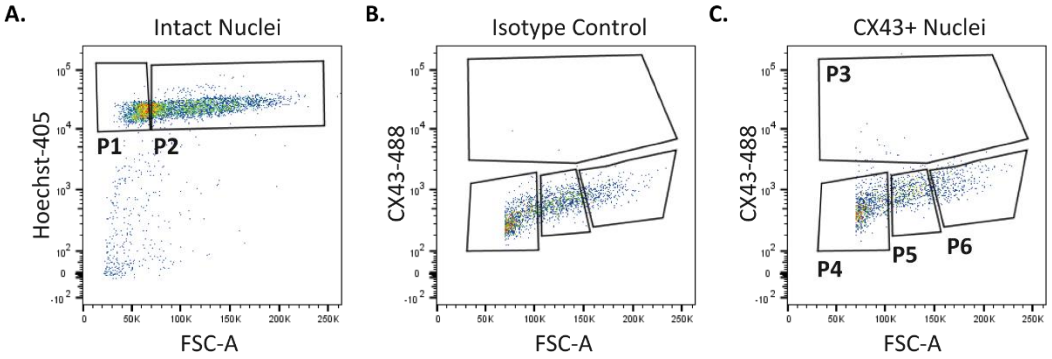

Figure S1. FACS Nuclei Isolation. Representative FACS dot plots for astrocytic nuclei isolation. **A.** Control-Hoechst sample. **B.** Control-Isotype sample. **C.** Sample-anti-CX43 tube. P1-P6 represent different nuclei populations. FSC-A: forward scatter area.

5.2. Detailed Procedures: Isolation of Astrocytes from Adult Mouse Brain Samples

Clean the working place and equipment with ethanol (70%) and RNaseZap. Pre-cool the DPBS and dissecting tools on ice. Work fast as possible.

Dissected brain tissue samples (Fig. 2.1) are kept on ice until the homogenization step.

Homogenization

1. Prepare beforehand the fire-polished Pasteur pipettes with medium and small bores by rotating glass Pasteur pipettes in a flame until the edges become rounded. Small bores are approximately 0.3-0.4 mm, and medium pores are around 0.6-0.8 mm internal diameter. Autoclave pipettes to sterilize.
2. Prepare enzyme mixtures as mentioned in the protocol (Adult Brain Dissociation Kit) and incubate them in the water bath for 15 min. at 37˚C.
    a. Enzyme mix 1: 50 µl Enzyme P + 1900 µl Buffer Z.
    b. Enzyme mix 2: 10 µl Enzyme A + 20 µl Buffer Y.
3. Minced the brain tissues (if the tissue is a whole-brain, cortex, somatosensory cortex, and hippocampus) and transfer into a 15 ml Falcon tube containing pre-heated Enzyme mix 1.
4. Incubate for 10 min. at 37˚C. Mix the tubes every 2-3 min., manually.
5. Add the Enzyme mix 2 and start the first round of trituration with an unpolished pipette. Avoid bubble formation.
    a. For the whole brain and cortex: 10 strokes.
    b. For somatosensory cortex, motor cortex, hippocampus, PFC, hypothalamus: 5 strokes.
6. Incubate for 5 min. at 37˚C. Mix the tubes every 2-3 min., manually.
7. Triturate 5 times slowly using a medium-sized fire-polished Pasteur pipette. Take out 1 ml of the triturated solution, put it into a new 15 ml tube, and keep it on ice.
8. Incubate the remaining homogenate for 10 min. at 37˚C. Mix the tubes every 2-3 minutes, manually.
9. Add 125 U/ml of DNase I and triturate 5 times slowly using a small-sized fire-polished Pasteur pipette.

10. Place MACS SmartStrainer on a 50 ml Falcon tube and wet it with 10 ml DPBS. Discard DPBS from the tube.
11. Gently mix the cell suspension and filter. Apply the remaining 1 ml of triturated samples that were kept on ice.
12. Wash the filter with 10 ml of cold DPBS.
13. Discard the filter and centrifuge the cell suspension at 300 × g for 10 min. at 4˚C. Aspirate supernatant completely.

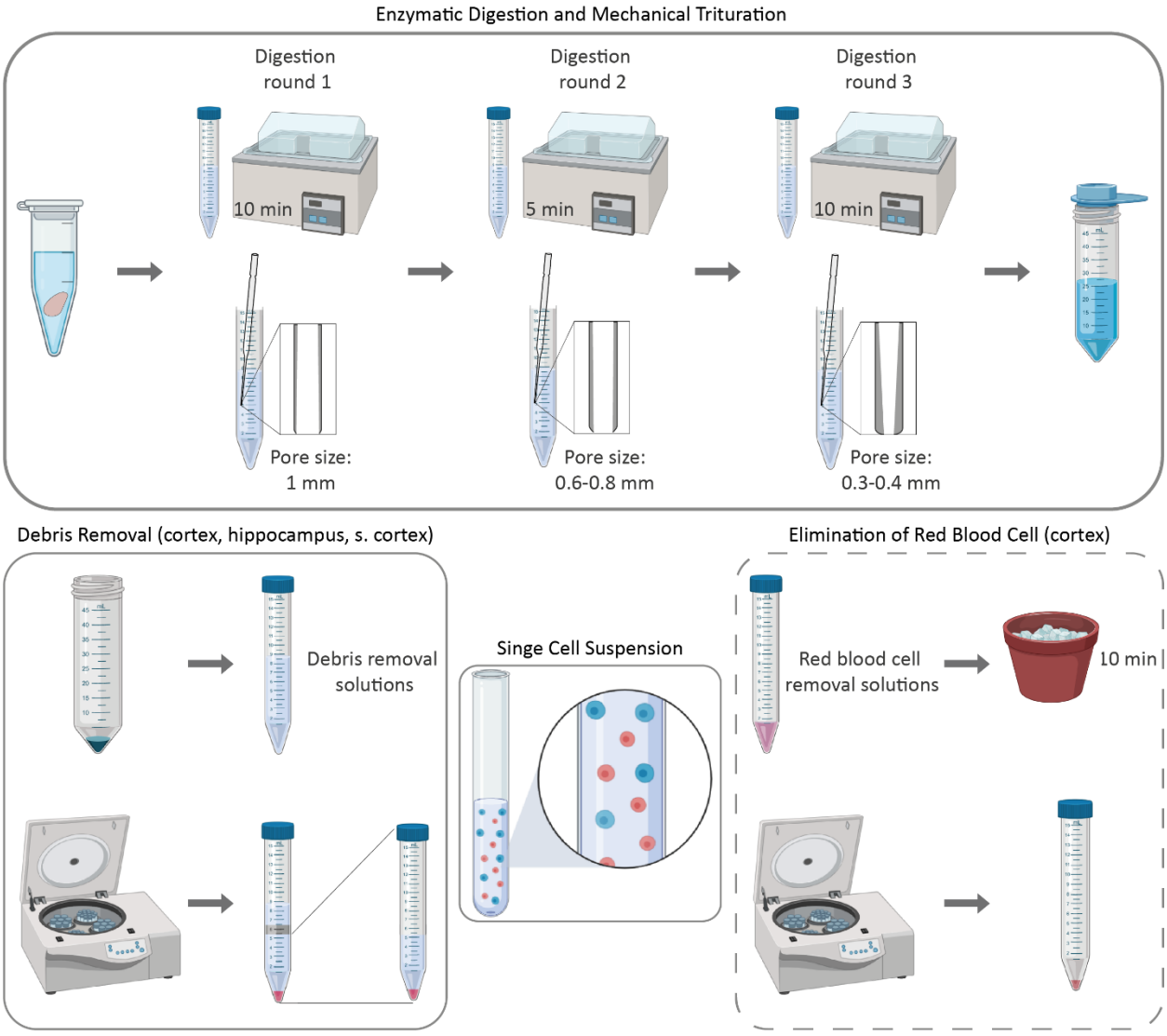

Figure S2. Generation of Single Cell Suspension. Schematic representation of the tissue homogenization steps.

Debris Removal

Omit debris removal when astrocytes are isolated from PFC, hypothalamus, and motor cortex. If simultaneously astrocytes need to be isolated from bigger-sized brain tissues, keep cells in 100 µl of PB buffer (DPBS, pH 7.2, and 0.5% BSA) on ice until debris removal is performed. Otherwise, proceed directly to myelin removal.

1. For debris removal, resuspend the cell pellet in an appropriate volume of cold DPBS and transfer it into 15 ml Falcon tubes.
    a. For the whole brain, follow the manufacturer's indications: 3100 µl.
    b. For cortex: 1500 µl.
    c. For hippocampus and somatosensory cortex: 1000 µl.
2. Add appropriate volume of cold debris removal solution and mix gently by pipetting up and down.
    a. For the whole brain, follow the manufacturer's indications: 900 µl.
    b. For cortex: 400 µl.
    c. For hippocampus and somatosensory cortex: 300 µl.
3. Overlay gently appropriate volume of cold DPBS. To obtain clear phases, use a glass Pasteur pipette and break the beginning with a slight angle before overlaying.
    a. For the whole brain, follow the manufacturers' indications: 4 ml.
    b. For cortex: 3 ml.
    c. For hippocampus and somatosensory cortex: 1 ml.
4. Centrifuge at 3000 × g for 10 min. at 4˚C with full acceleration and full brake.
5. Three phases should be formed. Aspirate the two top phases entirely and discard them.
6. Fill up with cold DPBS to a final volume of 15 ml and gently invert the tube three times.
7. Centrifuge at 1000 × g for 10 min. at 4˚C with full acceleration and full brake. Aspirate supernatant completely.

Elimination of Red Blood Cells

Perform red blood cell removal only when astrocytes are isolated from the whole cortex. Otherwise, proceed directly to myelin removal.

1. Dilute Red Blood Cell Removal Solution (10X) 1:10 with cold double-distilled water (ddH_2O). Do not use deionized water for dilution.

2. Resuspend the cell pellet in an appropriate volume of cold 1X Red Blood Cell Removal Solution:
    a. For the whole cortex (100-1000 mg): 1 ml. Do not vortex.
3. Incubate for 10 min. in the fridge (4˚C).
4. Add an appropriate amount of cold PB buffer:
    a. For the whole cortex (100-1000 mg): 10 ml.
5. Centrifuge at 1000 × g for 10 min. at 4˚C. Aspirate supernatant completely.

Myelin Removal

1. Resuspend the pellet from the previous step with an appropriate volume of cold PB buffer.
    a. For cortex: 720 µl.
    b. For hippocampus and smaller tissues: 100 µl.
2. Add an appropriate volume of Myelin Removal Beads.
    a. For cortex: 80 µl.
    b. For hippocampus and smaller tissues: 10 µl.
3. Mix well with a pipette and incubate for 15 min. in the fridge (4˚C).
4. Wash cells by adding an appropriate volume of cold PB buffer.
    a. For cortex: 7.2 ml.
    b. For hippocampus and smaller tissues: 1 ml.
5. Centrifuge at 300 × g for 10 min. at 4˚C. Aspirate the supernatant completely.
6. Place pre-cooled MS columns on the MACS separator attached to the magnetic stand. Wash the column with 1 ml of PB buffer.
7. Put an empty 15 ml Falcon collection tube on ice and place it under the MS column to collect the myelin negative cells (flowthrough). These cells will be further processed to isolate astrocytes.
8. Resuspend the pellet in 500 µl of cold PB buffer and apply the cell suspension onto the column. Avoid bubble formation.
9. As soon as the column is empty, start washing steps by adding 500 µl of cold PB buffer. Perform this step 3 times.
10. Collect the cells in the flowthrough. Centrifuge at 300 × g for 10 min. at 4˚C. Aspirate supernatant completely.

ACSA-2 Positive Cell Isolation

1. Resuspend the pellet in 80 µl of cold PB buffer.
2. Add 10 µl of FcR blocking reagent. Mix well with a pipette and incubate for 15 min. in the fridge (4˚C).
3. Add 10 µl of Anti-ACSA-2 Micro Beads. Mix well with a pipette and incubate for 15 min. in the fridge (4˚C).
4. Wash the cells by adding 1 ml PB buffer and centrifuge at 300 × g for 10 min. at 4˚C. Aspirate supernatant completely.
5. Place pre-cooled MS columns on the MACS separator attached to the magnetic stand. Wash the column with 1 ml of PB buffer.
6. Resuspend the pellet in 500 µl of cold PB buffer and apply the cell suspension onto the column. Avoid bubble formation.
7. As soon as the column is empty, start washing steps by adding 500 µl of cold PB buffer. Perform this step 3 times.
8. Remove the MS column from the MACS separator and place it on a 15 ml Falcon tube.
9. Add 500 µl of cold PB buffer onto the column. Immediately flush out the magnetically labelled cells by firmly pushing the plunger into the column.
10. Centrifuge at 300 × g for 10 min. at 4˚C. Aspirate supernatant completely.
11. Wash the pellet with 500 µl of cold DPBS and centrifuge at 300 × g for 5 min. at 4˚C. Aspirate supernatant completely.
12. Add 350 µl of RLT buffer containing β-mercaptoethanol (Add 10 µl of β-ME per 1 ml of RLT buffer). Mixed well and transfer into nonstick, RNase-free, 1.5 ml tubes. Store the cells at -80˚C.

5.3. Supplementary Tables

Table S1. List of Antibodies. The table represents information for the antibodies used in section 3.1 and section 3.3, including the working concentration for each technique and the thesis section, which was used. IF: immunofluorescence, WB: western blot.

Antibody Name	Supplier Name	Article Number	Final Concentration	Thesis Section
Anti-NeuN Antibody, clone A60	Merck-Millipore	MAB377	5 µg/ml (FACS)	3.1.2 3.1.3.2
Goat anti-Mouse IgG Secondary Antibody, Alexa Fluor 594	Thermo-Fisher	A11005	4 µg/ml (FACS)	3.1.2 3.1.3.2
Mouse IgG1 [B11/6] - Isotype Control	Abcam	ab91353	5 µg/ml (FACS)	3.1.2 3.1.3.2
Sox9	Abcam	ab185966	12 µg/ml (IF) 12 µg/ml (FACS)	3.1.3.1 3.1.3.2
Goat anti-Rabbit IgG Highly Cross-Adsorbed Secondary Antibody, Alexa Fluor 568	Thermo-Fisher	A-11036	8 µg/ml (IF)	3.1.3.1
Goat anti-Rabbit IgG Highly Cross-Adsorbed Secondary Antibody, PE	Thermo-Fisher	P-2771MP	4 µg/ml (FACS)	3.1.3.2
Uncoupled rabbit monoclonal [EPR25A] - isotype control	Abcam	ab172730	12 µg/ml (FACS)	3.1.3.2
Human SOX9 Antibody	R&D	AF3075-SP	2 µg/ml (FACS)	3.1.3.2
APC-donkey anti-goat IgG	Jackson Immuno	705-136-147	1 µg/ml (FACS)	3.1.3.2
Normal Goat IgG Control - isotype control	R&D	AB-108-C	2 µg/ml (FACS)	3.1.3.2
Anti-Gli1	Abcam	ab151796	10 µg/ml (FACS)	3.1.3.2
Anti-Gli3	Thermo-Fisher	PA5-28029	10 µg/ml (FACS)	3.1.3.2
Rabbit IgG, polyclonal - isotype control	Abcam	ab37415	10 µg/ml (FACS)	3.1.3.2
Goat anti-Mouse IgG Highly Cross-Adsorbed Secondary Antibody, Alexa Fluor 488	Thermo-Fisher	A11029	4 µg/ml (FACS)	3.1.3.2 3.1.5.2
Alexa Fluor® 488 Anti-SOX9 antibody	Abcam	ab196450	5 µg/ml (FACS)	3.1.3.2 3.1.4
Rabbit IgG, monoclonal [EPR25A] - Isotype Control	Abcam	ab199091	5 µg/ml (FACS)	3.1.3.2 3.1.4

Recombinant Alexa Fluor® 647 Anti-SOX9 antibody [EPR14335]	Abcam	ab196184	5 µg/ml (FACS)	3.1.5
Connexin 43 Monoclonal Antibody, monoclonal mouse IgG1 (CX-1B1)	Thermo-Fisher	13-8300	5 µg/ml (FACS)	3.1.5.2
Mouse IgG1, Kappa Monoclonal [B11/6] - Isotype Control	Abcam	ab91353	5 µg/ml (FACS)	3.1.5.2
Anti-EAAT2, mouse monoclonal	Santa Cruz	sc-365634	0.2 µg/ml (WB)	3.3.1.4.1
OATP14 Polyclonal antibody	Protein-tech	17163-1-AP	0.6 µg/ml (WB)	3.3.1.4.1
Anti-SLC4A4/NBC antibody	Abcam	ab56215	1 µg/ml (WB)	3.3.1.4.1
ZIP12 Polyclonal Antibody	Thermo-Fisher	PA5-90883	2.75 µg/ml (WB)	3.3.1.4.1
Monoclonal Anti-SLC25A18 antibody	Sigma	SAB1403390	1 µg/ml (WB)	3.3.1.4.1
β-Actin (8H10D10) Mouse monoclonal antibody	Cell Signaling	3700	0.5 µg/ml (WB)	3.3.1.4.1
Goat anti-Mouse IgG (H+L) Secondary Antibody, HRP	Thermo-Fisher	62-6520	0.75 µg/ml (WB)	3.3.1.4.1
Goat anti-Rabbit IgG (H+L) Secondary Antibody, HRP	Thermo-Fisher	62-6120	0.5 µg/ml (WB)	3.3.1.4.1

Table S2. Published Transcriptional Studies of MDD. The table represents previous studies reporting DEGs, which were enriched in astrocytes. dlPFC: dorsolateral prefrontal cortex, ACC: anterior cingulate cortex, vmPFC: ventromedial prefrontal cortex, OFC; orbitofrontal cortex, PFC: prefrontal cortex, snRNA-seq: single nucleus RNA sequencing. Cell-type-specific analysis was conducted by Dr. Michal Slezak.

Author Name	Published Year	Sequencing Technique	Brain Region	Astrocyte-enriched DEGs #
Evans S. J.	2004	Microarray	dlPFC, ACC	2
Choudary P. V.	2005	Microarray	dlPFC, ACC	3
Klempan T. A.	2009	Microarray	vmPFC, dlPFC	3
Ernst C.	2011	Microarray	dlPFC	27
Bernard R.	2011	Microarray	Locus coeruleus	8
Sequeira	2012	Microarray	dlPFC, ACC, nucleus accumbus	17

Darby M. M.	2016	RNA-seq	OFC, hippocampus	1
Labonte B.	2017	RNA-seq	PFC	43
Gandal M. J.	2018	Microarray, GWAS	Cortex	7
Nagy and Maitra	2020	snRNA-seq	dlPFC	8

Table S3. List of DEGs in CX43+ Population. The table represents genes differentially expressed in the CX43+ nuclei population in MDD. A total of 260 genes were significantly differentially expressed (FDR < 0.1) in the CX43+ nuclei population. FDR: False discovery rate. The analysis was performed by Intelliseq.

Gene ID	Gene Name	Gene Biotype	Log(FC)	FDR
ENSG00000164089	*ETNPPL*	protein coding	-3.03019	0.004258
ENSG00000121742	*GJB6*	protein coding	-2.54582	0.017294
ENSG00000139155	*SLCO1C1*	protein coding	-2.48772	0.001225
ENSG00000234377	*OBI1-AS1*	lncRNA	-2.27834	0.004486
ENSG00000103740	*ACSBG1*	protein coding	-2.24101	0.000763
ENSG00000117525	*F3*	protein coding	-2.1702	0.00303
ENSG00000211448	*DIO2*	protein coding	-2.15935	0.022274
ENSG00000251372	*LINC00499*	lncRNA	-2.12454	0.006033
ENSG00000182902	*SLC25A18*	protein coding	-2.04688	0.006033
ENSG00000156049	*GNA14*	protein coding	-2.00543	0.000763
ENSG00000136160	*EDNRB*	protein coding	-2.00327	0.015957
ENSG00000110436	*SLC1A2*	protein coding	-1.9821	0.000202
ENSG00000170425	*ADORA2B*	protein coding	-1.91845	0.000187
ENSG00000169006	*NTSR2*	protein coding	-1.91068	0.072162
ENSG00000134716	*CYP2J2*	protein coding	-1.89529	0.00679
ENSG00000170989	*S1PR1*	protein coding	-1.89522	0.051062
ENSG00000101198	*NKAIN4*	protein coding	-1.87069	0.008238
ENSG00000113721	*PDGFRB*	protein coding	-1.82248	0.006954
ENSG00000177133	*PRDM16-DT*	lncRNA	-1.79573	0.042723
ENSG00000215612	*HMX1*	protein coding	-1.77061	0.087533
ENSG00000135821	*GLUL*	protein coding	-1.75478	0.001164
ENSG00000140545	*MFGE8*	protein coding	-1.74644	0.003647
ENSG00000136378	*ADAMTS7*	protein coding	-1.72737	0.009045
ENSG00000161509	*GRIN2C*	protein coding	-1.71381	0.009045
ENSG00000100968	*NFATC4*	protein coding	-1.68878	0.034315

ENSG00000235180	*LINC00601*	lncRNA	-1.66519	0.008512
ENSG00000126785	*RHOJ*	protein coding	-1.65891	0.000507
ENSG00000116016	*EPAS1*	protein coding	-1.6566	0.00226
ENSG00000285082	*AL160272.2*	protein coding	-1.64758	0.021669
ENSG00000286387	*AC007432.1*	lncRNA	-1.62209	0.009665
ENSG00000068078	*FGFR3*	protein coding	-1.60028	0.062348
ENSG00000249240	*AC069368.1*	protein coding	-1.57929	0.023006
ENSG00000231246	*AL445426.1*	lncRNA	-1.5704	0.090129
ENSG00000286364	*AL512308.1*	lncRNA	-1.56187	0.061962
ENSG00000072952	*MRVI1*	protein coding	-1.55905	0.039662
ENSG00000124440	*HIF3A*	protein coding	-1.5557	0.008605
ENSG00000271904	*AC091826.3*	lncRNA	-1.5347	0.002453
ENSG00000250166	*AC053513.1*	lncRNA	-1.523	0.041842
ENSG00000134508	*CABLES1*	protein coding	-1.52296	0.000763
ENSG00000277196	*AC007325.2*	protein coding	-1.49885	0.019447
ENSG00000136235	*GPNMB*	protein coding	-1.48869	0.087533
ENSG00000135540	*NHSL1*	protein coding	-1.48817	0.061962
ENSG00000288542	*AL133318.1*	lncRNA	-1.48399	0.065161
ENSG00000064655	*EYA2*	protein coding	-1.47704	0.008647
ENSG00000287069	*AC061958.1*	lncRNA	-1.4764	0.090129
ENSG00000236790	*LINC00299*	lncRNA	-1.47064	0.02369
ENSG00000184232	*OAF*	protein coding	-1.45887	0.010584
ENSG00000235538	*AL078602.1*	lncRNA	-1.44695	0.097448
ENSG00000105852	*PON3*	protein coding	-1.43668	0.062605
ENSG00000179399	*GPC5*	protein coding	-1.43382	0.006033
ENSG00000116132	*PRRX1*	protein coding	-1.42207	4.01E-05
ENSG00000287277	*AL392086.3*	lncRNA	-1.41233	0.041117
ENSG00000105894	*PTN*	protein coding	-1.39517	0.000187
ENSG00000064787	*BCAS1*	protein coding	-1.39508	0.072162
ENSG00000136297	*MMD2*	protein coding	-1.37744	0.00226
ENSG00000287862	*AC114971.1*	lncRNA	-1.37417	0.069235
ENSG00000127249	*ATP13A4*	protein coding	-1.37099	0.013911
ENSG00000126878	*AIF1L*	protein coding	-1.36699	0.094277
ENSG00000186193	*SAPCD2*	protein coding	-1.3616	0.07449
ENSG00000109099	*PMP22*	protein coding	-1.35425	0.072103
ENSG00000134569	*LRP4*	protein coding	-1.34027	0.030636
ENSG00000144119	*C1QL2*	protein coding	-1.32003	0.019117

ENSG00000080493	*SLC4A4*	protein coding	-1.30962	0.003647
ENSG00000188770	*OPTC*	protein coding	-1.30362	0.062348
ENSG00000189058	*APOD*	protein coding	-1.28283	0.017294
ENSG00000119927	*GPAM*	protein coding	-1.2807	0.044627
ENSG00000251165	*F11-AS1*	lncRNA	-1.27687	0.037159
ENSG00000089472	*HEPH*	protein coding	-1.26195	0.072785
ENSG00000147509	*RGS20*	protein coding	-1.25729	0.028269
ENSG00000173546	*CSPG4*	protein coding	-1.25403	0.021792
ENSG00000225329	*LHFPL3-AS2*	lncRNA	-1.25078	0.067756
ENSG00000141756	*FKBP10*	protein coding	-1.24803	0.096604
ENSG00000118094	*TREH*	protein coding	-1.24731	0.045004
ENSG00000248528	*LINC02058*	lncRNA	-1.23455	0.079945
ENSG00000178722	*C5orf64*	lncRNA	-1.22564	0.023377
ENSG00000264015	*AC124254.2*	lncRNA	-1.2213	0.091777
ENSG00000148175	*STOM*	protein coding	-1.21991	0.045634
ENSG00000103196	*CRISPLD2*	protein coding	-1.21291	0.044063
ENSG00000168874	*ATOH8*	protein coding	-1.20936	0.070985
ENSG00000163884	*KLF15*	protein coding	-1.20568	0.006329
ENSG00000185942	*NKAIN3*	protein coding	-1.20045	0.000763
ENSG00000285867	*BX470102.2*	lncRNA	-1.19983	0.056373
ENSG00000287127	*AC009879.4*	lncRNA	-1.19569	0.028269
ENSG00000011201	*ANOS1*	protein coding	-1.19114	0.03609
ENSG00000188783	*PRELP*	protein coding	-1.18926	0.034315
ENSG00000226476	*LINC01748*	lncRNA	-1.1771	0.040041
ENSG00000164741	*DLC1*	protein coding	-1.15668	0.001164
ENSG00000183963	*SMTN*	protein coding	-1.14168	0.003937
ENSG00000231252	*AC099792.1*	lncRNA	-1.13854	0.071317
ENSG00000100399	*CHADL*	protein coding	-1.13686	0.072103
ENSG00000186583	*SPATC1*	protein coding	-1.13429	0.071317
ENSG00000144749	*LRIG1*	protein coding	-1.1335	0.048949
ENSG00000038427	*VCAN*	protein coding	-1.12506	0.023377
ENSG00000125462	*C1orf61*	protein coding	-1.12445	0.001266
ENSG00000115468	*EFHD1*	protein coding	-1.12009	0.078355
ENSG00000145794	*MEGF10*	protein coding	-1.11972	0.078369
ENSG00000167191	*GPRC5B*	protein coding	-1.11499	0.009045
ENSG00000226994	*AC012593.1*	lncRNA	-1.11461	0.044063
ENSG00000106278	*PTPRZ1*	protein coding	-1.08566	0.035975

ENSG00000116962	*NID1*	protein coding	-1.0783	0.084535
ENSG00000154493	*C10orf90*	protein coding	-1.07656	0.072103
ENSG00000150760	*DOCK1*	protein coding	-1.07562	0.082483
ENSG00000056736	*IL17RB*	protein coding	-1.07412	0.001266
ENSG00000287158	*AC117464.1*	lncRNA	-1.07179	0.086343
ENSG00000227036	*LINC00511*	lncRNA	-1.04553	0.00679
ENSG00000100906	*NFKBIA*	protein coding	-1.04365	0.09542
ENSG00000179403	*VWA1*	protein coding	-1.0414	0.018438
ENSG00000005513	*SOX8*	protein coding	-1.04122	0.059605
ENSG00000148672	*GLUD1*	protein coding	-1.03941	0.022783
ENSG00000107104	*KANK1*	protein coding	-1.03825	0.049341
ENSG00000134873	*CLDN10*	protein coding	-1.02823	0.017684
ENSG00000287550	*AL450345.2*	lncRNA	-1.02441	0.090626
ENSG00000117834	*SLC5A9*	protein coding	-1.02236	0.046882
ENSG00000163431	*LMOD1*	protein coding	-1.02012	0.072103
ENSG00000101542	*CDH20*	protein coding	-0.99698	0.034315
ENSG00000101311	*FERMT1*	protein coding	-0.9923	0.082137
ENSG00000079482	*OPHN1*	protein coding	-0.97822	0.000133
ENSG00000145555	*MYO10*	protein coding	-0.97656	0.059314
ENSG00000111961	*SASH1*	protein coding	-0.97358	0.021669
ENSG00000286288	*AL109809.4*	lncRNA	-0.96597	0.015218
ENSG00000008394	*MGST1*	protein coding	-0.96482	0.090239
ENSG00000164292	*RHOBTB3*	protein coding	-0.96434	0.087533
ENSG00000129244	*ATP1B2*	protein coding	-0.96079	0.009381
ENSG00000112769	*LAMA4*	protein coding	-0.95373	0.015911
ENSG00000187527	*ATP13A5*	protein coding	-0.95252	0.020058
ENSG00000152583	*SPARCL1*	protein coding	-0.93838	0.072162
ENSG00000101938	*CHRDL1*	protein coding	-0.93253	0.000202
ENSG00000175130	*MARCKSL1*	protein coding	-0.93027	0.076314
ENSG00000114166	*KAT2B*	protein coding	-0.92623	0.009045
ENSG00000118322	*ATP10B*	protein coding	-0.92602	0.06388
ENSG00000230490	*AL139383.1*	lncRNA	-0.92491	0.015218
ENSG00000163235	*TGFA*	protein coding	-0.92229	0.049641
ENSG00000198948	*MFAP3L*	protein coding	-0.91961	0.024167
ENSG00000285755	*AC132153.1*	lncRNA	-0.91789	0.060612
ENSG00000205336	*ADGRG1*	protein coding	-0.91524	0.073234
ENSG00000189221	*MAOA*	protein coding	-0.9149	0.052217

ENSG00000120896	*SORBS3*	protein coding	-0.91477	0.072162
ENSG00000124217	*MOCS3*	protein coding	-0.90667	0.050753
ENSG00000114646	*CSPG5*	protein coding	-0.89675	0.021925
ENSG00000196132	*MYT1*	protein coding	-0.89523	0.053454
ENSG00000197977	*ELOVL2*	protein coding	-0.89025	0.026368
ENSG00000135318	*NT5E*	protein coding	-0.88297	0.013225
ENSG00000112715	*VEGFA*	protein coding	-0.87206	0.062178
ENSG00000135919	*SERPINE2*	protein coding	-0.86775	0.050687
ENSG00000135424	*ITGA7*	protein coding	-0.85799	0.072848
ENSG00000105088	*OLFM2*	protein coding	-0.85573	0.009381
ENSG00000111962	*UST*	protein coding	-0.84236	0.000815
ENSG00000198822	*GRM3*	protein coding	-0.83697	0.004164
ENSG00000081913	*PHLPP1*	protein coding	-0.83662	0.017549
ENSG00000143878	*RHOB*	protein coding	-0.836	0.040041
ENSG00000157613	*CREB3L1*	protein coding	-0.8357	0.094617
ENSG00000144040	*SFXN5*	protein coding	-0.83028	0.047899
ENSG00000185920	*PTCH1*	protein coding	-0.82577	0.036745
ENSG00000178538	*CA8*	protein coding	-0.82372	0.022978
ENSG00000249096	*LINC02362*	lncRNA	-0.82123	0.02221
ENSG00000143842	*SOX13*	protein coding	-0.81724	0.023377
ENSG00000177303	*CASKIN2*	protein coding	-0.81678	0.041388
ENSG00000181350	*LRRC75A*	protein coding	-0.81518	0.084535
ENSG00000169129	*AFAP1L2*	protein coding	-0.80472	0.084535
ENSG00000134215	*VAV3*	protein coding	-0.80466	0.038601
ENSG00000127946	*HIP1*	protein coding	-0.8045	0.015911
ENSG00000139291	*TMEM19*	protein coding	-0.80018	0.037238
ENSG00000183762	*KREMEN1*	protein coding	-0.78804	0.086343
ENSG00000157890	*MEGF11*	protein coding	-0.78022	0.072103
ENSG00000104833	*TUBB4A*	protein coding	-0.77641	0.072162
ENSG00000186998	*EMID1*	protein coding	-0.77607	0.082137
ENSG00000072134	*EPN2*	protein coding	-0.76897	0.008512
ENSG00000130287	*NCAN*	protein coding	-0.76425	0.023533
ENSG00000103175	*WFDC1*	protein coding	-0.75392	0.093199
ENSG00000134824	*FADS2*	protein coding	-0.75031	0.072103
ENSG00000150625	*GPM6A*	protein coding	-0.74923	0.006852
ENSG00000109472	*CPE*	protein coding	-0.74447	0.023087
ENSG00000109458	*GAB1*	protein coding	-0.73278	0.079825

ENSG00000137177	*KIF13A*	protein coding	-0.72651	0.00401
ENSG00000141314	*RHBDL3*	protein coding	-0.72496	0.062605
ENSG00000136114	*THSD1*	protein coding	-0.71696	0.071343
ENSG00000145284	*SCD5*	protein coding	-0.71575	0.007648
ENSG00000130449	*ZSWIM6*	protein coding	-0.71503	0.072162
ENSG00000182667	*NTM*	protein coding	-0.71209	0.034938
ENSG00000019144	*PHLDB1*	protein coding	-0.70523	0.082483
ENSG00000141179	*PCTP*	protein coding	-0.70346	0.079689
ENSG00000179314	*WSCD1*	protein coding	-0.69746	0.087533
ENSG00000187068	*C3orf70*	protein coding	-0.69738	0.006329
ENSG00000140470	*ADAMTS17*	protein coding	-0.6875	0.031768
ENSG00000198768	*APCDD1L*	protein coding	-0.6871	0.082483
ENSG00000179241	*LDLRAD3*	protein coding	-0.68578	0.017294
ENSG00000196230	*TUBB*	protein coding	-0.68191	0.079713
ENSG00000152492	*CCDC50*	protein coding	-0.67112	0.072785
ENSG00000123595	*RAB9A*	protein coding	-0.66034	0.035975
ENSG00000162512	*SDC3*	protein coding	-0.66025	0.008512
ENSG00000187398	*LUZP2*	protein coding	-0.64985	0.047827
ENSG00000173674	*EIF1AX*	protein coding	-0.64783	0.072785
ENSG00000130787	*HIP1R*	protein coding	-0.63985	0.097473
ENSG00000135916	*ITM2C*	protein coding	-0.63952	0.009381
ENSG00000204899	*MZT1*	protein coding	-0.63706	0.086589
ENSG00000214941	*ZSWIM7*	protein coding	-0.6169	0.051715
ENSG00000010810	*FYN*	protein coding	-0.60277	0.062348
ENSG00000047365	*ARAP2*	protein coding	-0.59857	0.072103
ENSG00000104419	*NDRG1*	protein coding	-0.5695	0.049341
ENSG00000197965	*MPZL1*	protein coding	-0.55205	0.048949
ENSG00000170903	*MSANTD4*	protein coding	-0.55057	0.000569
ENSG00000136802	*LRRC8A*	protein coding	-0.54809	0.072103
ENSG00000172667	*ZMAT3*	protein coding	-0.54047	0.032236
ENSG00000167291	*TBC1D16*	protein coding	-0.53917	0.090239
ENSG00000168795	*ZBTB5*	protein coding	-0.53854	0.071317
ENSG00000235501	*AC105942.1*	lncRNA	-0.53714	0.090626
ENSG00000138413	*IDH1*	protein coding	-0.51812	0.021669
ENSG00000237036	*ZEB1-AS1*	lncRNA	-0.50491	0.069235
ENSG00000204128	*C2orf72*	protein coding	-0.48309	0.079713
ENSG00000156475	*PPP2R2B*	protein coding	-0.47684	0.088272

ENSG00000164300	*SERINC5*	protein coding	-0.4682	0.087533
ENSG00000067141	*NEO1*	protein coding	-0.46766	0.048949
ENSG00000123384	*LRP1*	protein coding	-0.45457	0.069768
ENSG00000136243	*NUP42*	protein coding	-0.45043	0.078369
ENSG00000148143	*ZNF462*	protein coding	-0.4459	0.072103
ENSG00000078124	*ACER3*	protein coding	-0.44578	0.072103
ENSG00000100225	*FBXO7*	protein coding	-0.44326	0.082137
ENSG00000156973	*PDE6D*	protein coding	-0.4375	0.082782
ENSG00000113742	*CPEB4*	protein coding	-0.40322	0.071934
ENSG00000166128	*RAB8B*	protein coding	-0.38652	0.090239
ENSG00000157985	*AGAP1*	protein coding	-0.38191	0.091717
ENSG00000012983	*MAP4K5*	protein coding	-0.3647	0.044063
ENSG00000136807	*CDK9*	protein coding	0.432068	0.090239
ENSG00000168016	*TRANK1*	protein coding	0.45526	0.042723
ENSG00000206561	*COLQ*	protein coding	0.4636	0.072103
ENSG00000160072	*ATAD3B*	protein coding	0.476558	0.078369
ENSG00000179889	*PDXDC1*	protein coding	0.477791	0.045004
ENSG00000144366	*GULP1*	protein coding	0.482668	0.099614
ENSG00000105486	*LIG1*	protein coding	0.483955	0.086589
ENSG00000156873	*PHKG2*	protein coding	0.533241	0.086589
ENSG00000154262	*ABCA6*	protein coding	0.533491	0.088422
ENSG00000152503	*TRIM36*	protein coding	0.540452	0.099352
ENSG00000186094	*AGBL4*	protein coding	0.544565	0.091717
ENSG00000162929	*KIAA1841*	protein coding	0.553205	0.079344
ENSG00000122966	*CIT*	protein coding	0.553904	0.086343
ENSG00000052126	*PLEKHA5*	protein coding	0.579403	0.099156
ENSG00000255557	*AP001266.2*	lncRNA	0.58955	0.041842
ENSG00000162105	*SHANK2*	protein coding	0.614034	0.023087
ENSG00000183426	*NPIPA1*	protein coding	0.615212	0.071317
ENSG00000126522	*ASL*	protein coding	0.64455	0.071317
ENSG00000277701	*AC159540.2*	lncRNA	0.645749	0.051715
ENSG00000186862	*PDZD7*	protein coding	0.67812	0.090239
ENSG00000163617	*CCDC191*	protein coding	0.706526	0.087533
ENSG00000153246	*PLA2R1*	protein coding	0.70916	0.094191
ENSG00000124749	*COL21A1*	protein coding	0.71179	0.052883
ENSG00000106077	*ABHD11*	protein coding	0.755975	0.048949
ENSG00000267780	*AC021594.2*	lncRNA	0.762521	0.098697

ENSG00000117245	*KIF17*	protein coding	0.862621	0.067922
ENSG00000149927	*DOC2A*	protein coding	0.990685	0.052217
ENSG00000276302	*AL021997.3*	protein coding	1.160171	0.048447
ENSG00000230453	*ANKRD18B*	protein coding	1.179536	0.037238
ENSG00000026559	*KCNG1*	protein coding	1.256528	0.00242
ENSG00000159674	*SPON2*	protein coding	1.422452	0.019117
ENSG00000189275	*LINC01164*	lncRNA	1.721807	0.087533

Table S4. GO Terms Related to Biological Functions Enriched for Downregulated Genes in the CX43 Nuclei Fraction. The table represents enriched biological terms linked to downregulated genes in the DEGs-CX43 list. DAVID Bioinformatics Resources was used to perform GO analysis. Count: number of genes involved in the term. %: involved genes/total genes related to that term.

Term	Count	%	P-Value
dermatan sulfate biosynthetic process	5	2.5	4.00E-06
glycosaminoglycan metabolic process	6	3	8.00E-06
cell adhesion	16	8.1	4.20E-05
angiogenesis	11	5.6	6.50E-05
chondroitin sulfate catabolic process	4	2	3.00E-04
chondroitin sulfate biosynthetic process	4	2	1.80E-03
regulation of cell shape	7	3.5	2.50E-03
positive regulation of positive chemotaxis	3	1.5	4.90E-03
cell migration	7	3.5	6.70E-03
positive regulation of cholesterol efflux	3	1.5	7.90E-03
negative regulation of neuron projection development	4	2	8.90E-03
unsaturated fatty acid biosynthetic process	3	1.5	9.10E-03
response to drug	9	4.5	9.80E-03
regulation of small GTPase mediated signal transduction	6	3	9.90E-03
positive regulation of endothelial cell migration	4	2	1.00E-02
regulation of actin cytoskeleton organization	4	2	1.10E-02
linoleic acid metabolic process	3	1.5	1.20E-02

extracellular matrix organization	7	3.5	1.20E-02
cytoskeleton-dependent intracellular transport	3	1.5	1.30E-02
cellular response to platelet-derived growth factor stimulus	3	1.5	1.30E-02
positive regulation of platelet-derived growth factor receptor-beta signaling pathway	2	1	1.90E-02
positive regulation of skeletal muscle acetylcholine-gated channel clustering	2	1	1.90E-02
phosphatidylinositol-mediated signaling	5	2.5	2.00E-02
regulation of synaptic transmission, glutamatergic	3	1.5	2.10E-02
positive regulation of epidermal growth factor receptor signaling pathway	3	1.5	2.20E-02
peripheral nervous system development	3	1.5	2.20E-02
nervous system development	8	4	2.20E-02
positive regulation of GTPase activity	12	6.1	2.20E-02
positive regulation of cell proliferation by VEGF-activated platelet derived growth factor receptor signaling pathway	2	1	2.90E-02
retinal rod cell differentiation	2	1	2.90E-02
regulation of transcription from RNA polymerase II promoter in response to hypoxia	3	1.5	3.00E-02
vascular endothelial growth factor receptor signaling pathway	4	2	3.30E-02
small GTPase mediated signal transduction	7	3.5	3.30E-02
iron ion homeostasis	3	1.5	3.40E-02
regulation of cell migration	4	2	3.50E-02
regulation of endocytosis	3	1.5	3.60E-02
positive regulation of phosphatidylinositol 3-kinase activity	3	1.5	3.60E-02
glutamate catabolic process	2	1	3.80E-02
negative regulation of protein catabolic process	3	1.5	3.80E-02
heart morphogenesis	3	1.5	3.80E-02
lung development	4	2	3.80E-02
regulation of phosphatidylinositol 3-kinase signaling	4	2	4.00E-02
bone mineralization	3	1.5	4.30E-02
activation of cysteine-type endopeptidase activity involved in apoptotic process	4	2	4.70E-02

Table S5. GO Terms Related to Cellular Component Enriched for Downregulated Genes in the CX43 Nuclei Fraction. The table represents enriched cellular component terms linked to downregulated genes in the DEGs-CX43 list. DAVID Bioinformatics Resources was used to perform GO analysis. Count: number of genes involved in the term. %: involved genes/total genes related to that term.

Term	Count	%	P-Value
proteinaceous extracellular matrix	14	7.1	2.60E-06
lysosomal lumen	8	4	2.00E-05
cell surface	18	9.1	2.60E-05
Golgi lumen	7	3.5	3.70E-04
plasma membrane	61	30.8	5.20E-04
synaptic membrane	4	2	6.80E-04
postsynaptic density	8	4	2.30E-03
ruffle membrane	5	2.5	8.70E-03
extracellular exosome	41	20.7	8.80E-03
extracellular matrix	9	4.5	9.10E-03
integral component of plasma membrane	24	12.1	1.20E-02
extracellular vesicle	4	2	1.30E-02
focal adhesion	10	5.1	1.50E-02
integral component of membrane	65	32.8	1.80E-02
perinuclear region of cytoplasm	13	6.6	2.00E-02
intrinsic component of plasma membrane	3	1.5	3.10E-02
neuronal cell body	8	4	3.60E-02
basement membrane	4	2	4.30E-02

Table S6. GO Terms Related to Molecular Function Enriched for Downregulated Genes in the CX43 Nuclei Fraction. The table represents enriched molecular function terms linked to downregulated genes in the DEGs-CX43 list. DAVID Bioinformatics Resources was used to perform GO analysis. Count: number of genes involved in the term. %: involved genes/total genes related to that term.

Term	Count	%	P-Value
heparin binding	9	4.5	1.50E-04
extracellular matrix structural constituent	6	3	4.40E-04
GTP binding	10	5.1	1.20E-02
G-protein coupled receptor binding	4	2	1.60E-02
GTPase activator activity	8	4	1.80E-02
collagen binding	4	2	2.00E-02
phosphatidylinositol-4,5-bisphosphate 3-kinase activity	4	2	2.10E-02
extracellular matrix binding	3	1.5	2.50E-02
GTPase activity	7	3.5	2.50E-02
stearoyl-CoA 9-desaturase activity	2	1	2.80E-02
epidermal growth factor receptor binding	3	1.5	3.50E-02
vascular endothelial growth factor binding	2	1	4.70E-02

Table S7. Pathways Enriched for Downregulated Genes in the CX43 Nuclei Fraction. The table represents enriched KEGG pathways linked to downregulated genes in the DEGs-CX43 list. DAVID Bioinformatics Resources was used to perform GO analysis. Count: number of genes involved in the pathway. %: involved genes/total genes related to that pathway.

Term	Count	%	P-Value
Nitrogen metabolism	3	1.5	1.40E-02
Fatty acid metabolism	4	2	1.50E-02
Cocaine addiction	4	2	1.50E-02
Focal adhesion	7	3.5	2.30E-02
Proximal tubule bicarbonate reclamation	3	1.5	2.50E-02

Biosynthesis of unsaturated fatty acids	3	1.5	2.50E-02
Renal cell carcinoma	4	2	3.40E-02

Table S8. Gene Functional Classification for Downregulated Genes in the CX43 Nuclei Fraction. The table represents the functional annotation clustering linked to downregulated genes in the DEGs-CX43 list. DAVID Bioinformatics Resources was used to perform this analysis. The functional annotation clustering uses a grouping algorithm to report similar genes together. Enrichment score: the geometric mean (in -log scale) of member's *p-values* in a corresponding annotation cluster.

Group 1 **Enrichment Score: 4.98**
glutamate metabotropic receptor 3 (GRM3)
myelin protein zero like 1 (MPZL1)
adenosine A2b receptor (ADORA2B)
transmembrane protein 19 (TMEM19)
olfactomedin 2 (OLFM2)
WSC domain containing 1 (WSCD1)
syndecan 3 (SDC3)
coagulation factor III, tissue factor (F3)
interleukin 17 receptor B (IL17RB)
uronyl 2-sulfotransferase (UST)
leucine rich repeats and immunoglobulin like domains 1 (LRIG1)
neurotensin receptor 2 (NTSR2)
integral membrane protein 2C (ITM2C)
solute carrier family 5 member 9 (SLC5A9)
microfibrillar associated protein 3 like (MFAP3L)
solute carrier family 4 member 4 (SLC4A4)
glycoprotein nmb (GPNMB)
protein tyrosine phosphatase, receptor type Z1 (PTPRZ1)
cadherin 20 (CDH20)

APC downregulated 1 like (APCDD1L)
thrombospondin type 1 domain containing 1 (THSD1)
peripheral myelin protein 22 (PMP22)
low density lipoprotein receptor class A domain containing 3 (LDLRAD3)
alkaline ceramidase 3 (ACER3)
leucine zipper protein 2 (LUZP2)
kringle containing transmembrane protein 1 (KREMEN1)
Na+/K+ transporting ATPase interacting 4 (NKAIN4)
neurotrimin (NTM)
neogenin 1 (NEO1)
chondroitin sulfate proteoglycan 5 (CSPG5)
multiple EGF like domains 11 (MEGF11)
G protein-coupled receptor class C group 5 member B (GPRC5B)
glycoprotein M6A (GPM6A)
Na+/K+ transporting ATPase interacting 3 (NKAIN3)
Group 2 **Enrichment score: 2.81**
Opticin (OPTC)
leucine rich repeat containing 8 family member A (LRRC8A)
chondroadherin like (CHADL)
PH domain and leucine rich repeat protein phosphatase 1 (PHLPP1)
proline and arginine rich end leucine rich repeat protein (PRELP)
leucine rich repeats and immunoglobulin like domains 1 (LRIG1)
Group 3 **Enrichment score: 1.6**
RAB8B, member RAS oncogene family (RAB8B)
RAB9A, member RAS oncogene family (RAB9A)
ras homolog family member J (RHOJ)
ras homolog family member B (RHOB)

Table S9. Astrocyte Yield, RNA Quantity and Quality Comparison Between CONT and CSDS Samples. The table represents the statistical analysis for the comparison of astrocyte yield, RNA quantity, and quality between CONT and CSDS groups, shown in Fig. 3.28. SD: Standard deviation. Either t-test or Mann-Whitney test was performed when the data was not normally distributes based on the Shapiro-Wilk test.

Astrocyte Yield		
Brain Region	**Cell Number, x 10^3 ± SD**	**CONT vs CSDS, *P- value***
Hippocampus	16 ± 6.4	0.48
Hypothalamus	3.8 ± 1.3	0.89
Somatosensory Cortex	13.9 ± 9.6	0.11
Prefrontal Cortex	3.7 ± 1.4	0.06
RNA Quantity		
Brain Region	**RNA Amount, ng ± SD**	**CONT vs CSDS, *P- value***
Hippocampus	34.3 ± 15.5	0.12
Hypothalamus	18.7 ± 10.9	0.18
Somatosensory Cortex	25 ± 16.1	0.07
Prefrontal Cortex	28 ± 10.9	0.28
RNA Quality		
Brain Region	**RIN Values ± SD**	**CONT vs CSDS, *P- value***
Hippocampus	7.7 ± 0.5	0.27
Hypothalamus	7.2 ± 0.4	0.69
Somatosensory Cortex	7.8 ± 0.4	0.14
Prefrontal Cortex	7.2 ± 0.5	0.06

5.4. Supplementary Figures

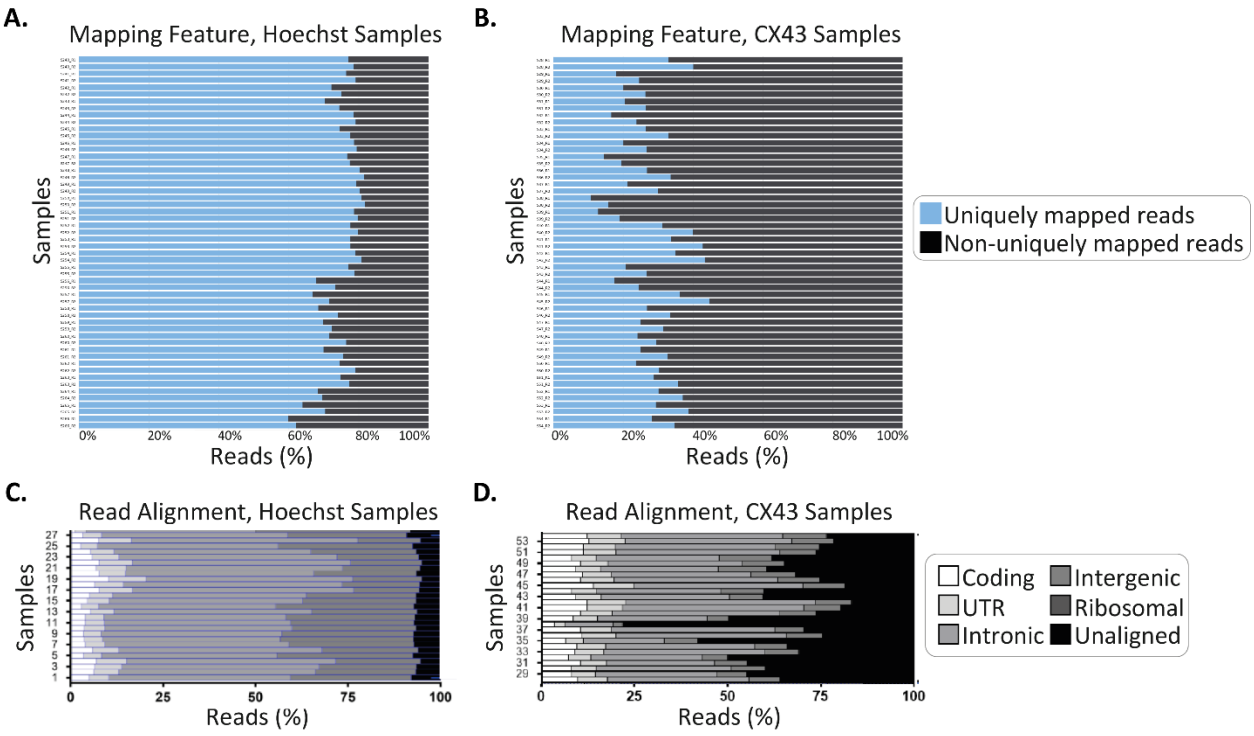

Figure S3. Quality Check of RNA Sequencing Data. Post RNA-seq quality analysis for Hoechst and CX43 samples. The analysis focused on the mapping features (**A**, **B**) representing the number of the reads that are mapped to a known sequence (assigned mapping) and the read alignments data (**C**, **D**), indicating the features of the sequenced data as coding, untranslated region (UTR), intronic, intergenic, ribosomal, and not aligned regions. Both results showed good mapping features illustrated with the high percentages of reads. The data was generated by the Computational Biology unit in Boehringer Ingelheim.

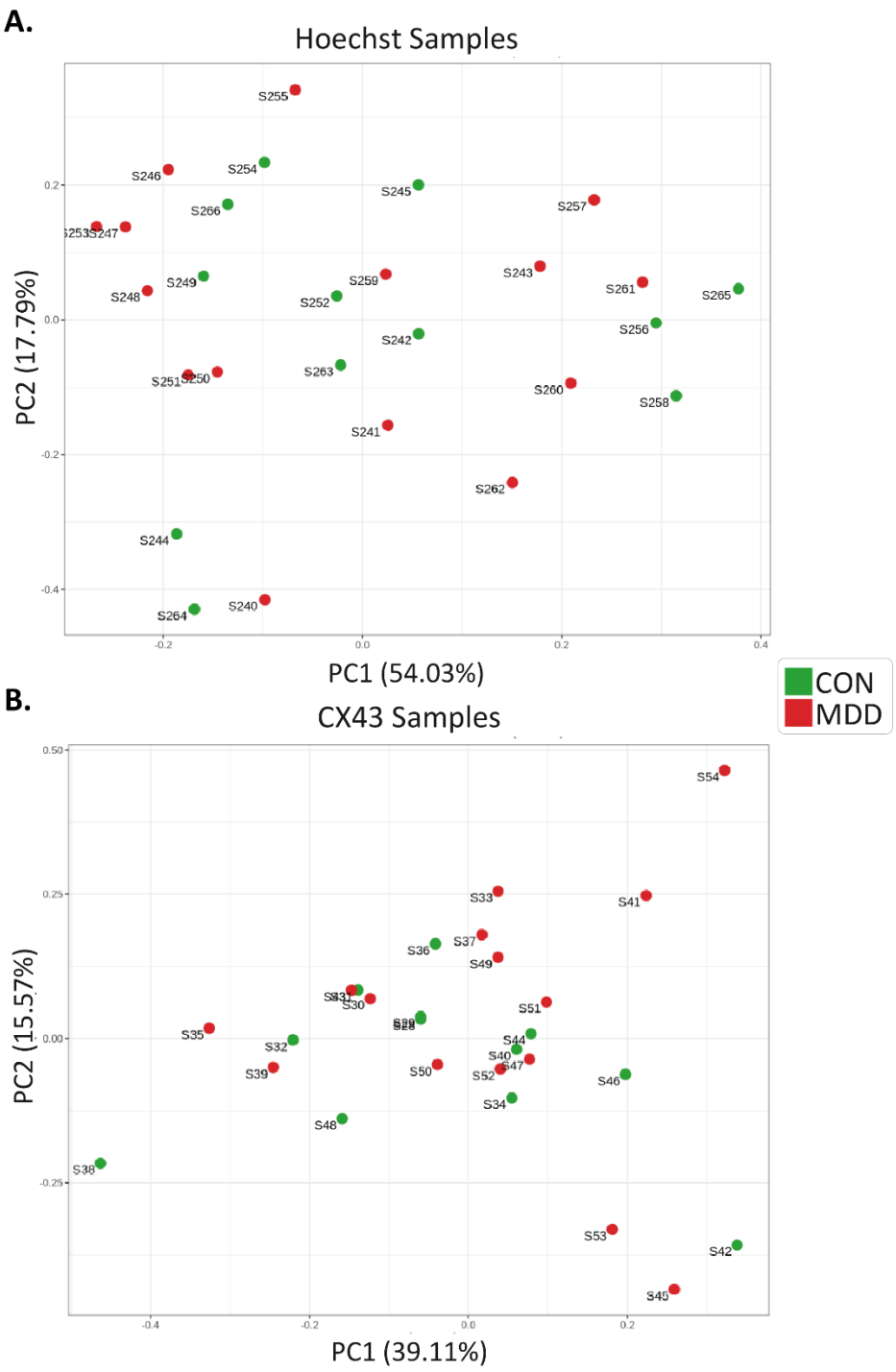

Figure S4. Principal Component Analysis for Subjects. PCA plots reveal the associations of subjects in Hoechst (**A**) and CX43 (**B**) samples. Each dot indicates a subject (green: CON, red: MDD). The proportion of variance explained is indicated in parentheses. **A.** and **B.** The subjects mostly clustered together irrespective of the study group. **A.** Possible outliers in Hoechst samples were S244, S254, and S240. **B.** Possible outliers in CX43 samples were S42, S53, and S45. Unbiased clustering through PCA did not reveal major effects of MDD on gene expression profiles. The data and PCAs were generated by Intelliseq.

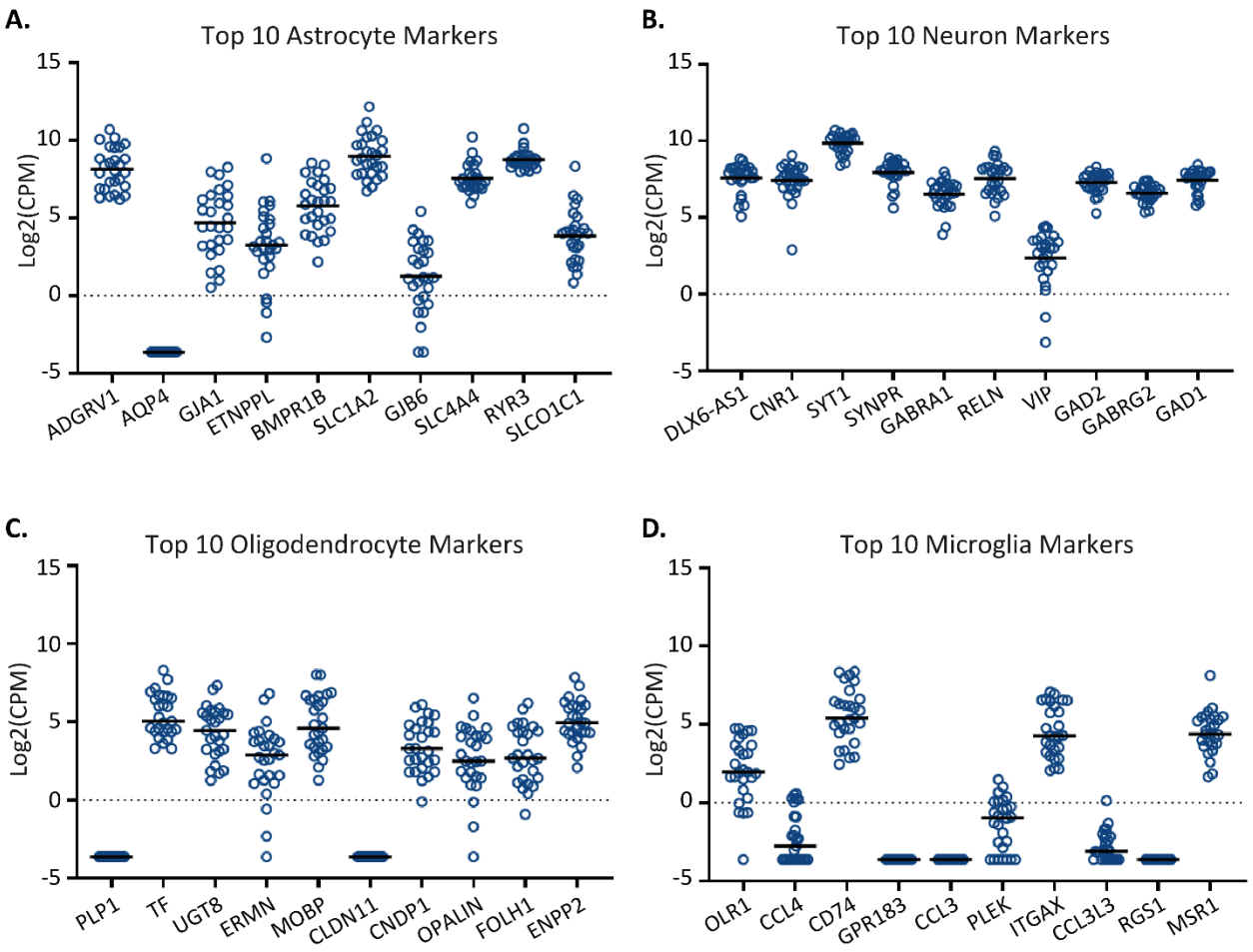

<u>Figure S5.</u> Cell-Type-Specific Gene Expression Analysis for CX43+ Nuclei Fraction. The abundance of cell-type-specific marker expression (mean Log2(CPM) value) was evaluated in the CX43+ nuclei population using transcriptomic data. The expression profiles of top 10 specific genes for human astrocytes (**A**), neurons (**B**), oligodendrocytes (**C**), and microglia (**D**). Markers were selected from McKenzie et al. (2018)[153]. CX43+ nuclei population was largely composed of astrocytes and neurons. Microglia markers were less expressed compared to other cell type-specific markers. Data from each donor is represented individually. The Log2(CPM) values were calculated by Intelliseq.

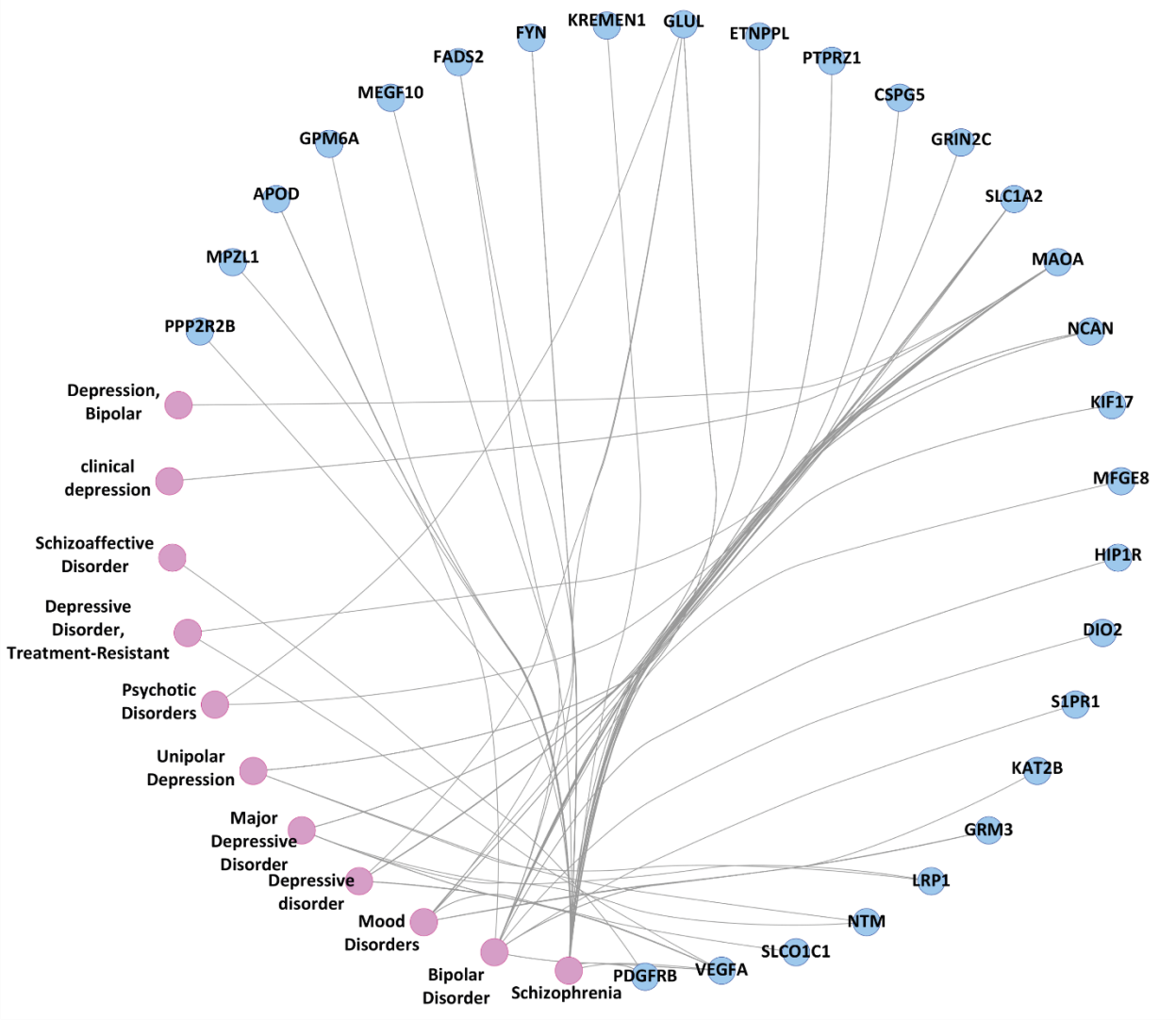

Figure S6. PsyGeNET Comparative Analysis. Psychiatric disorders and genes association network analysis revealed that 28 genes in the CX43-DEGs list were previously linked with mental disorders. A total of 10 genes in the CX43-DEGs list were associated with depression (pink). The top 5 genes linked to all the diseases are *MAOA*, *GLUL*, *VEGFA*, *SLC1A2*, and *FYN*. Cytoscape tool and DisGeNET plugin were employed for the integrative analysis.

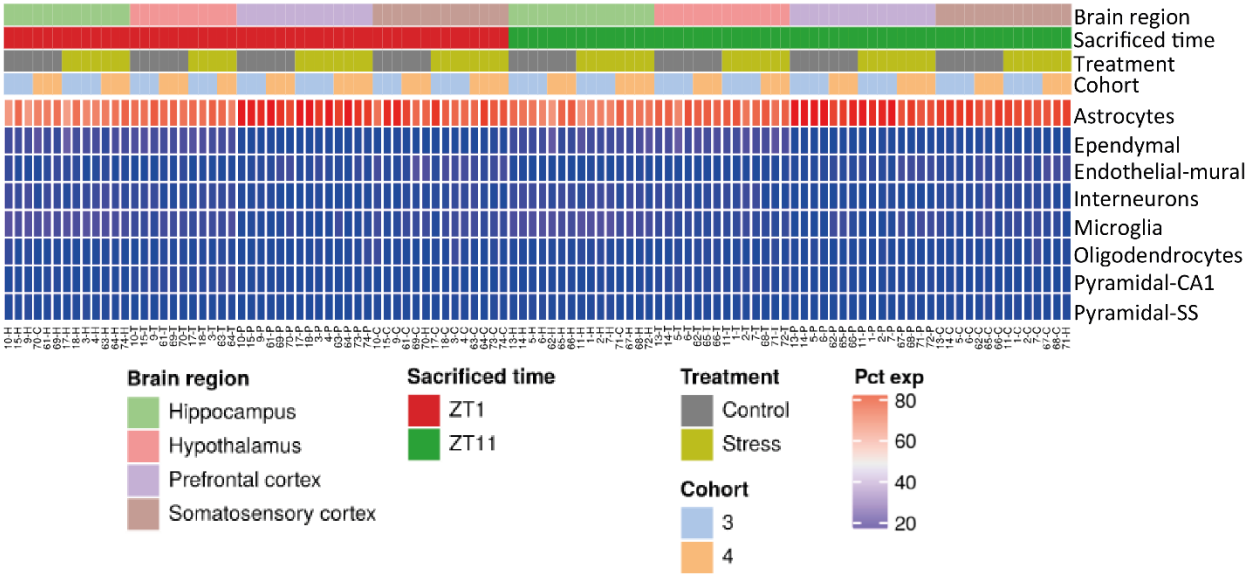

Figure S7. Analysis of Purity for MACS Isolated Astrocytes. The heatmap shows the percentage of variance explained by each cell type (rows) and sample (columns). The top 100 genes based on the database[221] from each cell type were used. MACS isolated ACSA-2+ cells displayed a strong association (> 80%) with mouse astrocytes. Brain samples were obtained at different times of the sleep-wake cycle of the animal (ZT1: 08:00 and ZT11: 18:00). The data in the heatmap consisted of cell isolation experiments conducted for two independent cohorts of mice (cohort 3 and 4). The heatmap was generated by Intelliseq. ZT: Zeitgeber time.

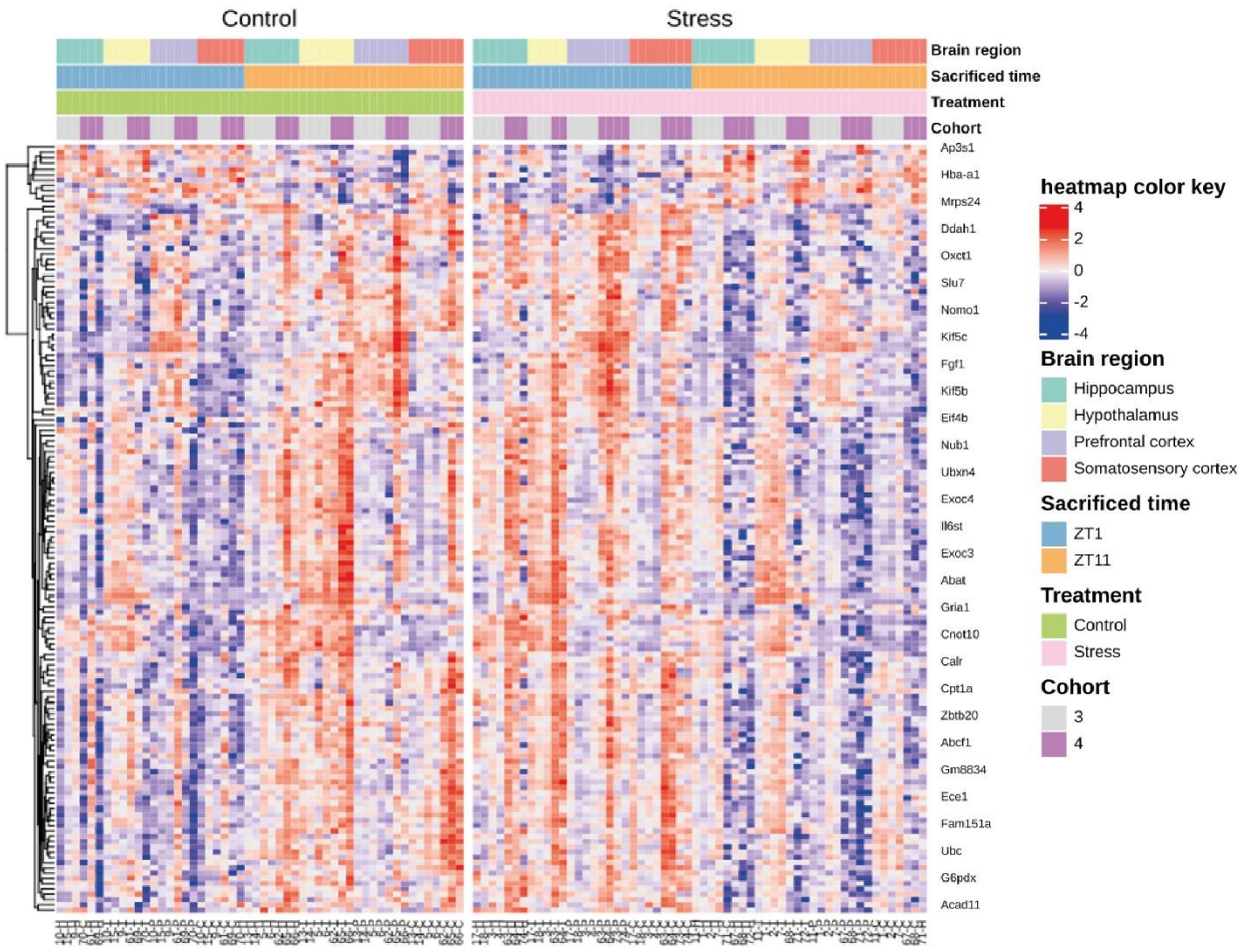

Figure S8. Heatmap for Differentially Expressed Transcripts in Mouse Astrocytes. Hierarchical clustering for differentially expressed transcripts ($P < 0.001$) per sample in each study group, CONT (green) and CSDS (pink). Representative transcript names were illustrated on the right, individual sample IDs on the bottom. Brain samples were obtained at different times of the sleep-wake cycle of the animal (ZT1: 08:00 and ZT11: 18:00). The data consisted of cell isolation experiments conducted for two independent cohorts of mice (N = 29). Heatmap color represents the normalized FPKM values (red shows high expression levels and blue shows low expression levels). The heatmap was generated by Intelliseq.

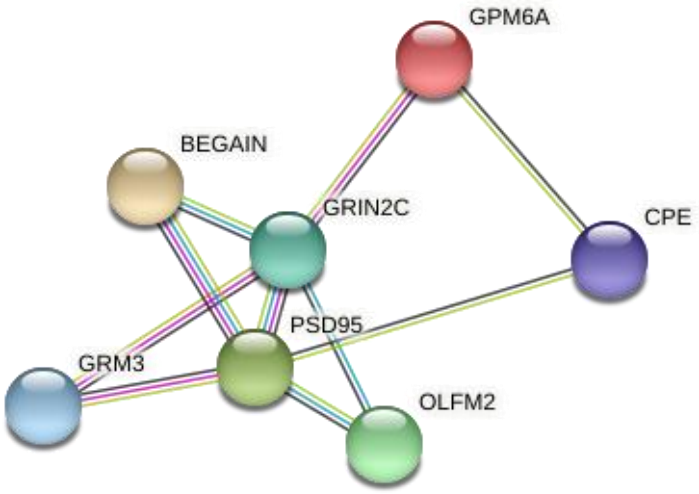

Figure S9. Protein Clustering Analysis. Interactions analysis between PSD95, BEGAIN, and the proteins in cluster A (Fig. 3.26) was conducted using the STRING clustering. The edges indicate functional and physical protein interactions. The hub protein was found as GRIN2C. The overall interaction among the proteins was significantly higher than for a random set of proteins of similar size ($P < 1.68x10^{-13}$, calculated by STRING).

BIBLIOGRAPHY

1. GBD 2017 Disease and Injury Incidence and Prevalence Collaborators. Global, regional, and national incidence, prevalence, and years lived with disability for 354 diseases and injuries for 195 countries and territories, 1990 – 2017: a systematic analysis for the Global Burden of Disease Study 2017. *Lancet* **392**, 1789–1858 (2018).
2. National Collaborating Centre for Mental Health. *Depression. The Nice Guideline on the Treatment and Management of Depression in Adults*. *National Institute for Health and Care Excellence* (2016).
3. Gaynes, B. N., Warden, D., Trivedi, M. H., Wisniewski, S. R., Fava, M. & Rush, A. J. What Did STAR∗D Teach Us? Results From a Large-Scale, Practical, Clinical Trial for Patients With Depression. *Psychiatr. Serv.* **60**, 1439–1445 (2009).
4. WHO. DEPRESSION. A Global Public Health Concern. *WHO Dep. Ment. Heal. Subst. Abus* 6–8 (2012) doi:10.1007/978-3-642-11688-9_20.
5. Dean, J. & Keshavan, M. The neurobiology of depression. *Asian J. Psychiatr.* **27**, 101–111 (2017).
6. Artigas, F., Bortolozzi, A. & Celada, P. Can we increase speed and efficacy of antidepressant treatments? Part I: General aspects and monoamine-based strategies. *Eur. Neuropsychopharmacol.* **28**, 445–456 (2018).
7. Otte, C., Gold, S. M., Penninx, B. W., Pariante, C. M., Etkin, A., Fava, M., Mohr, D. C. & Schatzberg, A. F. Major depressive disorder. *Nat. Rev. Dis. Prim.* **2**, 1–21 (2016).
8. American Psychiatric Association. Diagnostic and Statistical Manual of Mental Disorders, 5th Edition. *DSM-5* (2013).
9. Rohan, K. J., Rough, J. N., Evans, M., Ho, S., Meyerhoff, J., Roberts, L. M. & Vacek, P. M. A protocol for the Hamilton Rating Scale for Depression: Item scoring rules, Rater training, and outcome accuracy with data on its application in a clinical trial. *J. Affect. Disord.* **200**, 111–118 (2016).
10. WHO. *The ICD-10 Classification of Mental and Behavioural Disorders*. (2013).
11. Sharpley, C. F. & Bitsika, V. Validity, reliability and prevalence of four 'clinical content' subtypes of depression. *Behav. Brain Res.* **259**, 9–15 (2014).
12. McEwen, B. S., Bowles, N. P., Gray, J. D., Hill, M. N., Hunter, R. G., Karatsoreos, I. N. & Nasca, C. Mechanisms of stress in the brain. *Nat. Neurosci.* **18**, 1353–1363 (2015).
13. Koolhaas, J. M., Bartolomucci, A., Buwalda, B., de Boer, S. F., Flügge, G., Korte, S. M., Meerlo, P., Murison, R., Olivier, B., Palanza, P., Richter-Levin, G., Sgoifo, A., Steimer, T., Stiedl, O., van Dijk, G., Wöhr, M. & Fuchs, E. Stress revisited: A critical evaluation of the stress concept. *Neurosci. Biobehav. Rev.* **35**, 1291–1301 (2011).
14. Fuchs, E. & Flugge, G. Cellular consequences of stress and depression. *Dialogues Clin. Neurosci.* **6**, 171–183 (2004).
15. Hasler, G. Pathophysiology of depression: Do we have any solid evidence of interest to

clinicians? *World Psychiatry* **9**, 155–161 (2010).

16. Duman, R. S., Aghajanian, G. K., Sanacora, G. & Krystal, J. H. Synaptic plasticity and depression: new insights from stress and rapid-acting antidepressants. *Nat. Med.* **22**, 238–249 (2016).

17. Russo, S. J., Murrough, J. W., Han, M., Charney, D. S. & Nestler, E. J. Neurobiology of resilience. *Nat. Neurosci.* **15**, 1475–1484 (2012).

18. Ormel, J., Hartman, C. A. & Snieder, H. The genetics of depression: successful genome-wide association studies introduce new challenges. *Transl. Psychiatry* **9**, 1–10 (2019).

19. Yu, C., Baune, B. T., Licinio, J. & Wong, M. Whole-genome single nucleotide variant distribution on genomic regions and its relationship to major depression. *Psychiatry Res.* **252**, 75–79 (2017).

20. Jeon, S. W. & Kim, Y. Molecular Neurobiology and Promising New Treatment in Depression. *Int. J. Mol. Sci.* **17**, 1–17 (2016).

21. Saveanu, R. V & Nemeroff, C. B. Etiology of Depression: Genetic and Environmental Factors. *Psychiatr. Clin. North Am.* **35**, 51–71 (2012).

22. Caspi, A., Sugden, K., Moffitt, T. E., Taylor, A., Craig, I. W., Harrington, H. L., McClay, J., Mill, J., Martin, J., Braithwaite, A. & Poulton, R. Influence of life stress on depression: Moderation by a polymorphism in the 5-HTT gene. *Science (80-.).* **301**, 386–389 (2003).

23. Carrillo-roa, T., Labermaier, C., Weber, P., Herzog, D. P., Lareau, C., Santarelli, S., Wagner, K. V, Rex-haffner, M., Harbich, D., Scharf, S. H., Nemeroff, C. B., Dunlop, B. W., Craighead, W. E., Mayberg, H. S., Schmidt, M. V, Uhr, M., Holsboer, F., Sillaber, I., Binder, E. B., *et al.* Common genes associated with antidepressant response in mouse and man identify key role of glucocorticoid receptor sensitivity. *PLoS Biol.* **15**, 1–23 (2017).

24. Arloth, J., Bogdan, R., Weber, P., Frishman, G., Menke, A., Wagner, K. V., Balsevich, G., Schmidt, M. V., Karbalai, N., Czamara, D., Altmann, A., Trümbach, D., Wurst, W., Mehta, D., Uhr, M., Klengel, T., Erhardt, A., Carey, C. E., Conley, E. D., *et al.* Genetic Differences in the Immediate Transcriptome Response to Stress Predict Risk-Related Brain Function and Psychiatric Disorders. *Neuron* **86**, 1189–1202 (2015).

25. Klengel, T. & Binder, E. B. Gene – Environment Interactions in Major Depressive Disorder. *Can. J. Psychiatry* **58**, 76–83 (2013).

26. Yin H., and Galfavy, H., Pantazatos, S. P., Huang, Y., Rosoklija, G. B., Dwork, A. J., Burke, A., Arango, V., Oquendo, M. A. & Mann, J. J. Glucocorticoid Receptor-Related Genes: Genotype and Brain Gene Expression Relationships To Suicide And Major Depressive Disorder. *Depress. Anxiety* **33**, 531–540 (2016).

27. Smith, S. M. & Vale, W. W. The role of the hypothalamic-pituitary-adrenal axis in neuroendocrine responses to stress. *Dialogues Clin. Neurosci.* **8**, 383–395 (2006).

28. Menke, A. Is the HPA axis as target for depression outdated, or is there a new hope? *Front. Psychiatry* **10**, 1–8 (2019).

29. Almeida, D. & Turecki, G. Recent Progress in Functional Genomic Studies of Depression and Suicide. *Curr. Genet. Med. Rep.* **5**, 22–34 (2017).

30. Uchida, S., Yamagata, H., Seki, T. & Watanabe, Y. Epigenetic mechanisms of major depression: Targeting neuronal plasticity. *Psychiatry Clin. Neurosci.* **72**, 212–227 (2018).

31. Iii, H. E. C., Maze, I., Laplant, Q. C., Vialou, V. F., Ohnishi, Y. N., Berton, O., Fass, D. M., Renthal, W., Iii, A. J. R., Wu, E. Y., Ghose, S., Krishnan, V., Russo, S. J., Tamminga, C., Haggarty, S. J. & Nestler, E. J. Antidepressant Actions of Histone Deacetylase Inhibitors. *J. Neurosci.* **29**, 11451–11460 (2009).

32. Hobara, T., Uchida, S., Otsuki, K., Matsubara, T., Funato, H., Matsuo, K., Suetsugi, M. & Watanabe, Y. Altered gene expression of histone deacetylases in mood disorder patients. *J. Psychiatr. Res.* **44**, 263–270 (2010).

33. Iacono, L. Lo, Valzania, A., Viscomi, M. T., Coviello, M., Giampà, A., Roscini, L., Bisicchia, E., Siracusano, A. & Troisi, A. Adversity in childhood and depression: linked through SIRT1. *Transl. Psychiatry* **5**, 1–10 (2015).

34. Abe, N., Uchida, S., Otsuki, K., Hobara, T., Yamagata, H., Higuchi, F., Shibata, T. & Watanabe, Y. Altered sirtuin deacetylase gene expression in patients with a mood disorder. *J. Psychiatr. Res.* **45**, 1106–1112 (2011).

35. Portela, A. & Esteller, M. Epigenetic modifications and human disease. *Nat. Biotechnol.* **28**, 1057–1068 (2010).

36. Mcgowan, P. O., Sasaki, A., Alessio, A. C. D., Dymov, S., Labonte, B., Szyf, M., Turecki, G. & Meaney, M. J. Epigenetic regulation of the glucocorticoid receptor in human brain associates with childhood abuse. *Nat. Neurosci.* **12**, 342–348 (2009).

37. Nagy, C., Suderman, M., Yang, J., Szyf, M., Mechawar, N., Ernst, C. & Turecki, G. Astrocytic abnormalities and global DNA methylation patterns in depression and suicide. *Mol. Psychiatry* **20**, 320–328 (2015).

38. Howard, D. M., Adams, M. J., Clarke, T., Hafferty, J. D., Shirali, M., Coleman, J. R. I., Hagenaars, S. P., Ward, J., Whalley, C., Marioni, R. E., Porteous, D. J., Davies, G. & Deary, I. J. Genome-wide meta-analysis of depression identifies 102 independent variants and highlights the importance of the prefrontal brain regions. *Nat. Neurosci.* **22**, 343–352 (2019).

39. McIntosh, A. M., Sullivan, P. F. & Lewis, C. M. Uncovering the Genetic Architecture of Major Depression. *Neuron* **102**, 91–103 (2019).

40. Wray, N. R., Sullivan, P. F. & PGC. Genome-wide association analyses identify 44 risk variants and refine the genetic architecture of major depression. *Nat. Genet.* **50**, 668–681 (2018).

41. Choi, S. W., Mak, T. S. H. & O'Reilly, P. F. Tutorial: a guide to performing polygenic risk score analyses. *Nat. Protoc.* **15**, 2759–2772 (2020).

42. Halldorsdottir, T., Piechaczek, C., De Matos, A. P. S., Czamara, D., Pehl, V., Wagenbuechler, P., Feldmann, L., Quickenstedt-Reinhardt, P., Allgaier, A. K., Freisleder, F. J., Greimel, E., Kvist, T., Lahti, J., Räikkönen, K., Rex-Haffner, M., Arnarson, E. Ö., Craighead, W. E., Schulte-Körne, G. & Binder, E. B. Polygenic risk: Predicting depression outcomes in clinical and epidemiological cohorts of youths. *Am. J. Psychiatry* **176**, 615–625 (2019).

43. Franklin, T. B. & Mansuy, I. M. The Neural Bases of Emotions. in *Neurosciences - From Molecule to Behavior: a university textbook* (eds. C., G. & PM., L.) 525–552 (Springer Spektrum, Berlin, Heidelberg, 2013). doi:10.1007/978-3-642-10769-6.

44. Pariante, C. M. & Lightman, S. L. The HPA axis in major depression: classical theories and new developments. *Cell Press* **31**, 464–468 (2008).

45. Koning, A. C. A. M., Buurstede, J. C., Weert, L. T. C. M. Van & Meijer, O. C. Glucocorticoid and Mineralocorticoid Receptors in the Brain: A Transcriptional Perspective. *J. Endocr. Soc.* **3**, 1917–1930 (2019).

46. Mckay, M. S. & Zakzanis, K. K. The impact of treatment on HPA axis activity in unipolar major depression. *J. Psychiatr. Res.* **44**, 183–192 (2010).

47. Menke, A., Arloth, J., Putz, B., Weber, P., Klengel, T., Mehta, D., Gonik, M., Rex-haffner, M., Rubel, J., Uhr, M., Lucae, S., Deussing, J. M., Holsboer, F. & Binder, E. B. Dexamethasone Stimulated Gene Expression in Peripheral Blood is a Sensitive Marker for Glucocorticoid Receptor Resistance in Depressed Patients. *Neuropsychologia* **37**, 1455–1464 (2012).

48. Nutt, D., Wilson, S. & Paterson, L. Sleep disorders as core symptoms of depression. *Dialogues Clin. Neurosci.* **10**, 329–336 (2008).

49. Fang, H., Tu, S., Sheng, J. & Shao, A. Depression in sleep disturbance: A review on a bidirectional relationship, mechanisms and treatment. *J. Cell. Mol. Med.* **23**, 2324–2332 (2019).

50. Wirz-Justice, A., Benedetti, F., Berger, M., Lam, R. W., Martiny, K. & Terman, M. Chronotherapeutics (light and wake therapy) in affective disorders*. in *Psychological Medicine* vol. 35 939–944 (2005).

51. Cunningham, J. E. A., Stamp, J. A. & Shapiro, C. M. Sleep and major depressive disorder: a review of non-pharmacological chronotherapeutic treatments for unipolar depression. *Sleep Med.* **61**, 6–18 (2019).

52. Andrews, P. W., Bharwani, A., Lee, K. R., Fox, M. & Thomson, J. A. Is serotonin an upper or a downer? The evolution of the serotonergic system and its role in depression and the antidepressant response. *Neurosci. Biobehav. Rev.* **51**, 164–188 (2015).

53. Savitz, J. B. & Drevets, W. C. Neuroreceptor imaging in depression. *Neurobiol. Dis.* **52**, 49–65 (2013).

54. Meyer, J. H., Ginovart, N., Boovariwala, A., Sagrati, S., Hussey, D., Garcia, A., Young, T., Praschak-Rieder, N., Wilson, A. A. & Houle, S. Elevated Monoamine Oxidase A Levels in the Brain. *Arch. Gen. Psychiatry* **63**, 1209–1216 (2006).

55. Elhwuegi, A. S. Central monoamines and their role in major depression. *Prog. Neuropsychopharmacol. Biol. Psychiatry* **28**, 435–451 (2004).

56. Johnson, S., Stockmeier, C. A., Meyer, J. H., Austin, M. C., Albert, P. R., Wang, J., May, W. L., Rajkowska, G., Overholser, J. C., Jurjus, G., Dieter, L., Johnson, C., Sittman, D. B. & Ming Ou, X. The Reduction of R1, a Novel Repressor Protein for Monoamine Oxidase A, in Major Depressive Disorder. *Neuropsychopharmacology* **36**, 2139–2148 (2011).

57. Belujon, P. & Grace, A. A. Dopamine System Dysregulation in Major Depressive Disorders. *Int. J. Neuropsychopharmacol.* **20**, 1036–1046 (2017).

58. Leggio, G. M., Salomone, S., Bucolo, C., Platania, C., Micale, V., Caraci, F. & Drago, F. Dopamine D3 receptor as a new pharmacological target for the treatment of depression. *Eur. J. Pharmacol.* **719**, 25–33 (2013).

59. Admon, R., Kaiser, R. H., Dillon, D. G., Beltzer, M., Goer, F., Olson, D. P., Vitaliano, G. & Pizzagalli, D. A. Dopaminergic enhancement of striatal response to reward in major depression. *Am. J. Psychiatry* **174**, 378–386 (2017).

60. Grant, P. Neurotransmitters. in *International Encyclopedia of the Social & Behavioral Sciences, 2nd edition* vol. 16 749–754 (2015).

61. Moret, C. & Briley, M. The importance of norepinephrine in depression. *Neuropsychiatr. Dis. Treat.* **7**, 9–13 (2011).

62. Goddard, A. W., Ball, S. G., Martinez, J., Robinson, M. J., Yang, C. R., Russell, J. M. & Shekhar, A. Current perspectives of the roles of the central norepinephrine system in anxiety and depression. *Depress. Anxiety* **27**, 339–350 (2010).

63. Treadway, M. T. & Pizzagalli, D. A. Imaging the pathophysiology of major depressive disorder - from localist models to circuit-based analysis. *Biol. Mood Anxiety Disord.* **4**, (2014).

64. Ban, T. A. The role of serendipity in drug discovery. *Clin. Res.* 335–344 (2006).

65. Wong, M. & Licinio, J. From monoamines to genomic targets: a paradigm shift for drug discovery in depression. *Nat. Rev. Drug Discov.* **3**, 136–151 (2004).

66. Harmer, C. J., Duman, R. S. & Cowen, P. J. How do antidepressants work? New perspectives for refining future treatment approaches. *The Lancet Psychiatry* **4**, 409–418 (2017).

67. Kent, J. M. New drug classes SNaRIs, NaSSAs, and NaRIs: new agents for the treatment of depression. *Lancet* **355**, 911–918 (2000).

68. Reiner, A. & Levitz, J. Glutamatergic Signaling in the Central Nervous System: Ionotropic and Metabotropic Receptors in Concert. *Neuron* **98**, 1080–1098 (2018).

69. Sanacora, G., Zarate, C. A., Krystal, J. H. & Manji, H. K. Targeting the glutamatergic system to develop novel, improved therapeutics for mood disorders. *Nat. Rev. Drug Discov.* **7**, 426–437 (2008).

70. Li, C. T., Yang, K. C. & Lin, W. C. Glutamatergic dysfunction and glutamatergic compounds for major psychiatric disorders: Evidence from clinical neuroimaging studies. *Front. Psychiatry* **10**, 1–11 (2019).

71. Colic, L., von Düring, F., Denzel, D., Demenescu, L. R., Lord, A. R., Martens, L., Lison, S., Frommer, J., Vogel, M., Kaufmann, J., Speck, O., Li, M. & Walter, M. Rostral Anterior Cingulate Glutamine/Glutamate Disbalance in Major Depressive Disorder Depends on Symptom Severity. *Biol. Psychiatry Cogn. Neurosci. Neuroimaging* **4**, 1049–1058 (2019).

72. Bernard, R., Kerman, I. A., Thompson, R. C., Jones, E. G., Bunney, W. E., Barchas, J. D., Schatzberg, A. F., Myers, R. M., Akil, H. & Watson, S. J. Altered expression of glutamate

signaling, growth factor, and glia genes in the locus coeruleus of patients with major depression. *Mol. Psychiatry* **16**, 634–646 (2011).

73. Choudary, P. V, Molnar, M., Evans, S. J., Tomita, H., Li, J. Z., Vawter, M. P., Myers, R. M., Bunney, W. E., Akil, H., Watson, S. J. & Jones, E. G. Altered cortical glutamatergic and GABAergic signal transmission with glial involvement in depression. *PNAS* **102**, 15653–15658 (2005).

74. Ernst, C., Nagy, C., Kim, S., Yang, J. P., Deng, X., Hellstrom, I. C., Choi, K. H., Gershenfeld, H., Meaney, M. J. & Turecki, G. Dysfunction of Astrocyte Connexins 30 and 43 in Dorsal Lateral Prefrontal Cortex of Suicide Completers. *BPS* **70**, 312–319 (2011).

75. Kang, H. J., Voleti, B., Hajszan, T., Rajkowska, G., Stockmeier, C. A., Licznerski, P., Lepack, A., Majik, M. S., Jeong, L. S., Banasr, M., Son, H. & Duman, R. S. Decreased expression of synapse-related genes and loss of synapses in major depressive disorder. *Nat. Med.* **18**, 1413–1417 (2012).

76. Moda-Sava, R. N., Murdock, M. H., Parekh, P. K., Fetcho, R. N., Huang, B. S., Huynh, T. N., Witztum, J., Shaver, D. C., Rosenthal, D. L., Alway, E. J., Lopez, K., Meng, Y., Nellissen, L., Grosenick, L., Milner, T. A., Deisseroth, K., Bito, H., Kasai, H. & Liston, C. Sustained rescue of prefrontal circuit dysfunction by antidepressant-induced spine formation. *Science (80-.).* **364**, (2019).

77. Liston, C. & Gan, W. B. Glucocorticoids are critical regulators of dendritic spine development and plasticity in vivo. *PNAS* **108**, 16074–16079 (2011).

78. Shu, Y. & Xu, T. Chronic Social Defeat Stress Modulates Dendritic Spines Structural Plasticity in Adult Mouse Frontal Association Cortex. *Neural Plast.* **2017**, 1–13 (2017).

79. Lopez, J. P., Lim, R., Cruceanu, C., Crapper, L., Fasano, C., Labonte, B., Maussion, G., Yang, J. P., Yerko, V., Vigneault, E., Mestikawy, S. El, Mechawar, N., Pavlidis, P. & Turecki, G. miR-1202 is a primate-specific and brain-enriched microRNA involved in major depression and antidepressant treatment. *Nat. Med.* **20**, 764–770 (2014).

80. Petroff, O. A. C. GABA and glutamate in the human brain. *Neuroscientist* **8**, 562–573 (2002).

81. Mederos, S. & Perea, G. GABAergic-astrocyte signaling: A refinement of inhibitory brain networks. *Glia* **67**, 1842–1851 (2019).

82. Wu, C. & Sun, D. GABA receptors in brain development, function, and injury. *Metab. Brain Dis.* **30**, 367–379 (2014).

83. Karolewicz, B., MacIag, D., O'Dwyer, G., Stockmeier, C. A., Feyissa, A. M. & Rajkowska, G. Reduced level of glutamic acid decarboxylase-67 kDa in the prefrontal cortex in major depression. *Int. J. Neuropsychopharmacol.* **13**, 411–420 (2010).

84. Duman, R. S., Sanacora, G. & Krystal, J. H. Altered Connectivity in Depression: GABA and Glutamate Neurotransmitter Deficits and Reversal by Novel Treatments. *Neuron* **102**, 75–90 (2019).

85. Wang, Q., Jie, W., Liu, J. H., Yang, J.-M. & Gao, T. M. An astroglial basis of major depressive disorder ? An overview. *Glia* **65**, 1227–1250 (2017).

86. Abdallah, C. G., De Feyter, H. M., Averill, L. A., Jiang, L., Averill, C. L., Chowdhury, G. M. I., Purohit, P., de Graaf, R. A., Esterlis, I., Juchem, C., Pittman, B. P., Krystal, J. H., Rothman, D. L., Sanacora, G. & Mason, G. F. The effects of ketamine on prefrontal glutamate neurotransmission in healthy and depressed subjects. *Neuropsychopharmacology* **43**, 2154–2160 (2018).

87. Corriger, A. & Pickering, G. Ketamine and depression: A narrative review. *Drug Des. Devel. Ther.* **13**, 3051–3067 (2019).

88. Stenovec, M., Li, B., Verkhratsky, A. & Zorec, R. Astrocytes in rapid ketamine antidepressant action. *Neuropharmacology* **173**, 108158 (2020).

89. Aguilar-Valles, A., De Gregorio, D., Matta-Camacho, E., Eslamizade, M. J., Khlaifia, A., Skaleka, A., Lopez-canul, M., Torres-berrio, A., Bermudez, S., Rurak, G. M., Simard, S., Salmaso, N., Gobbi, G., Lacaille, J. & Sonenberg, N. Antidepressant actions of ketamine engage cell-specific translation via eIF4E. *Nature* **590**, 315–319 (2020).

90. Ratti, E., Bettica, P., Alexander, R., Archer, G., Carpenter, D., Evoniuk, G., Gomeni, R., Lawson, E., Lopez, M., Millns, H., Rabiner, E. A., Trist, D., Trower, M., Zamuner, S., Krishnan, R. & Fava, M. Full central neurokinin-1 receptor blockade is required for efficacy in depression: evidence from orvepitant clinical studies. *J. Psychopharmacol.* **27**, 424–434 (2013).

91. Ehrich, E., Turncliff, R., Du, Y., Leigh-pemberton, R., Fernandez, E., Jones, R. & Fava, M. Evaluation of Opioid Modulation in Major Depressive Disorder. *Neuropsychopharmacology* **40**, 1448–1455 (2015).

92. Kling, M. A., Coleman, V. H. & Schulkin, J. Glucocorticoid inhibition in the treatment of depression: can we think outside the endocrine hypothalamus? *Depress. Anxiety* **26**, 641–649 (2009).

93. Insel, T., Cuthbert, B., Garvey, M., Heinssen, R., Pine, D., Quinn, K., Sanislow, C. & Wang, P. Research Domain Criteria (RDoC): Toward a New Classification Framework for Research on Mental Disorders. *Am. J. Psychiatry* **167**, 748–751 (2010).

94. NIH. About RDoC. *National Institute for Health and Care Excellence* https://www.nimh.nih.gov/research/research-funded-by-nimh/rdoc/index.shtml (2017).

95. National Institute of Mental Health. About RDoC. Retrieved December 1, 2020. https://www.nimh.nih.gov/research/research-funded-by-nimh/rdoc/about-rdoc.shtml.

96. Anderzhanova, E., Kirmeier, T. & Wotjak, C. T. Animal models in psychiatric research: The RDoC system as a new framework for endophenotype-oriented translational neuroscience. *Neurobiol. Stress* **7**, 47–56 (2017).

97. Ross, C. A. & Margolis, R. L. Research Domain Criteria: Strengths, Weaknesses, and Potential Alternatives for Future Psychiatric Research. *Mol. Neuropsychiatry* **5**, 218–236 (2019).

98. Pandya, M., Altinay, M., Jr, D. A. M. & Anand, A. Where in the Brain Is Depression? *Curr. Psychiatry Rep.* **14**, 634–642 (2012).

99. Drevets, W. C., Price, J. L. & Furey, M. L. Brain structural and functional abnormalities in mood disorders: implications for neurocircuitry models of depression. *Brain Struct. Funct.*

213, 93–118 (2008).

100. Hamilton, J. P., Farmer, M., Fogelman, P. & Gotlib, I. H. Depressive Rumination, the Default-Mode Network, and the Dark Matter of Clinical Neuroscience. *Biol. Psychiatry* **78**, 224–230 (2015).

101. McEwen, B. S., Nasca, C. & Gray, J. D. Stress Effects on Neuronal Structure: Hippocampus, Amygdala, and Prefrontal Cortex. *Neuropsychopharmacology* **41**, 3–23 (2016).

102. Williams, L. M. Precision psychiatry: a neural circuit taxonomy for depression and anxiety. *The Lancet Psychiatry* **3**, 472–480 (2016).

103. Cole, M. W., Bassett, D. S., Power, J. D., Braver, T. S. & Petersen, S. E. Intrinsic and Task-Evoked Network Architectures of the Human Brain. *Neuron* **83**, 238–251 (2014).

104. Seghier, M. L. The angular gyrus: Multiple functions and multiple subdivisions. *Neuroscientist* **19**, 43–61 (2013).

105. Seeley, W. W., Menon, V., Schatzberg, A. F., Keller, J., Glover, G. H., Kenna, H., Reiss, A. L. & Greicius, M. D. Dissociable Intrinsic Connectivity Networks for Salience Processing and Executive Control. *J. Neurosci.* **27**, 2349–2356 (2007).

106. Kaiser, R. H., Andrews-Hanna, J. R., Wager, T. D. & Pizzagalli, D. A. Large-Scale Network Dysfunction in Major Depressive Disorder A Meta-analysis of Resting-State Functional Connectivity. *Am. Med. Assoc.* **72**, 603–611 (2015).

107. Stuhrmann, A., Suslow, T. & Dannlowski, U. Facial emotion processing in major depression: a systematic review of neuroimaging findings. *Biol. Mood Anxiety Disord.* **1**, 1–17 (2011).

108. Yang, Y., Wang, H., Hu, J. & Hu, H. Lateral habenula in the pathophysiology of depression. *Curr. Opin. Neurobiol.* **48**, 90–96 (2018).

109. Korgaonkar, M. S., Grieve, S. M., Etkin, A., Koslow, S. H. & Williams, L. M. Using Standardized fMRI Protocols to Identify Patterns of Prefrontal Circuit Dysregulation that are Common and Specific to Cognitive and Emotional Tasks in Major Depressive Disorder: First Wave Results from the iSPOT-D Study. *Neuropsychopharmacology* **38**, 863–871 (2013).

110. Gaynes, B., Lloyd, S. W., Lux, L., Gartlehner, G., Hansen, R. A., Brode, S., Jonas, D. E., Evans, T. S., Viswanathan, M. & Lohr, K. N. Repetitive Transcranial Magnetic Stimulation for Treatment-Resistant Depression: A Systematic Review and Meta-Analysis. *J. Clin. Psychiatry* **75**, 477–489 (2014).

111. Weiner, R. D. & Reti, I. M. Key updates in the clinical application of electroconvulsive therapy. *Int. Rev. Psychiatry* **29**, 54–62 (2017).

112. Group, T. U. E. R. Efficacy and safety of electroconvulsive therapy in depressive disorders: a systematic review and meta-analysis. *Lancet* **361**, 799–808 (2003).

113. Mayberg, H. S., Lozano, A. M., Voon, V., Mcneely, H. E., Seminowicz, D., Hamani, C., Schwalb, J. M. & Kennedy, S. H. Deep Brain Stimulation for Treatment-Resistant Depression. *Neuron* **45**, 651–660 (2005).

114. Riva-Posse, P., Choi, K. S., Holtzheimer, P. E., Crowell, A. L., Garlow, S. J., Rajendra, J. K., Mcintyre, C. C., Gross, R. E. & Mayberg, H. S. A connectomic approach for subcallosal cingulate deep brain stimulation surgery: prospective targeting in treatment-resistant depression. *Mol. Psychiatry* **23**, 843–849 (2018).

115. Cerqueira, J. J., Taipa, R., Uylings, H. B. M., Almeida, O. F. X. & Sousa, N. Specific configuration of dendritic degeneration in pyramidal neurons of the medial prefrontal cortex induced by differing corticosteroid regimens. *Cereb. Cortex* **17**, 1998–2006 (2007).

116. Hultman, R., D. Mague, S., Li, Q., M. Katz, B., Michel, N., Lin, L., Wang, J., K. David, L., Blount, C., Chandy, R., Carlson, D., Ulrich, K., Carin, L., Dunson, D., Kumar, S., Deisseroth, K., Moore, D. S. & Dzirasa, K. Dysregulation of prefrontal cortex-mediated slow evolving limbic dynamics drives stress-induced emotional pathology. *Neuron* **91**, 439–52 (2016).

117. Kumar, S., Hultman, R., Hughes, D., Michel, N., M. Katz, B. & Dzirasa, K. Prefrontal cortex reactivity underlies trait vulnerability to chronic social defeat stress. *Nat. Commun.* **5**, 4537 (2014).

118. Carlen, M. What constitutes the prefrontal cortex? *Science (80-.).* **353**, 478–482 (2017).

119. Myers-Schulz, B. & Koenigs, M. Functional anatomy of ventromedial prefrontal cortex: implications for mood and anxiety disorders. *Mol. Psychiatry* **17**, 132–141 (2012).

120. Delgado, M. R., Beer, J. S., Fellows, L. K., Huettel, S. A., Platt, M. L. & Quirk, G. J. Viewpoints: Dialogues on the functional role of the ventromedial prefrontal cortex. *Nat. Publ. Gr.* **19**, 1545–1552 (2016).

121. Hiser, J. & Koenigs, M. The multifaceted role of ventromedial prefrontal cortex in emotion, decision-making, social cognition, and psychopathology. *Biol. Psychiatry* **83**, 638–647 (2018).

122. Kimbrell, T. A., Ketter, T. A., George, M. S., Little, J. T., Benson, B. E., Willis, M. W., Herscovitch, P. & Post, R. M. Regional cerebral glucose utilization in patients with a range of severities of unipolar depression. *Biol. Psychiatry* **51**, 237–252 (2002).

123. Mayberg, H. S., Brannan, S. K., Tekell, J. L., Silva, J. A., Mahurin, R. K., McGinnis, S. & Jerabek, P. A. Regional metabolic effects of fluoxetine in major depression: Serial changes and relationship to clinical response. *Biol. Psychiatry* **48**, 830–843 (2000).

124. Pardo, J. V., Sheikh, S. A., Schwindt, G., Lee, J. T., Adson, D. E., Rittberg, B. & Abuzzahab, F. S. A preliminary study of resting brain metabolism in treatment-resistant depression before and after treatment with olanzapine-fluoxetine combination. *PLoS One* **15**, 1–18 (2020).

125. Alexander, L., Clarke, H. F. & Roberts, A. C. A focus on the functions of area 25. *Brain Sci.* **9**, 1–33 (2019).

126. Darby, M. M., Yolken, R. H. & Sabunciyan, S. Consistently altered expression of gene sets in postmortem brains of individuals with major psychiatric disorders. *Transl. Psychiatry* **6**, 1–10 (2016).

127. Flint, J. & Kendler, K. S. The Genetics of Major Depression. *Neuron* **81**, 484–503 (2014).

128. Pandey, G. N., Rizavi, H. S., Ren, X., Dwivedi, Y. & Palkovits, M. Region-specific alterations in glucocorticoid receptor expression in the postmortem brain of teenage suicide victims. *Psychoneuroendocrinology* **38**, 2628–2639 (2013).

129. Guintivano, J., Brown, T., Newcomer, A., Jones, M., Cox, O., Maher, B. S., Eaton, W. W., Payne, J. L., Wilcox, H. C. & Kaminsky, Z. A. Identification and Replication of a Combined Epigenetic and Genetic Biomarker Predicting Suicide and Suicidal Behaviors. *Am. J. Psychiatry* **171**, 1287–1296 (2014).

130. Sarubin, N., Hilbert, S., Naumann, F., Zill, P., Maria, A., Caroline, W., Rainer, N., Baghai, T. C., Bühner, M. & Schüle, C. The sex - dependent role of the glucocorticoid receptor in depression : variations in the NR3C1 gene are associated with major depressive disorder in women but not in men. *Eur. Arch. Psychiatry Clin. Neurosci.* **267**, 123–133 (2017).

131. Labonte, B., Yerko, V., Gross, J., Mechawar, N., Meaney, M. J., Szyf, M. & Turecki, G. Differential Glucocorticoid Receptor Exon 1B ,1C, and 1H Expression and Methylation in Suicide Completers with a History of Childhood Abuse. *BPS* **72**, 41–48 (2012).

132. Klempan, T. A., Sequeira, A., Canetti, L., Lalovic, A., Ernst, C. & Turecki, G. Altered expression of genes involved in ATP biosynthesis and GABAergic neurotransmission in the ventral prefrontal cortex of suicides with and without major depression. *Mol. Psychiatry* **14**, 175–189 (2009).

133. Pantazatos, S. P., Huang, Y., Rosoklija, G. B., Dwork, A. J., Arango, V. & Mann, J. J. Whole-transcriptome brain expression and exon-usage profiling in major depression and suicide: evidence for altered glial, endothelial and ATPase activity. *Nat. Publ. Gr.* **22**, 760–773 (2017).

134. Anderson, K. M., Collins, M. A., Kong, R., Fang, K., Li, J., He, T., Chekroud, A. M., Thomas Yeo, B. T. & Holmes, A. J. Convergent molecular, cellular, and cortical neuroimaging signatures of major depressive disorder. *PNAS* **117**, 25138–25149 (2020).

135. Gandal, M. J., Haney, J. R., Parikshak, N. N., Leppa, V., Ramaswami, G., Hartl, C., Schork, A. J., Appadurai, V., Buil, A., Werge, T. M. & Liu, C. Shared molecular neuropathology across major psychiatric disorders parallels polygenic overlap. *Science (80-.).* **697**, 693–697 (2018).

136. Lake, B. B., Chen, S., Sos, B. C., Fan, J., Kaeser, G. E., Yung, Y. C., Duong, T. E., Gao, D., Chun, J., Kharchenko, P. V & Zhang, K. Integrative single-cell analysis of transcriptional and epigenetic states in the human adult brain. *Nat. Biotechnol.* **36**, 70–80 (2018).

137. Darmanis, S., Sloan, S. A., Zhang, Y., Enge, M., Caneda, C. & Shuer, L. M. A survey of human brain transcriptome diversity at the single cell level. *PNAS* **112**, 1–6 (2015).

138. Bartheld, C. S. Von, Bahney, J. & Herculano-houzel, S. The Search for True Numbers of Neurons and Glial Cells in the Human Brain: A Review of 150 Years of Cell Counting. *J. Comp. Neurol.* **524**, 3865–3895 (2016).

139. Allen, N. J. & Eroglu, C. Cell Biology of Astrocyte-Synapse Interactions. *Neuron* **96**, 697–708 (2017).

140. Vasile, F., Dossi, E. & Rouach, N. Human astrocytes: structure and functions in the healthy

brain. *Brain Struct. Funct.* **222**, 2017–2029 (2017).

141. Attwell, D., Buchan, A. M., Charpak, S., Lauritzen, M., Macvicar, B. A. & Newman, E. A. Glial and neuronal control of brain blood flow. *Nature* **468**, 232–243 (2010).

142. Haydon, P. G. Astrocytes and the modulation of sleep. *Curr. Opin. Neurobiol.* **44**, 28–33 (2017).

143. Sofroniew, M. V & Vinters, H. V. Astrocytes: biology and pathology. *Acta Neuropathol.* **119**, 7–35 (2010).

144. Zhou, B., Zhu, Z., Ransom, B. R. & Tong, X. Oligodendrocyte lineage cells and depression. *Mol. Psychiatry* **26**, 103–117 (2021).

145. Bradl, M. & Lassmann, H. Oligodendrocytes: biology and pathology. *Acta Neuropathol.* **119**, 37–53 (2010).

146. Jäkel, S. & Dimou, L. Glial Cells and Their Function in the Adult Brain: A Journey through the History of Their Ablation. *Front. Cell. Neurosci.* **11**, 1–17 (2017).

147. Pfrieger, F. W. & Slezak, M. Genetic Approaches to Study Glial Cells in the Rodent Brain. **701**, 681–701 (2012).

148. Gittins, R. A. & Harrison, P. J. Brief report A morphometric study of glia and neurons in the anterior cingulate cortex in mood disorder. *J. Affect. Disord.* **133**, 328–332 (2011).

149. Deng, S. long, Chen, J. guo & Wang, F. Microglia: A Central Player in Depression. *Curr. Med. Sci.* **40**, 391–400 (2020).

150. Banasr, M., Dwyer, J. M. & Duman, R. S. Cell Atrophy and Loss in Depression: Reversal by Antidepressant Treatment. *Curr. Opin. Cell Biol.* **23**, 730–737 (2011).

151. Majo, M. De, Koontz, M., Rowitch, D. & Ullian, E. M. An update on human astrocytes and their role in development and disease. *Glia* **68**, 685–704 (2020).

152. Zhang, Y., Sloan, S. A., Clarke, L. E., Caneda, C., Plaza, C. A., Blumenthal, P. D., Vogel, H., Steinberg, G. K., Edwards, M. S. B., Li, G., Iii, A. D., Cheshier, S. H., Shuer, L. M., Chang, E. F., Grant, G. A., Gephart, M. G. H. & Barres, B. A. Purification and Characterization of Progenitor and Mature Human Astrocytes Reveals Transcriptional and Functional Differences with Mouse. *Neuron* **89**, 37–53 (2016).

153. Mckenzie, A. T., Wang, M., Hauberg, M. E., Fullard, J. F., Kozlenkov, A., Keenan, A., Hurd, Y. L. & Dracheva, S. Brain Cell Type Specific Gene Expression and Co-expression Network Architectures. *Sci. Rep.* **8**, 1–19 (2018).

154. Hodge, R. D., Bakken, T. E., Miller, J. A., Smith, K. A., Barkan, E. R., Graybuck, L. T., Close, J. L., Long, B., Johansen, N., Penn, O., Yao, Z., Eggermont, J., Höllt, T., Boaz, P., Shehata, S. I., Aevermann, B., Beller, A., Bertagnolli, D., Brouner, K., *et al.* Conserved cell types with divergent features in human versus mouse cortex. *Nature* **573**, 61–68 (2019).

155. Bayraktar, O. A., Bartels, T., Holmqvist, S., Kleshchevnikov, V., Martirosyan, A., Polioudakis, D., Haim, L. Ben, Young, A. M. H., Batiuk, M. Y., Prakash, K., Brown, A., Roberts, K., Paredes, M. F., Kawaguchi, R., Stockley, J. H., Sabeur, K., Chang, S. M., Huang, E., Hutchinson, P., *et al.* Astrocyte layers in the mammalian cerebral cortex revealed by a single-cell in situ transcriptomic map. *Nat. Neurosci.* **23**, 500–509 (2020).

156. Rajkowska, G., Miguel-Hidalgo, J. J., Wei, J., Dilley, G., Pittman, S. D., Meltzer, H. Y., Overholser, J. C., Roth, B. L. & Stockmeier, C. A. Morphometric evidence for neuronal and glial prefrontal cell pathology in major depression. *Biol. Psychiatry* **45**, 1085–1098 (1999).

157. Miguel-hidalgo, J., Baucom, C., Dilley, G., Overholser, J. C., Meltzer, H. Y., Stockmeier, C. A. & Rajkowska, G. Glial Fibrillary Acidic Protein Immunoreactivity in the Prefrontal Cortex Distinguishes Younger from Older Adults in Major Depressive Disorder. *Biol. Psychiatry* **48**, 861–873 (2000).

158. Torres-Platas, S. G., Hercher, C., Davoli, M. A., Maussion, G., Labonte, B., Turecki, G. & Mechawar, N. Astrocytic Hypertrophy in Anterior Cingulate White Matter of Depressed Suicides. *Neuropsychopharmacology* **36**, 2650–2658 (2011).

159. Rajkowska, G., Hughes, J., Stockmeier, C. A., Miguel-hidalgo, J. J. & Maciag, D. Coverage of Blood Vessels by Astrocytic Endfeet Is Reduced in Major Depressive Disorder. *Biol. Psychiatry* **73**, 613–621 (2013).

160. Banasr, M. & Duman, R. S. Glial Loss in the Prefrontal Cortex Is Sufficient to Induce Depressive-like Behaviors. *Biol. Psychiatry* **64**, 863–870 (2008).

161. John, C. S., Smith, K. L., Van'T Veer, A., Gompf, H. S., Carlezon, W. A., Cohen, B. M., Ngür, D. & Bechtholt-Gompf, A. J. Blockade of astrocytic glutamate uptake in the prefrontal cortex induces anhedonia. *Neuropsychopharmacology* **37**, 2467–2475 (2012).

162. Cao, X., Li, L. P., Wang, Q., Wu, Q., Hu, H. H., Zhang, M., Fang, Y. Y., Zhang, J., Li, S. J., Xiong, W. C., Yan, H. C., Gao, Y. B., Liu, J. H., Li, X. W., Sun, L. R., Zeng, Y. N., Zhu, X. H. & Gao, T. M. Astrocyte-derived ATP modulates depressive-like behaviors. *Nat. Med.* **19**, 773–777 (2013).

163. Akula, N., Marenco, S., Johnson, K., Feng, N., Zhu, K., Schulmann, A., Corona, W., Jiang, X., Cross, J., England, B., Nathan, A., Detera-Wadleigh, S., Xu, Q., Auluck, P. K., An, K., Kramer, R., Apud, J., Harris, B. T., Harker Rhodes, C., *et al.* Deep transcriptome sequencing of subgenual anterior cingulate cortex reveals cross-diagnostic and diagnosis-specific RNA expression changes in major psychiatric disorders. *Neuropsychopharmacology* 1–9 (2021) doi:10.1038/s41386-020-00949-5.

164. Foo, L. C., Allen, N. J., Bushong, E. A., Ventura, P. B., Chung, W., Zhou, L., Cahoy, J. D., Daneman, R., Zong, H., Ellisman, M. H. & Barres, B. A. Development of a Method for the Purification and Culture of Rodent Astrocytes. *Neuron* **71**, 799–811 (2011).

165. Cahoy, J. D., Emery, B., Kaushal, A., Foo, L. C., Zamanian, J. L., Christopherson, K. S., Xing, Y., Lubischer, J. L., Krieg, P. A., Krupenko, S. A., Thompson, W. J. & Barres, B. A. A Transcriptome Database for Astrocytes, Neurons, and Oligodendrocytes: A New Resource for Understanding Brain Development and Function. *J. Neurosci.* **28**, 264–278 (2008).

166. Zhang, Y., Chen, K., Sloan, S. A., Bennett, M. L., Scholze, A. R., O'Keeffe, S., Phatnani, H. P., Guarnieri, P., Caneda, C., Ruderisch, N., Deng, S., Liddelow, S. A., Zhang, C., Daneman, R., Maniatis, T., Barres, B. A. & Wu, J. Q. An RNA-sequencing transcriptome and splicing database of glia, neurons, and vascular cells of the cerebral cortex. *J. Neurosci.* **34**, 11929–11947 (2014).

167. Mizee, M. R., Miedema, S. S. M., van der Poel, M., Schuurman, K. G., Strien, M. E. Van,

Melief, J., Smolders, J., Hendrickx, D. A., Heutinck, K. M., Hamann, J. & Huitinga, I. Isolation of primary microglia from the human post-mortem brain: effects of ante- and post-mortem variables. *Acta Neuropathol. Comun.* **5**, 1–14 (2017).

168. Tome-Garcia, J., Doetsch, F. & Tsankova, N. FACS-based Isolation of Neural and Glioma Stem Cell Populations from Fresh Human Tissues Utilizing EGF Ligand. *Bio-Protocol* **7**, 1–23 (2017).

169. Pietersen, C. Y., Lim, M. P. & Woo, T. W. Obtaining High Quality RNA from Single Cell Populations in Human Postmortem Brain Tissue. *J. Vis. Exp.* **30**, 1–9 (2009).

170. Okaty, B. W., Sugino, K. & Nelson, S. B. Cell Type-Specific Transcriptomics in the Brain. *J. Neurosci.* **31**, 6939–6943 (2011).

171. Holt, L. M., Stoyanof, S. T. & Olsen, M. L. Magnetic Cell Sorting for In Vivo and In Vitro Astrocyte, Neuron, and Microglia Analysis. *Curr. Protoc. Neurosci.* **88**, 1–29 (2019).

172. Batiuk, M. Y., Vin, F. De, Duqué, S. I., Li, C., Saito, T., Saido, T., Fiers, M., Belgard, T. G. & Holt, M. G. An immunoaffinity-based method for isolating ultrapure adult astrocytes based on ATP1B2 targeting by the ACSA-2. *J. Biol. Chem.* **292**, 8874–8891 (2017).

173. Poel, M. Van Der, Ulas, T., Mizee, M. R., Hsiao, C., Miedema, S. S. M., Schuurman, K. G., Helder, B., Tas, S. W., Schultze, J. L., Hamann, J. & Huitinga, I. Transcriptional profiling of human microglia reveals grey-white matter heterogeneity and multiple sclerosis-associated changes. *Nat. Commun.* **10**, 1–13 (2019).

174. Martin, D., Xu, J., Porretta, C. & Nichols, C. D. Neurocytometry: Flow Cytometric Sorting of Specific Neuronal Populations from Human and Rodent Brain. *ACS Chem. Neurosci.* **8**, 356–367 (2017).

175. Tagliafierro, L., Bonawitz, K., Glenn, O. C. & Chiba-falek, O. Gene Expression Analysis of Neurons and Astrocytes Isolated by Laser Capture Microdissection from Frozen Human Brain Tissues. **9**, 1–9 (2016).

176. Chandley, M. J., Szebeni, K., Szebeni, A., Crawford, J., Stockmeier, C. A., Turecki, G., Miguel-hidalgo, J. J., Ordway, G. A., Szebeni, K., Szebeni, A. & Quillen, J. H. Gene expression deficits in pontine locus coeruleus astrocytes in men with major depressive disorder. *J. Psychiatry Neurosci.* **38**, 276–285 (2013).

177. Hilker, C. A., Bhagwate, A. V, Jang, J. S., Meyer, J. G., Nair, A. A., Davila, J. I., McDonald, A. M., Winters, J. L., Wehrs, R. N., Jackson, R. A., Gorman, J. A., Cicek, M. S., Oliveira, A. M., Aubrey, T. E., Eckloff, B. W., Halling, K. C., Sun, Z. A. & Jen, J. Impact of RNA Extraction and Target Capture Methods on RNA Sequencing Using Formalin-Fixed, Paraffin Embedded Tissues. *bioRxiv* 1–22 (2019).

178. Xu, X., Stoyanova, E. I., Lemiesz, A. E., Xing, J., Mash, D. C. & Heintz, N. Species and cell-type properties of classically defined human and rodent neurons and glia. *Elife* **7**, 1–47 (2018).

179. Okada, S., Saiwai, H., Kumamaru, H., Kubota, K., Harada, A., Yamaguchi, M., Iwamoto, Y. & Ohkawa, Y. Flow Cytometric Sorting of Neuronal and Glial Nuclei From Central Nervous System Tissue. *J. Cell. Physiol.* **226**, 552–558 (2011).

180. Issler, O., van der Zee, Y. Y., Ramakrishnan, A., Wang, J., Tan, C., Loh, Y. H. E.,

Purushothaman, I., Walker, D. M., Lorsch, Z. S., Hamilton, P. J., Peña, C. J., Flaherty, E., Hartley, B. J., Torres-Berrío, A., Parise, E. M., Kronman, H., Duffy, J. E., Estill, M. S., Calipari, E. S., *et al.* Sex-Specific Role for the Long Non-coding RNA LINC00473 in Depression. *Neuron* **106**, 912–926 (2020).

181. Lutz, P., Ph, D., Tanti, A., Ph, D., Gasecka, A., Ph, D., Barnett-burns, S., Sc, B., Kim, J. J. & Sc, B. Association of a History of Child Abuse With Impaired Myelination in the Anterior Cingulate Cortex: Convergent Epigenetic, Transcriptional, and Morphological Evidence. *Am. J. Psychiatry Online* **174**, 1185–1194 (2017).

182. Matevossian, A. & Akbarian, S. Neuronal Nuclei Isolation from Human Postmortem Brain Tissue. *J. Vis. Exp.* **20**, 1–2 (2008).

183. Mendizabal, I., Berto, S., Usui, N., Toriumi, K., Chatterjee, P., Douglas, C., Huh, I., Jeong, H., Layman, T., Tamminga, C. A., Preuss, T. M., Konopka, G. & Yi, S. V. Cell type-specific epigenetic links to schizophrenia risk in the brain. *Genome Biol.* **20**, 1–21 (2019).

184. Nagy, C., Maitra, M., Tanti, A., Suderman, M., Théroux, J. F., Davoli, M. A., Perlman, K., Yerko, V., Wang, Y. C., Tripathy, S. J., Pavlidis, P., Mechawar, N., Ragoussis, J. & Turecki, G. Single-nucleus transcriptomics of the prefrontal cortex in major depressive disorder implicates oligodendrocyte precursor cells and excitatory neurons. *Nat. Neurosci.* **23**, 771–781 (2020).

185. Habib, N., Avraham-davidi, I., Basu, A., Burks, T., Shekhar, K., Hofree, M., Choudhury, S. R., Aguet, F., Gelfand, E., Ardlie, K., Weitz, D. A., Rozenblatt-rosen, O., Zhang, F. & Regev, A. Massively parallel single-nucleus RNA-seq with. *Nat. Methods* **14**, 955–958 (2017).

186. Krishnaswami, S. R., Grindberg, R. V, Novotny, M., Venepally, P., Lacar, B., Bhutani, K., Linker, S. B., Pham, S., Erwin, J. A., Miller, J. A., Hodge, R., Mccarthy, J. K., Kelder, M., Mccorrison, J., Aevermann, B. D., Fuertes, F. D., Scheuermann, R. H., Lee, J., Lein, E. S., *et al.* Using single nuclei for RNA-seq to capture the transcriptome of postmortem neurons. *Nat. Protoc.* **11**, 499–524 (2016).

187. Czéh, B., Fuchs, E., Wiborg, O. & Simon, M. Animal models of major depression and their clinical implications. *Prog. Neuropsychopharmacol. Biol. Psychiatry* **64**, 293–310 (2016).

188. Azzinnari, D., Sigrist, H., Staehli, S., Palme, R., Hildebrandt, T., Leparc, G., Hengerer, B., Seifritz, E. & Pryce, C. R. Mouse social stress induces increased fear conditioning, helplessness and fatigue to physical challenge together with markers of altered immune and dopamine function. *Neuropharmacology* **85**, 328–341 (2014).

189. Bagot, R. C., Cates, H. M., Purushothaman, I., Shen, L., Zhang, B. & Nestler, E. J. Circuit-wide Transcriptional Profiling Reveals Brain Article Circuit-wide Transcriptional Profiling Networks Regulating Depression Susceptibility. *Neuron* **90**, 969–983 (2016).

190. Veeraiah, P., Noronha, J. M., Maitra, S., Bagga, P., Khandelwal, N., Chakravarty, S., Kumar, A. & Patel, A. B. Dysfunctional Glutamatergic and γ-Aminobutyric Acidergic Activities in Prefrontal Cortex of Mice in Social Defeat Model of Depression. *Biol. Psychiatry* **76**, 231–238 (2014).

191. Huang, D., Li, C., Zhang, W., Qin, J., Jiang, W. & Hu, C. Dysfunction of astrocytic connexins 30 and 43 in the medial prefrontal cortex and hippocampus mediates depressive-

like behaviours. *Behav. Brain Res.* **372**, 111950 (2019).

192. Guillot, F., Garcia, A., Salou, M., Brouard, S., Laplaud, D. A. & Nicot, A. B. Transcript analysis of laser capture microdissected white matter astrocytes and higher phenol sulfotransferase 1A1 expression during autoimmune neuroinflammation. *J. Neuroinflammation* **12**, 1–14 (2015).

193. Doyle, J. P., Dougherty, J. D., Heiman, M., Schmidt, E. F., Stevens, T. R., Ma, G., Bupp, S., Shrestha, P., Shah, R. D., Doughty, M. L., Gong, S. & Greengard, P. Application of a Translational Profiling Approach for the Comparative Analysis of CNS Cell Types. *Cell* **135**, 749–762 (2008).

194. Simard, S., Rudyk, C. A., Hayley, S., Mcquaid, R. J. & Salmaso, N. Profiling changes in cortical astroglial cells following chronic stress. *Neuropsychopharmacology* **43**, 1961–1971 (2018).

195. Pan, J. & Wan, J. Methodological comparison of FACS and MACS isolation of enriched microglia and astrocytes from mouse brain. *J. Immunol. Methods* **486**, 1–7 (2020).

196. Sneeboer, M. A. M., Snijders, G. J. L. J., Berdowski, W. M., Fernández-andreu, A., Donor, P., Bank, B., Mierlo, H. C. Van & Berlekom, A. B. Van. Microglia in post-mortem brain tissue of patients with bipolar disorder are not immune activated. *Transl. Psychiatry* **9**, 1–10 (2019).

197. Amamoto, R., Zuccaro, E., Curry, N. C., Khurana, S., Chen, H. H., Cepko, C. L. & Arlotta, P. FIN-Seq: Transcriptional profiling of specific cell types from frozen archived tissue of the human central nervous system. *Nucleic Acids Res.* **48**, 1–12 (2020).

198. Picelli, S., Faridani, O. R., Björklund, Å. K., Winberg, G., Sagasser, S. & Sandberg, R. Full-length RNA-seq from single cells using Smart-seq2. *Nat. Protoc.* **9**, 171–181 (2014).

199. Ravasi, T., Suzuki, H., Cannistraci, C. V., Katayama, S., Bajic, V. B., Tan, K., Akalin, A., Schmeier, S., Kanamori-katayama, M., Kamburov, A., Kaur, M., Kawaji, H., Kubosaki, A. & Lassmann, T. An Atlas of Combinatorial Transcriptional Regulation in Mouse and Man. *Cell* **140**, 744–752 (2010).

200. Sun, X. W., Cornwell, X. A., Li, J., Peng, X. S., Osorio, M. J., Aalling, X. N., Wang, S., Benraiss, A., Lou, N., Goldman, S. A. & Nedergaard, X. M. SOX9 Is an Astrocyte-Specific Nuclear Marker in the Adult Brain Outside the Neurogenic Regions. *J. Neurosci.* **37**, 4493–4507 (2017).

201. García-Cabezas, M. Á., John, Y. J., Barbas, H. & Zikopoulos, B. Distinction of Neurons, Glia and Endothelial Cells in the Cerebral Cortex: An Algorithm Based on Cytological Features. *Front. Neuroanat.* **10**, 1–28 (2016).

202. Thomsen, E. R., Mich, J. K., Yao, Z., Hodge, R. D., Doyle, A. M., Jang, S., Shehata, S. I., Nelson, A. M., Shapovalova, N. V, Levi, B. P. & Ramanathan, S. Fixed single-cell transcriptomic characterization of human radial glial diversity. *Nat. Methods* **13**, 87–93 (2016).

203. Stelzer, G., Rosen, N., Plaschkes, I., Zimmerman, S., Twik, M., Fishilevich, S., Iny Stein, T., Nudel, R., Lieder, I., Mazor, Y., Kaplan, S., Dahary, D., Warshawsky, D., Guan-Golan, Y., Kohn, A., Rappaport, N., Safran, M. & Lancet, D. The GeneCards suite: From gene data

mining to disease genome sequence analyses. *Curr. Protoc. Bioinforma.* **54**, 1.30.1-1.30.33 (2016).

204. Bateman, A., Martin, M. J., Orchard, S., Magrane, M., Agivetova, R., Ahmad, S., Alpi, E., Bowler-Barnett, E. H., Britto, R., Bursteinas, B., Bye-A-Jee, H., Coetzee, R., Cukura, A., Silva, A. Da, Denny, P., Dogan, T., Ebenezer, T. G., Fan, J., Castro, L. G., *et al.* UniProt: The universal protein knowledgebase in 2021. *Nucleic Acids Res.* **49**, D480–D489 (2021).

205. The Genotype-Tissue Expression (GTEx). *Broad Institute of MIT and Harvard* https://gtexportal.org/home/.

206. Lafzi, A., Moutinho, C., Picelli, S. & Heyn, H. Tutorial: guidelines for the experimental design of single-cell RNA sequencing studies. *Nat. Protoc.* **13**, 2742–2757 (2018).

207. Hrdlickova, R., Toloue, M. & Tian, B. RNA-Seq methods for transcriptome analysis. *Wiley Interdiscip. Rev. RNA* **8**, 1–24 (2016).

208. Jungblut, M., Tiveron, M. C., Barral, S., Abrahamsen, B., Pennartz, S., Urgen, J., Pfrieger, F. W., Stoffel, W., Cremer, H. & Bosio, A. Isolation and Characterization of Living Primary Astroglial Cells Using the New GLAST-Specific Monoclonal Antibody ACSA-1. *Glia* **60**, 894–907 (2012).

209. Feldmann, M., Pathipati, P., Sheldon, R. A., Jiang, X. & Ferriero, D. M. Isolating astrocytes and neurons sequentially from postnatal murine brains with a magnetic cell separation technique. *J. Biol. Methods* **1**, 1–7 (2014).

210. Holt, L. M. & Olsen, M. L. Novel Applications of Magnetic Cell Sorting to Analyze Cell-Type Specific Gene and Protein Expression in the Central Nervous System. *PLoS One* **11**, 1–18 (2016).

211. Kantzer, C. G., Boutin, C., Herzig, I. D., Wittwer, C., Reiß, S., Catherine, M., Jan, T., Thomas, D., Ohlig, S., Ninkovic, J., Cremer, H., Pennartz, S., Jungblut, M. & Bosio, A. Anti-ACSA-2 defines a novel monoclonal antibody for prospective isolation of living neonatal and adult astrocytes. *Glia* **65**, 990–1004 (2017).

212. Allen Developing Mouse Brain Atlas. *Allen Institute for Brain Science* http://developingmouse.brain-map.org/ (2008).

213. Ehret, F., Vogler, S. & Kempermann, G. Neurosphere Co-culture Assay. *Bio-protocol* **6**, 1–14 (2016).

214. Lake, B. B., Ai, R., Kaeser, G. E., Salathia, N. S., Yung, Y. C., Liu, R., Wildberg, A., Gao, D., Fung, H., Chen, S., Vijayaraghavan, R., Wong, J., Chen, A., Sheng, X., Kaper, F., Shen, R., Ronaghi, M., Fan, J. & Chun, J. Neuronal subtypes and diversity revealed by single-nucleus RNA sequencing of the human brain. **352**, 352–357 (2016).

215. Gutierrez-Sacristan, A., Grosdidier, S., Valverde, O., Torrens, M., Bravo, A., Piñero, J., Sanz, F. & Furlong, L. I. PsyGeNET: A knowledge platform on psychiatric disorders and their genes. *Bioinformatics* **31**, 3075–3077 (2015).

216. Huang, D. W., Sherman, B. T. & Lempicki, R. A. Systematic and integrative analysis of large gene lists using DAVID bioinformatics resources. *Nat. Protoc.* **4**, 44–57 (2009).

217. Szklarczyk, D., Gable, A. L., Lyon, D., Junge, A., Wyder, S., Huerta-Cepas, J., Simonovic,

M., Doncheva, N. T., Morris, J. H., Bork, P., Jensen, L. J. & Von Mering, C. STRING v11: Protein-protein association networks with increased coverage, supporting functional discovery in genome-wide experimental datasets. *Nucleic Acids Res.* **47**, D607–D613 (2019).

218. Bernstein, H. G., Meyer-Lotz, G., Dobrowolny, H., Bannier, J., Steiner, J., Walter, M. & Bogerts, B. Reduced density of glutamine synthetase immunoreactive astrocytes in different cortical areas in major depression but not in bipolar I disorder. *Front. Cell. Neurosci.* **9**, 1–12 (2015).

219. Lalovic, A., Klempan, T., Sequeira, A., Luheshi, G. & Turecki, G. Altered expression of lipid metabolism and immune response genes in the frontal cortex of suicide completers. *J. Affect. Disord.* **120**, 24–31 (2010).

220. Labonté, B., Engmann, O., Purushothaman, I., Menard, C., Wang, J., Tan, C., Scarpa, J. R., Moy, G., Loh, Y. E., Cahill, M., Lorsch, Z. S., Hamilton, P. J., Calipari, E. S., Hodes, G. E., Issler, O., Kronman, H., Pfau, M., Obradovic, A. L. J., Dong, Y., *et al.* Sex-specific transcriptional signatures in human depression. *Nat. Med.* **23**, 1102–1111 (2017).

221. Zeisel, A., Manchado, A. B. M., Codeluppi, S., Lönnerberg, P., Manno, G. La, Juréus, A. & Marques, S. Cell types in the mouse cortex and hippocampus revealed by single-cell RNA-seq. *Science (80-.).* **347**, 1138–1142 (2015).

222. Batiuk, M. Y., Martirosyan, A., Wahis, J., de Vin, F., Marneffe, C., Kusserow, C., Koeppen, J., Viana, J. F., Oliveira, J. F., Voet, T., Ponting, C. P., Belgard, T. G. & Holt, M. G. Identification of region-specific astrocyte subtypes at single cell resolution. *Nat. Commun.* **11**, 1–15 (2020).

223. Coe Clough, N. E. & Hauer, P. J. Using polyclonal and monoclonal antibodies in regulatory testing of biological products. *ILAR J.* **46**, 300–306 (2005).

224. Xia, C. Y., Wang, Z. Z., Yamakuni, T. & Chen, N. H. A novel mechanism of depression: role for connexins. *Eur. Neuropsychopharmacol.* **28**, 483–498 (2018).

225. Orthmann-Murphy, J. L., Abrams, C. K. & Scherer, S. S. Gap junctions couple astrocytes and oligodendrocytes. *J. Mol. Neurosci.* **35**, 101–116 (2008).

226. Esseltine, J. L. & Laird, D. W. Next-Generation Connexin and Pannexin Cell Biology. *Trends Cell Biol.* **26**, 944–955 (2016).

227. Reichard, A. & Asosingh, K. Best Practices for Preparing a Single Cell Suspension from Solid Tissues for Flow Cytometry. *Physiol. Behav.* **95**, 219–226 (2019).

228. Srinivasan, K., Friedman, B. A., Etxeberria, A., Huntley, M. A., van der Brug, M. P., Foreman, O., Paw, J. S., Modrusan, Z., Beach, T. G., Serrano, G. E. & Hansen, D. V. Alzheimer's Patient Microglia Exhibit Enhanced Aging and Unique Transcriptional Activation. *Cell Rep.* **31**, 107843 (2020).

229. Schnell, U., Dijk, F., Sjollema, K. A. & Giepmans, B. N. G. Immunolabeling artifacts and the need for live-cell imaging. *Nat. Methods* **9**, 152–158 (2012).

230. Wu, C., Bendriem, R. M., Garamszegi, S. P., Song, L. & Lee, C.-T. RNA sequencing in post-mortem human brains of neuropsychiatric disorders. *Psychiatry Clin. Neurosci.* **71**, 663–672 (2017).

231. Price, A. J., Hwang, T., Tao, R., Burke, E. E., Rajpurohi, A., Shin, J. H., Hyde, T. M., Kleinman, J. E., Jaffe, A. E. & Weinberger, D. R. Characterizing the nuclear and cytoplasmic transcriptomes in developing and mature human cortex uncovers new insight into psychiatric disease gene regulation. *Genome Res.* **30**, 1–11 (2020).

232. Bakken, T. E., Hodge, R. D., Miller, J. A., Yao, Z., Nguyen, N., Aevermann, B., Barkan, E., Bertagnolli, D., Casper, T., Dee, N., Garren, E., Goldy, J., Graybuck, L. T., Kroll, M., Lasken, R. S., Lathia, K., Parry, S., Rimorin, C., Scheuermann, R. H., *et al.* Single-nucleus and single-cell transcriptomes compared in matched cortical cell types. *PLoS One* **13**, 1–24 (2018).

233. Gerrits, E., Heng, Y., Boddeke, E. W. G. M. & Eggen, B. J. L. Transcriptional profiling of microglia; current state of the art and future perspectives. *Glia* **68**, 740–755 (2020).

234. Tome-Garcia, J., Nudelman, G., Mussa, Z., Caballero, E., Jiang, Y., Beaumont, K. G., Wang, Y. C., Sebra, R., Akbarian, S., Pinto, D., Zaslavsky, E. & Tsankova, N. M. Cell type-specific isolation and transcriptomic profiling informs glial pathology in human temporal lobe epilepsy. *bioRxiv* 1–34 (2020) doi:10.1101/2020.12.11.421370.

235. Nott, A., Schlachetzki, J. C. M., Fixsen, B. R. & Glass, C. K. Nuclei isolation of multiple brain cell types for omics interrogation. *Nat. Protoc.* **16**, 1629–1646 (2021).

236. Yogarajah, M., Matarin, M., Vollmar, C., Thompson, P. J., Duncan, J. S., Symms, M., Moore, A. T., Liu, J., Thom, M., van Heyningen, V. & Sisodiya, S. M. PAX6, brain structure and function in human adults: Advanced MRI in aniridia. *Ann. Clin. Transl. Neurol.* **3**, 314–330 (2016).

237. White, K., Yang, P., Li, L., Farshori, A., Medina, A. E. & Zielke, H. R. Effect of Postmortem Interval and Years in Storage on RNA Quality of Tissue at a Repository of the NIH NeuroBioBank. *Biopreserv. Biobank.* **16**, 148–157 (2018).

238. Mexal, S., Berger, R., Adams, C. E., Ross, R. G., Freedman, R. & Leonard, S. Brain pH has a significant impact on human postmortem hippocampal gene expression profiles. *Brain Res.* **1106**, 1–11 (2006).

239. De Sousa, R. T., Loch, A. A., Carvalho, A. F., Brunoni, A. R., Haddad, M. R., Henter, I. D., Zarate, C. A. & MacHado-Vieira, R. Genetic Studies on the Tripartite Glutamate Synapse in the Pathophysiology and Therapeutics of Mood Disorders. *Neuropsychopharmacology* **42**, 787–800 (2017).

240. Skowrońska, K., Obara-Michlewska, M., Czarnecka, A., Dąbrowska, K., Zielińska, M. & Albrecht, J. Persistent Overexposure to N-Methyl-d-Aspartate (NMDA) Calcium-Dependently Downregulates Glutamine Synthetase, Aquaporin 4, and Kir4.1 Channel in Mouse Cortical Astrocytes. *Neurotox. Res.* **35**, 271–280 (2019).

241. Chandley, M. J., Szebeni, A., Szebeni, K., Crawford, J. D., Stockmeier, C. A., Turecki, G., Kostrzewa, R. M. & Ordway, G. A. Elevated gene expression of glutamate receptors in noradrenergic neurons from the locus coeruleus in major depression. *Int. J. Neuropsychopharmacol.* **17**, 1569–1578 (2014).

242. Dean, B., Gibbons, A. S., Boer, S., Uezato, A., Meador-Woodruff, J., Scarr, E. & McCullumsmith, R. E. Changes in cortical N-methyl-d-aspartate receptors and post-synaptic density protein 95 in schizophrenia, mood disorders and suicide. *Aust. N. Z. J.*

Psychiatry **50**, 275–283 (2016).

243. Sugiyama, M., Banno, R., Yaginuma, H., Taki, K., Mizoguchi, A., Tsunekawa, T., Onoue, T., Takagi, H., Ito, Y., Iwama, S., Goto, M., Suga, H., Komine, O., Yamanaka, K. & Arima, H. Hypothalamic glial cells isolated by MACS reveal that microglia and astrocytes induce hypothalamic inflammation via different processes under high-fat diet conditions. *Neurochem. Int.* **136**, 104733 (2020).

244. Montana, V., Malarkey, E. B., Verderio, C., Matteoli, M. & Parpura, V. Vesicular Transmitter Release from Astrocytes. *Glia* **54**, 700–715 (2006).

245. Zeisel, A., Hochgerner, H., Lonnerberg, P., Johnsson, A., Memic, F., Zwan, J. Van Der, Haring, M., Braun, E., Borm, L. E., La Manno, G., Codeluppi, S., Furlan, A., Lee, K., Skene, N. G., Harris, K. D., Hjerling-leffler, J., Arenas, E., Ernfors, P., Marklund, U., *et al.* Molecular Architecture of the Mouse Nervous System. *Cell* **174**, 999–1014 (2018).

246. Orre, M., Kamphuis, W., Osborn, L. M., Melief, J., Kooijman, L., Huitinga, I., Klooster, J., Bossers, K. & Hol, E. M. Acute isolation and transcriptome characterization of cortical astrocytes and microglia from young and aged mice. *Neurobiol. Aging* **35**, 1–14 (2014).

247. Tertil, M., Skupio, U., Barut, J., Dubovyk, V., Wawrzczak-Bargiela, A., Soltys, Z., Golda, S., Kudla, L., Wiktorowska, L., Szklarczyk, K., Korostynski, M., Przewlocki, R. & Slezak, M. Glucocorticoid receptor signaling in astrocytes is required for aversive memory formation. *Transl. Psychiatry* **8**, 1–11 (2018).

248. Cui, Y., Yang, Y., Ni, Z., Dong, Y., Cai, G., Foncelle, A., Ma, S. & Sang, K. Astroglial Kir4.1 in the lateral habenula drives neuronal bursts in depression. *Nat. Publ. Gr.* **554**, 323–327 (2018).

249. Czéh, B. & Nagy, S. A. Clinical Findings Documenting Cellular and Molecular Abnormalities of Glia in Depressive Disorders. *Front. Mol. Neurosci.* **11**, 1–16 (2018).

250. Andrus, B. M., Blizinsky, K., Vedell, P. T., Dennis, K., Shukla, P. K., Schaffer, D. J., Radulovic, J., Churchill, G. A. & Redei, E. E. Gene expression patterns in the hippocampus and amygdala of endogenous depression and chronic stress models. *Mol. Psychiatry* **17**, 49–61 (2012).

251. Sequeira, A., Klempan, T., Canetti, L., Ffrench-Mullen, J., Benkelfat, C., Rouleau, G. A. & Turecki, G. Patterns of gene expression in the limbic system of suicides with and without major depression. *Mol. Psychiatry* **12**, 640–655 (2007).

252. Schneider, E., El Hajj, N., Müller, F., Navarro, B. & Haaf, T. Epigenetic Dysregulation in the Prefrontal Cortex of Suicide Completers. *Cytogenet. Genome Res.* **146**, 19–27 (2015).

253. Quesseveur, G., Portal, B., Basile, J. A., Ezan, P., Mathou, A., Halley, H., Leloup, C., Fioramonti, X., Déglon, N., Giaume, C., Rampon, C. & Guiard, B. P. Attenuated levels of hippocampal connexin 43 and its phosphorylation correlate with antidepressant-and anxiolytic-like activities in mice. *Front. Cell. Neurosci.* **9**, 1–12 (2015).

254. Slezak, M. & Pfrieger, F. W. New roles for astrocytes: Regulation of CNS synaptogenesis. *Trends Neurosci.* **26**, 531–535 (2003).

255. Barres, B. A. The Mystery and Magic of Glia: A Perspective on Their Roles in Health and Disease. *Neuron* **60**, 430–440 (2008).

256. Hillen, A. E. J., Burbach, J. P. H. & Hol, E. M. Cell adhesion and matricellular support by astrocytes of the tripartite synapse. *Prog. Neurobiol.* **165**–**167**, 66–86 (2018).

257. Sild, M., Ruthazer, E. S. & Booij, L. Major depressive disorder and anxiety disorders from the glial perspective: Etiological mechanisms, intervention and monitoring. *Neurosci. Biobehav. Rev.* **83**, 474–488 (2017).

258. Evans, S. J., Choudary, P. V., Neal, C. R., Li, J. Z., Vawter, M. P., Tomita, H., Lopez, J. F., Thompson, R. C., Meng, F., Stead, J. D., Walsh, D. M., Myers, R. M., Bunney, W. E., Watson, S. J., Jones, E. G. & Akil, H. Dysregulation of the fibroblast growth factor system in major depression. *Proc. Natl. Acad. Sci. U. S. A.* **101**, 15506–15511 (2004).

259. Cattaneo, A., Gennarelli, M., Uher, R., Breen, G., Farmer, A., Aitchison, K. J., Craig, I. W., Anacker, C., Zunsztain, P. A., Mcguffin, P. & Pariante, C. M. Candidate Genes Expression Profile Associated with Antidepressants Response in the GENDEP Study: Differentiating between Baseline 'Predictors' and Longitudinal 'Targets'. *Neuropsychopharmacology* **38**, 377–385 (2013).

260. Rial, D., Lemos, C., Pinheiro, H., Duarte, J. M., Gonçalves, F. Q., Real, J. I., Prediger, R. D. & Gonçalves, N. Depression as a Glial-Based Synaptic Dysfunction. *Front. Cell. Neurosci.* **9**, 1–11 (2016).

261. Kimelberg, H. K. & Nedergaard, M. Functions of Astrocytes and their Potential As Therapeutic Targets. *Neurotherapeutics* **7**, 338–353 (2010).

262. Sani, G., Napoletano, F., Maria Forte, A., D. Kotzalidis, G., Panaccione, I., Maria Porfiri, G., Simonetti, A., Caloro, M., Girardi, N., Ludovica Telesforo, C., Serra, G., Romano, S., Manfredi, G., Savoja, V., Maria Tamorri, S., E. Koukopoulos, A., Serata, D., Rapinesi, C., Del Casale, A., *et al.* The Wnt Pathway in Mood Disorders. *Curr. Neuropharmacol.* **10**, 239–253 (2012).

263. Mahmoud, S., Gharagozloo, M., Simard, C. & Gris, D. Astrocytes Maintain Glutamate Homeostasis in the CNS by Controlling the Balance between Glutamate Uptake and Release. *Cells* **8**, 1–27 (2019).

264. Schousboe, A., Bak, L. K. & Waagepetersen, H. S. Astrocytic control of biosynthesis and turnover of the neurotransmitters glutamate and GABA. *Front. Endocrinol. (Lausanne).* **4**, 1–11 (2013).

265. Miguel-hidalgo, J. J., Waltzer, R., Whittom, A. A., Austin, M. C., Rajkowska, G. & Stockmeier, C. A. Glial and glutamatergic markers in depression, alcoholism, and their comorbidity. *J. Affect. Disord.* **127**, 230–240 (2010).

266. Medina, A., Burke, S., Thompson, R. C., Bunney, W., Myers, R. M., Schatzberg, A., Akil, H. & Watson, S. J. Glutamate transporters: A key piece in the glutamate puzzle of major depressive disorder. *J. Psychiatr. Res.* **47**, 1150–1156 (2013).

267. Blacker, C. J., Millischer, V., Webb, L. M., Ho, A. M. C., Schalling, M., Frye, M. A. & Veldic, M. EAAT2 as a Research Target in Bipolar Disorder and Unipolar Depression: A Systematic Review. *Mol. Neuropsychiatry* **5**, 44–59 (2019).